Fabrication, structural and optical study of self-assembled hyperbolic metamaterial

Xuan Wang

université de BORDEAUX

Ecole doctorale Sciences Chimique

Centre de Recherche Paul Pascal, CNRS-Université Bordeaux

Thèse

Présentée pour l'obtention du grade de DOCTEUR DE L'UNIVERSITE DE BORDEAUX

Par

Xuan WANG

Fabrication, structural and optical study of self-assembled hyperbolic metamaterial

---

Spécialité: Physico-chimie de la matière condensée

Soutenue le devant un jury composé de :

M. BILLON Laurent	Professeur des Universités, IPREM	Rapporteur
Mme TESTARD Fabienne	Chercheur,CEA	Rapportrice
M. BACHELOT Renaud	Professeur, UTT	Examinateur
M. KILDEMO Morten	Professeur, NTNU	Examinateur
Mme PANSU Brigitte	Professeur, Université Paris Sud	Examinatrice
Mme ZAKRI Cécile	Professeur,Université Bordeaux	Présidente
Mme PONSINET Virginie	Chargée de Recherches, CRPP	Directice de thèse

Acknowledgements

This thesis was carried out at the Centre de Recherche Paul Pascal in Bordeaux. These four years of PhD research constitute one of the most important period in my life. The result of the PhD is not only the academic papers, but also most importantly, how I am thinking and acting in the academic field, which will definitely change my future.

This PhD work could not be finished without the contribution of many people. I would like to express my best gratitude to my supervisor, colleagues, friends, and family.

Firstly, I would like to thank Virginie Ponsinet, director of my thesis, for her patience and advice during these four years, also for providing me the opportunity of joining the META team. I learnt a lot of things from her, the academic knowledge, the way of doing research, and the way of communicating efficiently with people. This will be precious wealth in all my future academic life. Our communication is always flexible and efficient. She is always supporting me in my research and daily life which I truly appreciate.

Thanks to Philippe Barois for his kindness and for helping me with the X-ray reflectivity. Thanks to Isabelle Ly for her help in the electron microscopy work. Also I would like to thank the BIC team (Bordeaux Imaging Center) for training me in ultramicrotomy. Thanks to Hassan Saadaoui for the AFM measurements. Thanks to Ahmed Bentaleb for his help on small angle X-rays scattering. Thanks to Kévin Ehrhardt for his help with ellipsometric measurements.

I also would like to thanks to Johann Toudert now at ICFO, Morten Kildemo from NTNU, Marc Warenghem from UCCS, Enric Garcia-Caurel from LPICM and Alexandre Baron and Ashod Aradian from CRPP for their help on the analysis of optical properties.

I extend my deepest thanks to the master students who worked with me during this thesis. Thanks to Anirudh Peyyeti, Chloé Paquet and Nicolas Benoot.

Thanks to all the members from the Metamaterials group for their kindness, humor, suggestions and pleasant atmosphere to work with.

I would like to address special thanks to the LabEx AMADEus, the China Scholarship Council (CSC) and the Université de Bordeaux for the financial support of my study in France.

Finally, I devoted my deep love and thanks to my friends from different countries and to my lovely family. With the support from all of you, I can finish this work successfully. Love you forever!

Xuan WANG

Oct. 2017

Bordeaux, France

Abstract

Novel optical properties in the visible range are foreseen when organizing nanoresonators, which can be performed by the self-assembly of plasmonic nanoparticles prepared by wet chemistry. In this project, we use templating block copolymers structures to organize plasmonic particles. Our goal is to relate the structure of the prepared nanocomposites thin films, and in particular the nature, density and spatial organization of the nanoparticles, with their optical index.

For this purpose, we first fabricate lamellar superlattices of diblock copolymers (poly(styrene)-*block*-poly(2-vinylpyridine) of controlled thickness (100nm-700nm), controlled lamellar period size(17 nm-70 nm) and optimized alignment and homogeneity.

Following the fabrication of the multilayer templates, an *in situ* and reproducible synthesis of metallic nanoparticles was developed in order to generate nanocomposites selectively inside the P2VP layers. The size of Au nanoparticles can be well controlled around 7-10 nm. We also found that the reduction process could influence the shape (sphere, triangle or cylinder) and size by using different solvents or reducing agents. Because the extraction of accurate optical responses from the spectroscopic ellipsometry data, which will come in the last part, critically relies on the precise knowledge of the sample structure, we have used several experimental techniques to access a precise description of the produced materials. In particular, we used a Quartz Crystal Microbalance as a measurement tool to 'kinetically' study the volume fraction of Au loading as we increase the number of gold introduction cycles. We find that the amount of gold in the composite layers can be varied up to typically 40 volume%.

The optical properties of the nanocomposite films are determined by variable angle spectroscopic ellipsometry and analyzed by appropriately developed effective medium models. The films are structurally uniaxial and homogeneous, and we can define their dielectric permittivity tensor with the ordinary (parallel to the substrate) and extraordinary (normal to the substrate) components. The analysis of the lamellar structures allows the extraction of the components ε_o and ε_e, both presenting a

resonance close to λ=540nm, with a significantly stronger amplitude for ε_o. When the gold load is high enough and the couplings between particles are strong enough, the values of ε_o become negative close to the resonance, and the material reaches the so-called hyperbolic regime, which constitutes a step towards applications in hyper-resolution imaging.

Résumé

Des propriétés optiques inédites sont prédites si des nanorésonateurs optiques sont organisés dans un matériau, ce qui peut être réalisé par l'auto-assemblage de nanoparticules plasmoniques synthétisées chimiquement. Dans ce travail de doctorat, nous utilisons des structures ordonnées de copolymères à blocs pour organiser des nanoparticules plasmoniques. Nous étudions le lien entre la structure des nanocomposites en films minces, et en particulier la nature, la densité et l'organisation des nanoparticules, et leurs propriétés optiques.

Pour cela, nous avons tout d'abord produit des phases lamellaires de copolymères diblocs poly(styrène)-*block*-poly(2-vinylpyridine) (PS-b-P2VP) en films minces d'épaisseur (100nm-700nm) et de période lamellaire (17nm-70nm) contrôlées, et dont l'alignement et l'homogénéité sont optimisés.

Nous avons développé une synthèse in situ, au sein de ces films lamellaires, qui permet de produire de façon contrôlée et reproductible, des nanoparticules plasmoniques de diamètre 7-10nm sélectivement dans les domaines P2VP. Nous avons montré que la taille et la forme des particules d'or formées in situ peuvent être modifiées en jouant sur le solvant et le réducteur chimique mis en jeu. Nous avons étudié en détail la structure des nanocomposites formulés, ce qui est en particulier nécessaire à la bonne exploitation des données d'ellipsométrie spectroscopique afin de déterminer les réponses optiques. La structure des échantillons a été étudiée par différentes méthodes de microscopie (électronique en transmission ou à balayage, à force atomique), ainsi que de la diffusion des rayons X. Nous avons utilisé une microbalance à Quartz pour étudier la quantité d'or introduite dans les matrices lamellaires de manière « cinétique » au fil de son augmentation progressive. La quantité d'or atteint des valeurs de 40 % en volume.

Les propriétés optiques des films nanocomposites sont déterminées par ellipsométrie spectroscopique à angle variable et analysées à l'aide de modèles de milieux effectifs. Les films sont homogènes et anisotropes uniaxes, et on peut définir leur tenseur de permittivité diélectrique avec une composante ordinaire ε_o (parallèle au substrat) et une composante extraordinaire ε_e (perpendiculaire au substrat). L'analyse permet de montrer que les deux composantes ε_o and ε_e présentent une résonance

proche de la longueur d'onde λ=540nm, avec une amplitude très supérieure pour ε_o. Lorsque la quantité d'or dans la structure lamellaire est suffisante, ε_o devient négatif au voisinage de la résonance et le matériau atteint le régime appelé hyperbolique, ce qui constitue un jalon essentiel pour le développement de matériaux pour des applications en imagerie hyper-résolue.

Contents

General Introduction

Over the past decades, big interest in fabrication and utilization of nanocomposites has grown. Thanks to advances both in manufacturing and measurement. Artificial materials structurally designed with the purpose of producing extraordinary optical electrical or magnetic properties. The principle of which was proposed in 1968 by Veselago, and which has been a very active field of research since 20 years ago.By combining nanostructuration and anisotropy, it is possible to engineer novel and non-natural dispersion relations, in order to control original propagation properties. This is why a recent interest has focused on a special case of uniaxial anisotropic metamaterials, called hyperbolic materials. At the nano-scale, lithographic manufacturing processes used for producing such metamaterials, are no longer adequate due to the complex fabrication process and limited dimensional size. Self-assembly and nano-chemistry appearance provide a new ways of manufacturing.

This thesis was carried out within the big project in “meta group”, which aims to formulate new generations of metamaterials with innovative optical properties in the visible light domain. For this purpose, the aim of this PhD thesis is to study methodologies for the fabrication of nanocomposites of block copolymers with gold nanoparticles specifically in lamellar systems in metallic nanoparticles, and to control their nanostructure also to study the relation between the nanoscale structure of these self-assembled materials and their optical properties.

In first chapter we are interested in the context of our study. We will discuss the concepts and fabrication of metamaterials and hyperbolic metamaterial. The various strategies envisaged for periodically organizing gold nanoparticles in self-assembled diblock copolymers will be described. In order to achieve hyperbolic metamaterial in visible range, the anisotropic plasmonic nanocomposites will be produced by periodically organizing gold particles in nanostructured matrices of block copolymers. Because gold nanoparticles have a well-defined plasmon resonance between 300 and 900 nm and the block copolymers are known for their self-assembly properties, and give access to a wide variety of sizes and shapes of nanostructures with characteristic sizes ranging from 10 to 100 nm. The physicochemical and optical properties of gold

nanoparticles, and more particularly the parameters influencing surface plasmon resonance, will be described. Finally, the thermodynamics and the shaping of lamellar systems of diblock copolymers will also be explained.

In the second chapter, we present the different experimental techniques used to study the structure and the optical responses of the target material. The study of the optical properties of gold nanoparticles dispersed in a matrix of copolymer will be measured by spectroscopic measurements. More particularly, the spectroscopic ellipsometry will be described, which is an advanced technique that makes it possible in particular to study the optical properties of a material as a function of the photon energy or wavelength of the incident beam. The organization of the nanocomposites and gold nanoparticles dispersed in the layer will be analyzed by small- angle X-ray scattering and electron microscopy.

The third chapter is devoted to fabrication controlled nanostructure by diblock copolymers using poly(styrene)-block-poly(2-vinylpyridine)(PS-block-P2VP)). We try to organize characteristic at scales far below the wavelength (typically <λ / 10). Their characteristic size and morphology will be determined by small-angle X-ray scattering, transmission and scanning electron microscopy. Knowledge of controlling structural size of lamellar fabricated by PS-block-P2VP (ie. thickness of sample and thickness of layer) will be required to properly achieve the designed nanostructure.

In the fourth chapter, we will study the method to fabricate gold nanocomposite with two different ways. The aim in this chapter is to find a way of selectively organizing plasmonic gold nanoparticles in one of blocks of the lamellar diblock copolymer. The mechanism of the gold loading and limitation of strategy also discussed here. Furthermore, the shape and size of gold nanoparticles analyzed by small-angle X-ray scattering, and we provide a method giving access to determine the volume fraction of gold in nanocomposite by quartz crystal microbalance. Knowledge of the structure information will be required to properly analyze the optical responses of nanocomposites.

The fifth chapter is devoted to the optimizing the target structure by manipulate the process of gold loading in chemical ways. The use of self-assembly block and loading process in chapter four leads irregular gold particles on the surface of films. The aim of this chapter is to find a good after treatment to achieve “better films” for

optical properties analyzing. Furthermore, the influence of reducing agent, the solvent we use and thermal annealing are going to be discussed here.

In the sixth chapter, we are going to choose several samples to study how the structure influence the optical responses. According to spectroscopic ellipsometry data, sample with different thickness, layer thickness and volume fraction of gold are analyzed. The optical indices, real and imaginary part of permittivity, are extracted from the with various model base on ellipsometry data. More particularly, the influence of the volume fraction of gold in the nanostructure were discussed and if the target structure could be hyperbolic metamaterial are discussed also based on isofrequency dispersion relations.

Chapter I Context and state-of-the-art

The aim of this PhD thesis is to study methodologies for the fabrication of nanocomposites of block copolymers and gold nanoparticles to control their nanostructure and to make the link between the nanometric structure of these self-assembled materials and their optical properties. This structure can be used as an optical metamaterials, which are envisioned breakthroughs in the near future: they are artificial materials structurally designed with the purpose of producing extraordinary optical properties. Their potential in revolutionizing the optical technologies has been largely recognized.

In this first chapter, we are interested in the context of our study, ie research on nanostructured and plasmonic materials for optics, and hyperbolic metamaterials that may have new optical properties, especially in the visible domain light. We discuss the experimental strategies envisaged for the fabrication of these new materials.

I.1 Metamaterial

I.1.1 Optics of materials

A metamaterial is an artificial composite material whose internal structure generates electromagnetic properties that do not exist in natural environments. “Meta” is from the Greek word μετά meta, meaning "beyond"[1,2]. In general, metamaterial is an artificially engineered structures. It consists of periodically or randomly distributed structured elements, whose size and spacing are much smaller than the wavelength (λ) of electromagnetic waves (EM) waves. In order to treat the metamaterial as an effective medium and avoid diffractive effects, the length scale of the structures is much smaller than the wavelength of the electromagnetic (EM) wave: in generally $\alpha<\lambda/10$, where α is the characteristic scale, λ is wavelength of light. In such systems, it is the sub-wavelength features that control the macroscopic electromagnetic properties. In the past decades, metamaterials is so attractive mostly due to their wide applications including subwavelength imaging[3–6], hyperlens[6,7] and optical cloaking[8,9]. Recent advances in nanofabrication technologies allow for producing metamaterial systems where the dielectric permittivity and magnetic permeability tensor can be designed and engineered at will. This ability to control the material they are made from assemblies of multiple elements fashioned from composite materials such as metals or dielectrics. The materials are usually arranged in repeating patterns, at scales that are smaller than the wavelengths of the wave they influence. Metamaterials derive their properties

not from the properties of the base materials, but from their designed structures. Their precise shape, geometry, size, orientation and arrangement gives them their smart properties capable of manipulating electromagnetic waves: by blocking, absorbing, enhancing, or bending waves, to achieve benefits that go beyond what is possible with conventional materials. In these realizations, one of metamaterial is attracted for us, which is called hyperbolic metamaterial. We are going to introduce deeply in I.2.

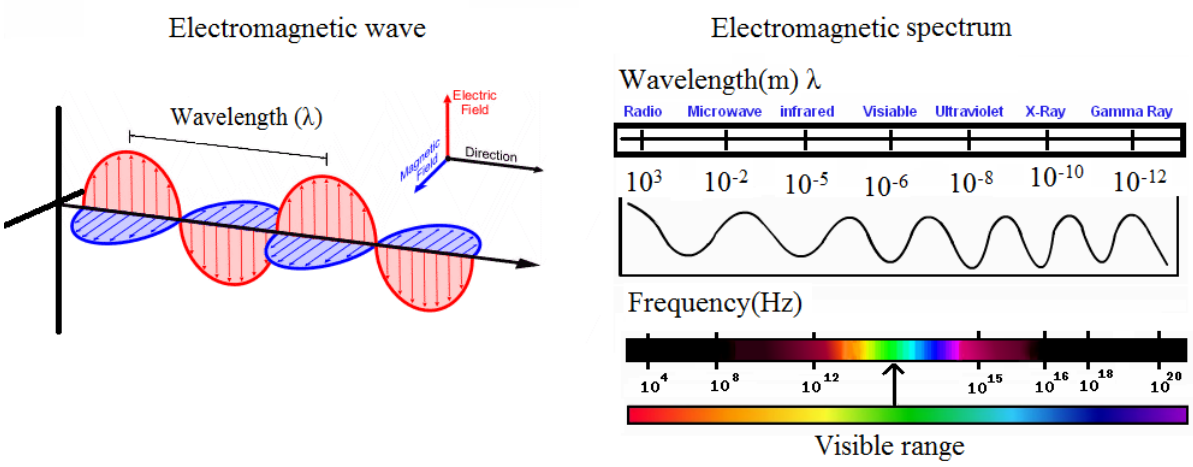

Figure I. 1 Left is a schematic of an electromagnetic wave, which consist of an oscillating electric field and an oscillating magnetic field. Right is the electromagnetic spectrum, and the position of the visible wavelengths region.

It is characterized by its complex refractive index[10], which is noted as $\tilde{n}$ (Equation 1- 1) and defined from Maxwell's equations in a material**.**

Equation 1- 1 $$\tilde{n}(\lambda) = n(\lambda) + i\,k(\lambda)$$

where n is the real part of the complex refractive index, also called optical refractive index. The imaginary part is the absorption coefficient, noted as k, which represents the energy loss of an electromagnetic radiation which passes through the medium.[11] From Equation 1- 1, we can see that the complex refractive index $\tilde{n}$ depends on the wavelength λ of the EM wave (Figure I. 1). If the complex number is real at some wavelength, it means that the electromagnetic wave passes through the medium without being absorbed ($k(\lambda) = 0$), the medium is transparent for this wavelength.

For all media, the complex refractive index $\tilde{n}(\lambda)$ can be described by 2 parameters: the complex electrical permittivity $\tilde{\varepsilon}(\lambda)$ and the complex magnetic permeability $\tilde{\mu}(\lambda)$), which describe the response of the medium (see Equation 1- 2) to electrical and magnetic excitation, respectively.

Equation 1- 2 $$\tilde{n}(\lambda) = \sqrt{\tilde{\varepsilon}(\lambda)\tilde{\mu}(\lambda)}$$

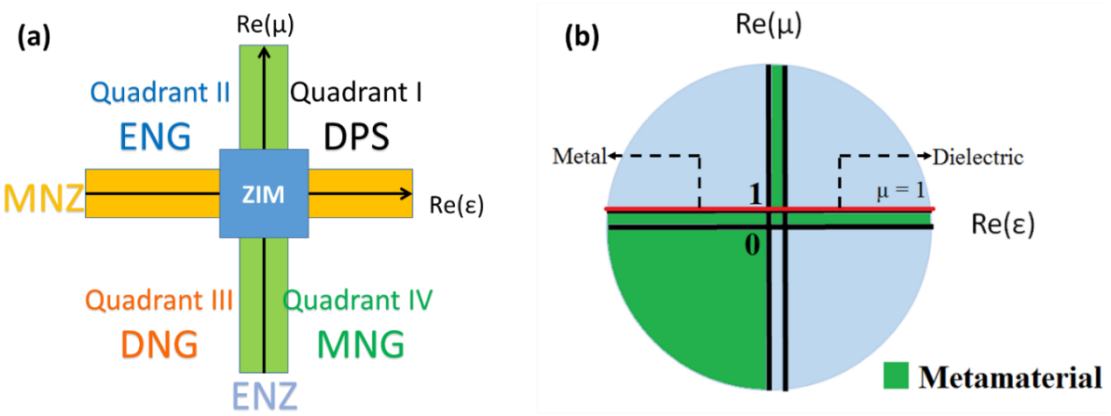

Figure I. 2 (a) The nomenclature of metamaterials, based on the values of the real parts of their permittivity and permeability[24,25]. DPS: double positive media, ENG: ε negative media, MNG: μ negative media, DNG: double negative media, ENZ: ε near zero media, MNZ: μ near zero media, ZIM: zero index media. (b) Schematic of all the material. Green part is metamaterial. At visible wavelengths, μ is equal to or close to 1, dielectrics have positive ε and metals have negative ε.

The dielectric permittivity $\tilde{\varepsilon}(\lambda)$ and magnetic permeability $\tilde{\mu}(\lambda)$ are the two fundamental parameters characterizing the EM property of a medium[12,13]. They classified metamaterial (see Figure I. 2(a)) according to their real part of electrical permittivity $\tilde{\varepsilon}(\lambda)$ and magnetic permeability $\tilde{\mu}(\lambda)$. Quadrant I including most dielectric materials covers material with simultaneously positive permittivity and permeability and DPS stands for "double positive". In quadrant II and IV, there are two kinds of metamaterial with only the permittivity (in IV, called ENG ε negative media) or the permeability (in II, called MNG μ negative media) negative. For examples, metals, ferroelectric materials, and doped semiconductors shows negative permittivity, which are present in quadrant II. Quadrant IV contains some ferrite materials with negative permeability. A very interesting part is quadrant III, corresponding to double negative media (DNG), which have both a negative permittivity and a negative permeability, and which cannot be found in nature. Such metamaterials concept originates from the 1960's, when Veselago[14] initially discussed the propagation properties of a material with simultaneously negative ε and μ, and showed that it would have a negative refractive index. Interest for such materials actually really arised only after Pendry proposed, in the early 2000's, that they could produce perfect lenses[15] as well as cloaking devices[16]. DNG are also called left-handed media or negative refractive index media. DNG present many other interesting phenomena[17–23]: anomalous refraction,

reversed Doppler shift, inverse Cherenkov radiation, opposite group velocity and phase velocity, etc.

According to Figure I. 2(b), natural materials (in blue) represent only a part of the ε_r and μ_r values. All other parts (in green) correspond to the metamaterials. In the visible range, all natural materials have a permeability μ equal to or close to 1, and lie along the red line in Figure I. 2(b). Dielectrics have positive ε and metals have negative ε.

When light travels in an ordinary material medium, it is typically slowed down. The amount of slowing depends upon the properties of the medium, and the fraction n by which the speed of light is reduced is referred to as the refractive index. According to Snell's law[26](Equation 1- 3), when a light is incident from a positive-index medium (n_1) to another positive-index medium (n_2), the light ray is deflected at an angle θ_2 with θ_1, the angle between the incident light ray and the axis perpendicular to the interface (see Figure I. 3 left):

Equation 1- 3 $$n_1 \sin\theta_1 = n_2 \sin\theta_2$$

When light travels in a negative material medium, Snell's law is still satisfied. When a light beam is incident from a positive-index material to a negative-index one, the refracted beam lies on the same side of the normal as the incident. In other words, the refracted light bends "negatively" at the interface (see Figure I. 3 right).

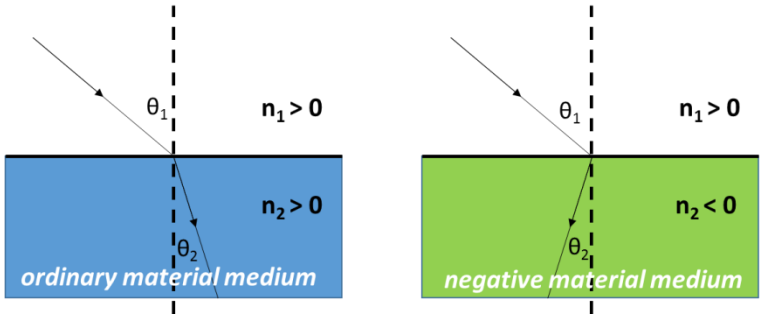

Figure I. 3 Schematic of refraction of ordinary material medium (left) and negative material medium (right)

To obtain a negative refraction in a homogeneous and isotropic material, the refractive index must be negative, which requires that the electrical permittivity and the magnetic permeability must be simultaneously negative. For an anisotropic material with a complex refractive index, a negative refraction can be obtained without

necessarily having both negative permittivity and permeability. This is called hyperbolic metamaterial, which is going to discuss later in I.2.

I.1.2 Basic theories of EM propagation

The Maxwell's equations are used for describing all electromagnetic (EM) phenomena (Shown from Equation 1- 4 to Equation 1- 7) in vacuum.

Equation 1- 4 $$\nabla \cdot \boldsymbol{E} = 0$$

Equation 1- 5 $$\nabla \cdot \boldsymbol{B} = 0$$

Equation 1- 6 $$\nabla \times \boldsymbol{E} = -\frac{\partial \boldsymbol{B}}{\partial t}$$

Equation 1- 7 $$\nabla \times \boldsymbol{B} = \mu_0 \left(\varepsilon_0 \frac{\partial \boldsymbol{E}}{\partial t}\right)$$

where **E** is the electric field and **B** is the magnetic induction, $\varepsilon_0$and μ_0 are the permittivity and permeability of vacuum, respectively.

In a material medium, the equations additionally include the electric charge density ρ, and the current density given by **J**=σ**E**, where σ is the conductivity, and the relative permittivity ε and permeability μ of the medium.

Equation 1- 8 $$\nabla \cdot \boldsymbol{D} = \rho$$

Equation 1- 9 $$\nabla \cdot \boldsymbol{B} = 0$$

Equation 1- 10 $$\nabla \times \boldsymbol{E} = -\frac{\partial \boldsymbol{B}}{\partial t}$$

Equation 1- 11 $$\nabla \times \boldsymbol{H} = \boldsymbol{J} + \frac{\partial \boldsymbol{D}}{\partial t}$$

Where, $\boldsymbol{D} = \varepsilon\varepsilon_0\boldsymbol{E}$**,** $\mu\mu_0\boldsymbol{H} = \boldsymbol{B}$**.** Equation 1- 4 & Equation 1- 8 represents Gauss's law, and Equation 1- 5 & Equation 1- 9 implies that the north and south poles of magnets do not exist separately. Equation 1- 6 & Equation 1- 10 and Equation 1- 7 & Equation 1- 11 describe Faraday's induction law and Ampère's law modified by Maxwell, respectively.

Combining the Maxwell's equations, the equations of wave propagation can be derived Equation 1- 12 and Equation 1- 13.

Equation 1- 12 $$\boldsymbol{\nabla^2 E} - \mu\mu_0\varepsilon\varepsilon_0\frac{\partial^2 \boldsymbol{E}}{\partial t^2} = 0$$

Equation 1- 13 $$\nabla^2 \boldsymbol{B} - \varepsilon\varepsilon_0\mu\mu_0\frac{\partial^2 \boldsymbol{B}}{\partial t^2} = 0$$

When a monochromatic plane wave $f(x,t) = g(x)\cos\omega t$ propagates in an isotropic, homogenous medium, it must follow Equation 1- 14, and this results in a spatial oscillation of the electric and magnetic components of the plane wave as shown on the Equation 1- 15:

Equation 1- 14 $$g(x)'' + \varepsilon\varepsilon_0\mu\mu_0\omega^2 g(x) = 0$$

Equation 1- 15 $$g(x) = g_0 e^{i(\pm\sqrt{\varepsilon\varepsilon_0\mu\mu_0}\omega x)}$$

with the wavevector k ($k^2 = \varepsilon\varepsilon_0\mu\mu_0\omega^2$), which defines the optical index of the media $\tilde{n} = \sqrt{\varepsilon\mu}$. We are going to discuss more details of specific propagation properties in hyperbolic metamaterials in the Chapter I.2 and VI.3.

I.2 Hyperbolic metamaterial

I.2.1 Definition

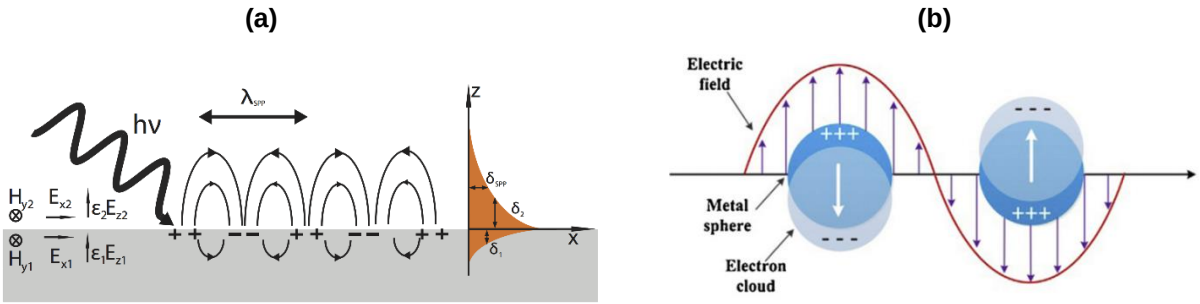

Figure I. 4 (a) Schematic representation of an electron oscillation propagating along a metal-dielectric interface. λ_{SPP} is the wavelength of surface plasmon-polariton, which is caused by the charge density oscillations and associated to an electromagnetic field. The right coordinate shows the exponential dependence of the electromagnetic field intensity on the distance away from the interface (from Wikipedia) (b) Illustration of the excitation of localized surface plasmon[31]

After the pioneer works of Veselago and Pendry, various nanostructures[12] were demonstrated to exhibit optical properties unobtainable from natural media. Among the various metamaterial proposed in the past decades, hyperbolic metamaterials (HMMs) were significant noticed, due to their ability of presenting subwavelength resolution imaging, as well as of manipulating the near-field of a light emitter or a light scattered.

Near-field is defined by the distance, which is relatively shorter than the wavelength of light in vacuum. The propagation properties of HMMs originate from the coupling of several surface plasmon modes in their volume[27–30]. They present the interesting particularity of having non-natural light propagation properties, without requiring engineering of the permeability μ, which is notably more complex than playing on the permittivity ε.

A surface plasmon is a collective oscillation of electrons, which is confined to the interface between a metal and a dielectric and propagates along this interface (see Figure I. 4 (a)). If the metal is a nanoparticle, localized surface plasmons are excited at the surface of the metallic domain (see Figure I. 4(b)).

I.2.2 Optics of anisotropic materials

In an anisotropic medium, the relative permittivity and permeability entering into the Maxwell's equations take the form of tensors. In the present study, we are going to talk about nonmagnetic medium, so $\boldsymbol{\mu}$ is unit tensor in this work. Permittivity tensor is assumed as the following tensor:

Equation 1- 16

$$\varepsilon = \begin{bmatrix} \varepsilon_{xx} & 0 & 0 \\ 0 & \varepsilon_{yy} & 0 \\ 0 & 0 & \varepsilon_{zz} \end{bmatrix}$$

In the Equation 1- 16, the three components generally depend on the wavelength, or equivalently the angular frequency ω. When $\varepsilon_{xx} = \varepsilon_{yy} = \varepsilon_{zz}$, the material is isotropic. When $\varepsilon_{xx} = \varepsilon_{yy} \neq \varepsilon_{zz}$, the material is known as uniaxial. When $\varepsilon_{xx} \neq \varepsilon_{yy} \neq \varepsilon_{zz}$, the crystal is known as biaxial.

In order to determine the dispersion relation of light in the medium with **ε** described by Equation 1- 16, we should combine the anisotropic Maxwell's equations. For a plane wave expressed as:

Equation 1- 17

$$\boldsymbol{E} = \boldsymbol{E_0} e^{-i(\omega t - k \cdot r)}$$

Equation 1- 18

$$\boldsymbol{H} = \boldsymbol{H_0} e^{-i(\omega t - k \cdot r)}$$

the Equation 1- 12 of the wave propagation then becomes :

Equation 1- 19

$$\boldsymbol{k} \times (\boldsymbol{k} \times \boldsymbol{E}) + \omega^2 \mu_0 \varepsilon_0 \varepsilon \boldsymbol{E} = \boldsymbol{0}$$

which can be developed into matrix in Equation 1- 20:

Equation 1- 20

$$\begin{bmatrix} k_0^2\varepsilon_{xx} - k_y^2 - k_z^2 & k_x k_y & k_x k_z \\ k_x k_y & k_0^2\varepsilon_{yy} - k_x^2 - k_z^2 & k_x k_y \\ k_x k_z & k_y k_z & k_0^2\varepsilon_{zz} - k_x^2 - k_y^2 \end{bmatrix} \begin{bmatrix} E_x \\ E_y \\ E_z \end{bmatrix} = 0$$

where $k_0 = \frac{\omega}{c} = \omega\sqrt{\mu_0\varepsilon_0}$ is the magnitude of the wavevector and c is the speed of light in vacuum. In this thesis, we focus our attention on uniaxial media with $\varepsilon_{xx} = \varepsilon_{yy} \equiv \varepsilon_{//}$ and $k_{//} = \sqrt{k_x^2 + k_y^2}$. Substituting $k_{//}$ and $k_0^2 = \varepsilon_o \mu_o \omega^2$ in Equation 1- 20 yields the isofrequency dispersion relation in this material ($\varepsilon_z = \varepsilon_{zz}$)[32,33]:

Equation 1- 21

$$\left(k_{//}^2 + k_z^2 - \varepsilon_{//}\varepsilon_o\mu_o\omega^2\right)\left(k_{//}^2\varepsilon_{//} + k_z^2\varepsilon_z - \varepsilon_{//}\varepsilon_z\varepsilon_o\mu_o\omega^2\right) = 0$$

where the two terms describe the behavior of waves of different polarizations: polarization in the (x,y) plane for the first term (p-polarized) and polarization in a plane containing the z direction for the second (s-polarized waves)[34]. When set to zero, the two terms above correspond respectively to a spherical and an ellipsoidal isofrequency surface in the k-space.

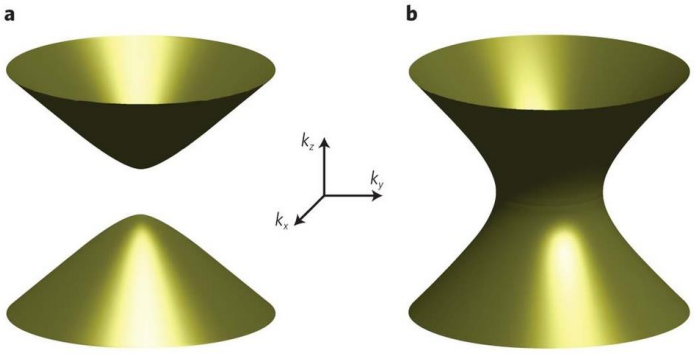

Figure I. 5 Schematics of the isofrequency surface $\omega(k_x, k_y, k_z) = const.$ in the 3-dimensional k-space for 2 types of HMMs (a) dielectric (type I) HMMs with $\varepsilon_{//} < 0$ and $\varepsilon_z > 0$ and (b) metallic (type II) HMMs with $\varepsilon_{//} > 0$ and $\varepsilon_z < 0$[38]

The term “hyperbolic” describes uniaxial materials in which the anisotropy is extremely strong, when one of the two components $\varepsilon_{//}$ and ε_z is negative, and another one of them is positive, which is extremely rare[35] in natural materials in the visible wavelength range. We can represent such materials as behaving optically as a metal

in one direction and as a dielectric in another direction. Then, the first term defines either an isotropic propagation or vanishes because it is algebraically impossible. The second term results in a hyperboloidal isofrequency surface, which defines a hyperbolic medium. The latter can be written:

Equation 1- 22

$$\frac{k_{//}^2}{\varepsilon_z} + \frac{k_z^2}{\varepsilon_{//}} = k_0^2 \text{ with } k_0^2 = \varepsilon_o \mu_o \omega^2 \text{ and } k_{//} = \sqrt{k_x^2 + k_y^2}$$

There are two choice for the product $\varepsilon_{//}\varepsilon_z < 0$. If $\varepsilon_{//} > 0 \; and \; \varepsilon_z < 0$, the hyperbolic medium is called dielectric hyperbolic (with reference to its behavior in the xy plane) or Type I hyperbolic. Its isofrequency surfaces and the dispersion relation are showed in Figure I. 5 (a); if $\varepsilon_{//} < 0 \; and \; \varepsilon_z > 0$, the hyperbolic medium is called metallic or Type II hyperbolic. Its isofrequency surfaces and the dispersion relation are showed in Figure I. 5 (b)[36,37].

I.2.3 Application of HHMs and super-resolution

As we described previously, HHMs are materials with extreme anisotropy, which leads to specific light propagation. Such structures have displayed a variety of promising properties, generating a surge in the activity on the topic over the recent years: negative refraction[39], super-resolution[40], sub-wavelength modes[41], perfect multi-band absorption[42], optical topological transition[43], epsilon-near-zero light propagation[44], spontaneous emission and Purcell effect enhancement[36,45–48], thermal emission engineering[49] including super-Planckian regimes[50], or biosensing[51,52].

One very attractive property is the so-called “super-resolution” (i.e., sub-diffraction imaging), because super-resolution could be profitable to several technological fields. Optical microscopy is indeed an essential tool in many fields such as microelectronics, biology and medicine. But it is hindered by the intrinsic diffraction limitation as it cannot obtain a better resolution than half the wavelength of light. ‘Diffraction limit’ in optics is well known: whenever an object is imaged by an optical system, the objects with sizes smaller than half the wavelength of the light are unresolved in the image. This loss of information is caused by the fact that the object fine features are carried by components with high spatial frequency (large wavevectors), which becomes evanescent in a usual material. HMMs offer a completely new paradigm to tackle the problem.

When a beam of light hits an object, the object information is transferred to propagating waves and evanescent waves. The propagating waves carry large features information which can reach the far field, whereas evanescent waves carry fine details which are confined to the near field. Due to the 'diffraction limit', if the scattered light is collected by a conventional glass lens, the evanescent waves are permanently lost before reaching the image plane (Figure I. 6(a)). The hyperlens made by a strongly anisotropic metamaterial, can transfer the deep subwavelength information into the far field (Figure I. 6(b)). The evanescent waves from the object can become propagating waves. With the help of the hyperlens geometry, the waves gradually reduce their[40] wavevector values along the propagation direction in the metamaterial, and thus the waves can continue to propagate even after leaving the hyperlens.

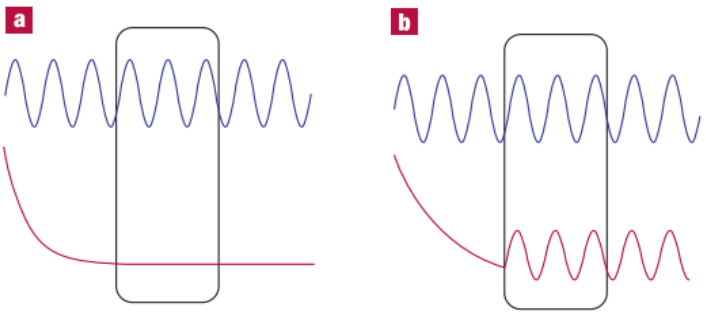

Figure I. 6 Light propagation through (a) Conventional lens, and (b) Hyperlens. The blue curves and red curves represent propagating waves and evanescent waves, respectively. [40]

Near-field scanning techniques[53], and fluorescence-based imaging methods[54] have proposed and validated ways to circumvent this limitation and have brought optical microscopy into the nano-world, with the fascinating and revolutionary goal to visualize the pathways of individual molecules inside living cells[55]. Similar intrinsic resolution limitations also hinder optical lithography, one of the most important tools equipping the semiconductor industry, ubiquitous in our societies.

The principle of subwavelength imaging was proven by some published works. For example, an extremely thin Ag slab can act as a superlens, which enhances evanescent waves via resonant excitation of surface plasmons [4040,56].

I.2.4 Achievement of HHMs

HHMs are considered amongst the most promising metamaterials, because of their ability to provide a multi-functional platform[32] to reach different meta-properties.

There are two main approaches to achieving the desired hyperbolic isofrequency surface using metamaterials. 1) The first type consists in lamellar superlattices with subwavelength layer thicknesses fabricated by multilayer showed in Figure I. 11 (a), is which a coupling of surface plasmons occurs. 2) The second type consists in lattices of metallic nanowires, showed in Figure I. 11(b). The physical mechanism is realized by localized surface plasmons[29,57]. Both of the systems have been studied theoretically and experimentally[32,38,58,59].

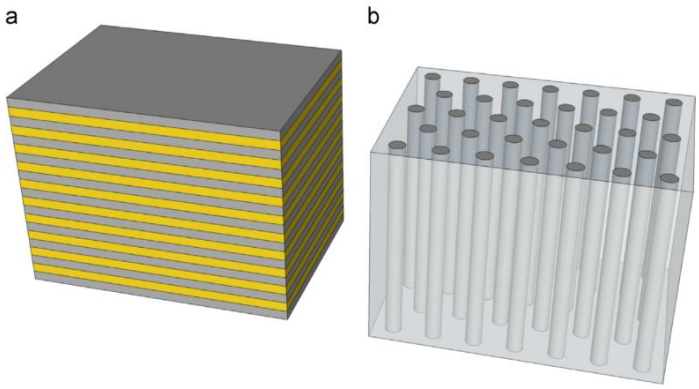

Figure I. 7 Schematics of 2 types of HMMs (a) multilayer of deeply subwavelength alternating metallic and dielectric layers (b) lattice of metallic nanowires embedded in a dielectric matrix with subwavelength characteristic diensions[34]

These 2 designs can achieve the required extreme anisotropy and can be tuned to be HHMs in all wavelength ranges from the UV, visible, near-IR to mid-IR with the appropriate choice of metal and metallic filling fraction, which can be shown using an effective medium theory as following.

I.2.4.1 Effective medium theory for multilayer structures[41,58]

Effective medium theories relate the permittivity of a composite medium to the permittivities of the constituents, with some degree of structural information included in the relation. In the case of multilayer structures, a simple relation has been proposed and is valid if the thickness of the layers is much smaller than the operating wavelength, typically smaller than $\lambda/10$. Then, if the relative permittivities of the dielectric and metal layers are ε_d and ε_m, respectively, the uniaxial components of the dielectric tensor $\varepsilon_{//}$ and ε_z , are given by

Equation 1- 23 $$\varepsilon_{//} = \rho\varepsilon_m + (1-\rho)\varepsilon_d$$

Equation 1- 24 $$\frac{1}{\varepsilon_z} = \frac{\rho}{\varepsilon_m} + \frac{(1-\rho)}{\varepsilon_d}$$

where ρ is the fill fraction of the metal in the unit cell, $\rho = \frac{d_m}{d_m+d_d}$ if the thickness of metal is d_m and the thickness of dielectric is d_d. From the Equation 1- 23 and Equation 1- 24, the wavelength and strength of the plasmon resonance given by $\varepsilon_{//}$ can be tunable by the fill fraction of the metal.

Such systems have been fabricated by electron-beam or sputter deposition in vacuum of both the metallic and dielectric constituents. One limitations of these deposition techniques is that there is often a limit to the number of periods that can be stacked while preserving an actual superlattice structure, which may be a problem to achieve bulk samples. However, high number may not be necessary, since as little as six layers were shown to achieve an effective hyperbolic behavior by using an electron-beam evaporator[60,61].

I.2.4.2 Effective medium theory for cylindrical nanowires[62,63]

Following a similar approach, an equivalent effective medium representation of the nanowire geometry can be given by the generalized Maxwell–Garnett approach. In the case of perfectly aligned cylindrical nanorods, the permittivity tensor components are given by:

Equation 1- 25 $$\varepsilon_{//} = \frac{(1-\rho)\varepsilon_m\varepsilon_d+(1-\rho)}{(1-\rho)\varepsilon_m+(1+\rho)\varepsilon_d}$$

Equation 1- 26 $$\varepsilon_z = \rho\varepsilon_m + (1-\rho)\varepsilon_d$$

In Equation 1- 25 and Equation 1- 26, where ρ is the volume fraction of metal, or equivalently the relative area occupied by the nanowires in a xy section of the medium. Also like multilayer HHMs, the response of the media can be tuned to different regimes (2 type of HHMs) and different amplitudes by varying frequency and characteristic size of the structure.

Most of the HMMs nanowires are fabricated by electrochemical deposition of Ag or Au inside a self-assembled porous alumina (Al_2O_3) template[64–67]. Another method to realize nanowire material is to use the arrays of carbon nanotubes as the metallic domains[68].

The chemical processes and the self-organization mechanisms, through which cylindrical porous templates are manufactured and used for nanowire HHMs fabrication, are considered easier and cheaper than the processes used to produce multilayer HHMs. In this thesis, we focus on the development of alternative routes for multilayer HHMs fabrication, possibly allowing large sample production and low cost.

I.2.4.3 Fabrication of multilayer HHMs

One can define two main families of fabrication methodologies to achieve 3-D nanostructured materials, usually called top–down and bottom-up. Top-down refers to methodologies similar to sculpting or machining matter, like lithography or printing. This is very efficient to produce well-defined patterns on surfaces, but is more difficult to apply to bulk materials. In particular, nanolithography has been successful in manufacturing nanostructured surfaces, evidencing meta-material properties, such as hyperlensing[15] and cloaking[16], at wavelengths larger or close to the visible domain[69]. Bottom-up refer to constructions from elementary molecular or supramolecular bricks into a design assembly. In particular the use of chemistry and self-assembly of metallic nanoparticles, acting as plasmonic resonators, into dense ordered structures, was anticipated as a promising 'bottom-up' fabrication route[70,71], especially in order to produce large-scale, 3D and tunable metamaterials. We develop below a particular combination of chemical synthesis and mechanisms of self-assembly, which can be used to produce materials with both nano-structuration and anisotropy, and presenting hyperbolic propagation properties in the visible or infrared ranges.

I.3 Self-assembly of block copolymers

I.3.1 Definitions

I.3.1.1 Polymer

A polymer is a macromolecule consisting of a repeated sequence of the same units called segment, each bound to its neighbors by covalent bonds. Generally, the polymer chains are entangled and therefore in a disordered state. A polymer may be natural or chemically synthesized, characterized by degree of polymerization *N*, corresponding to the number of segments in the polymer[72,73].

Its molar mass M is equal to $M=N\times M_{segment}$. Polymer synthesis routes generally lead to macromolecules which have a size distribution. More precisely, the number average molar mass M_n and the weight average molar mass M_w (see Equation 1- 27) are defined with N_i and M_i, the degree of polymerization and the molar mass of a polymer chain, respectively.

Equation 1- 27 $$\overline{M_n} = \frac{\sum_i N_i M_i}{\sum_i N_i} \text{ and } \overline{M_w} = \frac{\sum_i N_i M_i^2}{\sum_i N_i M_i}$$

The radius of gyration R_g of a polymer chain describes the size of the polymer coil. The square radius of gyration is the average squared distance of any point in the polymer coil from its mass center. The radius of gyration of an equivalent freely joint polymer chain is given by $R_g^2 = \frac{1}{6} N l_k^2$ with N being the number of Kuhn segment, l_k being the Kuhn length, with the Kuhn segment usually approximated to a chemical segment.

The polydispersity index PDI equals the ratio of the weight average molecular weight M_w to the number average molecular weight M_n. This index describes the width of the polymer molecular weight distribution.

Equation 1- 28 $$PDI = M_w/M_n$$

When the PDI is 1.0, all the polymers chains have identical length. For real polymers, PDI is always larger than 1.0.

Most polymers have a refractive index n between 1.3 and 1.7. The present a glass transition from a vitreous state (hard and rigid polymer) to a rubbery state (soft and flexible polymer) characterized by a temperature T_g. A useful parameter is the solubility parameter δ, depending on the chemical nature of the polymer segments, which is a quantification of the degree of potential interactions between the polymer and other species. It was simply defined by Hildbrand as the energy required to completely remove a molecule from its neighbors to infinite separation.

I.3.1.2. Diblock copolymers

A polymer consisting of a single type of monomers is a homopolymer. When two or more different monomers unite together to polymerize, they are called copolymer. Block copolymers is one kind of copolymers, which comprises two or more blocks (homopolymer subunits) linked by covalent bonds. The latter are arranged according

to a more or less complex architecture, they may be linear (diblock, triblock, multiblock) or branched (dendrimers, star) (see Figure I. 8).

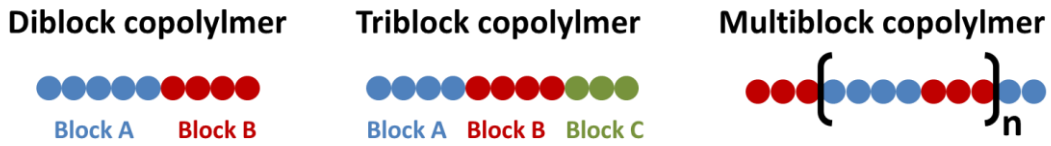

Figure I. 8 Schematics of different type of block copolymer

More particularly, we are interested in diblock copolymers denoted A-B, which are defined by their degree of polymerization *N,* and the mass and volume fraction of each block. The expressions of the mass fraction f_m(A) and volume fraction f_v(A) of the block A in an A-B diblock copolymer are the following:

Equation 1- 29

$$f_m(A) = \frac{M_n(A)}{M_n(A)+M_n(B)} \text{ and } f_v(A) = \frac{M_n(A)/\rho(A)}{M_n(A)/\rho(A)+M_n(B)/\rho(B)}$$

where ρ(A) and ρ(B) are the densities of the polymer blocks A and B. M_n(A) and M_n(B) are number average molar mass of the blocks A and B, respectively.

Diblock copolymers are polymers derived from the successive copolymerization of two types of chemically different monomers. They can be synthesized by controlled anionic or radical polymerization. Advances in polymerization syntheses in recent decades have made it possible to have access to a large variety of chemistries and structures of diblock copolymers.

I.3.2 Thermodynamics of diblock copolymers

I.3.2.1 Phase transition of the diblock copolymers

A diblock copolymer is a polymer consisting of two types of monomers, A and B, linked together by a covalent bond. In the particular case where the two blocks A and B are completely miscible, the properties of the diblock copolymer are intermediate between those of the two blocks. However, in generally the two blocks are immiscible because of the different chemical nature of the two blocks. This incompatibility causes the system to try to minimize the interfacial energy between the two blocks, which leads to a phase separation of the copolymer into domains with a characteristic period. The most characteristic feature of a block copolymer is the strong repulsion between the two unlike blocks even when the repulsion between segments is relatively weak. As

the blocks A and B are linked together by a covalent bond, the size of the domains is restricted to spatial scales of the order of the size of the macromolecules, from 10 to 100 nm. The propagation of these ordered domains continues to the macroscopic scale. This self-assembly process is called the phenomenon of microphase separation. The monomer segments will segregate and form regular, often periodic structures[73–77].

The phase micro separation is controlled by the free energy of the system ΔG, which depends on a competition between entropy ΔS and enthalpy ΔH.

The entropy contribution ΔS, which present the configuration energy gain during mixing to deform the chains of each of the blocks, is proportional to the number of N repeat patterns.

The enthalpy contribution ΔH, which shows the energy cost of a contact between the two blocks A and B, is linked to the Flory-Huggins interaction parameter χ_{AB} which reflects the interaction energy between blocks A and B. The parameter χ_{AB} depends on the temperature and the chemical nature of the blocks. It can be written in two ways.

With a network model:

Equation 1- 30
$$\chi_{AB} = \frac{Z}{k_B T}\left[\frac{\varepsilon_{AB}-(\varepsilon_{AA}+\varepsilon_{BB})}{2}\right]$$

where k_B is the Boltzmann constant, T is the temperature, Z is the network coordination number, and ε_{ij} the interaction energy between two monomer i and j. For example: ε_{AA} is the energy interaction between two A monomers.

With the solubility coefficients:

Equation 1- 31
$$\chi_{AB} = \frac{V_{seg}(\delta_A-\delta_B)^2}{N_A k_B T}$$

where N_A is the Avogadro's constant, δ_A and δ_B are the solubility parameters of segment A and segment B, respectively. V_{seg} is the mean volume occupied by a segment of the polymer.

The microphase separation is stronger when the product $\chi_{AB}N$ is high, which defines the segregation power of the system. When the interaction parameter increases, the incompatibility between the two blocks increases and the phase separation is naturally favored. Also, the increase of the polymer chains size leads to a relative decrease in the entropy gain and also favors the microphase separation.

When $\chi_{AB}N$ becomes greater than a certain critical value denoted as $(\chi_{AB}N)_{OD}$, a microphase separation occurs (see Figure I. 9). Below this characteristic value $(\chi N)_{OD}$, the system is mixed and described as in a disordered state.

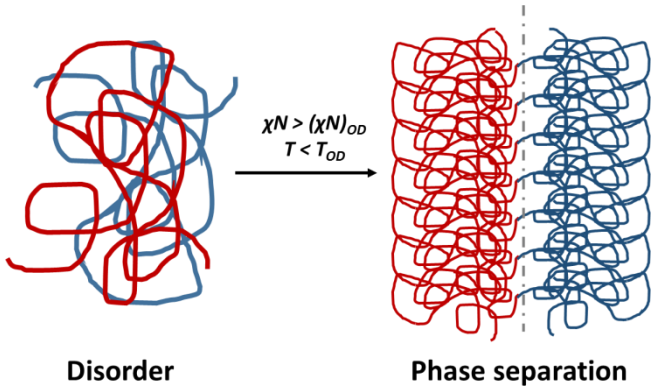

Figure I. 9 Schematic representation of the states of a diblock copolymer

The microphase separation also depends on the temperature. When the temperature is high, the thermal agitation dominates and the repulsive interactions between the segments of the blocks A and B no longer lead to the separation of the blocks. Beyond a certain temperature, denoted as order-disorder temperature T_{OD}, the system is in a disordered state. On the contrary, when the temperature is lower than T_{OD}, the blocks are segregated into microdomains (Figure I. 9). The order-disorder transition temperature T_{OD} can be measured by scattering of electromagnetic radiation, especially small angle X-ray scattering, or rheological techniques[78–83].

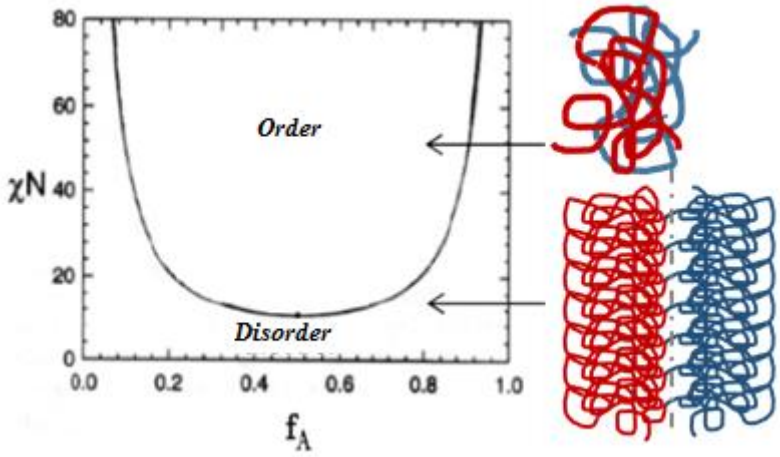

Figure I. 10 Simplified theoretical phase diagram of a diblock copolymer[78]

The order-disorder transition is characterized by the parameters $(\chi)_{OD}N$ and T_{OD} interconnected by Equation 1- 32, with two constants a and b.

Equation 1- 32 $$\chi_{OD} = a + \frac{b}{T_{OD}}$$

The order-disorder transition can be modified by varying the degree of polymerization N of the copolymer or the interactions between the blocks A and B by changing their chemical nature. In both cases, this requires the synthesis of a novel diblock copolymer. The simplest option to change the order-disorder transition is to vary the temperature of the system.

The order-disorder transition of a diblock copolymer also can be tuned by volume fraction of one block relative to the other. The simplified theoretical phase diagram of a diblock copolymer A-B is plotted as function of the volume fraction of block A in Figure I. 10. It shows how the boundary between the ordered and disordered states varies with the composition of the diblock, described by the volume fraction f_A of block A.

I.3.2.2 Phase Diagram of Diblock Copolymers

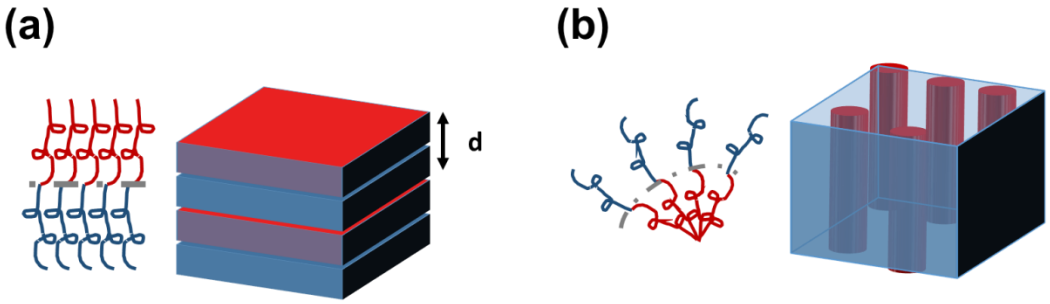

Figure I. 11 Micro phase separation of (a) lamellar phase and (b) cylinder phase

When the diblock copolymer A-B is in an ordered state, the morphology it adopts depends on three factors. The Flory-Huggins parameter χ_{AB}, the degree of polymerization N and the volume fraction of one block in copolymers affect the conformation of the chains and the spontaneous curvature adopted by the interface between the two blocks. For a symmetrical diblock copolymer ($f_A \approx f_B \approx 0.5$), the minimum free energy is obtained for an identical stretching of the two species and leads to the formation of a plane interface between the two blocks. The microdomains are then organized into alternating lamellar phase (Figure I. 11(a)). For an asymmetric diblock copolymer ($f_A > 0.5$

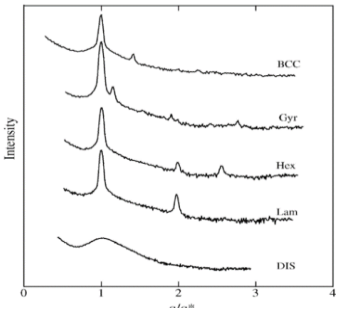

Figure I. 12 Typical SAXS patterns observed for equilibrium structures formed in diblock copolymer melts[128,129]

or f_A <0.5), a plane interface would induce a high entropy stress in the minority block. The system then curves its interface to relax this constraint, which can lead to cylindrical or spherical morphologies (Figure I. 11(b)).

The different morphologies (spherical, cylindrical, gyroid and lamellar) of a diblock copolymers are shown in Figure I. 13 as a function of $\chi_{AB}N$ and the volume fraction of one block f.

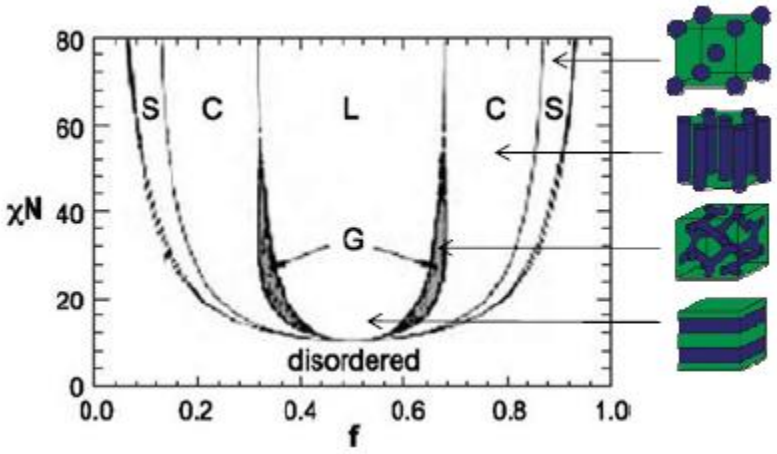

Figure I. 13 Diagram of the theoretical phase of a diblock copolymers and corresponding morphologies These morphologies can be characterized by transmission electron microscopy (TEM) or small-angle X-ray scattering (SAXS), experimental techniques described in Chapter 2. In X-ray scattering at small angles, the intensity of the signal scattered by the diblock copolymer is observed as a function of the diffusion wave vector q. When the system presents an organization, there are peaks due to the scattering by the structure. The relative positions of these peaks, defined by the ratio q/q_0, are characteristic of the morphology (see Table I. 1 and Figure I. 12).[77]

Table I. 1 Peak relative positions (expressed as q/q*) of Bragg reflections for various structures

Structure	Ratio q/q^*
Lamellar	1, 2, 3,4,5,6…
Spherical	$1,\sqrt{2}, \sqrt{3}, \sqrt{4}, \sqrt{5}, \sqrt{6}$…
Cylinder	$1, \sqrt{3}, 2, \sqrt{7}$ …
Gyroid	$1, \sqrt{4/3}, \sqrt{7/3}, \sqrt{8/3}, \sqrt{10/3}, \sqrt{11/3}$…

Our goal is to produce lamellar systems, which is why we are interested in the following in the specific case of symmetrical diblock copolymers, with $f_A \approx f_B \approx 0.5$.

I.3.2.3 Symmetric diblock copolymers in different segregation regimes

When an A-B symmetrical diblock copolymer is in an ordered phase, it has a lamellar morphology within a period (or bilayer thickness) denoted as d (Figure I. 11(a)). The ability of segregation of the system depends on the segregation power χN and we can distinguish four regimes as shown in Figure I. 14[84].

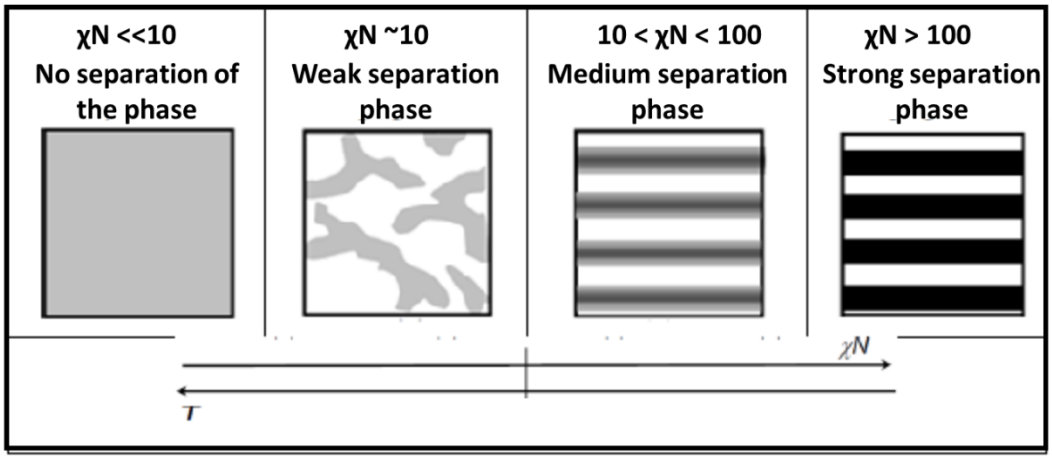

Figure I. 14 The phase separation regimes for diblock copolymers[84]

I.3.2.3.1 Strong segregation regime

When the value of χN is very large (typically larger than 100 for a symmetrical diblock copolymer), the blocks of the copolymers are very incompatible, there is formation of microdomains with net interfaces, the system is within the strong segregation limit. As explained in section 1.3.2.1, the free energy of the micro-separated system of a diblock copolymer is given by the sum of the entropic contribution to deform the chains away from their conformation of random coils and the interfacial energy between the A and B domains. According to Semenov's theory[85], the two corresponding terms in free energy are given by Equation 1- 33:

Equation 1- 33
$$\frac{F}{kT} = \frac{3p}{8Na^2} d^2 + \frac{2pNa}{d} \left(\frac{\chi}{6}\right)^{0.5}$$

Equation 1- 34
$$d = 2N^{2/3} a \left[\frac{1}{3}\left(\frac{\chi}{6}\right)^{1/2}\right]^{1/3}$$

where d is the lamellar period, N is the total number of segments of statistical length a, p is the number of polymer chains in the system per unit volume and $\chi=\chi_{AB}$ is the interaction parameter. The equilibrium lamellar period d of a diblock copolymer is obtained by minimizing Equation 1- 33 and is given by Equation 1- 34.

It can be seen that the lamellar period (or bilayer thickness) d depends rather strongly on the degree of polymerization N but little on the interaction parameter. We are going to control d by controlling the N of the polymers in the Chapter III.

I.3.2.3.2 Low segregation regime

On the contrary, when the value of χN is low (χN ≈ 10 for a symmetrical diblock copolymer), the blocks are mixed and the copolymer is in the vicinity of the order-disorder transition. It is subject to fluctuations in composition which are organized in ordered microdomains with large interfaces. In this case, the system is in a weak segregation regime and the lamellar period of the microdomains d varies in $N^{1/2}$.

I.3.3 Experimental shaping

The experimental conditions for obtaining ordered symmetrical diblock copolymers are described below, according to two types of evaporation.

I.3.3.1 Slow evaporation

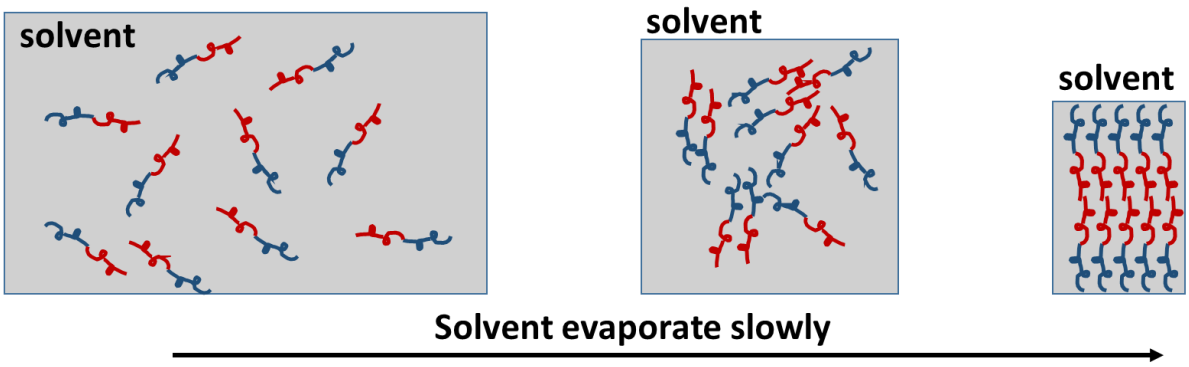

Figure I. 15 Schematic illustration of the shaping of a symmetrical diblock copolymer by slow evaporation of the solvent

The diblock copolymer may spontaneously self-assemble under certain specific conditions, for example by slowly evaporating the solvent. At the beginning of the process, the copolymer chains are diluted in a common (or neutral) solvent. As the solvent begins to evaporate slowly, the polymer chains get closer and unfavorable interactions occur. These repulsions between the blocks A and B cause the chains of copolymers to rearrange in order to minimize their contact with each other: the self-assembly begins. The microdomains are then gradually formed and propagate during the evaporation of the solvent until the solvent has completely evaporated. At the end,

an ordered sample of lamellar morphology is obtained in the case of a symmetrical diblock copolymer (see Figure I. 15).

I.3.4.2 Rapid evaporation

In some preparation processes, like the spin-coating deposition of thin films, the evaporation of the solvent is very rapid, so the system does not have time to reach its thermodynamic equilibrium and the polymer chains therefore do not have time to organize. In the rapid evaporation case, the system is amorphous that is, in a disordered state, or in a uncontrolled or intermediate state of organization. In order to organize the system, it is necessary to provide mobility to the chains later on, like thermal annealing, or exposure to a swelling solvent or mechanical shear (see Figure I. 16).

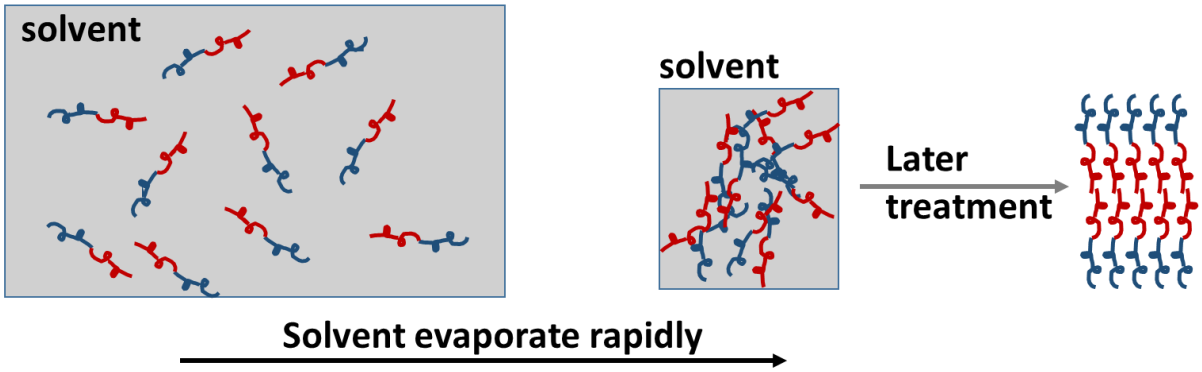

Figure I. 16 Schematic illustration of the shaping of a symmetrical diblock copolymer by rapid evaporation of the solvent

I.3.4 Thermodynamics of symmetrical diblock copolymers in thin films

This is particularly the case for thin films which are produced by spin coating (rapid evaporation as described in I.3.4.2). The spin-coating is a technique to form a film in several seconds (details are given in Chapter III.1). According to the rapid evaporation experimental conditions, the equilibrium state of the system must be obtained by a post-spin-coating treatment, for example, thermal annealing or solvent annealing. Both of them can induce the alignment of the lamellar phase, which may be perpendicular or parallel to the substrate[73,86,87].

I.3.4.1 Alignment perpendicular to substrate

It is possible to obtain a diblock copolymer film aligned perpendicularly to the substrate after annealing in the particular situation where the surface of the substrate is chemically neutral with respect to the two blocks. The interfacial interactions between the substrate and each block are then identical and there is no preferential wetting for the two blocks.

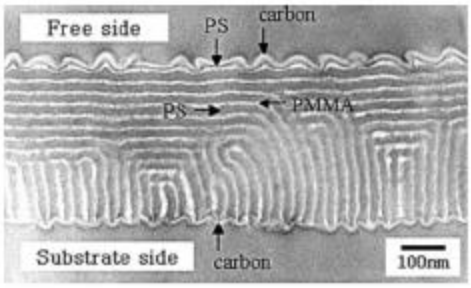

Figure I. 17 TEM cross-view of a PS-PMMA film on a substrate consisting of a random mixture of PS and PMMA[86]

During annealing, which is performed for providing mobility to the chains, the latter form microdomains and orient themselves perpendicularly to the neutral substrate. However, in most of the cases, one of the blocks of the diblock copolymers has a preferential chemical affinity with air, the film orientates parallel to its upper surface, which forms mixed alignment films (see Figure I. 17).

I.3.4.2 Alignment parallel to substrate

As we mentioned in I.3.4.1, in most of cases, for thin films of diblock copolymers, the interfacial energies of each block with the substrate and with air generally induce preferential wetting of one of the blocks at the interface of substrate/film and film/air. During annealing of the thin film, the lamellar morphology propagates from the two interfaces (air / film and film / substrate) to the interior of the film, and parallel alignment to the substrate of a diblock copolymer film can be obtained. Depending on the thickness of the thin film, the configuration adopted after annealing may be symmetrical, unsymmetrical, or more complex.

I.3.4.2.1 Symmetric and unsymmetrical configuration

In the particular case, when the thickness of the thin film L of symmetrical diblock copolymers is the exactly quantized value dependent on the lamellar period d, the film adopts a symmetrical or unsymmetrical configuration.

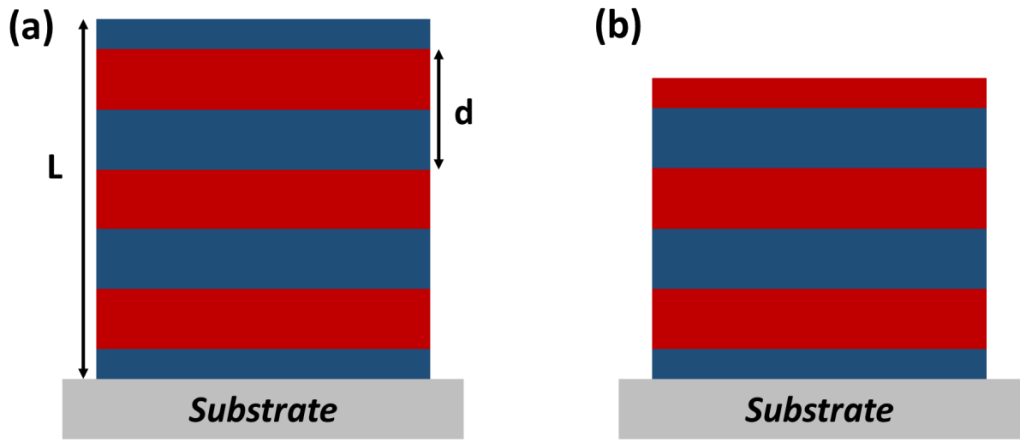

Figure I. 18 Schematic representation of an alignment of a lamellar diblock copolymer film in symmetrical (a) and unsymmetrical (b) configurations.

When L=n*d, where n is an integrate number, and one of the blocks of the copolymers has a preferential chemical affinity with both the substrate and air, a symmetrical configuration forms (see Figure I. 18(a)).

And when L=(n+1/2)*d, and one of the blocks has a preferential affinity with air and the other block has a preferential affinity with the substrate, an unsymmetrical configuration forms (see Figure I. 18(b)).

I.3.4.2.2 Other configuration

However the “perfect film” (symmetrical or unsymmetrical configuration) is uncommon in real fabrication. Most of the time[88], the thickness of the film L is not strictly commensurate to the equilibrium lamellar size d(L ≠ n*d and L≠(n+1/2)*d), the copolymer will then organize during annealing so as to compensate for this difference in thickness[89]. Holes or islands are formed on the surface of the film (see Figure I. 19) with a specific step height (see Figure I. 20) equal to a period size.

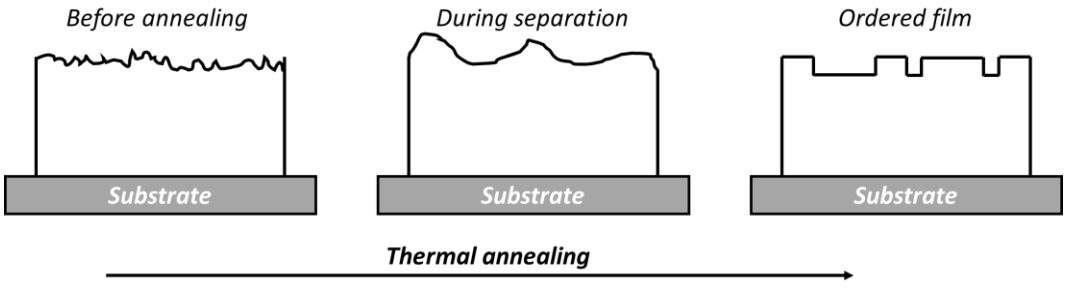

Figure I. 19 Illustration of the thin film topography formed by diblock copolymers as a function of time

The surface energy and material quantity constraints result in the generation of areas on the surface of the film. The arrangement adopted by the chains of a symmetrical diblock copolymer during annealing is shown in Figure I. 20. The difference of thickness between holes and islands on the surface is equal to the lamellar period d of the copolymer[90]. Moreover, the two thicknesses of the thin film are equal to n d or (n + 1) d, with n integrate number.

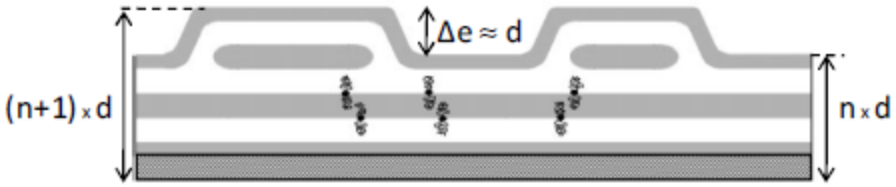

Figure I. 20 Schematic of a thin film of diblock copolymers aligned parallel to the substrate[91]

The type of surface topography and the fraction of the surface occupied by islands or holes depend upon the initial thickness. This holes or islands have micron-size lateral dimensions and can be observed under optical microscope and AFM from our samples that will be seen in Chapter III and Chapter IV.

I.3.5 Dispersion in Solvents

If the interaction between a solvent and a polymer is favorable, the polymer segments will rather be surrounding by the solvent than by other segments, and the polymer swells and eventually dissolves. If it is unfavorable, the polymer does not or very little swell. In intermediate situations, it may swell but not dissolve. The nature of the interaction may be assessed from the difference in solubility parameters δ_{polym}-δ_{solv}. What will happen when an ordered symmetrical diblock copolymer film is put in contact with a neutral or selective solvent? For a diblock copolymers, when we say neutral solvents, it means the solvent has a good chemical affinity with the two blocks. When swelling an ordered diblock copolymer film in a neutral solvent, the solvent is uniformly distributed within the blocks, the structure swells and the interfaces deform strongly until the copolymer is completely dissolved in the solvent[92]. However, for many of block copolymers systems, there is no true neutral solvent[93]. A selective solvent is a solvent having a preferential chemical affinity for one of the two blocks of the copolymers. By immersing an ordered diblock copolymers A-B in a selective solvent of block B

preferential, the solvent swells the B domains of the ordered phase. This results in the increase of the layer B thickness.

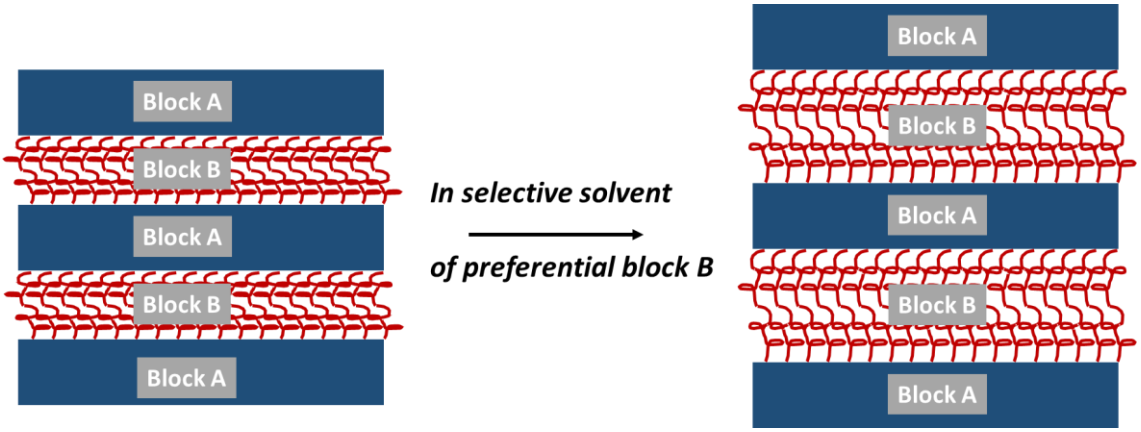

Figure I. 21 Scheme of a lamellar copolymer A-B dispersed in a selective solvent of block B (without thermodynamic equilibrium)

At thermodynamic equilibrium, the interfaces of the system pushed to minimize its free energy and this induces morphological transitions. In the particular case, when the block A is not soluble in the solvent, which is the selective solvent for block B, and block A is glassy (like poly(styrene)), there is no morphological transition. The solvent then selectively swells the B domains of the ordered phase of the A-B diblock copolymer without affecting the A domains or the curvature at the A / B interfaces. The A domains are then fixed in a state not at thermodynamic equilibrium and they keep their shape and size (see Figure I. 21)

Table I. 2 Hilderbrandt solubility parameter for some chemicals

Compound	Hilderbrandt solubility parameter, δ $(MPa)^{1/2}$
Toluene	18.3
THF	18.5
ethanol	26.2
methanol	29.5
poly(styrene)	18.3
poly(2-vinylpyrridine)[95]	21.3

According to the work of H. Lin et all[94] a solvent that dissolves both blocks would easily penetrate into the multilayered structure. When the solvent is selective for only one block, the other block will retard the diffusion of the solvent. On the other hand,

defects in the multilayers will provide channels through which the solvent can easily migrate.

The poly(styrene)-*block*-poly(2-vinylpyridine) (PS-PVP) is the main diblock used in our study. The solubility parameters of used chemicals are shown in Table I. 2.

Both toluene and THF are good solvents for PS and moderately good solvent for P2VP. THF is a slightly better neutral solvent for the diblock, than toluene. P2VP exhibits the swelling characteristics in contact with ethanol and methanol. Water is a non-solvent for PS, which is strongly hydrophobic, and a bad solvent for P2VP, with unfavorable interactions between the polymer backbone with water only slightly compensated by the polar nature of the amine[94,96].

I.4 Gold nanoparticles

A nanoparticle is a solid particle, which is at the nanometer scale in at least one dimension. At this scale, the physicochemical and electronic properties of a nanoparticle are significantly different from the properties of a bulk material which has the same chemical composition. In this thesis work, we are interested in the specific case of gold nanoparticles.

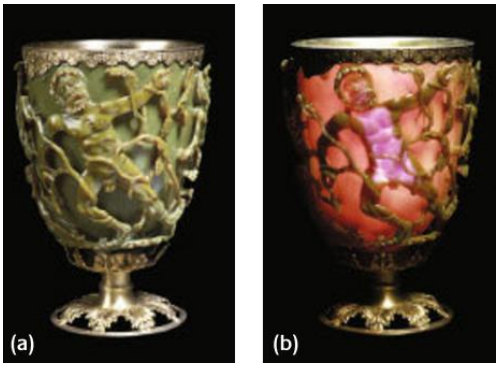

Figure I. 22 Lycurgus Cup in (a) reflected and (b) transmitted light.[97]

The first application of the optical properties of gold nanoparticles is found[97] in Lycurgus Cup of 4th-century(see ***Figure I. 22***), which is made of a mixture of Roman glass with gold nanoparticles. It shows a different color according to the lighting conditions. If the light lit inside the cup, it is red and it is green when lit the light in front of the cup. Also the use of metallic nanoparticles can be found in the windows of certain cathedrals (Bourges, Troyes ...) from the middle ages and in certain colored glasses from the Renaissance period. Today, the gold are mainly used in jewelry, currency, electronics and dentistry because of the noble character of gold bulk.

I.4.1 Synthesis of gold nanoparticles of solution based

In the year 1875, Michael Faraday[98] found a method to obtain gold colloids. Since then, continued researches[99–105] led to the publication of different methods of synthesis of gold nanoparticles, which can control the size, shape (nanospheres, nanorods, nanoshells, nanocages etc, (see **Figure I. 23**) and surface functionality of gold nanoparticles.

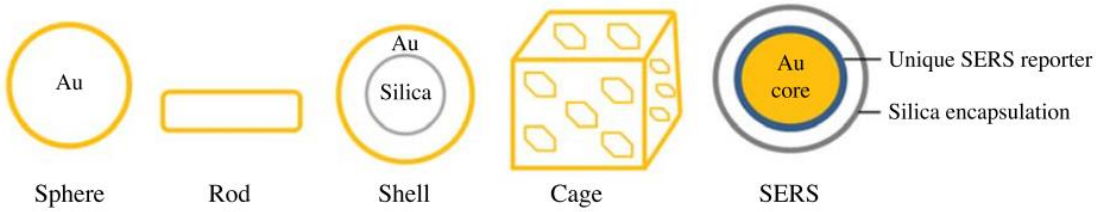

Figure I. 23 Schematic of different shape of Au nanoparticles

In this section, we are particularly interested in chemical synthesis of gold nanoparticles (NPs), which includes reduction of gold salts based on chemical or non-chemical reducers.

1.4.1.1 Reaction based on chemical reducer

The synthesis of gold nanoparticles by chemical reaction is carried out by reaction between a gold salt, a reducing agent and a stabilizing agent. The gold salt is used as a precursor and mostly is chloroauric acid ($HAuCl_4$), in which the gold is in oxidation state (III). A reducing agent is added to reduce gold ions Au^{3+} to gold Au^0 and often is sodium borohydride ($NaBH_4$), sodium citrate (Na_3Ct) or ascorbic acid.

Table I. 3 Serveral ligands affinity for gold surface

Stabilization agent	thiol≈amines≈phosphines≈silanes>alkane≈halide≈alcohols≈Carboxylic Acid
Formula	RSH ≈RNH ≈ R_3P ≈ R_3Si > R_3C ≈ RX ≈ ROH ≈ COOH

As the reaction continues, the solution becomes supersaturated in gold atoms and the particles begin to aggregate and precipitate. The addition of a stabilizing agent (also called a ligand) makes it possible to control the precipitation and to prevent the uncontrolled growth of the nanoparticles. It should be noted that not all ligands have the same affinity for the gold surface[106] (see Table I. 3).

In the majority of syntheses, the shape and size of the nanoparticles can be controlled depending on many parameters: different chemical reducing agents and their concentration, order of addition of the reactants, stirring speed, pH of the reaction solutions, temperature[100,101,103–105,107,108].

1.4.1.2 Reaction based on non-chemical reducer

The gold precursor also can be reduced by non-chemical reducing methods such as temperature, ultrasound or irradiation (UV, gamma ray). In this case, the reduction is caused by temperature or ionizing radiation consisting of a light beam, electrons or gamma rays[109]. By controlling the intensity of the beam, the temperature and the exposure time, the gold nanoparticles size, shape and dispersion can be well controlled. These method have the advantage of reducing the gold salts in films, but reports[109,110] claimed that the mechanism of thermal annealing process are complex, which involved several side reactions and lead to various shape of gold nanoparticles (see Figure I. 24). For example, with a thermal annealing in the presence of poly(vinylpyrrolidone), which is one of the most frequently used stabilizer, protective agent or reactant, various shape of gold NPs can be achieved.

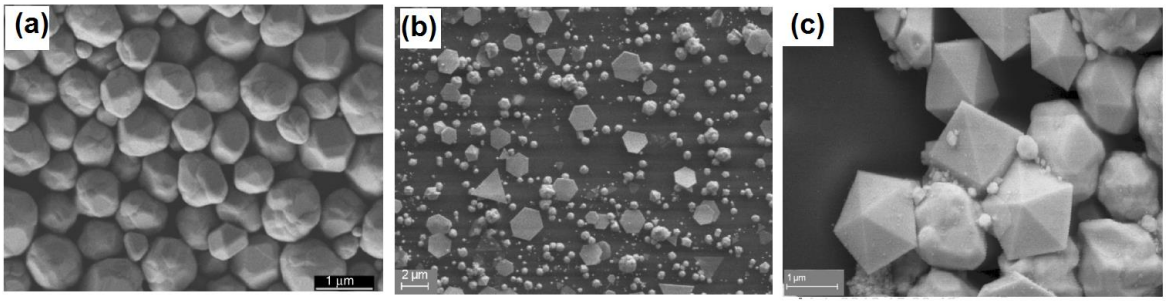

Figure I. 24 SEM images of gold nanoparticles synthesized by thermal annealing in the presence of poly(vinylpyrrolidone) at 60° (a) with 10 g.dm^{-3} concentration of gold salt, and 95° (b)& (c) with 2 g.dm^{-3} & 88 g.dm^{-3} concentration of gold salt respectively.[110]

In this thesis work, we are going to use poly(vinlypyridine) playing a role somewhat similar to that of poly(vinylpyrrolidone) in the latter study.

I.4.2 Chemical and physical properties of gold nanoparticles

Gold is a noble metal because of the stability of its chemistry and its properties. The physical –chemistry parameters of gold are listed in Table I. 4.

Different from the bulk gold, gold nanoparticles exhibit unique properties in color, density, melting point (due to the large ratio of surface atoms to inner atoms), mechanical strength and conductivity (due to increases of surface scattering). In addition, even slight change of the environment will cause the change of physical or chemical properties of gold nanoparticles, which make them a good sensor. Also, gold nanoparticle based catalysis can provide better yield, selectivity and are effective even at low temperatures in many reactions[111] due, in particular, to the high surface area/volume ratio.

Table I. 4 properties of gold (referred from Wikipedia)

Atomic number	79	Standard atomic weight	196.97 g/mol
Melting point	1064.18°C	Electron configuration	$[Xe]4f^{14}\ 5d^{10}\ 6s^{1}$
Density	19.30 g/cm^3	Boiling point	2970 °C

I.4.3 Optical properties of gold nanoparticles

I.4.3.1 Permittivity of bulk gold

The optical response of gold is dominated by two electronic contributions: interband and intraband transitions. The complex electrical permittivity of gold is written as the sum of the interband and intraband contributions according to Equation 1- 35.

Equation 1- 35
$$\tilde{\varepsilon}_{Au} = \tilde{\varepsilon}_{Au,interband} + \tilde{\varepsilon}_{Au,intraband}$$

Equation 1- 36
$$\tilde{\varepsilon}_{Au,intraband} = \varepsilon_{\infty} - \frac{{\omega_p}^2}{\omega^2 + i\gamma_0\omega}$$

Several researchers[112,113] determined the values of the real ε_r and imaginary ε_i part of Au permittivity for wavelengths ranging from 200 to 2000 nm experimentally, with some differences between them. In the present thesis, we chose to use the data of Johnson and Christy[109] (JC), which is shown in Figure I. 25 (dots). In the visible red and near-infrared regions, the dielectric function is dominated by the intraband component, which can be well approximated by a free-electron Drude model (continuous lines in Figure I. 25), written according to Equation 1- 36[114,115]. Where the frequency of the photons of the incidence beam is ω, ε_∞ is a constant which gives the permittivity of gold in very large frequencies and γ_0 is the damping rate of the gold, which will be discussed later.

The plasma frequency ω_p of the conduction electrons of gold is defined by ${\omega_p}^2 = \frac{N_e e^2}{\varepsilon_0 m_{eff}}$ with the density of electrons N_e, the elementary charge e, the permittivity of vacuum ε_0 and the effective mass of an electron m_{eff}.

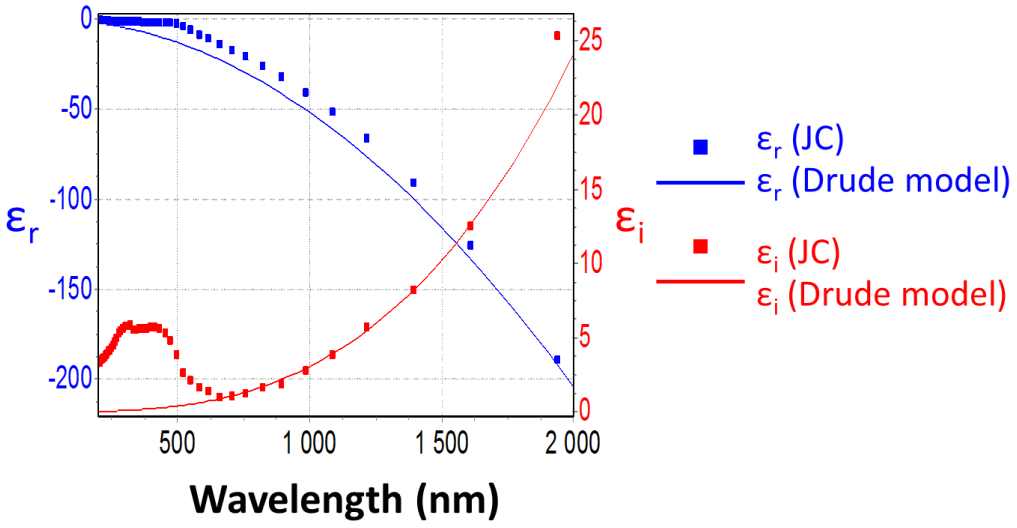

Figure I. 25 Permittivity of gold taken from JC (dots) and compared with the Drude model approximation (continuous curves)

The continuous lines in Figure I. 25 represent the adjustment of the JC data by the Drude model taking the values of the parameters listed in Table I. 5.

From Figure I. 25, we can see that the fit between the experimental data of JC and the Drude model agrees well in the wavelengths ranging from 600 to 2000 nm, where the permittivity is dominated by the intraband response (Equation 1- 35 $\tilde{\varepsilon}_{Au,intraband}$ and the first term $\tilde{\varepsilon}_{Au,interband}$ is negligible). On the contrary, for short wavelengths below 600nm, the interband contribution $\tilde{\varepsilon}_{Au,interband}$ cannot be neglected, which causes the disagreement between the experimental (JC) data and the Drude model. There is no proper model for the interband component of the gold permittivity, but we use the JC data for reference. Note that the absorption response at 400 nm shown in Figure I. 25, which corresponds to the interband contribution, explains the golden yellow color of the bulk gold.

Table I. 5 Values of the Drude parameters for bulk gold (JC)

Parameter	ε_∞	${\omega_p}^2$	γ_0	ι
Value	9.4	8.92 eV	0.073 eV	12.5 nm

The damping of the free (Drude) electrons motion in bulk gold is due to collisions with the crystal lattice and the imperfections of the material. So γ_0 is related to the mean free path of electrons l, which is the average distance the electrons travel between collisions (see Equation 1- 37 and Figure I. 26(a)).

Equation 1- 37 $$\gamma_0 = \frac{v_F}{l}$$

With Fermi velocity $v_F = 1.4 \times 10^6\ m/s$. For bulk gold, $\gamma_0 = 0.073\ eV$ and $l = 12.5\ nm$.

I.4.3.2 Absorption of gold nanoparticles

The properties of gold nanoparticles differ significantly from that of bulk. In the early 20th century, Maxwell-Garnett[116,117] explained many of the scattering effects and color changes, while the size dependent optical properties of metal spheres were explained by Mie[118]. Because they exhibit novel properties, theoretical and experimental studies of metallic nanoparticles have been continuous since then.

Due to the extremely high surface area/volume ratio, the gold nanoparticles generate a phenomenon negligible at the macroscopic scale. When a gold nanoparticle is placed in an electromagnetic field whose wavelength is much greater than the particle size, all the conduction electrons can be considered as a plasma (gas of ionized species of high density). The external field induces a collective oscillation on the surface of the nanoparticle in a macroscopic scale. When the frequency of the incident field corresponds to the natural frequency ω_0 of these oscillations (see Equation 1- 38), a resonance phenomenon occurs, which is called surface plasmon resonance (as we mentioned before, see Figure I. 4).

Equation 1- 38 $$\omega_0 = \frac{1}{2\pi}\sqrt{\frac{k}{m_{eff}}}$$

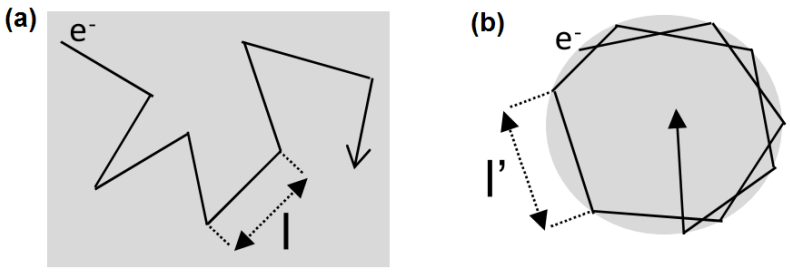

Figure I. 26 the mean free path of electrons in (a) bulk gold and (b) gold nanoparticles[84]

This resonance of gold nanoparticles which takes place at a visible wavelength and induces a strong absorption, gives gold nanoparticles red-to-green color depending on the size and shape of the NPs[119–121].

When gold is confined to the nano-scale, the mean free path of electrons l' is also modified. Colliding with the crystal lattice, electrons also can collide with the surface of the particle (see Figure I. 26(b)).

So the total damping is caused by γ_0 in the collision term of bulk gold and the collision of surfaces γ_{conf} (see Equation 1.7).

Equation 1- 39 $$\gamma_{tot} = \gamma_0 + \gamma_{conf} = \frac{v_F}{l} + A\frac{v_F}{l_c}$$

Where A is the surface diffusion coefficient and is equal to 1 and l_c is a correction to the mean free path of the electrons in a gold nanoparticle[122]. The effective mean path l' is defined by the mean free path of bulk gold l and the correction l_c with Equation 1- 40(see Figure I. 26).

Equation 1- 40 $$l' = \frac{l \times l_c}{l_c + A \times l}$$

From Equation 1- 39 and Equation 1- 40, the interband component is not modified by small size effect, so that the intraband contribution of the complex permittivity of gold nanoparticles is Equation 1- 41.

Equation 1- 41 $$\tilde{\varepsilon}_{AuNPs,intraband} = \varepsilon_\infty - \frac{\omega_p}{\omega^2 + i\omega(\gamma_0 + \gamma_{conf})}$$

From Equation 1- 41, $\tilde{\varepsilon}_{\mathrm{AuNPs,intraband}}$ depends on the correction of the mean free path of electrons l_c. The value of l_c depends on the size of the nanoparticles.

In Figure I. 27, dots lines and continuous lines represent the electrical permittivities in the case of bulk gold and gold nanoparticle (NPs), respectively. The continuous lines in Figure I. 27 represent the adjustment of the JC data by the Drude model as we mentioned before. The continuous lines corresponds to the value of ε for nanoparticles of diameter of 10.7nm[122].

Table I. 6 values of parameters in JC

Parameter	ε_∞	${\omega_p}^2$	γ_0	ι	ι_c	ι'
Value	9.4	8.92 eV	0.073 eV	12.5 nm	10.7nm	5.9nm

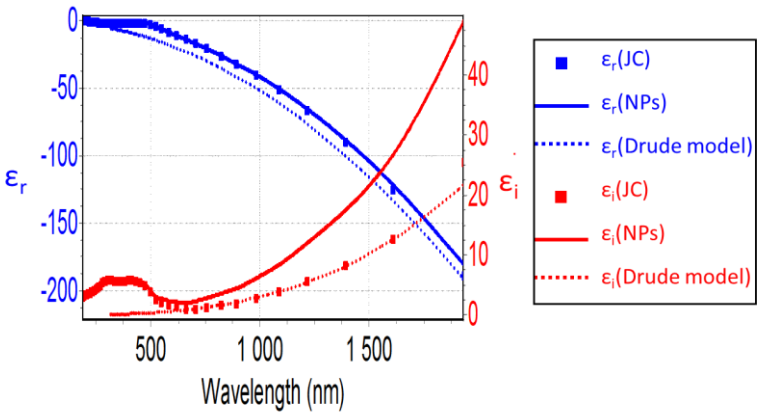

Figure I. 27 permittivity of gold taken from JC (dots curves), gold nanoparticles (NPs) (continuous lines) and the Drude model approximation (dash curves).

Due to their surface plasmon resonance (as we mentioned in section I.2, Figure I. 4)[119], gold nanoparticles have a strong interaction with light, which induces interesting optical properties[120],. The surface plasmon resonance of a gold nanoparticle is evidenced by a strong absorption on a narrow wavelength band. This absorption can be detected when measuring the absorbance of a suspension of gold nanoparticles. The absorbance is defined by Beer-Lambert's law:

Equation 1- 42 $$A = log(I_0/I) = S_c L \sigma_{ext}$$

Equation 1- 43 $$\sigma_{ext} = \sigma_{abs} + \sigma_{scatt}$$

where I and I_0 are the incident intensity and transmitted intensity, respectively. S_c and L are the concentration of the sample solution (in mol/L) and the length of light path (in cm). σ_{ext} is the extinction coefficient. This extinction consists of the absorption and the scattering of the suspension with particles (see Equation 1- 43). Because gold nanoparticle (typically <50 nm) are much smaller than the wavelength of light, so the contribution of scattering is negligible ($\sigma_{ext} \approx \sigma_{abs}$). And this absorption represents the energy loss of the beam that interacts with the particles and is written as follows[26].

Equation 1- 44 $$\sigma_{ext} = \sigma_{abs} = k \times Im(\alpha) \text{ where } k = n\, 2\pi/\lambda$$

Where k is the wave number and $Im(\alpha)$ is the imaginary part of the polarizability α of the nanoparticle (see Equation 1- 45). n is the refractive index of the surrounding medium and λ is the wavelength of the incidence beam. α represents the ability of a nanoparticle to polarize by creating oriented dipoles (or by reorganizing existing dipoles) along an applied electric field. For a spherical gold nanoparticle, it can be

written according to Equation 1- 45, with the sphere volume V, and the permittivity of the medium ε_m. Combining Equation 1- 42, Equation 1- 44 and Equation 1- 45, the absorbance of suspension can be written in Equation 1- 46.

Equation 1- 45 $$\alpha = 3V\varepsilon_m\left(\frac{\tilde{\varepsilon}_{Au}-\varepsilon_m}{\tilde{\varepsilon}_{Au}+2\varepsilon_m}\right)$$

Equation 1- 46 $$A = S_c L\frac{24\pi^2}{\lambda}R^3 n\varepsilon_m\frac{\varepsilon_{i,Au}}{\left(\varepsilon_{r,Au}+2\varepsilon_m\right)^2+\varepsilon_{i,Au}{}^2}$$

Where R is the radius of nanoparticles, $\varepsilon_{r,Au}$ and $\varepsilon_{i,Au}$ are real and imaginary parts of the permittivity of gold nanoparticles. According to Equation 1- 46, the plasmonic peak depends on: the refractive index n and permittivity of the surrounding medium, the size and the permittivity of gold nanoparticles.

The absorbance shows[84] a strong increase when $\varepsilon_{r,Au}=-2\varepsilon_m$, which corresponds to the surface plasmon resonance of spherical gold nanoparticles. According to Figure I. 28, this resonance is around 520 nm, so the suspension appears red. The interband contribution is also visible on an optical density measurement, between 400 and 450 nm and is independent from the particles size.

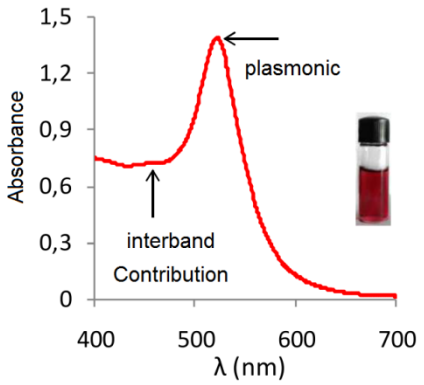

Figure I. 28 absorbance of aqueous suspension of gold particles with radius R=5nm[84]

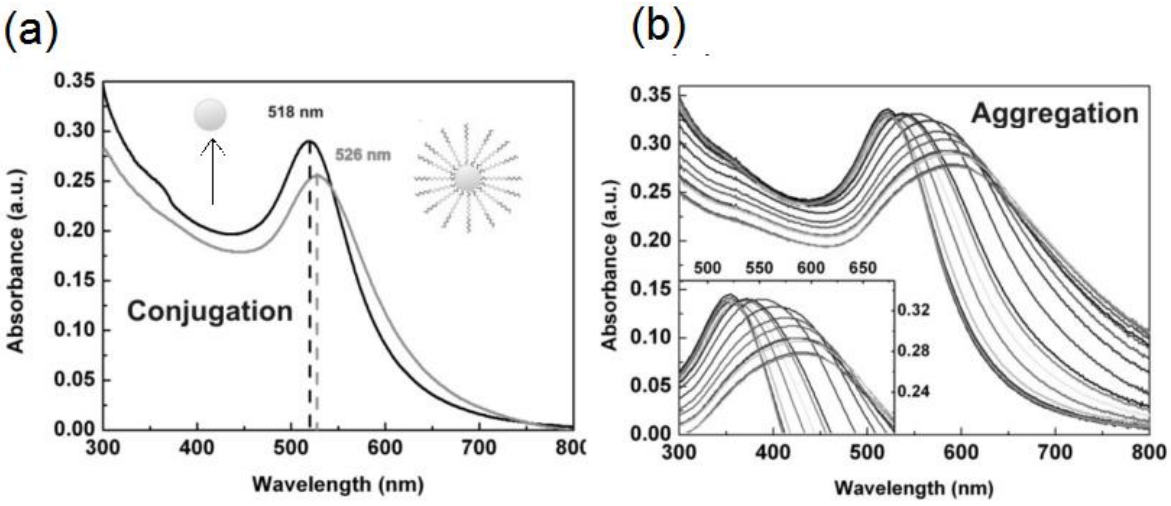

Figure I. 29 (a) The position of surface plasmon resonant band depend on the chemical composition of particle surfactant shell by changing the refractive index of the surrounding

environment. (b) The aggregation of Au NPs correlates with a red-shift of the surface plasmon resonant band position along with an increase in the absorbance from 600 to 800 nm[123]

According to Equation 1- 46, the absorbance depends on the refractive index n and permittivity of the surrounding medium ε_m. In particular case, when gold nanoparticles bind with other molecules or aggregates, the position of the surface plasmon resonance changes[123] (see Figure I. 28). This phenomenon can also be observed in our studies in Chapters IV and VI.

When the refractive index of the surrounding medium increases, the net charge at the surface of the particle is attenuated, which reduces the resonant force of the oscillator and cause the wavelength of resonance towards the red.

Depending on the size and shape, the suspension of gold nanoparticles shows different colors (see Figure I. 29(a) lower image). Compared to spheres, rods give more colors, which is due to the difference nature of their plasmon bands. The rods have two bands, while spheres have one only which gives rods response more sensitivity to their size.

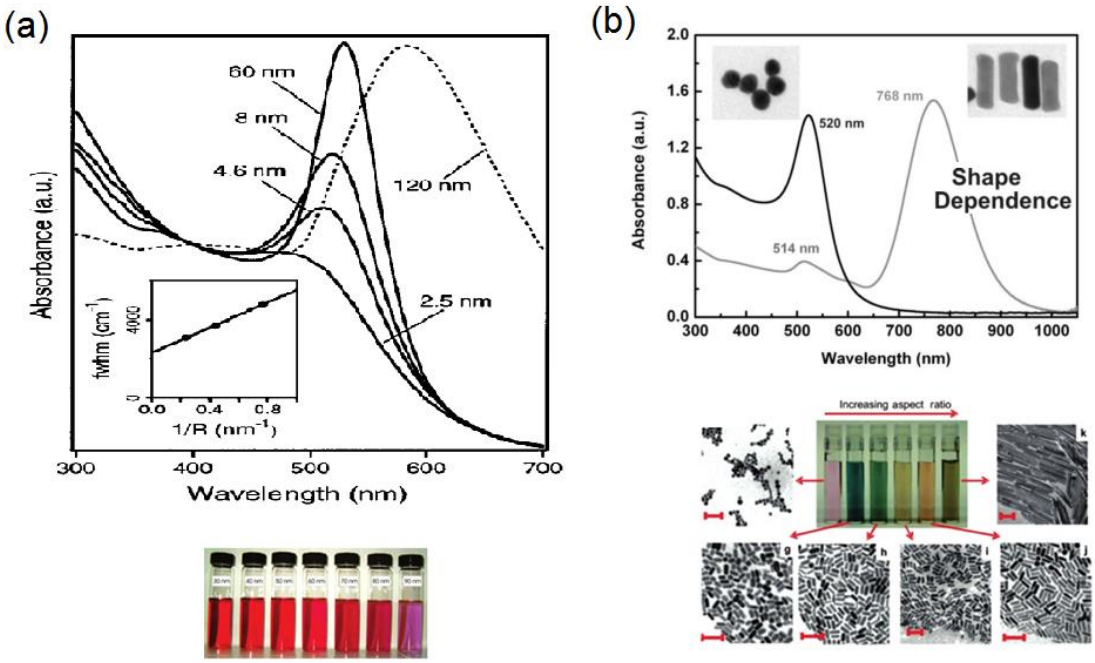

Figure I. 30 The position of surface plasmon resonant band depend on (a)[124,125] different size of nanoparticles, and the color of suspensions with gold nanospheres for diameters ranging from 30nm to 90nm (lower plot from left to right) and (b)[121,123,126]gold nanorods shape of nanoparticles, and the color of suspensions with increasing dimensions (scale bars is 100 nm).

In our study, we are interested in gold nanoparticles with a diameter of less than 50 nm. For gold nanoparticles with a diameter of between 10 and 50 nm, the plasmonic peak is around 520 nm in an aqueous medium. As the particle diameter increases, the peak becomes finer and more intense (see Figure I. 30). For nanoparticles with a diameter between 2 and 10 nm, the volume accessible to the conduction electrons is very restricted, which leads to a decrease in the mean free path of the electrons. The damping of the electronic oscillation caused by the collisions between the electrons and the walls of the particle is responsible for the widening of the plasmon resonance. Thus, for nanoparticles with a diameter of less than 2 nm, the confining effects dominate the signal and the plasmonic peak is totally masked.

I.4.4 Gold nanoparticles in polymers

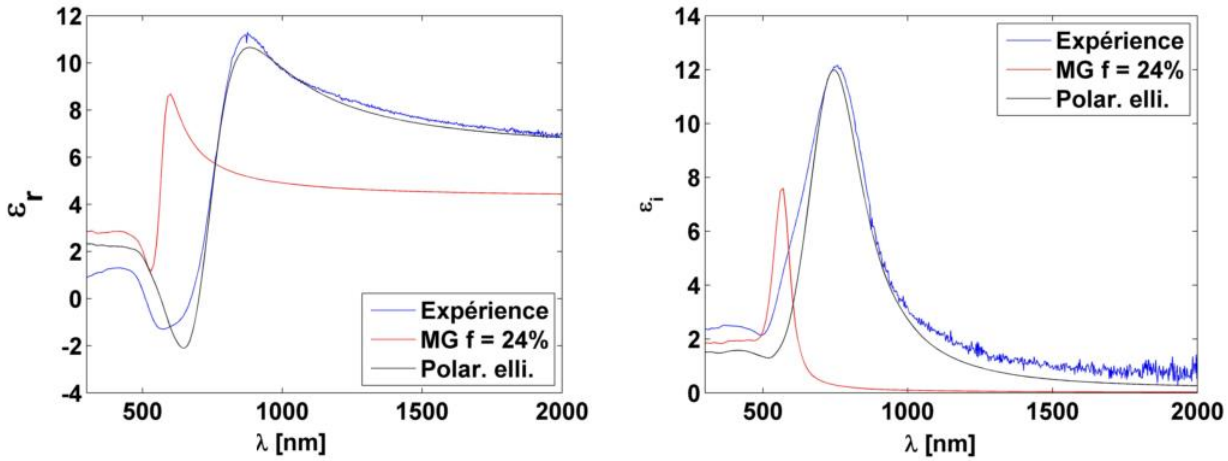

Figure I. 31 Real (left) and imaginary (right) part of the nanocomposite permittivity, which consists of 50 nm poly(vinyl alcohol) with 24% volume fraction of gold nanoparticles (diameter around 14nm). The blue lines are experimental data, the red lines are fitting lines with a Maxwell Garnett effective medium model. The black lines are fitting lines with a improved MG model.[127]

After the nanoparticles of gold suspended in a liquid, we are interested in gold nanoparticles dispersed in a film of polymer. The optical parameters can be determined by spectroscopic ellipsometry (see Chapter II.1). Julien Vieaud[122] and Kevin Ehrhardt[127] studied during their thesis nanocomposite systems composed of gold nanoparticles randomly dispersed in a polymer film. It has been shown that such systems can exhibit negative permittivity close to the plasmon resonance for dense nanocomposite systems with volume fraction of gold larger than 24% (see Figure I. 31).

This negative responses give us a possibility to realize the hyperbolic metamaterial by lamellar stacks of nanocomposite layer and polymer instead of metallic layer and dielectric layer. The organization of the nanoparticles will influence the optical responses, and we plan to organize the nanoparticles using block copolymers as a structuring matrix.

References

1. Kshetrimayum, R. S. A brief intro to metamaterials. *IEEE Potentials* **23,** 44–46 (2004).
2. Zouhdi, S., Sihvola, A. & Vinogradov, A. P. *Metamaterials and plasmonics: fundamentals, modelling, applications*. (Springer Science & Business Media, 2008).
3. Fang, N., Lee, H., Sun, C. & Zhang, X. Sub–diffraction-limited optical imaging with a silver superlens. *Science* **308,** 534–537 (2005).
4. Melville, D. O. S. & Blaikie, R. J. Super-resolution imaging through a planar silver layer. *Opt. Express* **13,** 2127–2134 (2005).
5. Taubner, T., Korobkin, D., Urzhumov, Y., Shvets, G. & Hillenbrand, R. Near-field microscopy through a SiC superlens. *Science* **313,** 1595 (2006).
6. Liu, Z., Lee, H., Xiong, Y., Sun, C. & Zhang, X. Far-field optical hyperlens magnifying sub-diffraction-limited objects. *Science* **315,** 1686 (2007).
7. Jacob, Z., Alekseyev, L. V & Narimanov, E. Optical hyperlens: far-field imaging beyond the diffraction limit. *Opt. Express* **14,** 8247–8256 (2006).
8. Ergin, T., Stenger, N., Brenner, P., Pendry, J. B. & Wegener, M. Three-dimensional invisibility cloak at optical wavelengths. *Science* **328,** 337–339 (2010).
9. Shalaev, V. M. Optical cloaking with metamaterials, Nat. in (Photon, 2007).
10. Born, M. & Wolf, E. *Principles of optics: electromagnetic theory of propagation, interference and diffraction of light*. (Elsevier, 2013).

11. Fujiwara, H. *Spectroscopic ellipsometry: principles and applications*. (John Wiley & Sons, 2007).

12. Liu, Y. & Zhang, X. Metamaterials: a new frontier of science and technology. *Chem. Soc. Rev.* **40,** 2494–2507 (2011).

13. Smith, D. R., Pendry, J. B. & Wiltshire, M. C. K. Metamaterials and negative refractive index. *Science* **305,** 788–792 (2004).

14. Veselago, V. G. The electrodynamics of substances with simultaneously negative values of and μ. *Sov. Phys. uspekhi* **10,** 509 (1968).

15. Pendry, J. B. Negative refraction makes a perfect lens. *Phys. Rev. Lett.* **85,** 3966 (2000).

16. Pendry, J. B., Schurig, D. & Smith, D. R. Controlling electromagnetic fields. *Science* **312,** 1780–1782 (2006).

17. Smith, D. R., Padilla, W. J., Vier, D. C., Nemat-Nasser, S. C. & Schultz, S. Composite medium with simultaneously negative permeability and permittivity. *Phys. Rev. Lett.* **84,** 4184 (2000).

18. Shelby, R. A., Smith, D. R. & Schultz, S. Experimental verification of a negative index of refraction. *Science* **292,** 77–79 (2001).

19. Yen, T.-J. *et al.* Terahertz magnetic response from artificial materials. *Science* **303,** 1494–1496 (2004).

20. Linden, S. *et al.* Magnetic response of metamaterials at 100 terahertz. *Science* **306,** 1351–1353 (2004).

21. Soukoulis, C. M., Linden, S. & Wegener, M. Negative refractive index at optical wavelengths. *Science* **315,** 47–49 (2007).

22. Zhou, J. *et al.* Saturation of the magnetic response of split-ring resonators at optical frequencies. *Phys. Rev. Lett.* **95,** 223902 (2005).

23. Zhang, S. *et al.* Experimental demonstration of near-infrared negative-index metamaterials. *Phys. Rev. Lett.* **95,** 137404 (2005).

24. Lapine, M. & Tretyakov, S. Contemporary notes on metamaterials. *IET microwaves, antennas Propag.* **1,** 3–11 (2007).

25. Alù, A., Engheta, N., Erentok, A. & Ziolkowski, R. W. Single-negative, double-negative, and low-index metamaterials and their electromagnetic applications. *IEEE Antennas Propag. Mag.* **49,** 23–36 (2007).

26. Jackson, J. D. Classical electromagnetics. *J. Wiley Sons* 330–335 (1999).

27. Yang, F. *et al.* Period reduction lithography in normal UV range with surface plasmon polaritons interference and hyperbolic metamaterial multilayer structure. *Appl. Phys. Express* **8,** 62004 (2015).

28. Schasfoort, R. B. M. *Handbook of surface plasmon resonance*. (Royal Society of Chemistry, 2017).

29. Maier, S. A. *Plasmonics: fundamentals and applications*. (Springer Science & Business Media, 2007).

30. Pitarke, J. M., Silkin, V. M., Chulkov, E. V & Echenique, P. M. Theory of surface plasmons and surface-plasmon polaritons. *Reports Prog. Phys.* **70,** 1 (2006).

31. Sun, L., Chen, P. & Lin, L. in *Applications of Molecular Spectroscopy to Current Research in the Chemical and Biological Sciences* (InTech, 2016).

32. Ferrari, L., Wu, C., Lepage, D., Zhang, X. & Liu, Z. Hyperbolic metamaterials and their applications. *Prog. Quantum Electron.* **40,** 1–40 (2015).

33. Mackay, T. G. Toward optical sensing with hyperbolic metamaterials. *Opt. Eng.* **54,** 67102 (2015).

34. Ferrari_PrQuantElectr2015.pdf.

35. Esslinger, M. *et al.* Tetradymites as natural hyperbolic materials for the near-infrared to visible. *Acs Photonics* **1,** 1285–1289 (2014).

36. Cortes, C. L., Newman, W., Molesky, S. & Jacob, Z. Quantum nanophotonics using hyperbolic metamaterials. *J. Opt.* **14,** 63001 (2012).

37. Rytov, S. M. Electromagnetic properties of a finely stratified medium. *Sov. Phys. JETP-USSR* **2,** 466–475 (1956).

38. Poddubny, A., Iorsh, I., Belov, P. & Kivshar, Y. Hyperbolic metamaterials. *Nat. Photonics* **7,** 948–957 (2013).

39. Yao, J. *et al.* Optical negative refraction in bulk metamaterials of nanowires.

Science **321,** 930 (2008).

40. Zhang, X. & Liu, Z. Superlenses to overcome the diffraction limit. *Nat. Mater.* **7,** 435–441 (2008).

41. Narimanov, E. E. & Shalaev, V. M. Optics: beyond diffraction. *Nature* **447,** 266–267 (2007).

42. Sreekanth, K. V. *et al.* A multiband perfect absorber based on hyperbolic metamaterials. *Sci. Rep.* **6,** (2016).

43. Krishnamoorthy, H. N. S., Jacob, Z., Narimanov, E., Kretzschmar, I. & Menon, V. M. Topological transitions in metamaterials. *Science* **336,** 205–209 (2012).

44. Kurilkina, S. N., Binhussain, M. A., Belyi, V. N. & Kazak, N. S. Features of hyperbolic metamaterials with extremal optical characteristics. *J. Opt.* **18,** 85102 (2016).

45. Jacob, Z. *et al.* Engineering photonic density of states using metamaterials. *Appl. Phys. B Lasers Opt.* **100,** 215–218 (2010).

46. Sreekanth, K. V., Krishna, K. H., De Luca, A. & Strangi, G. Large spontaneous emission rate enhancement in grating coupled hyperbolic metamaterials. *Sci. Rep.* **4,** 6340 (2014).

47. Jacob, Z., Smolyaninov, I. I. & Narimanov, E. E. Broadband Purcell effect: Radiative decay engineering with metamaterials. *Appl. Phys. Lett.* **100,** 181105 (2012).

48. Lu, D., Kan, J. J., Fullerton, E. E. & Liu, Z. Enhancing spontaneous emission rates of molecules using nanopatterned multilayer hyperbolic metamaterials. *Nat. Nanotechnol.* **9,** 48–53 (2014).

49. Biehs, S.-A., Tschikin, M. & Ben-Abdallah, P. Hyperbolic metamaterials as an analog of a blackbody in the near field. *Phys. Rev. Lett.* **109,** 104301 (2012).

50. Guo, Y., Cortes, C. L., Molesky, S. & Jacob, Z. Broadband super-Planckian thermal emission from hyperbolic metamaterials. *Appl. Phys. Lett.* **101,** 131106 (2012).

51. Kabashin, A. V *et al.* Plasmonic nanorod metamaterials for biosensing. *Nat. Mater.* **8,** 867–871 (2009).

52. Sreekanth, K. V. *et al.* Extreme sensitivity biosensing platform based on hyperbolic metamaterials. *Nat. Mater.* (2016).

53. Dürig, U., Pohl, D. W. & Rohner, F. Near-field optical-scanning microscopy. *J. Appl. Phys.* **59,** 3318–3327 (1986).

54. Klar, T. A., Jakobs, S., Dyba, M., Egner, A. & Hell, S. W. Fluorescence microscopy with diffraction resolution barrier broken by stimulated emission. *Proc. Natl. Acad. Sci.* **97,** 8206–8210 (2000).

55. Boettiger, A. N. *et al.* Super-resolution imaging reveals distinct chromatin folding for different epigenetic states. *Nature* **529,** 418–422 (2016).

56. Liu, Z. *et al.* Far-field optical superlens. *Nano Lett.* **7,** 403–408 (2007).

57. Raether, H. *Surface plasmons on smooth and rough surfaces and on gratings*. **111,** (Springer, 2006).

58. Wood, B., Pendry, J. B. & Tsai, D. P. Directed subwavelength imaging using a layered metal-dielectric system. *Phys. Rev. B* **74,** 115116 (2006).

59. Zhukovsky, S. V, Kidwai, O. & Sipe, J. E. Physical nature of volume plasmon polaritons in hyperbolic metamaterials. *Opt. Express* **21,** 14982–14987 (2013).

60. Ishii, S., Kildishev, A. V, Narimanov, E., Shalaev, V. M. & Drachev, V. P. Sub-wavelength interference pattern from volume plasmon polaritons in a hyperbolic medium. *Laser Photon. Rev.* **7,** 265–271 (2013).

61. Yang, X., Yao, J., Rho, J., Yin, X. & Zhang, X. Experimental realization of three-dimensional indefinite cavities at the nanoscale with anomalous scaling laws. *Nat. Photonics* **6,** 450–454 (2012).

62. Elser, J., Wangberg, R., Podolskiy, V. A. & Narimanov, E. E. Nanowire metamaterials with extreme optical anisotropy. *Appl. Phys. Lett.* **89,** 261102 (2006).

63. Podolskiy, V. A. & Narimanov, E. E. Strongly anisotropic waveguide as a nonmagnetic left-handed system. *Phys. Rev. B* **71,** 201101 (2005).

64. Yao, J. *et al.* Design, fabrication and characterization of indefinite metamaterials of nanowires. *Philos. Trans. R. Soc. London A Math. Phys. Eng. Sci.* **369,** 3434–3446 (2011).

65. Noginov, M. A. *et al.* Bulk photonic metamaterial with hyperbolic dispersion. *Appl. Phys. Lett.* **94,** 151105 (2009).

66. Evans, P. *et al.* Growth and properties of gold and nickel nanorods in thin film alumina. *Nanotechnology* **17,** 5746 (2006).

67. Sulka, G. D. Highly ordered anodic porous alumina formation by self-organized anodizing. *Nanostructured Mater. Electrochem.* **1,** 1–116 (2008).

68. Nefedov, I. S. Electromagnetic waves propagating in a periodic array of parallel metallic carbon nanotubes. *Phys. Rev. B* **82,** 155423 (2010).

69. Soukoulis, C. M. & Wegener, M. Past achievements and future challenges in the development of three-dimensional photonic metamaterials. *Nat. Photonics* **5,** 523–530 (2011).

70. Baron, A., Aradian, A., Ponsinet, V. & Barois, P. Self-assembled optical metamaterials. *Opt. Laser Technol.* **82,** 94–100 (2016).

71. Gong, J., Li, G. & Tang, Z. Self-assembly of noble metal nanocrystals: Fabrication, optical property, and application. *Nano Today* **7,** 564–585 (2012).

72. Grulke, E. A., Immergut, E. H. & Brandrup, J. *Polymer handbook*. (John Wiley & Sons, 1999).

73. Bates, F. S. & Fredrickson, G. H. Block copolymer thermodynamics: theory and experiment. *Annu. Rev. Phys. Chem.* **41,** 525–557 (1990).

74. Ohta, T. & Kawasaki, K. Equilibrium morphology of block copolymer melts. *Macromolecules* **19,** 2621–2632 (1986).

75. Bates, F. S. & Fredrickson, G. H. Block copolymers—designer soft materials. *Phys. Today* **52,** 32–38 (1999).

76. Hamley, I. W. & I W, H. *The physics of block copolymers*. **19,** (Oxford University Press New York, 1998).

77. Leibler, L. Theory of microphase separation in block copolymers. *Macromolecules* **13,** 1602–1617 (1980).

78. Nojima, S. & Roe, R. J. Effect of molecular weight of added polystyrene on the order-disorder transition of styrene-butadiene diblock copolymer.

Macromolecules **20,** 1866–1876 (1987).

79. Zin, W. C. & Roe, R. J. Phase equilibria and transition in mixtures of a homopolymer and a block copolymer. 1. Small-angle x-ray scattering study. *Macromolecules* **17,** 183–188 (1984).

80. Roe, R.-J., Fishkis, M. & Chang, J. C. Small-angle x-ray diffraction study of thermal transition in styrene-butadiene block copolymers. *Macromolecules* **14,** 1091–1103 (1981).

81. Hashimoto, T., Kowsaka, K., Shibayama, M. & Kawai, H. Time-resolved small-angle x-ray scattering studies on the kinetics of the order-disorder transition of block polymers. 2. Concentration and temperature dependence. *Macromolecules* **19,** 754–762 (1986).

82. Helfand, E. & Wasserman, Z. R. Macromolecules 1978, l.

83. Han, C. D., Kim, J. & Kim, J. K. Determination of the order-disorder transition temperature of block copolymers. *Macromolecules* **22,** 383–394 (1989).

84. Tallet, C. Nanocomposites plasmoniques anisotropes à base de copolymères à blocs et de nanoparticules d'or. (Université Sciences et Technologies-Bordeaux I, 2012).

85. Semenov, N. N. & Khimicheskoy, N. N. S. O. N. P. Kinetiki i Reaktsionnoy Sposobnosti. *Acad. Sci. USSR, Moscow* 41 (1958).

86. Sohn, B. H. & Yun, S. H. Perpendicular lamellae induced at the interface of neutral self-assembled monolayers in thin diblock copolymer films. *Polymer* **43,** 2507–2512 (2002).

87. Morkved, T. L. & Jaeger, H. M. Thickness-induced morphology changes in lamellar diblock copolymer ultrathin films. *Europhysics Lett.* **40,** 643 (1997).

88. Sohn, B. H. & Seo, B. H. Fabrication of the multilayered nanostructure of alternating polymers and gold nanoparticles with thin films of self-assembling diblock copolymers. *Chem. Mater.* **13,** 1752–1757 (2001).

89. Hu, M. *et al.* Gold nanostructures: engineering their plasmonic properties for biomedical applications. *Chem. Soc. Rev.* **35,** 1084–1094 (2006).

90. Ausserre, D., Chatenay, D., Coulon, G. & Collin, B. Growth of two dimensional

domains in copolymer thin films. *J. Phys.* **51,** 2571–2580 (1990).

91. Xu, T., Hawker, C. J. & Russell, T. P. Interfacial interaction dependence of microdomain orientation in diblock copolymer thin films. *Macromolecules* **38,** 2802–2805 (2005).

92. Lodge, T. P., Hamersky, M. W., Hanley, K. J. & Huang, C.-I. Solvent distribution in weakly-ordered block copolymer solutions. *Macromolecules* **30,** 6139–6149 (1997).

93. Peng, J. *et al.* Morphologies in solvent-annealed thin films of symmetric diblock copolymer. *J. Chem. Phys.* **125,** 64702 (2006).

94. Lin, H., Steyerl, A., Satija, S. K., Karim, A. & Russell, T. P. Solvent penetration into ordered thin films of diblock copolymers. *Macromolecules* **28,** 1470–1474 (1995).

95. Arichi, S., Matsuura, H., Tanimoto, Y. & Murata, H. Studies of poly-2-vinylpyridine. ii. solubilities in various solvents. *Bull. Chem. Soc. Jpn.* **39,** 434–439 (1966).

96. Noshay, A. & McGrath, J. E. *Block copolymers: overview and critical survey*. (Elsevier, 2013).

97. Freestone, I., Meeks, N., Sax, M. & Higgitt, C. The Lycurgus cup—a roman nanotechnology. *Gold Bull.* **40,** 270–277 (2007).

98. Faraday, M. The Bakerian lecture: experimental relations of gold (and other metals) to light. *Philos. Trans. R. Soc. London* **147,** 145–181 (1857).

99. Chow, M. K. & Zukoski, C. F. Gold Sol Formation Mechanisms: Role of Colloidal Stability. *J. Colloid Interface Sci.* **165,** 97–109 (1994).

100. Sun, Y. & Xia, Y. Shape-Controlled Synthesis of Gold and Silver Nanoparticles. *Science* **298,** 2176 LP-2179 (2002).

101. Kimling, J. *et al.* Turkevich method for gold nanoparticle synthesis. *J. Phys. Chem. B* **110,** 15700–15707 (2006).

102. Tsung, C. *et al.* Shape-and Orientation-Controlled Gold Nanoparticles Formed within Mesoporous Silica Nanofibers. *Adv. Funct. Mater.* **16,** 2225–2230 (2006).

103. Ji, X. *et al.* Size Control of Gold Nanocrystals in Citrate Reduction: The Third Role of Citrate. *J. Am. Chem. Soc.* **129,** 13939–13948 (2007).

104. Yeh, Y.-C., Creran, B. & Rotello, V. M. Gold nanoparticles: preparation, properties, and applications in bionanotechnology. *Nanoscale* **4,** 1871–1880 (2012).

105. Khan, Z., Singh, T., Hussain, J. I. & Hashmi, A. A. Au(III)–CTAB reduction by ascorbic acid: Preparation and characterization of gold nanoparticles. *Colloids Surfaces B Biointerfaces* **104,** 11–17 (2013).

106. Neouze, M.-A. & Schubert, U. Surface modification and functionalization of metal and metal oxide nanoparticles by organic ligands. *Monatshefte für Chemie/Chemical Mon.* **139,** 183–195 (2008).

107. Castro, H. P. S. *et al.* Third-order nonlinear optical response of colloidal gold nanoparticles prepared by sputtering deposition. *J. Appl. Phys.* **114,** 183104 (2013).

108. Tsutsui, G., Huang, S., Sakaue, H., Shingubara, S. & Takahagi, T. Well-size-controlled colloidal gold nanoparticles dispersed in organic solvents. *Jpn. J. Appl. Phys.* **40,** 346 (2001).

109. Porel, S., Venkatram, N., Narayana Rao, D. & Radhakrishnan, T. P. In situ synthesis of metal nanoparticles in polymer matrix and their optical limiting applications. *J. Nanosci. Nanotechnol.* **7,** 1887–1892 (2007).

110. Zhou, M., Bron, M. & Schuhmann, W. Controlled synthesis of gold nanostructures by a thermal approach. *J. Nanosci. Nanotechnol.* **8,** 3465–3472 (2008).

111. Hayashi, T., Tanaka, K. & Haruta, M. Selective vapor-phase epoxidation of propylene over Au/TiO2catalysts in the presence of oxygen and hydrogen. *J. Catal.* **178,** 566–575 (1998).

112. Johnson, P. B. & Christy, R.-W. Optical constants of the noble metals. *Phys. Rev. B* **6,** 4370 (1972).

113. Palik, E. D. *Handbook of optical constants of solids*. **3,** (Academic press, 1998).

114. Myroshnychenko, V. *et al.* Modelling the optical response of gold nanoparticles.

Chem. Soc. Rev. **37,** 1792–1805 (2008).

115. Kreibig, U. & Vollmer, M. in *Optical Properties of Metal Clusters* 13–201 (Springer, 1995).

116. Garnett, J. C. M. Colours in metal glasses and in metallic films. *Philos. Trans. R. Soc. London Ser. A* **203,** 385–420 (1904).

117. Garnett, J. C. M. Colours in metal glasses, in metallic films, and in metallic solutions. II. *Philos. Trans. R. Soc. London. Ser. A, Contain. Pap. a Math. or Phys. Character* 237–288 (1906).

118. Mie, G. Contributions to the optics of turbid media, particularly of colloidal metal solutions. *Contrib. to Opt. Turbid media, Part. Colloid. Met. Solut. Transl. into ENGLISH from Ann. Phys.(Leipzig), v. 25, no. 3, 1908 p 377-445* (1976).

119. Kelly, K. L., Coronado, E., Zhao, L. L. & Schatz, G. C. The optical properties of metal nanoparticles: the influence of size, shape, and dielectric environment. (2003).

120. Jain, P. K., Huang, X., El-Sayed, I. H. & El-Sayed, M. A. Noble metals on the nanoscale: optical and photothermal properties and some applications in imaging, sensing, biology, and medicine. *Acc. Chem. Res.* **41,** 1578–1586 (2008).

121. Mody, V. V, Siwale, R., Singh, A. & Mody, H. R. Introduction to metallic nanoparticles. *J. Pharm. Bioallied Sci.* **2,** 282 (2010).

122. Vieaud, J. Propriétés optiques effectives de films composites de polymère et de nanoparticules d'or. (2011).

123. Bastús, N. G., Casals, E., Ojea, I., Varon, M. & Puntes, V. in *The Delivery of Nanoparticles* (InTech, 2012).

124. Njoki, P. N. *et al.* Size correlation of optical and spectroscopic properties for gold nanoparticles. *J. Phys. Chem. C* **111,** 14664–14669 (2007).

125. Hodak, J. H., Henglein, A. & Hartland, G. V. Photophysics of Nanometer Sized Metal Particles: Electron−Phonon Coupling and Coherent Excitation of Breathing Vibrational Modes. *J. Phys. Chem. B* **104,** 9954–9965 (2000).

126. Jain, P. K., Lee, K. S., El-Sayed, I. H. & El-Sayed, M. A. Calculated absorption

and scattering properties of gold nanoparticles of different size, shape, and composition: applications in biological imaging and biomedicine. *J. Phys. Chem. B* **110,** 7238–7248 (2006).

127. Ehrhardt, K. Mesures, modélisations et simulations numériques des propriétés optiques effectives de métamatériaux auto-assemblés. (2014).

128. Mai, S.-M. *et al.* Microphase separation in poly (oxyethylene)-b-poly (oxybutylene) diblock copolymers. *Macromolecules* **31,** 8110–8116 (1998).

129. Hamley, I. W. & Castelletto, V. Small-angle scattering of block copolymers: in the melt, solution and crystal states. *Prog. Polym. Sci.* **29,** 909–948 (2004).

Chapter II Instrument and method

Introduction

In this chapter, we are presenting the structural and optical techniques we have used during this study. This presentation focuses on the use we have made of these techniques for the cases of our specific experimental systems: gold nanoparticles, polymer and block copolymer thin films, self-organized block copolymers and their nanocomposites.

II.1 Spectroscopic Ellipsometry

Ellipsometry is an optical measurement technique, based on the measurement of the change in the polarization state of a light beam caused by the reflection on the material surface or the transmission through the material. From the change in polarization, one can deduce the film thickness and/or the optical properties of the material. The principle was discovered already more than a century ago. However, over the past few decades the technique has progressed rapidly due to the availability of computers and thus simulations of high accuracy. Ellipsometry is very efficient and precise for homogeneous films of thickness between a few nm and a few tens of nm. It has, however, no submicron lateral resolution and the application of ellipsometry to nanostructured samples is still quite recent, and usually requires the use of effective medium models.[1]

II.1.1 General Introduction

The name ‘ellipsometry’ comes from the fact that polarized light often becomes ‘elliptical’ upon light reflection. Spectroscopic ellipsometry (SE) is an optical technique used for thin films and measures the change of polarization of the reflected (or transmitted) light as a function of the wavelength[2–5]. The two fundamental values in the measurements are Ψ and Δ, which represent the module ratio and phase difference between light waves known as p- and s-polarized light waves, respectively (see Figure II. 1). These are defined with respect to the plane of incidence, which contains by definition the incident beam and the normal to the sample surface. The p-polarized light is a wave polarized parallel to the plane of incidence and s-polarized light is a wave polarized perpendicular, which identifies from the German word “senkrecht”, to the plane of incidence.

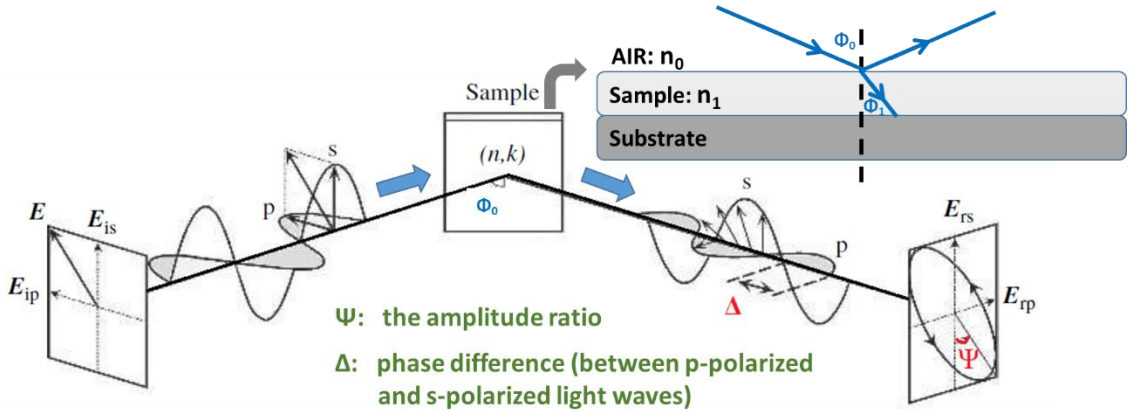

Figure II. 1 Schematic of the principle of ellipsometry

The measured parameters Ψ and Δ are the ellipsometric angles, and are related to the ratio of the complex reflection coefficients (Equation 2- 1) r_s and r_p , where r_s and r_p are the reflection coefficient for s-polarized light and p-polarized light, respectively.

Equation 2- 1

$$r_p = |r_p| e^{i\delta_p}$$

$$r_s = |r_s| e^{i\delta_s}$$

where Φ_0 is the angle of incidence and Φ_1 is the angle of refraction. n_0 is the refraction index of surrounding material (usually air with $n_0 = 1$) and n_1 is the refractive index of the sample. $|r_p|$ and $|r_s|$ are the modules and δ_p and δ_s are the phases of the reflection coefficients .

The relation between the ellipsometric angles Ψ and Δ and the reflection coefficients for parallel and perpendicular polarizations is given by Equation 2- 2:

Equation 2- 2

$$\rho = \frac{r_p}{r_s} = \frac{|r_p|}{|r_s|} e^{i(\delta_p - \delta_s)} = tan(\Psi)\, e^{i\Delta}$$

Where

$$tan(\Psi) = \frac{|r_p|}{|r_s|} \qquad 0° \leq \Psi \leq 90°$$

$$\Delta = \delta_p - \delta_s \qquad 0° \leq \Delta \leq 360°$$

In this manuscript, we will also present the ellipsometric data with the so-called "pseudo-permittivity" < ε >, defined by: $< \varepsilon >= \varepsilon_1 + i\varepsilon_2 = sin^2(\emptyset)\left\{1 + \left[\frac{1-\rho}{1+\rho}\right]^2 tan^2(\emptyset)\right\}$

For a single semi-infinite material of index n_1, the reflection coefficients for parallel and perpendicular polarization can be expressed using the Fresnel coefficients of the interface as:

Equation 2- 3

$$r_p = \frac{n_1 \cos \Phi_0 - n_0 \cos \Phi_1}{n_1 \cos \Phi_0 + n_0 \cos \Phi_1} = |r_p| e^{i\delta_p}$$

$$r_s = \frac{n_0 \cos \Phi_0 - n_1 \cos \Phi_1}{n_0 \cos \Phi_0 + n_1 \cos \Phi_1} = |r_s| e^{i\delta_s}$$

Where, Φ_0 is the angle of incidence and Φ_1 is the angle of refraction, n_0 is the refraction index of surrounding medium.

The advantages of SE are as follows: high precision (thickness sensitivity: ~0.1Å), nondestructive, wide application area, various characterizations including optical constants and film thicknesses. The disadvantages of SE are as follows: indirect characterization, an optical model is needed in data analysis and data analysis tends to be complicated.

II.1.2 Set-up of ellipsometry

In general, the spectroscopic ellipsometry measurement is carried out in the near ultraviolet/visible/near infrared region. Measuring the change of polarization of a polarized light after reflection on a surface for a wavelength range, this technique then offers the possibility of determining the optical indices (n, k) of thin films as a function of the wavelength λ.

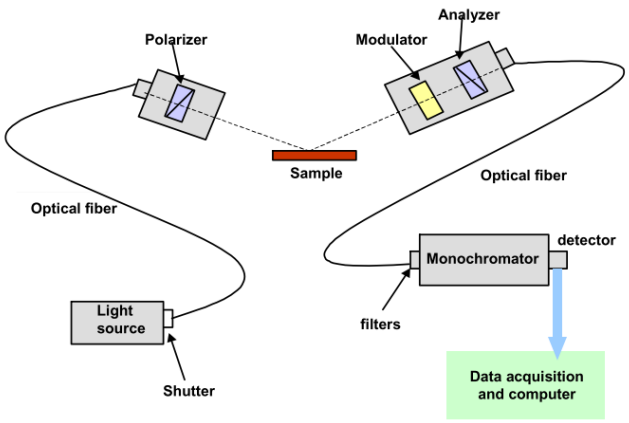

Figure II. 2 Experimental set-up of a phase modulated ellipsometer (from Horiba Scientific UVISEL model)

The experiments were performed at the CRPP with a Horiba spectroscopic ellipsometer. A non-polarized white light beam is generated by a Xenon lamp in a spectral range of wavelengths ranging from 260 to 2060 nm. The beam exposure time is controlled by a shutter after the source, it then passes through a polarizer which polarizes the beam linearly before illuminating the sample with an angle Φ_0. The

reflected light, whose polarization induced by the sample is elliptical, passes through a photoelastic modulator, which modulates the phase shift between its components p- and s- periodically at 50kHz. Finally, the beam passes through an analyzer before reaching a monochromator, which selects the wavelength to be measured by the detector. The set-up of the experiment is shown in Figure II. 2.

Polarizer and analyzer

To transform unpolarized light into polarized light, one or more polarizers are used to absorb, reflect or refract the unwanted polarization state, depending on the level of polarization purity required. There are many varieties of polarizers and polarizing beamsplitters, from crystal calcite prisms to wire grids. Here a Rochon polarizer (see Figure II. 3) is used in the ellipsometer.

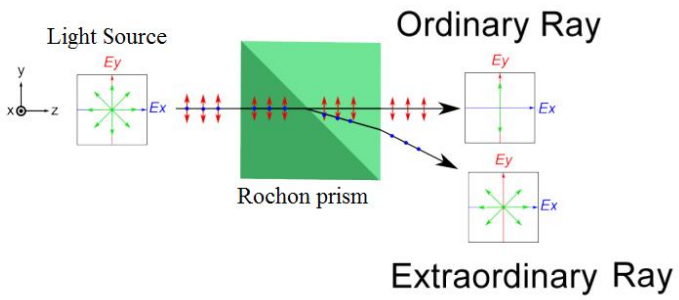

Figure II. 3 Schematics of a Rochon polarizer. The z-axis is the direction of light propagation.

Photoelastic Modulator

Another important element in the UVISEL SE set-up is the photoelastic modulator. It is an optical device based on the photoelastic effect of an isotropic transparent material becoming birefringent when subjected to a mechanical stress and able to induce a modulation of the state of polarization. The modulator used in the spectroscopic ellipsometer of this thesis is a silica bar (see Figure II. 4). When stress is applied to the silica bar, its optical properties are modified. In its equilibrium state, the modulator is optically isotropic with one index of refraction, and becomes birefringent (with two indices) under mono-axial stress. A cosine variation of the stress, using a piezoelectric transducer, modulates the birefringent state of the silica bar (frequency $f = \frac{\Omega}{2\pi} = 50kHz$).

The phase retardation between the two components of the electric field is:

Equation 2- 4 $\delta(t) = A_0 \sin \Omega t$ *where* $A_0 = \frac{2\pi d(n_e - n_o)}{\lambda}$

where (n_e-n_o) is the induced birefringence of the silica bar and d is the size of the piezo electric bar. The applied stress is wavelength dependent. It is regulated with a modulation voltage, so that the modulation amplitude is kept constant.

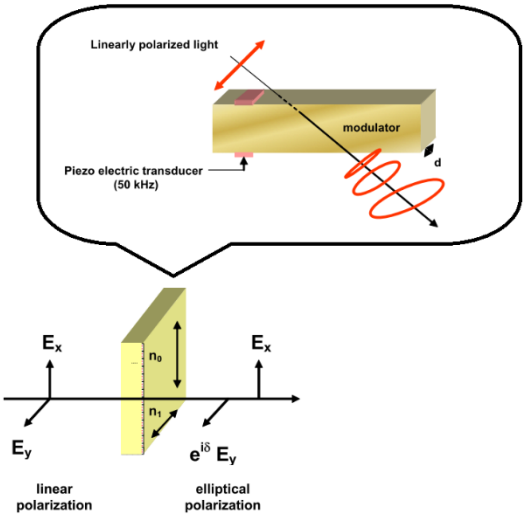

Figure II. 4 Schematic of Photoelastic Modulator.

Two configurations

The UVISEL can acquire data for various azimuth settings of the polarizer, modulator and analyzer angles. The two most used configurations in this thesis are described as following: they are usually referred to as configuration II for P=± 45º, M=0º, M - A=± 45º, and configuration III for P=± 45º, M=45º, M - A=± 45º, where P=angle of the polarizer, M=angle of the modulator, A=angle of the analyzer, with all angles defined with respect to the incidence plane. Configuration II allows an accurate determination of Δ in the whole range but cannot determined Ψ precisely at ca. 45°. Configuration III allows accurate determination of Ψ in the whole range but cannot determine Δ precisely at around 90° and 270°.

Through the thesis, the measurement conditions are as follows:

- the incident beam is circular with a radius of 250 µm

- several angles of incidence Φ_0 are used among: 50º, 55º, 60º, 65º, 70º, 75º.

- λ (photon energy) ranges from 260 to 2060nm (0.6 to 4.0eV) with a increment of 2nm (0.025eV)

- the integration time is 200msec for each measuring point

- the configuration II (M=0º and A=+45º) has been used for most of the studied samples, and both configurations II and and III (M=-45º and A=+45º) have been used for a selection of samples

- all the thin films observed by SE are obtained by spin-coating on silicon wafers of optical index (n_{Si}, k_{Si}) with a thin layer of SiO_2 (2nm) with optical index (n_{SiO2}, k_{SiO2}).

In the case of the phase modulated ellipsometry, like the UVISEL setup, we acquire the ellipsometric quantities Is=sin2ΨsinΔ, Ic=sin2ΨcosΔ and Ic'=cos2Ψ, which are extracted from the parts of the reflected intensity synchronized with the modulator oscillations:

Equation 2- 5 $$I = I_0 + I_s.\sin(\delta) + I_c.\cos(\delta)$$ *in configuration II*

Equation 2- 6 $$I = I_0 + I_s.\sin(\delta) + I_c'.\cos(\delta)$$ *in configuration III*

The quantities Is and Ic (or Ic') will be the quantities calculated and modeled in the model adjustments on the SE data, in order to extract the material characterizations.

II.1.3 Determination of thickness and optical properties of a simple film

We consider here the case of a single sample film on the substrate. The ellipsometric model, shown in Figure II. 5, takes into account the thickness and the optical indices of the two layers: above the semi-infinite silicon substrate, a first layer consists in the silica layer always present on the wafer, and a second layer is the sample to be studied, before the ambient surrounding medium (usually air). Depending on the sample, more layers may be present and included in the ellipsometric model. The model supposes homogeneous and planar layers.

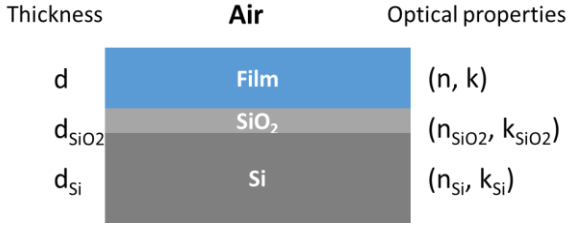

Figure II. 5 Model of samples' determination

As a reminder, the complex index of a material is written according to Equation 2-7, where n is the refractive index and k is the absorption coefficient.

Equation 2- 7

$$\tilde{n} = n + ik = \sqrt{(\varepsilon_{re} + i\varepsilon_{im})}$$

The measurement provides the experimental values of the pair (I_s, I_c) as a function of the wavelength λ (or photon energy) at the different angles of incidence (AOI) Φ_o. The extraction of the unknown parameters, which are d the thickness of the layer and (n(λ), k(λ)) the optical indices or alternatively the permittivity (ε'(λ)+ i ε"(λ)) of the layer, is done by a fit procedure. The optical properties of the layer are initially guessed depending on the material nature (dielectric, metal, etc) and are parameterized with an analytical dispersion function chosen from the software.

Tabulated values of the optical indices of silicon Si and silica SiO_2 are tabulated and found in the software DeltaPsi2 provided by Jobin Yvon/Horiba and shown in Figure II. 6(a) as a function of the photon energy.

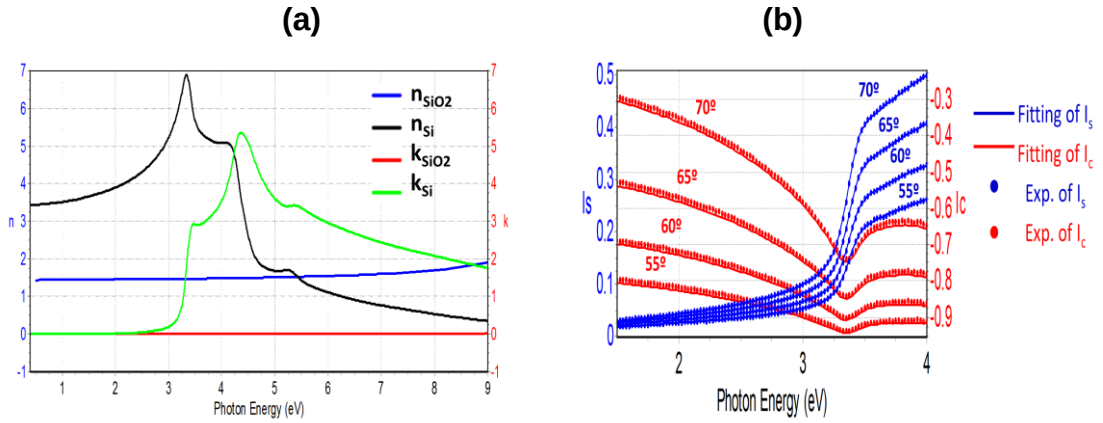

Figure II. 6 (a) Optical properties of Si and SiO_2 from the Jobin Yvon/Horiba database (b) ellipsometric data Is and Ic acquired on a bare wafer, and fit of an ellipsometric model to determine the thickness of the SiO_2 layer, 55º, 60º, 65º and 70º indicate the angle of incidence of each measurement.

Using these values, we first determine the thickness d_{SiO2} of the silica layer of the substrate, with an ellipsometric measurement made on a bare silicon wafer (see Figure II. 6(b)), and d_{SiO2}=2.0 nm is found. All these data concerning the substrate are necessary to minimize the number of unknowns and optimize the fit procedure used to determine the thickness d and the optical indices (n, k) of the thin film studied with the ellipsometric model represented in Figure II. 5.

For a thin film of polymers or diblock copolymers, the optical properties can be described by several conventional dispersion functions. We use a dispersion function called "New Amorphous"[6] for describing the pure polymers, which is originally derived from the Forouhi-Bloomer function[7] and is shown in Equation 2- 8. The new amorphous model works well for amorphous materials exhibiting an absorption in the visible and/or UV range (absorbing dielectrics, semi- conductors, and polymers).

Equation 2- 8

$$n(\omega) = n_\infty + \frac{B\cdot(\omega-\omega_j)+C}{(\omega-\omega_j)^2+\Gamma_j^2}$$

$$k(\omega) = \begin{cases} \frac{f_j\cdot(\omega-\omega_g)^2}{(\omega-\omega_j)^2+\Gamma_j^2}, & \omega > \omega_g \\ 0, & \omega < \omega_g \end{cases}$$

where $B = \frac{f_j}{\Gamma_j}\cdot\left(\Gamma_j^2 - (\omega_j-\omega_g)^2\right)$ and $C = 2\cdot f_j\cdot\Gamma_j\cdot(\omega_j-\omega_g)$. In the equations, the term n_∞ is the value of the refractive index when $\omega\to\infty$. f_j is the oscillator strength, related to the amplitude of the extinction coefficient peak, Γ_j is the broadening factor of the absorption peak, ω_j is the energy at which the extinction coefficient is maximum and ω_g is the energy band gap, which equals the minimum energy required for a transition from the valence band to the conduction band.

For a nanocomposite thin film made of polymer and gold nanoparticles, no conventional dispersion function can describe the sample. We then have two different methods to describe the optical response of the composite layer.

1) The first method consists in using a mixing law based on an effective medium model, as was explained in chapter IV. Knowing the index of both components $n_{Au}+ik_{Au}$, $n_{polym}+ik_{polym}$ or equivalently their dispersion functions $\varepsilon'_{Au}+i\varepsilon''_{Au}$, $\varepsilon'_{polym}+i\varepsilon''_{polym}$, as analytic functions of the wavelength, we can use an effective medium model to define analytically the optical properties of the composite. For example, we can choose the Maxwell-Garnett effective medium law already presented, and we will use :

Equation 2- 9

$$\varepsilon_{eff} = \varepsilon'_{polym} + 3f\varepsilon'_{polym}\left(\frac{\varepsilon'_{Au}+i\varepsilon''_{Au}-\varepsilon'_{polym}}{\varepsilon'_{Au}+i\varepsilon''_{Au}+2\varepsilon'_{polym}-f(\varepsilon'_{Au}+i\varepsilon''_{Au}-\varepsilon'_{polym})}\right)$$

with $\varepsilon''_{polym} \cong 0$.

2) The second method consists in the build-up of a complex dielectric function by the addition of several units, providing a dispersion function of the appropriate shape for the nanocomposite and including resonances described as Tauc Lorentz[6] (see Equation 2- 10) or Lorentz[8] oscillators.

Equation 2- 10

$$\varepsilon = \varepsilon_1 + i\varepsilon_2 \quad \textit{where}$$

$$\varepsilon_1 = \frac{2}{\pi} \cdot P \cdot \int_{E_g}^{\infty} \frac{\xi \cdot \varepsilon_2(\xi)}{\xi^2 - E^2} d\xi$$

$$\varepsilon_2 = \begin{cases} \frac{1}{E} \cdot \frac{A \cdot E_0 \cdot C \cdot (E - E_g)^2}{(E^2 - E_0^2)^2 + C^2 \cdot E^2} & , E > E_g \\ 0 & , E \leq E_g \end{cases}$$

Where:

- E is photon energy;

- E_g is the optical band gap;

- E_0 is the peak central energy;

- C is the broadening term of the peak;

- P is the Cauchy principal value containing the residues of the integral at poles located on lower half of the complex plane and along the real axis.

The real part of the dielectric function ε_1 is derived from the expression of ε_2 using the Kramers-Kronig integration.

Equation 2- 11

$$\varepsilon = \frac{f_j \omega_{0j}^2}{\omega_{0j}^2 - \omega^2 + i\gamma_j \omega}$$

With ω_{oj} the resonance frequency f_j an amplitude factor and γ_j the dissipation term.

The goodness of fit is represented by the χ^2 value (Equation 2- 12). High χ^2 values are usually indicative of a poor fit to the experimental data. If we measure and simulate the spectra of I_s and I_c, then the χ^2 value is a comparison of n theoretically calculated pairs (I_s^{th}, I_c^{th}) and n experimentally determined pairs (I_s^{exp}, I_c^{exp}):

Equation 2- 12

$$\chi^2 = min \sum_{i=1}^{n} \left[\frac{\left(I_s^{th} - I_s^{exp}\right)_i^2}{\Gamma_{I_S,i}} + \frac{\left(I_c^{th} - I_c^{exp}\right)_i^2}{\Gamma_{I_C,i}} \right]$$

Where Γ_i the standard deviation of each data point (generally set to 1), n is the number of measurement points.

The amount of light scattering by the surface is an additional experimental parameter, which must be determined to assess the quality of the measurements. Indeed when light is scattered, for instance by surface roughness, it is also depolarized, which induces errors in the ellipsometry analysis. It can also reduce the reflected light intensity. Therefore, the surface roughness of samples has to be rather small.

II.1.4 Dispersion relation of poly(styrene) and poly(2-vinylpyridine)

In this thesis, we are using poly(styrene)-*block*-poly(2-vinylpyridine) (PS-*block*-P2VP) diblock copolymers. In order to minimize the number of fitting parameters, films of pure poly(styrene) (PS), pure poly(2-vinylpyridine) (P2VP) and PS-*block*-P2VP (M_n 25000-25000) were studied first.

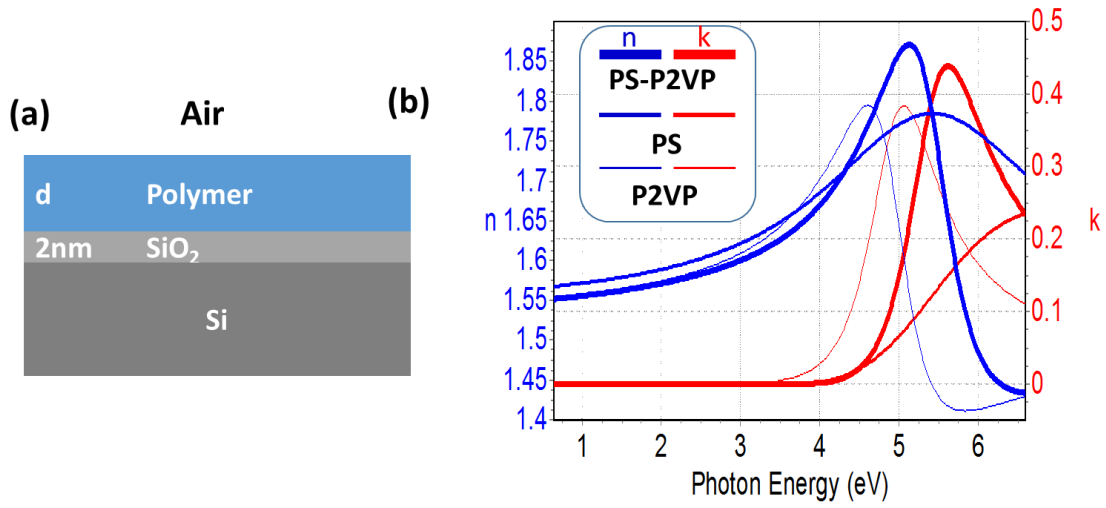

Figure II. 7 (a) model used for analyzing the pure polymer layers (b) index of refraction n and absorption coefficient k extracted from experiment for polystyrene (PS) in blue and Poly (2-vinylpyridine) (P2VP) in red.

The polymers were spin-coated on silicon wafer from solutions of various concentration in order to realize films with different thicknesses. Following the deposition, films were measured by SE and multifited with the DeltaPsi2 software. The same dispersion function was fitted on several data sets corresponding to films of different thicknesses. A model was set up with a Si substrate, 2nm SiO_2 and PS layer or P2VP layer from bottom to top (see Figure II. 7 (a)), with the tabulated indices for Si and SiO_2. The fitting parameters were the thickness of the polymer layer and the optical parameters of the polymers described by dispersion functions of the type 'New

Amorphous'. The extracted optical parameters for PS and P2VP, which are used for the analyses presented in the following chapters, are shown in Figure II. 7 (b) and .

Table II. 1 Parameters of Polymers used in New Amorphous dispersion relation (Equation 2-8)

Parameters	PS-P2VP	PS	P2VP
n_∞	1.507	1.541	1.509
ω_g(eV)	3.833	3.713	2.895
f_j(eV)	0.055	0.124	0.025
ω_j(eV)	5.397	5.408	4.922
Γ_j(eV)	0.593	1.728	0.536

As we see from these results, the optical parameters for the two polymers are very similar, which is due to their close chemical nature and density. When organized in ordered domain, the PS-b-P2VP block copolymer films present a relatively low contrast both in SE and in EM.

II.2 Small angle X-ray scattering

II.2.1 General Introduction

Small angle X-ray scattering (SAXS)[9–11] is a technique for obtaining information on the structure (size, shape and spatial organization) of solids, liquids or gels at dimensions between a few nm and a few tens of nm. X-ray scattering is based on the fundamental Bragg relation between the angle of diffraction 2θ and the spacing of a diffracting lattice:

Equation 2- 13 $$m\lambda = 2d\,sin\,2\theta$$

Where m is an integer; λ is the wavelength of the incident X-ray beam; 2θ is the angle of diffraction (small angle means 2θ < 1°); d is the spacing of the diffracting lattice. Unlike the conventional X-rays diffraction, SAXS can detect large lattice spacing, of the order of hundreds of interatomic distances, which makes it a useful tool for the study of block copolymer morphologies and other macro- or supramolecular systems.

Figure II. 8 shows the geometry of the SAXS. Measurements are commonly performed in transmission geometry, using a narrow, collimated, and intense X-ray beam of wavelength λ. The beam impinges on a sample and a two-dimensional

detector records the scattered intensity in the forward direction. The high intensity transmitted primary beam is blocked by a beam-stop to protect the detector. The entire flight path before and after the sample is in vacuum to avoid absorption and scattering of X-rays by air.

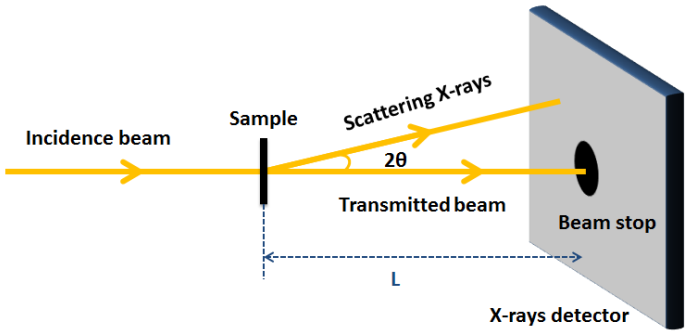

Figure II. 8 Schematic of Small Angle X-ray Scattering (SAXS) geometry

Depending on the morphologies of the samples, different diffraction patterns (see Figure II. 9) are formed on the detector. From the position and intensity of the scattered beam, the period size and the morphology or other structural features of the sample can be determined. For an pattern that is isotropic along the azimuthal direction, polar coordinates are typically used. This is applicable to our systems both for suspensions of nanoparticles and block copolymer bulk sample morphology study, as they are typically randomly oriented and therefore have isotropic scatterings (see Figure II. 9).

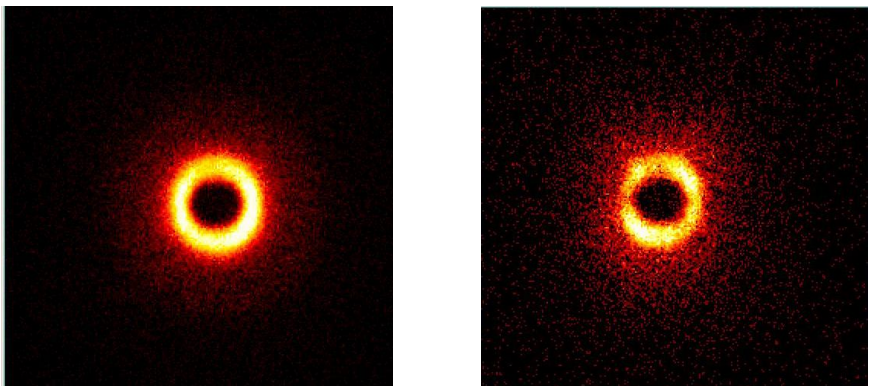

Figure II. 9 Examples of patterns formed on the detector of Small Angle X-ray Scattering (SAXS)

Like other complementary scattering methods using visible light or neutrons, SAXS is a non-invasive structural technique. Unlike the direct imaging methods, the determination of the sample structure from scattering experiments requires a more complex analysis whether it is fitting to a model or a model-independent analysis. The

deduced structural parameters are average values over the entire scattering volume involving a large number of scattering units.

II.2.2 Principle of SAXS

When an X-ray beam encounters a medium, a secondary radiating source is induced by the interaction between the beam and the electrons of the material, producing scattering. In the elastic scattering, the wavelength of the incident beam (wave vector noted by $\mathbf{k_i}$) and scattered wave (wave vector noted by $\mathbf{k_s}$) are the same. The magnitudes of the incident and scattered wave vectors are equal, $|\mathbf{k_i}|=|\mathbf{k_s}|=2\pi/\lambda$. When the scattering angle is 2θ, the momentum transfer or scattering vector $\mathbf{q=k_s - k_i}$, and its magnitude are given in Equation 2- 14 and Figure II. 10.

Equation 2- 14 $$q = |\vec{q}| = \frac{4\pi}{\lambda} sin\,\theta$$

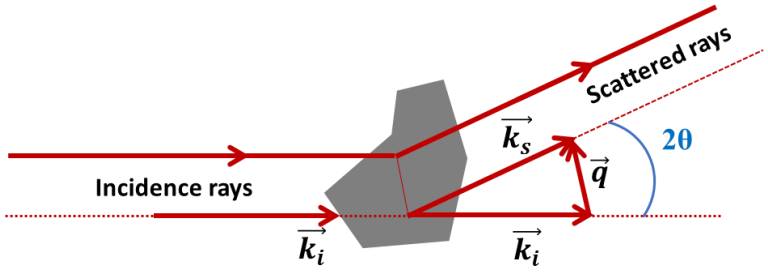

Figure II. 10 Principle of scattering. X-rays are scattered with an angle 2θ. $\vec{k_i}$ is the incident plane wave, $\vec{k_s}$ is the scattered spherical wave and $\vec{q}$ is the scattering vector

This quantity (q) indicates the typical length scales probed by the scattering experiment in reciprocal space and the corresponding dimension d in real space is:

Equation 2- 15 $$d = \frac{2\pi}{q}$$

In order to obtain information I(q), we are going to present how to get I(q) in theory. As the starting point, the total amplitude A(q) of the scattered waves (Equation 2- 15) is related to the Fourier transform of the electron density distribution, which is noted as ρ(r), where the electron density is $\rho_{el} = N_A d \frac{\sum_k n_k Z_k}{\sum_k n_k M_k}$, with the Avogadro number N_A, the density d, the atomic number Z, the molar mass M and the number n of atoms k.

Equation 2- 16 $$A(\boldsymbol{q}) = A_0 r_{el} P(\theta) \frac{e^{ik\boldsymbol{R}}}{R} \int_V \rho(\boldsymbol{r}) e^{i\boldsymbol{q}\cdot\boldsymbol{r}} d\boldsymbol{r}$$

where A_0 is the amplitude of the incident wave, r_{el} is the classical electron radius, P (θ) is a constant factor related to the polarization of the incident wave, ρ(**r**)d**r** is the number of electrons at position **r** in a volume element d**r** and R is the distance from the scattering volume V to the observation point (detector).

When a sample consists in distinct objects, the scattered intensity is proportional to the number of scattering objects N and their contrast of density relative to the solvent (see Equation 2- 17). For a very dilute suspension containing N uniform particles (scatterers) per unit volume, the interparticle interactions can be neglected and I(q) mainly depends on the shape and the size of the particles. The scattering intensity, I(q), from the scatterers with a scattering length density of ρ_{el} embedded in a matrix with scattering length density of ρ_{matrix} can then be described as follows[12]:

Equation 2- 17 $$I(\boldsymbol{q}) = d_N \Delta\rho_{el}{}^2 \int_0^\infty N(r)[V(r)F(\boldsymbol{q},r)]^2 dr$$

where d_N is the number density, $\Delta\rho_{el}=\rho_{el}-\rho_{matrix}$, N(r) is the normalized size distribution function, V(r) is the volume, and F(q,r) is the form factor of the scatterer, containing the information on their shape and size. The form factors can be calculated for some simple scatterers shapes.

When the scatterers are less dilute and present mutual interactions, the scattered signal is the convolution of the previous form factor with the structure factor, containing the information on the inter-particles correlations and the translational order of the system. In periodic structures, the structure factor presents a number of high order scattering maxima, called Bragg peaks, with positions related to the order symmetry.

II.2.3 SAXS performance

In our studies, we use a “Nanostar" set-up from Bruker. The source is a copper anode tube operating at a voltage of 40 kV and a current of 35 mA. An optic consisting of two Göbels mirrors selects the copper Kα line (λ=1.54 Å). The incident beam is obtained after collimation by three slits; it is circular with a diameter of 700µm. The sample transmits the X-ray beam to a detector of dimension 22x22cm² placed at a distance D from the sample. The resolution of the signal is determined by the width at half height of the direct beam without sample and is of the order of 0.003Å^{-1}. The

domains of studied wave vectors **q** differ according to the configuration, with large or small sample-to-detector distances D giving access to ranges of small or large angles, and defines the ranges of dimensions probed in the real space. According to Equation 2- 14, the scattering vector q in the reciprocal space is defined by the scattering angle 2θ. For each scattering vector, there corresponds a size in the real space. Therefore, at large angles (D=26cm), for wave vectors between 0.04 and 0.8Å^{-1}, the corresponding characteristic sizes are very small, of the order of nanometers. At small angles (D=106cm), the accessible wave vectors are smaller, between 0.01 and 0.2Å^{-1}, which corresponds to larger characteristic sizes, of the order of ca. 10 nanometers.

If samples are liquid, they are placed in 1 mm diameter cylindrical capillaries sealed and placed in a sample holder. If samples are solid, they can be directly placed in the sample holder. The holder is then placed in the sample chamber, under vacuum to avoid scattering by air, which is important at small angles. A two-dimensional spectrum is recorded and, if isotropic, is integrated by an angular grouping, in order to obtain the intensity as a function of the scattered vector I(q).

We are going to discuss the use of this technique for the study of the PS-b-P2VP block copolymers in Chapter III and Chapter IV.

II.2.4 SAXS in diblock copolymers

Small Angle X-ray Scattering (SAXS) can be used for quantitatively analyzing the microdomains structure. The structure factor is analyzed to extract the order symmetry and the peak positions in scattering vector **q** provide the domain spacing d from the Equation 2- 15 $d = 2\pi/q$, in the case of simple lamellar spacing for diblock copolymers.

Table II. 2 Symmetry and scattering maxima relationships[12]

Symmetry	Ratio of q values at the scattering maxima peaks
Lamellar	1:2:3:4:5:6…….
Hexagonal	$1{:}\sqrt{3}{:}\sqrt{4}:\sqrt{7}:\sqrt{9}{:}\sqrt{11}$….
Cubic bcc	$1{:}\sqrt{2}:\sqrt{4}:\sqrt{5}:\sqrt{6}$:….
Cubic fcc	$1{:}\sqrt{4/3}:\sqrt{8/3}:\sqrt{11/3}:\sqrt{12/3}:\sqrt{16/3}$ ……
Cubic gyroid	$1{:}\ \sqrt{4/3}:\sqrt{7/3}:\sqrt{8/3}:\sqrt{10/3}:\sqrt{11/3}$ ……

Depending on the nature of the microdomain order, the scattering peaks exhibit a specific spatial relationship. Table II. 2 gives some of them. In the present work, the

SAXS technique is employed to determine the the structure of the polymers, and in the case of lamellar phases, the bi-layer thickness, equal to the lamellar period, in the following chapters.

II.2.5 SAXS used for nanoparticles in solutions

SAXS is also an effective tools used for analyzing the size and distribution of nanoparticles in solutions. Depicting spherical particles, the scattered intensity I(q) consists in two components, (1) the form factor P(q), which provides information regarding the mean structural properties of the individual particles (i.e., size and shape) and (2) the structure factor S(q), which provides the positional correlation of the particles.

Equation 2- 18 $$I(\boldsymbol{q}) = S(\boldsymbol{q}) * P(\boldsymbol{q})$$

The form factor P(q) provides information on the size and shape of the individual particles and the structure factor S(q) provides the positional correlation of the particles and is equal to 1 when the particles are dilute (see Equation 2- 18). In that case, the analysis of SAXS spectra then corresponds to the form factor analysis and give access to the physical characteristics of the particles. For spherical monodisperse particles with radius R, the form factor can be written as following:

Equation 2- 19 $$P(q) = F^2(q,R) = (\Delta\rho V_{sp} \frac{3(sin(qR) - qR\,cos(qR))}{(qR)^3})^2$$

where $V_{sp}$is the volume of the spheres and $\Delta\rho = \rho_p - \rho_s$. ρ_p and ρ_s stand for the scattering length density of the particles and the solvent, respectively.

For polydisperse particles, the particles size distribution needs to be taken into account, and the form factor is defined as:

Equation 2- 20 $$P(q) = \int D(R)\langle|F(q,R)|^2\rangle dR$$

Where R is the radius D(R) is the size distribution function. In our study, we assume that all the particles are spheres, and the distribution function can be described by a Gaussian function (see Equation 2- 21).

Equation 2- 21 $$D(R, R_o, \sigma) = \frac{e^{-(R-R_0)^2/(2\sigma^2)}}{\sigma\sqrt{2\pi}}$$

where R_0 is the mean radius, σ is the standard deviation.

Equation 2- 22 $$P_{mono}(q,R_0) \propto \frac{3(sin(qR_0)-qR\,cos(qR_0))}{(qR_0)^3}$$

Equation 2- 23 $$P_{poly} = D(R_0,\sigma) \otimes P_{mono}(q,R_0)$$

Equation 2- 24 $$P_{poly}(q,R_0,\sigma) = \frac{\alpha-(\beta\,cos\,2qR_0+\gamma\,sin\,2qR_0)\cdot e^{-2q^2\sigma^2}}{2q^6}$$

$$\text{where, } \begin{cases} \alpha = 1+q^2(\sigma^2+{R_0}^2) \\ \beta = 1-q^2(\sigma^2+{R_0}^2)+4q^2\sigma^2(1+q^2\sigma^2) \\ \gamma = (1+2q^2\sigma^2)2qR_0 \end{cases}$$

Equation 2- 25 $$D(R_0,\sigma) = \frac{1}{\sqrt{2\pi}\sigma} e^{-(R-R_0)^2/2\sigma^2}$$

In our system, we assume that the nanoparticles are dense homogenous spheres in diluted suspensions. Figure II. 11 shows an example of experimental data (EXP) fitted with the monodisperse model (Equation 2- 22) with R=4.2nm and the polydisperse model (Equation 2- 24 and Equation 2- 23) with a Gaussian distribution (Equation 2- 25 and Figure II. 11 inset) of D=2R=8.4nm and σ=1.2nm. The Equation 2- 24 used in polydisperse model is determined by Denis Bendejacq[13].

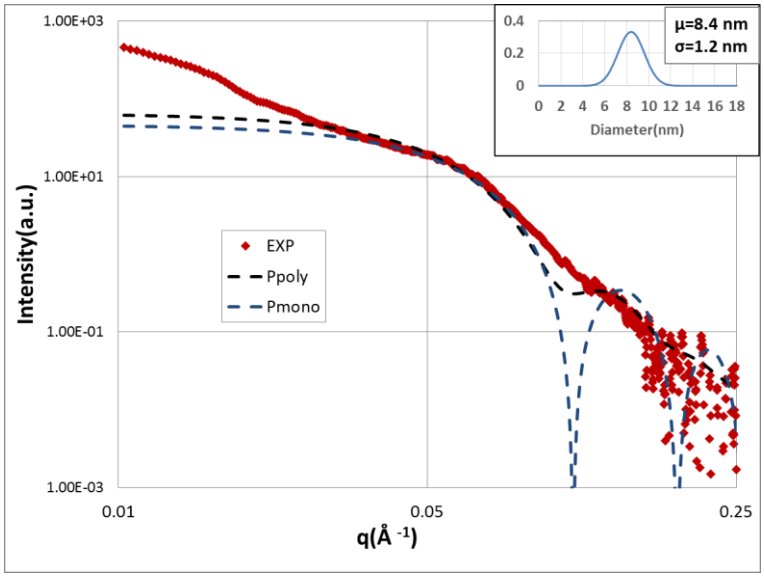

Figure II. 11 Illustration of an example of SAXS experimental data (EXP) and the fits by monodisperse (Pmono) and polydisperse (Ppoly) form factor for spheres. The diameter is 8.4 nm(2R), the standard deviation is 1.2 nm.

II.3 Electron Microscopy

Direct observations of the samples were performed by electron microscopy. Scanning Electron Microscopy (SEM) is employed to observe global view of films nanostructure, while nanoparticles are observed by Transmission Electron Microscopy (TEM).

Electron microscopes[14,15] have electron optical lens systems that are analogous to the glass lenses of an optical light microscope. It is used to investigate the ultrastructure of a wide range of biological and inorganic specimens including microorganisms, cells, large molecules, biopsy samples, metals, and crystals.

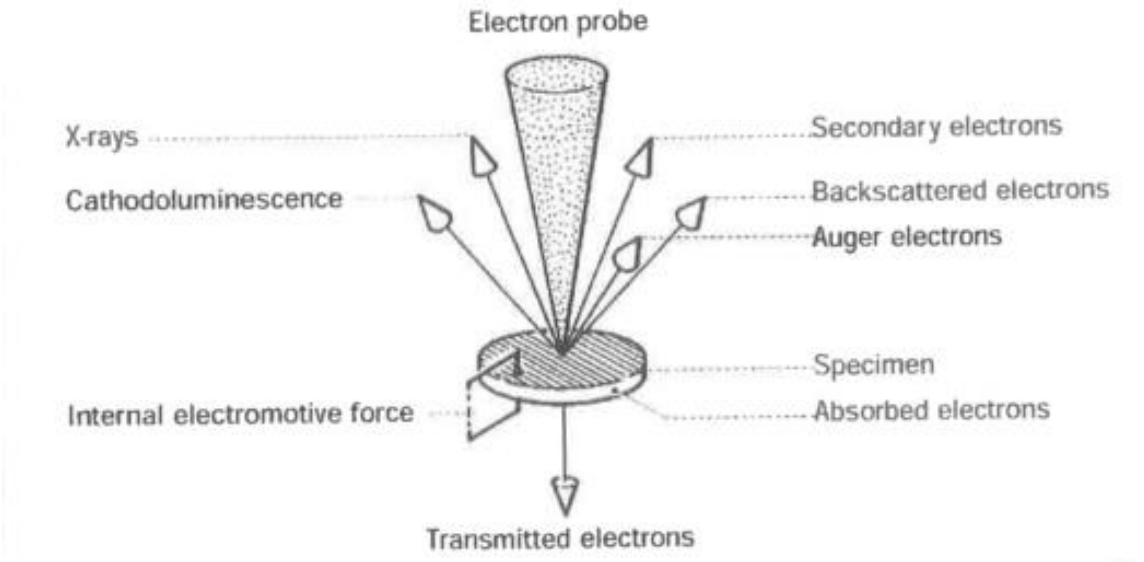

Figure II. 12 Different signals used from imaging of a specimen in electron microscopy (From Hand book of JSM6700F published by JEOL LTD.)

The used beam in an electron microscope is accelerated electrons. As the wavelength of an electron can be up to 100,000 times shorter than that of visible light photons, electron microscopes have a higher resolving power than light microscopes and can reveal the structure of smaller objects. Once the electron probe illuminates a sample, then transmitted or scattered electrons (shown in Figure II. 12) carrying information on the sample structure are collected and used to produce the images of the sample.

II.3.1 Transmission Electron Microscopy

Transmission electron microscopy (TEM) is based on the transmitted electrons (Figure II. 12) and allows a magnification of hundreds of thousands of times. A filament generally of tungsten or lanthanum hexaboride is heated in order to produce an electron beam, which is then accelerated by a high voltage of the order of 100 kV. The beam passes through the microscope column under a high vacuum and is focused by magnetic lenses. A thin sample, with a thickness of less than a few tens of nanometers is placed in the electron beam, and the detection of the electrons transmitted through the sample produces an image. Depending on the thickness, chemical nature or electron density of the sample, the electrons are more or less absorbed, which forms the observed image. The limit of resolution of the TEM depends on the wavelength of the electrons; it is of the order of the picometer. Because of the presence of several types of aberration of the lenses, the real resolution is of the order of a few nanometers[14,16].

Since the TEM is the signal from transmitted electrons, the dark parts correspond to dense material while the light parts correspond to transparent material. For example, the dark parts in Figure II. 13 dark parts correspond to gold particles rich layer and light part corresponds to the polystyrene layers.

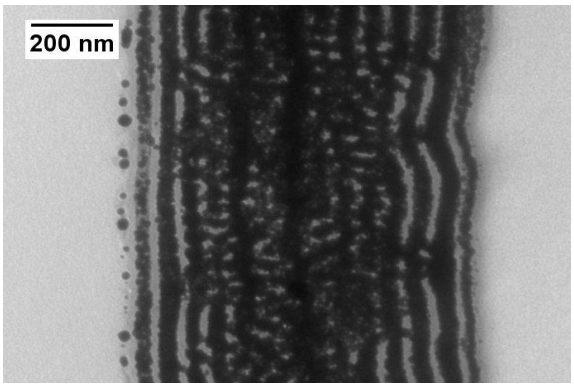

Figure II. 13 Multilayer of polystyrene and nanocomposite layer (consists of gold nanoparticle and poly (vinylpyridinie) imaged by TEM

The transmission electron microscope present at the CRPP is a Hitachi H600, having an acceleration voltage of 75 kV, for magnifications ranging from 700 to 300,000 times. A CCD camera takes digital pictures.

A high-resolution transmission electron microscope (MET-HR), located at the Bordeaux Imaging Center at the Bordeaux University, was also used to study nanometer-scale samples more precisely. The TEM-HR is a Hitachi H7650, having an acceleration voltage ranging from 80 to 120 kV, for magnitudes ranging from 4000 to 600000 with a resolution of approximately 1 nm.

II.3.2 Scanning Electron Microscopy

The scanning electron microscope[17,18] present at PLACAMAT in Université de Bordeaux is a JSM 6700F. Most samples were observed under the acceleration voltage of 10.0 kV, ca. 8mm working distance for focusing, and magnifications ranging from 3000 to 80,000.

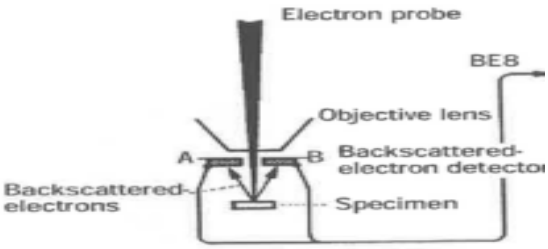

Figure II. 14 Schematic of backscattered electron image

The observation can be performed in two different imaging modes: 1) SEI and 2) BSEI. 1) SEI refers to the most common SEM mode, which is detection of secondary electrons emitted by surface atoms excited by the electron beam. By scanning the sample and collecting the emitted secondary electrons using a specific detector, an image displaying the topography of the surface is created. 2) BSEI refers to backscattered-electron imaging (Figure II. 14), which is formed using an optional backscattered-electron detector and is mostly sensitive to the chemical contrast in the sample, with heavier and electron-rich elements scattering more, and appearing brighter in the images.[19] Combining both imaging modes can be a way to determining the number of phases in a material and their mutual textural relationships.

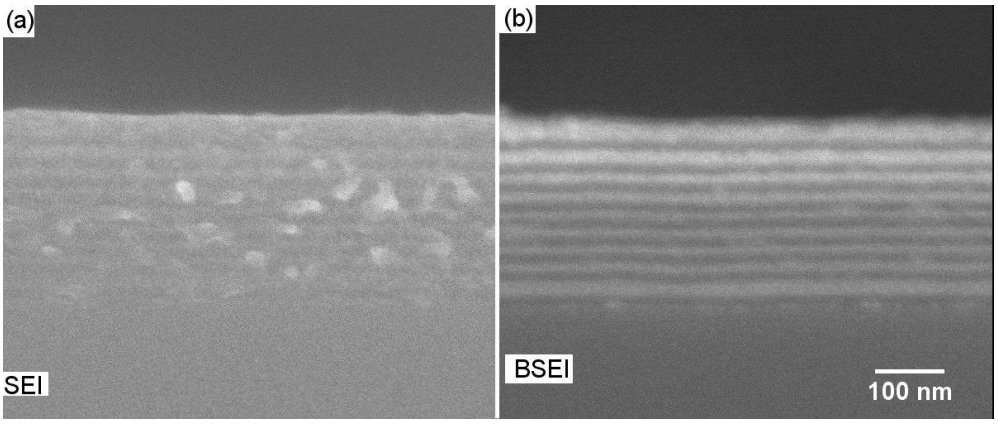

Figure II. 15 SEM images of the side of a lamellar film consisting of polymer layers and nanocomposite layers (polymer with gold nanoparticles) under (a) SEI and (b) BSEI, at the same position.

For example, Figure II. 15 are the SEM images of the side of a lamellar film consisting of alternate layers of pure polymer (PS) and nanocomposite (P2VP with gold nanoparticles) under (a) SEI and (b) BSEI at the same position. In the BSEI image, the white part corresponds to the gold-rich areas and dark parts correspond to the polymer domains. The SEI image shows the topography of the sample section, and how the structure was damaged by the breaking in two pieces, while the BSEI image clearly shows the different material domains but is insensitive to topography. In this work, we are combining both imaging modes to analyze the samples.

References

1. Losurdo, M. *et al.* Spectroscopic ellipsometry and polarimetry for materials and systems analysis at the nanometer scale: state-of-the-art, potential, and perspectives. *J. Nanoparticle Res.* **11,** 1521–1554 (2009).
2. Tompkins, H. & Irene, E. A. *Handbook of ellipsometry*. (William Andrew, 2005).
3. Azzam, R. M. A. & Bashara, N. M. *Ellipsometry and polarized light*. (North-Holland. sole distributors for the USA and Canada, Elsevier Science Publishing Co., Inc., 1987).
4. Schubert, M. *Infrared ellipsometry on semiconductor layer structures: phonons, plasmons, and polaritons*. (Springer Science & Business Media, 2004).
5. Fujiwara, H. *Spectroscopic ellipsometry: principles and applications*. (John Wiley & Sons, 2007).
6. Jellison Jr, G. E. & Modine, F. A. Parameterization of the optical functions of amorphous materials in the interband region. *Appl. Phys. Lett.* **69,** 371–373 (1996).
7. Forouhi, A. R. & Bloomer, I. Optical dispersion relations for amorphous semiconductors and amorphous dielectrics. *Phys. Rev. B* **34,** 7018 (1986).
8. Chen, H. & Shen, W. Z. Perspectives in the characteristics and applications of Tauc-Lorentz dielectric function model. *Eur. Phys. J. B-Condensed Matter Complex Syst.* **43,** 503–507 (2005).

9. Glatter, O. & Kratky, O. *Small angle X-ray scattering*. (Academic press, 1982).

10. Guiner, A., Fournet, G. & Walker, C. B. Small angle scattering of X-rays. *J. Wiley Sons, New York* (1955).

11. Chu, B. & Hsiao, B. S. Small-Angle X-ray Scattering of Polymers. *Chem. Rev.* **101,** 1727–1762 (2001).

12. Goderis, B., Reynaers, H., Koch, M. H. J. & Mathot, V. B. F. Use of SAXS and linear correlation functions for the determination of the crystallinity and morphology of semi-crystalline polymers. Application to linear polyethylene. *J. Polym. Sci. Part B Polym. Phys.* **37,** 1715–1738 (1999).

13. Bendejacq, D. D., Ponsinet, V. & Joanicot, M. Chemically tuned amphiphilic diblock copolymers dispersed in water: From colloids to soluble macromolecules. *Langmuir* **21,** 1712–1718 (2005).

14. ROBLIN, G. Microscopie. *Tech. l'ingénieur. Mes. contrôle* R6710-1 (1998).

15. Flegler, S. L., Heckman Jr, J. W. & Klomparens, K. L. Scanning and transmission electron microscopy: an introduction. *Oxford Univ. Press. 1993,* 225 (1993).

16. Knoll, M. & Ruska, E. Beitrag zur geometrischen Elektronenoptik. I. *Ann. Phys.* **404,** 607–640 (1932).

17. Lee, R. E. *Scanning electron microscopy and X-ray microanalysis*. (PTR Prentice Hall, 1993).

18. Krinsley, D. H., Pye, K., Boggs Jr, S. & Tovey, N. K. *Backscattered scanning electron microscopy and image analysis of sediments and sedimentary rocks*. (Cambridge University Press, 2005).

19. Venables, J. A. & Harland, C. J. Electron back-scattering patterns—a new technique for obtaining crystallographic information in the scanning electron microscope. *Philos. Mag.* **27,** 1193–1200 (1973).

Chapter III Lamellar structure fabrication by block copolymers

Introduction

In this chapter, we are interested in the fabrication of polymer templates with a lamellar structure and their structural study, using the characterization techniques detailed in previous chapter. Indeed, lamellar multilayer nanocomposite could be one approach to hyperbolic metamaterial, as detailed in The Chapter I.2. In particular, the period size α must be smaller than λ/10, so that they can be treated as effective medium. Also, we would like to control the optical properties of material by controlling the structure of films. In this chapter, we are going to focus on fabricating different thickness of film, different thickness of layers and more morphology.

This chapter comprises three parts. The first part will present the film fabrication and thickness control; the second part will present the study of the copolymers morphology; the third part will present the layer thickness study.

III.1 Film preparation by spin-coating

III.1.1 Effect of the concentration on the films thickness

III.1.1.1 Spin coating technique

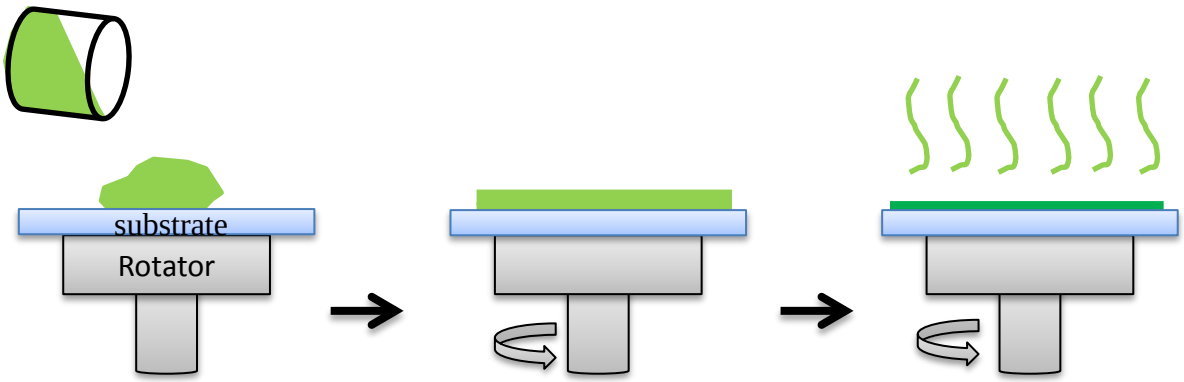

Figure III. 1 Scheme for spin-coating process

Spin-coating[1] is a simple process for rapidly depositing uniform thin films onto flat substrates. The substrate is clamped on a rotator and maintained fixed by aspiration (see Figure III. 1). Usually the process can be separated into 3 steps. First of all, the material to deposit must be dissolved into a volatile solvent. In the second step, a small amount of the solution is applied on the center of the substrate. In the third step, the substrate is accelerated up to desired speed by spin coater. During the third step, the

fluid spreads on the whole substrate because of centrifugal force, meanwhile the volatile solvent evaporates. A film deposits homogenously on the substrate, except for the edge.[2] Due to the high speed of rotation, droplets form at the edge of the substrate to be flung off. Thus, a small difference in the thickness may be found between the center and the fringe at the edge.

During the spin-coating, several parameters influence the thickness and appearance of the film. They include the characteristics of the coating solution (the solution viscosity, the concentration of the coating material, the volatility of the solvent, etc), the acceleration and speed of rotation, the time of rotation, the volume of coating solution used in the 3rd step. For each different film formation case, we need to optimize the process by varying these parameters in order to obtain a film with the desire thickness and a homogenous appearance.

The SCS G3 Spin Coater from A KISCO Company was used in this thesis. It provides the access to control rotation speed, spin time, acceleration and deceleration time.

III.1.1.2 Experiment

Material

The diblock copolymers poly(styrene)-*block*-poly(2-vinylpyridine) (M_n25000-25000, PDI 1.06) were purchased from Polymer Source Inc., denoted as PS_{25k}-$P2VP_{25k}$. Toluene and tetrahydrofuran (THF) were purchased from Sigma-Aldrich. The polymers, chemicals, and solvent described in this chapter were used without any further purification.

Two types of substrates were employed in this work: silicon wafers and Aclar substrates. Silicon substrates were purchased from Wafer Word inc. (thickness of the wafer is 450±50μm, P type/Boron, cut 001). Ellipsometric analysis of bare wafers established that the wafer surfaces had a 2nm silicon oxide layer on them. Aclar substrates (melting point 202°) were purchased from Agar Scientific Limited., and used for the preparation of samples for TEM imaging, since they can be sectioned without damage with ultramicrotomy knives and are as transparent as glass[3]. Prior to use, the substrates were cleaned by sonicating (Branson 1510DTH, AC input 115 V) for 15min in ethanol, following by 10 min in water and dried under a stream of nitrogen. Substrates were immediately used for the spin-coating.

Film preparation

PS_{25k}-P_2VP_{25k} were generally dissolved in toluene to yield 0.8 weight%, 1.5 weight%, 3.0 weight%, 6.0 weight% and 10.0 weight% solution and stirred overnight at room temperature to ensure complete solution.

The spin-coating was accomplished by dropping 55 µL of the polymer solution onto 1cm^2 silicon wafers at 5000 rpm with acc/dec time 3s for 30 s at room temperature. It gives homogenous films.

Measurement

The topography of films is first observed by optical microscopy.

The thickness of the films is measured by variable angle spectroscopic ellipsometry (VASE) in the spectral range [0.6-4.0ev] in configurations UVISEL II and AOI=55º, 60º, 65º, 70º and 75º.

III.1.1.3 Results and discussion

After the deposition, the top view of films were observed by optical microscopy (see Figure III. 2). We see that the polymer is deposited on silicon wafer homogenously. As the concentration of the polymer solution increase, the colors change obviously, which indicate the increasing of film thickness. The color on the surface of films is caused by interference of reflected light from the upper and lower surfaces of films.

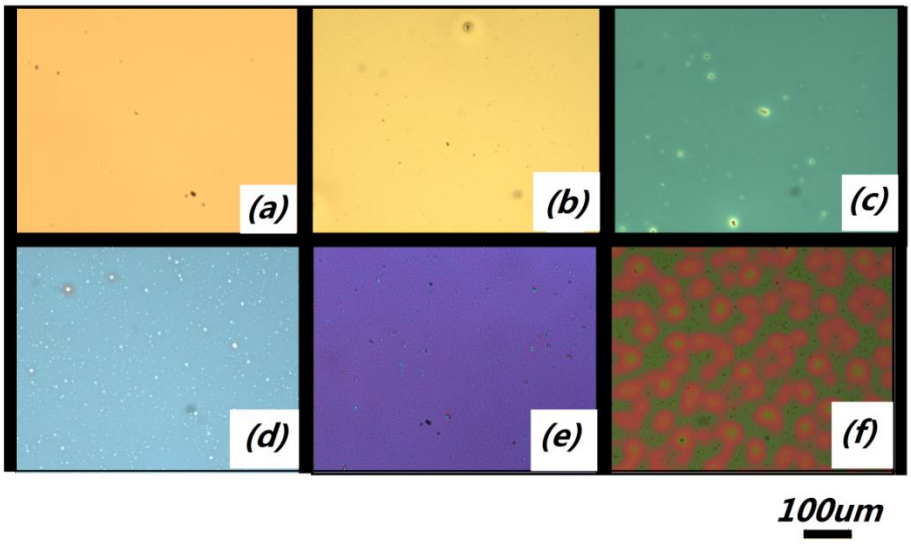

Figure III. 2 Films with different thickness under optical microscope. (a) surface of silicon wafer; (b) surface of film made by 0.8wt.% PS-P_2VP in toluene; (c) surface of film made by 1.5wt.% PS-P_2VP in toluene (d) surface of film made by 3.0wt.% PS-P_2VP in toluene (e) surface of film made by 6.0wt.% PS-P_2VP in toluene; (f) surface of film made by 10.0wt.% PS-P_2VP in toluene.

The thickness of films was analyzed by VASE with the simple model presented in the Figure III. 3 and the polymer material PS-PVP was described with a New Amorphous dispersion formula (detailed in Chapter II 2.1.1 PS-PVP). The film thickness is the only fitting parameter in model 1. Figure III. 4(a) is an example of the fitting result, corresponding to the films prepared with the 6.0 wt.% PS-P2VP solution in toluene. The thickness of the sample is 272.33nm±0.05 with χ^2 equal to 37.30. Figure III. 4 (b) and (c) show I_s and I_c as function of the photon energy in various thickness of films, at the AOI=55º. We can see that as the concentration of polymer in the solution increases, the oscillations number of the curves increases, which demonstrate the increase of the film thickness.

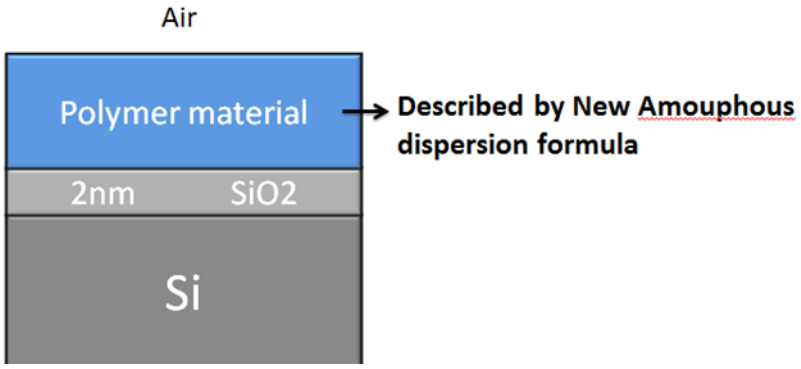

Figure III. 3 Model built for extracting the thickness of the studied copolymer films

The thickness results for all concentrations analyzed from the VASE data are shown in the Table III. 1., and displayed on the Figure III.5.(the condition of spin coating are the same in most case expect for the 0.8wt.% with the spin speed of 4000rpm.When the polymer solution is less thicker, a high speed of rotation results inhomogeneity of film due to the low solution griping substrate).

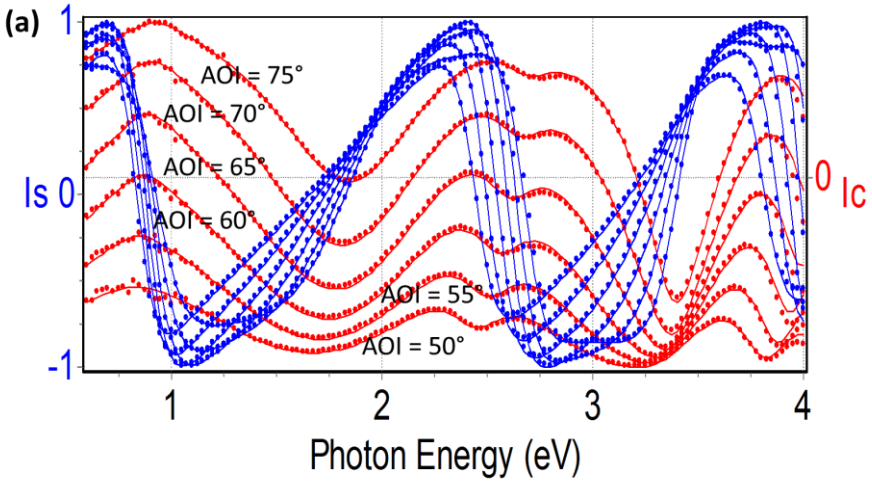

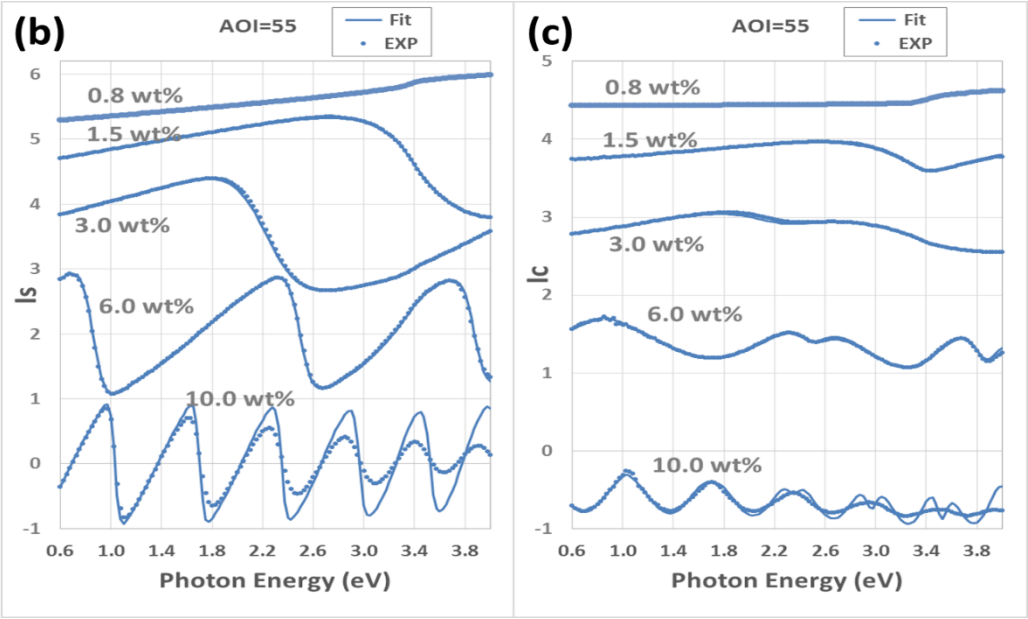

Figure III. 4 I_s and I_c as a function of the photon energy. (a) Fitting result for the film produced with the 6.0 wt.% PS-P2VP/toluene polymer solution at 5 angles of incidence. Blue and red dots (continuous lines) are experimental data (fitting curves) of I_s and I_c respectively. (b) and (c) shows I_s and I_c respectively, as function of the photon energy at AOI=55°, dots are experimental data(EXP) and lines are fitting results (Fit). The curves are vertically shifted for clarity, which show the various oscillations of the samples produced with different concentrations of polymer solutions.

Table III. 1 Relation between the thickness of the films and the concentration of the copolymer solutions

Concentration of the polymer solution	0.8 wt.%	1.5 wt.%	3.0 wt.%	6.0 wt.%	10 wt.%
Thickness of the film (nm)	26.33	59.42	100.71	272.33	677.33

On the data of the Figure III. 5, we can adjust the relation between the film thickness and the copolymer solution concentration with a quadratic equation (Equation 3- 1):

Equation 3- 1 $$D = 4.8683x^2 + 18.591x \quad (R^2 = 0.9978)$$

Where D is the thickness of the film, x is the concentration of the copolymer solution in weight percentage and R^2 is the coefficient of correlation.

As can be seen from the graph and from the value of the coefficient of determination close to 1, the equation is a good adjustment of the measurements. It can be used for the direct estimation of the thickness of the films from the concentrations of PS-P2VP in toluene.

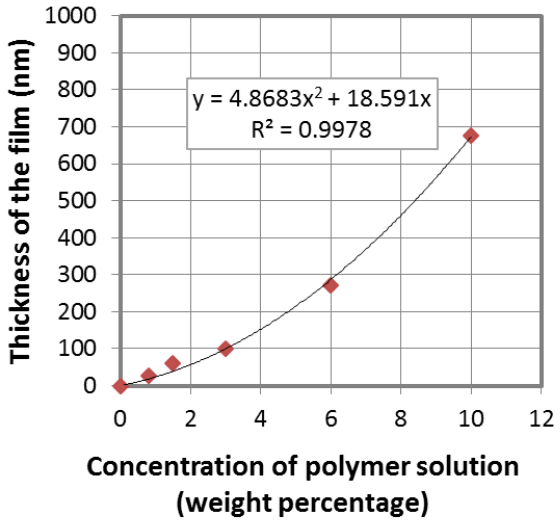

Figure III. 5 Thickness of the films as a function of the concentration of the copolymer solution (PS-P_2VP in toluene). The red dots are the experimental data and the black line is the fitting curve described by equations $y=4.868x^2 + 18.591x$. R^2 is coefficient of determination

In conclusion, the concentration of copolymer in solution controls the thickness of the films. In particular, the thickness of the PS-P2VP films can be anticipated using Equation 3- 1. We can control the thickness of the films on the range 20nm-700nm.

III.1.2 Effect of different spin-coating conditions on the thickness of the films

Previous section III.1.1 focused on the influence of the concentration of the copolymer solutions. In this section, we studying the influence of the spin-coating conditions. Since the spin coating process involves several parameters: spin speed, volume of solution and acceleration and deceleration time (Acc/Dec time), Taguchi optimization methodology was employed to simplify the experiment.

III.1.2.1 Taguchi optimization methodology

This study utilizes the Taguchi optimization methodology (L_9 orthogonal array) to optimize various parameters, which are involved in the spin coating process (spin speed, volume of solution and Acceleration and deceleration time).

Taguchi method[4–6] is a powerful tool designed by Dr. Genichii Taguchi, which provides a simple, efficient, and systematic approach to optimize operating conditions under designated ranges of all selected parameters. The conventional method used in the optimization of experimental parameters requires a large number of experiments.

Compared to a conventional method, Taguchi experimental strategy can reduce the number of experiments as well as identify and quantify the interactions among parameters and the contribution of individual parameters. For example, to study the effect of four parameters taking three different values, 81(=3^4) different experiments are needed for conventional method and 9 (=$L_9(3^4)$) designed experiments are needed by Taguchi method. Over the decades, this design method has been used in scientific world widely, since it can not only simplify experiments, but also inspect the interaction among the experimental factors. It is based on orthogonal experimental design tables, which is designed $L_n(r^m)$, where, n stands for the number of measures in using the Taguchi method; r stands for the level (number of taken values) of each factor; m stands for the number of factors.

In the present work, we use 3 factors and 3 levels in the experiments. 3^3=27 experiments will be needed if we would like to study all the variables. Instead, 9=$L_9(3^4)$ experiments are enough with the Taguchi method. The Table III. 2 shows the selected factors and their values. Factor A is the spin speed (Level 1:4500 rpm; Level 2: 4800 rpm; Level 3: 5100 rpm); Factor B is the volume of solution (Level 1: 55µl; Level 2: 58µl; Level 3: 61µl); Factor C is the acceleration and deceleration time (Level 1: 2s/2s; Level 2: 3s/3s; Level 3: 4s/4s). The Table III. 3 shows the L_9 array for the design of the experiment by the Taguchi method, with orthogonal columns. A blank row is introduced as a control group in the table in order to compare with experimental groups.

The results are statistically analyzed using the variance analysis, referred to as ANOVA[5–7], to determine the percentage contribution of each individual parameter to the response. It is a type of regression analysis, which is employed in this study to find out the influence of each factor on the thickness of the films. ANOVA is used to calculate the sum of squares (SS), degree of freedom (*df*), variance, and F value. We first determine the sums, K1, K2 and K3 and the mean values. $\overline{K1}$,$\overline{K2}$ and $\overline{K3}$ $\overline{Kj}$ of the measures yi (here the thickness measures) for the level 1, level 2 and level 3 respectively. As examples, for parameter A (volume), K1=y_1+y_2+y_3 and $\overline{K1}$=(y_1+y_2+y_3)/3, because these are the three measurements where the volume is 55µL (level 1), whereas for parameter B (spin speed), K1=y_1+y_4+y_7 and $\overline{K1}$=(y_1+y_4+y_7)/3. For each parameter, the value Range(K), which is the difference between the largest and the smallest values of K, is already an indication of the

influence of the parameter on the measurements, especially when compared to the value obtained for the blank row, acting like a random selection of measures.

Table III. 2 Selected factors and their levels

Factor / level	FactorA: Volume (µl)	FactorB: spin speed (rpm/s)	FactorC: acc/dec time (s)
1	55	4500	2/2
2	58	4800	3/3
3	61	5100	4/4

Table III. 3 L9 Array for design of experiment by Taguchi method

exp. No.	Operating parameters			Blank	measure
	Volume (µl)	spin speed (rpm/s)	acc/dec time (s)		
1	1	1	1	1	y_1
2	1	2	2	2	y_2
3	1	3	3	3	y_3
4	2	1	2	3	y_4
5	2	2	3	1	y_5
6	2	3	1	2	y_6
7	3	1	3	2	y_7
8	3	2	1	3	y_8
9	3	3	2	1	y_9

We then calculate the total sum of squares SS_T:

Equation 3- 2 $$SS_T = \sum_{i=1}^{n}(y_i - \bar{y})^2 \ , \quad T = \sum_{i=1}^{n} y_i$$

the sum of squares caused by the parameter j SS_j:

Equation 3- 3 $$SS_j = \frac{r}{n}(\sum_{i=1}^{r} {K_i}^2) - \frac{T^2}{n} \ , \ SS_T = \sum_{j=1}^{m} SS_j$$

and $SS_4=SS_e$, the sum of squares caused by blank row is (error row), the degrees of freedom:

Equation 3- 4 $$df_T = n - 1 \ , \ df_j = r - 1$$

the mean squares is MSj (for example MS_A is mean square of the parameter A):

Equation 3- 5 $$MS_j = \frac{SS_j}{df_j} \ , \ MS_e = \frac{SS_e}{df_e}$$

and the variance ratio:

Equation 3- 6 $$F_j = \frac{MS_j}{MS_e}$$

The F ratio is a key criterion, which is used to distinguish the important influential factor. If the F is more than or equal to 90%, the factor has a significant influence in the results. The other terms in the table are discussed in Roy's book[5,6], which we are not going to talk in this study.

III.1.2.2 Experiment

"Material" and "film preparation" are the same as described in III.1.1.2, expect for the concentration of polymer solution (a single concentration 6.0 wt. % PS_{25k}-$P2VP_{25k}$ in toluene was used here) and spin-coating conditions. The experiments were carried out according to the experimental conditions as shown in Table III. 3.

Measurement

The topographies of the films are observed by AFM and Optical Microscopy.

The thickness of the films is measured by Variable angle spectroscopic ellipsometry (VASE) with the spectral range [0.6-4.0eV] in configurations UVISEL II and AOI=60º, 65º and 70º.

III.1.2.3 Results and discussion

After the nine designed samples were ready, the samples surface was observed by optical microscope (see Figure III. 6). We can tell that the thicknesses of the nine films are a little different due to the different colors of the surfaces.

Note that the films are not perfectly flat in this series, which is visible by the color stripes they present in the micrographs. We believe this is due to an experimental problem with the used solvent, but we also believe the thickness study presented here is still valid.

The thickness of the samples were extracting from the VASE data with the model shown in Figure III. 3. The illustration of the measured and adjusted I_s and I_c at different angles of incidence (AOI) are shown in the Figure III. 7. The Figure III. 7(g) evidences

the slight shift of the I_s oscillations with the photon energy, which is due to the slightly different thickness among the nine samples.

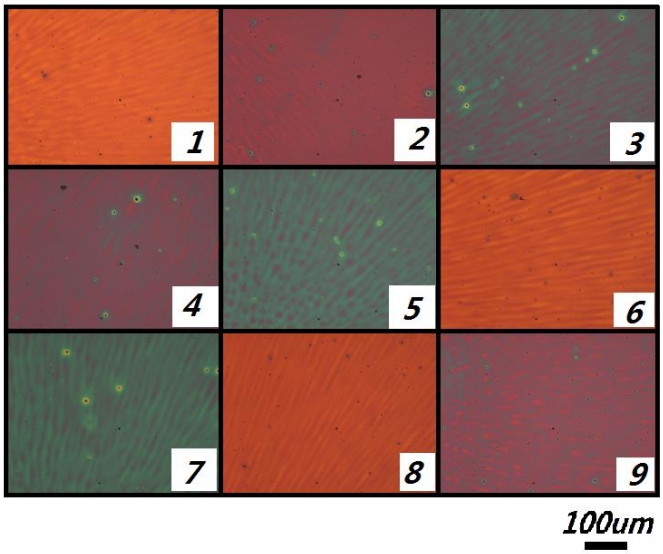

Figure III. 6 Nine designed samples under the microscope.

Table III. 4 Experimental matrix and results obtained following L_9 orthogonal array

Factor / Level	A	B	C	Blank	outcomes	
Exp. No.	Volume (µl)	Spin speed (rpm)	Acc/Dec time (s)		Thickness (nm)	Noted name (nm)
1	A1 (55)	B1 (4500)	C1 (2/2)	D1	y_1=231	A1B1C1D1
2	A1 (55)	B2 (4800)	C2 (3/3)	D2	y_2=250	A1B2C2D2
3	A1 (55)	B3 (5100)	C3 (4/4)	D3	y_3=278	A1B3C3D3
4	A2 (58)	B1 (4500)	C2 (3/3)	D3	y_4=266	A2B1C2D3
5	A2 (58)	B2 (4800)	C3 (4/4)	D1	y_5=283	A2B2C3D1
6	A2 (58)	B3 (5100)	C1 (2/2)	D2	y_6=228	A2B3C1D2
7	A3 (61)	B1 (4500)	C3 (4/4)	D2	y_7=284	A2B1C3D2
8	A3 (61)	B2 (4800)	C1 (2/2)	D3	y_8=233	A2B2C1D3
9	A3 (61)	B3 (5100)	C2 (3/3)	D1	y_9=260	A2B3C2D1

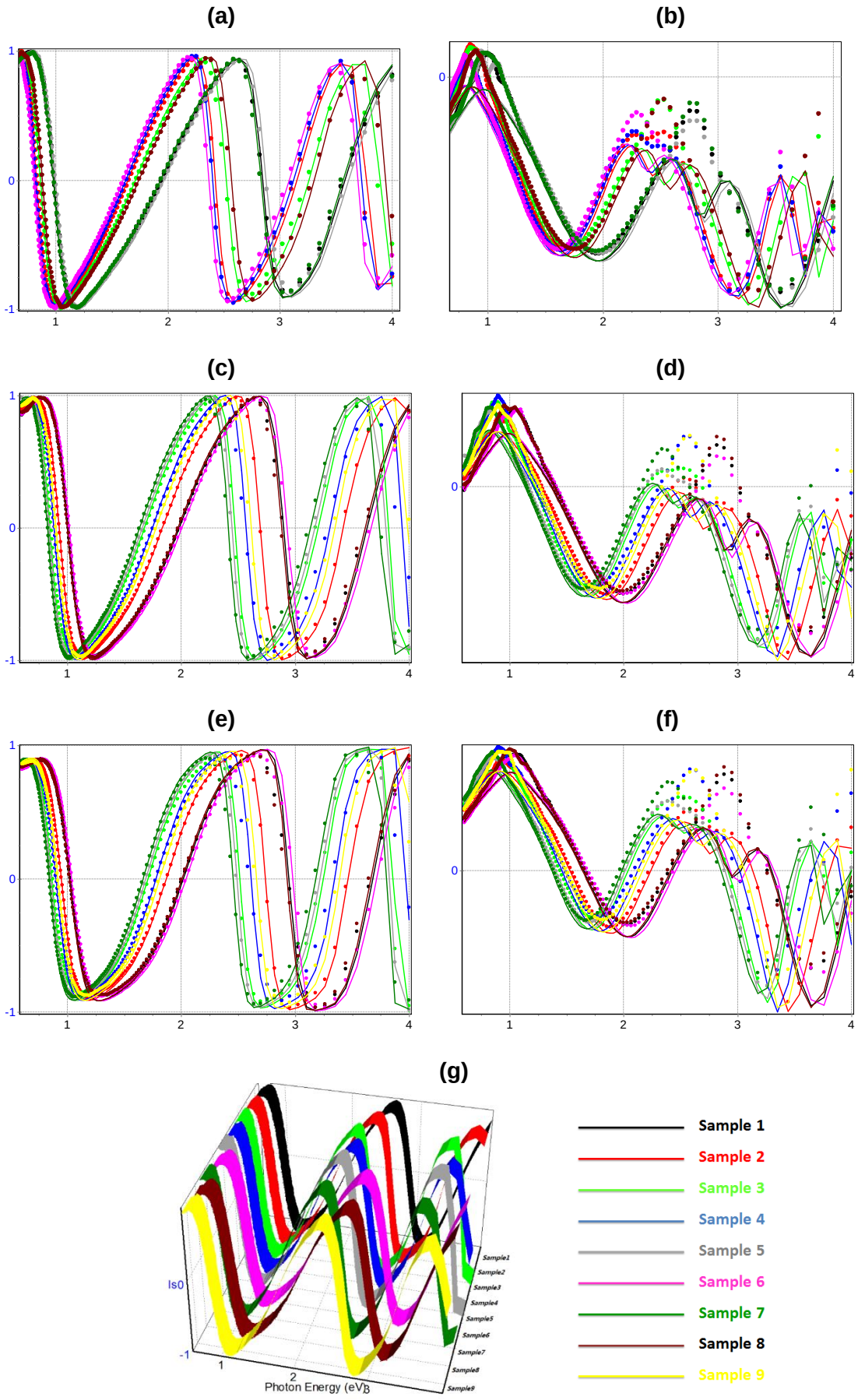

Figure III. 7 Ellipsometry results for the nine designed samples. Dots are experimental data and solid lines are fitting curves (a) and (b) for AOI=60°; (c) and (d) for AOI=65°; (e) and (f) for AOI=70°;

(g) is a 3D representation of the experimental values of I_s, which shows the slight shift of the oscillations due to slight differences in the film thickness.

Table III. 5 Results of ANOVA for film thickness

Factor	A(volume)	B(spin speed)	C(acc/dec time)	Blank
K1	759	781	692	774
K2	777	766	776	762
K3	777	766	845	777
$\overline{K1}$	253	260.3333333	230.6666667	258
$\overline{K2}$	259	255.3333333	258.6666667	254
$\overline{K3}$	259	255.3333333	281.6666667	259
Range(K)	18	15	153	15
Range($\overline{K}$)	6	5	51	5
SSj	72	50	3914	42
T	2313			
SS_T	4078			
df_T	8			
df_j	2	2	2	
df_e				2
MS	36	25	1957	
MS_e				21
F	1.714285714	1.19047619	93.19047619	

Film thickness results are listed in Table III. 4. All the values of ANOVA are summarized in Table III. 5, which is used to determine the percentage contribution of each parameter to the thickness of the films.

From the values of Range$\overline{K}$ and F, it appears that the volume (parameter A) and the spin speed (parameter B) have a very small influence on the thickness of films, whereas the acceleration and deceleration time parameter C) has a strong influence on the thickness of films. , because the value of F is 93%.

III.2 Orientation and period size

We showed that the spin-coating process can produce good films of controlled thickness but the produced films have no controlled nanostructure. This is because the deposition process is too fast to allow the evolution of the copolymer towards its microphase separated equilibrium nanostructure. In this part, we are focusing on obtaining controlled lamellar structures in the films. As was explained in Chapter I, the block copolymers (BCP) present spontaneous spatial organization depending on the polymerization degree and the composition of the block copolymers. In our experiments, we restrict the study to symmetric or nearly symmetric diblock, in order to produce lamellar morphology. We will then assess how the polymerization degree of PS-*block*-PVP influences the obtained morphologies and period size.

III.2.1 Experiment

"Material" is the same as III.1.1.2.

Table III. 6 Molecular characteristics of the PS-block-P2VP copolymers

Polymer PS_{MnPS}-*block*-PVP_{Mnpvp}	Total M_n ($*10^3$ g•mol^{-1})	M_w/M_n (PDI)	P2VP fraction In weight (%)	Degree of Polymerization(N)
PS_{34k}-*block*-$P2VP_{18k}$	52.0	1.12	0.35	506
PS_{102k}-*block*-$P2VP_{97k}$	199.0	1.12	0.49	1899
PS_{106k}-*block*-$P2VP_{75k}$	181.0	1.10	0.41	1762
PS_{25k}-*block*-$P2VP_{25k}$	50.0	1.06	0.50	487
$PS_{8.2k}$-*block*-$P2VP_{8.3k}$	16.5	1.08	0.50	161

The diblock copolymers used in this study were purchased from Polymer Source Inc. (list in Table III. 6) and were used without any further purification.

Equation 3- 7
$$N = \frac{M_{nPS}}{m_{PS}} + \frac{M_{nP2VP}}{m_{P2VP}}$$

M_{nPS} and M_{nP2VP} are the molar mass of the PS and P2VP blocks. N is the degree of polymerization calculated by Equation 3- 7, with molar mass of monomer m_{PS} (102.15 g•mol^{-1})and m_{P2VP} (103.14 g•mol^{-1}).

Samples for electron microscope

Polymers were dissolved in THF to yield 6.0 weight% solutions and stirred overnight at room temperature to ensure complete dissolution. The spin-coating was accomplished by dropping 55 µL (or 65 µL) of the polymer solution onto 1*1cm^2 silicon wafers (or 1.5*1.5cm^2 Aclar substrates) at 5000 rpm for 30 s at room temperature. This step provided homogenous films.

Following the deposition, thermal annealing at 180^o in vacuum (15hours for samples on silicon wafers, 2hours for samples coated on Aclar substrates) was used to generate well-defined periodic structure. Indeed, it is known that the fast solvent evaporation during spin-coating does not allow the copolymer chains to reach the equilibrium phase-separated nanostructures, and that thermal annealing can then provide the chains with the necessary mobility to reach their equilibrium organization.

Samples enhanced by iodine and gold nanoparticles were studied by SEM. Because the I_2 or gold NPs can selectively located in the PVP domains, they induce a strong enhancement of the electronic contrast observable by SEM BSEI mode, and make the measurement of the lamellar period more accurate (samples enhanced by iodine were place in a container with vapor of iodine for 1hour and the gold nanoparticles loading process can be found in the following Chapter IV.2.2.) Note that the presence of gold nanoparticles may change slightly the thickness of layers or films.

The samples are then broken into two pieces, to expose the section of the films, and are ready for SEM observation.

Samples for SAXS

The copolymers were dissolved in toluene or THF to yield 15.0 weight% solutions and were stirred overnight at room temperature to ensure complete dissolution.

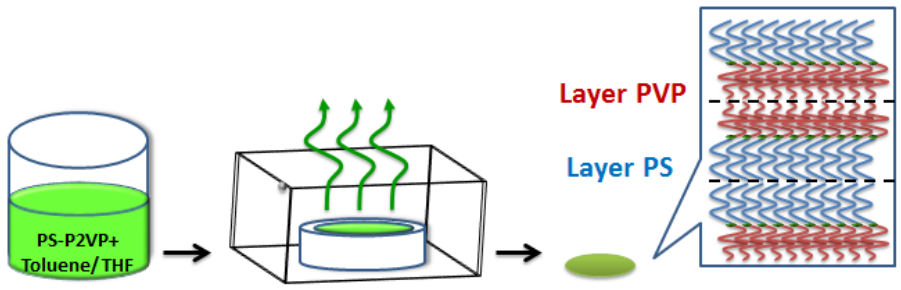

Figure III. 8 Scheme of the preparation of the bulk samples of copolymer PS-block-P2VP

Approximately 3ml copolymer solutions were filled in Teflon molds (Figure III. 8) and then placed in glass container with a lid, in order to slow down the solvent evaporation, so that the complete drying of the films takes 3~5 days at room temperature. Unlike in the spin-coating process, the slow evaporation used here allows for the copolymer chains to have a significant mobility for an extended period of time and reach their equilibrium phase-separated nanostructure. The final samples have a thickness of the order of 1mm. They are then placed in a vacuum chamber at room temperature for one day to ensure that the residual solvent is completely evaporated.

Bulk samples are then ready for SAXS measurements.

III.2.2 Measurement

SAXS, SEM and TEM are used for the morphology study of the diblock copolymers. In order to observe the sections of the sample, in TEM study, we use ultramicrotomy to cut the thin films on aclar substrates into approximate 60nm thick sections and in SEM study, samples on silicon substrate were broken in 2 pieces and their side is ready for observation.

SAXS

The description of SAXS principle was given in Chapter II 2.2. Before analyzing the scattered intensities obtained after azimuthal integration of the detector 2D spectra, we corrected the data for background scattering. This is a combination of background by air, sample holder (capillary) if any, and electronic noise and is usually significant only at high wavevector **q** when the scattered signal is small. The correction can be done in two ways, direct and indirect. In the direct route, the scattering pattern is first recorded on the detector with a blank sample: empty sample holder or capillary. The recorded scattering pattern then contains the information of the background when there is no sample and can be subtracted from the signal obtained with sample. In the other route, the background is mathematically corrected, using the two assumptions that the background signal is a constant, and that the intensity scattered by the studied samples follow an asymptotic q^{-4} trend at high q. Thus, we can write the total measured intensity in the high q region as:

Equation 3- 8 $$I(q) = A(q) \times q^{-4} + B$$

Where I (q) is the total measured scattered intensity;

A(q) is the scattered intensity from the sample, which we want to determine, and which is asymptotically constant at high q;

B is the constant background.

When multiplied by q^4 on both sides, Equation 3- 8 transforms into:

Equation 3- 9 $$I(q) \times q^4 = B \times q^4 + A(q)$$

In the Equation 3- 9 B represents the slope at high q of a $I(q) \times q^4$ versus q^4 plot. The obtained slope is then subtracted from the measured data to give only the scattering from the sample.

Ultramicrotomy technique

Because TEM electrons cannot travel across matter on long (>100nm) distances, the study of the nanometric structures of polymer composites by TEM requires very thin sections carried out by ultramicrotomy.

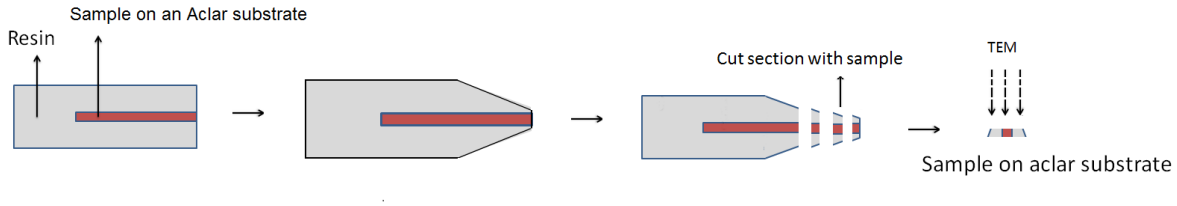

Figure III. 9 Schema of the TEM sample preparation by ultramicrotomy technique

Ultramicrotomy[3,8] is a cutting sample technique commonly used in the preparation of ultrafine sections of films with a thickness between 40 and 80 nm, and can be used either at room temperature or in cryogenic conditions. First, the film is cut into mm-size pieces and embedded in an epoxy resin, which is cross-linked by baking at 60 ºC for 72 hours. 1mL of the embedding media is based on 46% Agar 100 resin contain 36% Dodecenyl Succinic Anhydride (DDSA) and 18% Methyl-5-Norbornene-2,3-Dicarboxilic Anhydride (MNA), and 1 drop of the accelerator 2,4,6-tri (dimethylaminoethyl) phenol (DMP).

After the resin containing the sample is completely cross-linked, it is cut into the shape of a pencil (see Figure III. 9), and a mm-large even flat tip exposing the sample is cut with a glass. Once the surface is flat, automatic cutting is realized by a diamond

knife (2 mm, Knife angle 35º, purchased from Diatome Ltd.), in order to obtain ultrafine sections of the sample embedded in resin with the thickness of 70nm.

Ultramicrotomy cannot be performed on hard materials and films on silicon wafers cannot be observed with TEM. This is the reason why we use Aclar substrates.

The Ultramicrotomy was performed in the Bordeaux Imaging Center, a service unit of the CNRS-INSERM and Bordeaux University, member of the national infrastructure France BioImaging.

III.2.3 Results

In certain cases, annealing was extended to 3 days to ensure equilibrium was reached, although there was no significant change of the ordering of lamellae after 15 h. In order to minimize the surface energy[9], the P2VP block has a preferential interaction with the polar substrate while PS block prefer the free interface with air[10]. This leads to the asymmetric wetting configuration (see Chapter I.3) and during the annealing process, the PVP stay at the substrate interface and PS stays at the air surface which can be seen in the following SEM images.

III.2.3.1 Results of electron microscope

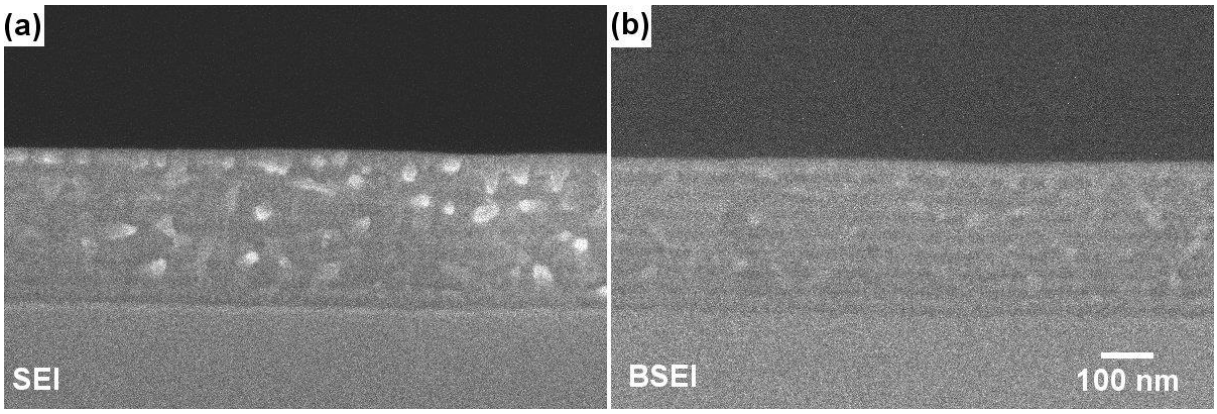

Figure III. 10 Section SEM micrographs of a film of PS_{25k}-block-$P2VP_{25k}$ copolymers enhanced by iodine after thermal annealing under (a) SEI and (b) BSEI mode

As we mentioned in the Chapter II.3, in the TEM images, the contrast is dominated by the absorption of the electrons beam by the samples, which is increasing with the electronic density so that metallic nanoparticles appear dark and polymer appear light. On the contrary, the dark parts correspond to polymers and light parts correspond to metallic NPs in the images formed by back scattered electrons under the BSEI SEM.

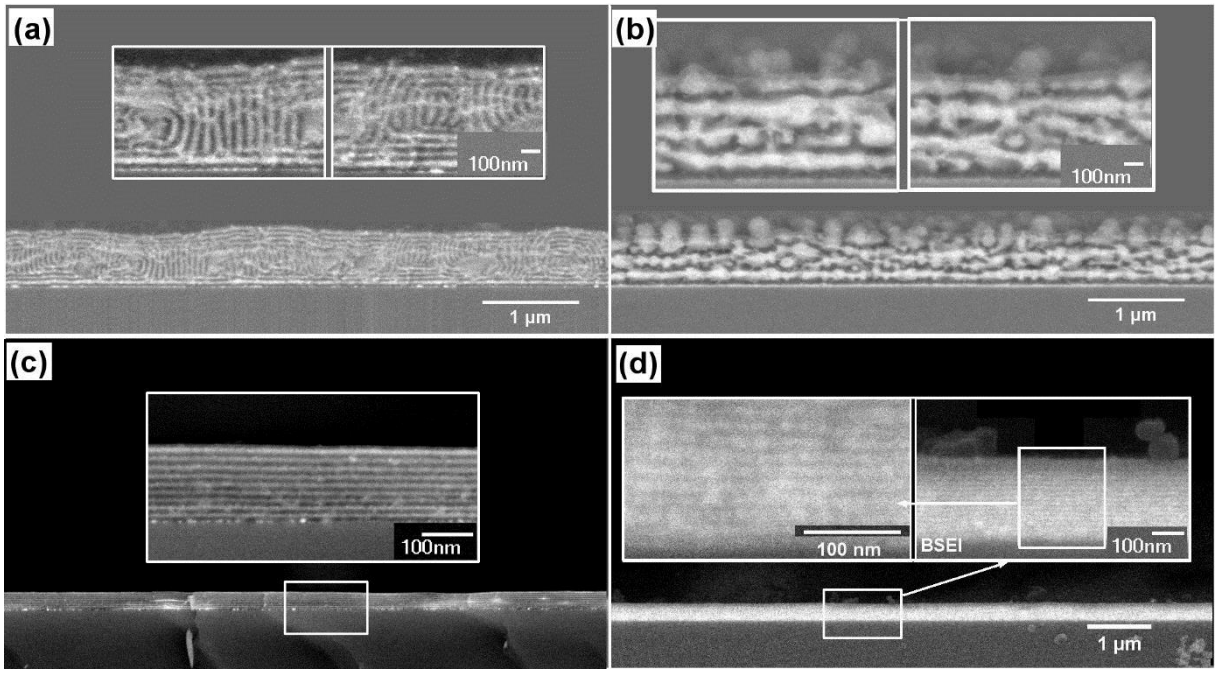

Figure III. 11 Section SEM micrographs of films of PS-block-P2VP copolymers of different composition, after thermal annealing and gold impregnation, (the process is explained in Chapter IV.2.2). (a) PS_{34k}-block-$P2VP_{18k}$ (b) PS_{102k}-block-$P2VP_{97k}$ (c) PS_{25k}-block-$P2VP_{25k}$ (d) $PS_{8.2k}$-block-$P2VP_{8.3k}$

For a pure diblock copolymers, there is no contrast under electron microscope. We enhanced the contrast of PVP by iodine and gold nanoparticles. The images of the films enhanced by iodine are illustrated in Figure III. 10, which shown the morphology of PS_{25k}-*block*-$P2VP_{25k}$ after thermal annealing self-assembly into lamellar structures. However the contrast of the two domains PS and P2VP with iodine is not strong enough to measure the thickness. In order to get a better contrast, we use gold nanoparticles to increase the contrast. Comparing the contrast enhanced by iodine Figure III. 10 and gold nanoparticles Figure III. 11(c), we can see gold nanoparticles loading preserves the structure. The other copolymers morphologies were enhanced by gold nanoparticles, and are shown in Figure III. 11 and Figure III. 12.

From the TEM images (see Figure III. 12) and SEM images (see Figure III. 11), we know that PS_{102k}-*block*-$P2VP_{96k}$, PS_{25k}-*block*-$P2VP_{25k}$, and $PS_{8.2k}$-*block*-$P2VP_{8.3k}$ form lamellar phases when annealed. These results are in good agreement with the generic phase diagram of block copolymers, where symmetrical compositions (f_{PVP}≈0.5, Table III. 6) correspond to the lamellar phase. When the compositions of diblock copolymers are non-symmetrical as with PS_{34k}-*block*-$P2VP_{18k}$ (f_{PVP}=0.35) and

PS_{106k}-*block*-$P2VP_{75k}$ (f_{PVP}=0.41), it is not easy to obtain lamellar phases parallel to substrates.

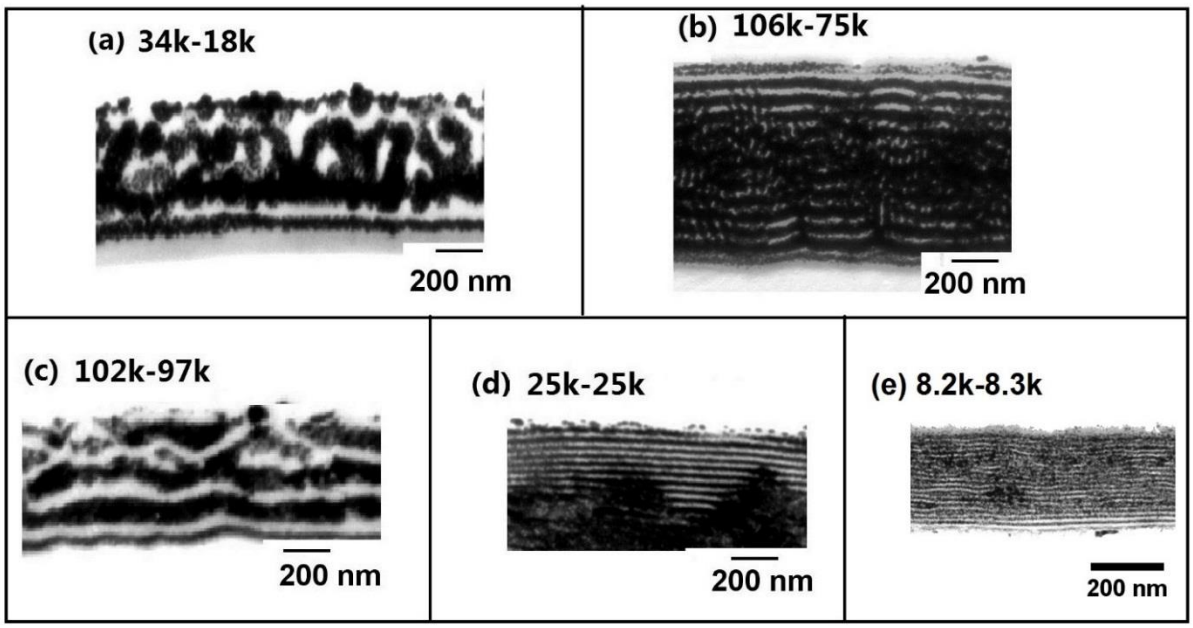

Figure III. 12 Section TEM micrographs of films ofPS-block-P2VP copolymers of different compositions. The sections were prepared by ultramicrotomy of films after thermal annealing and gold impregnation process to increase the contrast of two blocks (see detail in Chapter IV.2.2)). (a) PS_{34k}-block-$P2VP_{18k}$ (b) PS_{106k}-block-$P2VP_{75k}$ (c) PS_{102k}-block-$P2VP_{97k}$ (d) PS_{25k}-block-$P2VP_{25k}$ (e) $PS_{8.2k}$-block-$P2VP_{8.3k}$

PS block prefers[9,11] an air interface due to its smaller surface energy, and PVP stay in the interface of polymer and substrates (silicon or aclar). We can see that clearly when polymer deposited both in silicon substrates Figure III. 11 and aclar substrates Figure III. 12, half layer of PVP attaching with substrates and an asymmetric lamellar film formed. The bilayer thickness d measured by SEM and TEM are listed in Table III. 9.

III.2.3.2 Results of SAXS

Table III. 7 solubility parameters

Compound	Toluene	THF	poly(styrene)	poly(2vinylpyrridine)[12]
Hilderbrandt solubility parameter, δ $(MPa)^{1/2}$	18.3	18.5	18.3	21.3

The dry films are set directly in the beam in the sample chamber. The intensity is accumulated for 2.6h. Based on Equation 3- 9, the background B is obtained from the

slope of the linear fitting of $I(q) \times q^4$ versus q^4 plot in the high *q* region. The Figure III. 13 shows an example of such data treatment for the case of the PS_{34k}-*block*-$P2VP_{18k}$ copolymer. The higher order peaks of *I(q)* are usually better defined after background subtraction.

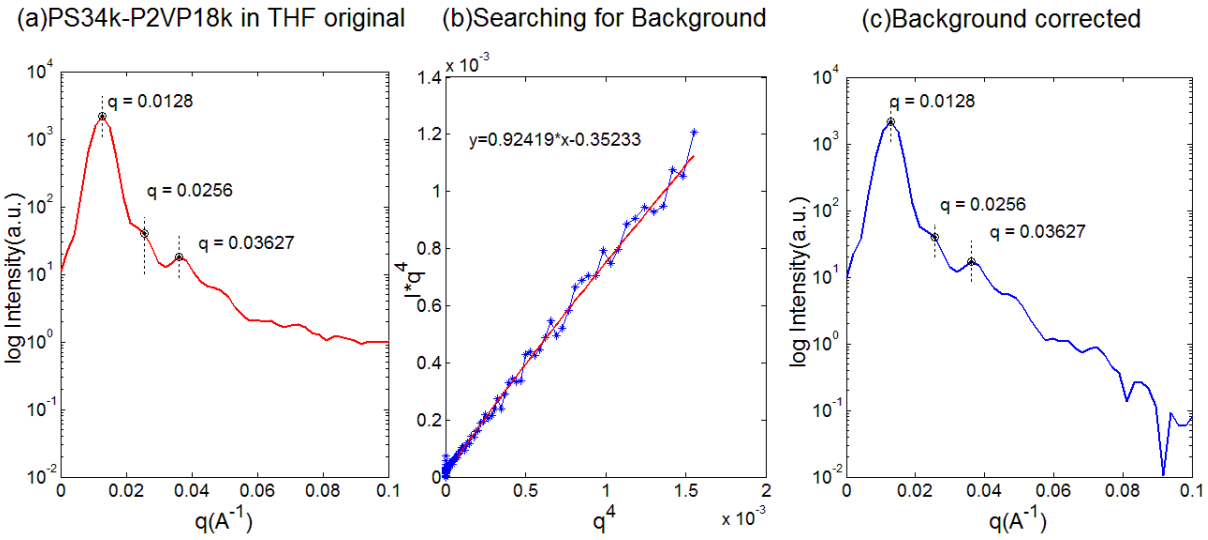

Figure III. 13 Example of SAXS analyzing for the PS_{34k}-block-$P2VP_{18k}$ copolymer. (a) Experimental measured intensity as a function of the scattering vector q in semi-log coordinates; (b) the plot of $I*q^4$ as a function of q^4. The red line is the linear fit at high q (see Equation 3- 9), giving the background here B=0.92419; (c) Background corrected scattered intensity in semi-log coordinates.

All the SAXS results are shown in **Erreur ! Source du renvoi introuvable.**. We compared the results obtained with copolymers of different polymerization degrees cast from THF or from toluene solutions. The **Erreur ! Source du renvoi introuvable.** shows that, in general, samples prepared from THF solutions present better defined peaks than samples prepared from toluene solutions. This could be due to the fact that THF is a slightly more neutral solvent for the diblock copolymer, while toluene is a better solvent for PS than for P2VP[12], thus swelling more the PS domains and impacting the capacity of the copolymer to reach the equilibrium structure.

From the TEM (see Figure III. 12) and SEM images (see Figure III. 11), and in agreement with the copolymers composition, we know that PS_{102k}-*block*-$P2VP_{96k}$, PS_{25k}-*block*-$P2VP_{25k}$, and $PS_{8.2k}$-*block*-$P2VP_{8.3k}$ are lamellar phases. The sample of largest molecular mass PS_{102k}-*block*-$P2VP_{96k}$ presents a series of Bragg peaks characteristic of a lamellar order at positions 1:2:3:4 and corresponding to a period of 75.5nm. The sample PS_{25k}-*block*-$P2VP_{25k}$ presents two Bragg peaks at positions 1:3,

and corresponding to a period of 37.2nm, with a lack of second order peak probably due to a minimum of the lamellae form factor, as is classical with very symmetrical compositions[13]. Finally, the sample $PS_{8.2k}$-*block*-$P2VP_{8.3k}$ presents one well defined peak, corresponding to a period of 17.0nm. The absence of higher order peaks could be due to the fact that the 2d peak would be near the edge of the q-window, or to the proximity of the sample to the order-disorder transition line for small diblocks.

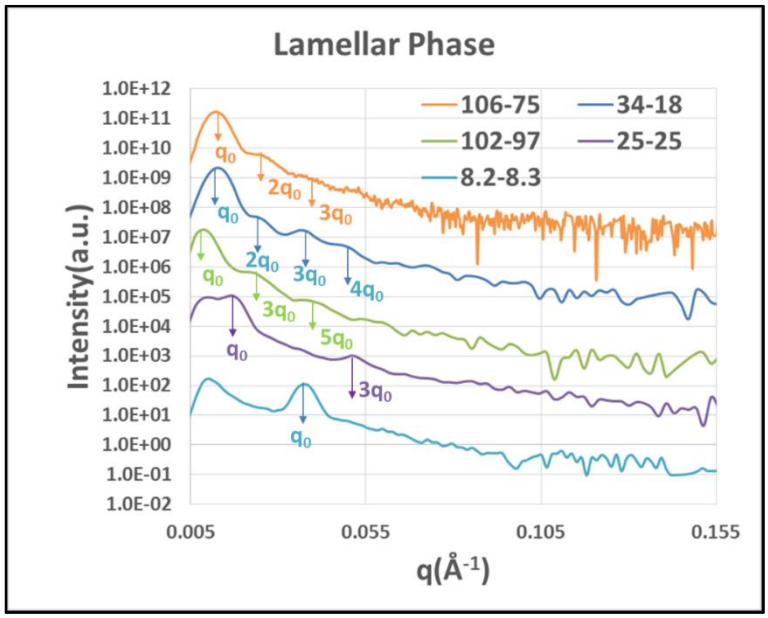

Figure III. 14 SAXS profiles depending on polymer degrees of polymerization in semi-log coordinates. The curves are vertically shifted for clarity

Table III. 8 Peak positions and the period sizes

Copolymers	Solvent	P2VP fraction	q_0 (A^{-1})	Ratio of peaks	Period size based on q_0
PS_{34k}-*block*-$P2VP_{18k}$	THF	0.35	0.0128	1.0 :2.0:3.0:3.83…	49.0nm
PS_{106k}-*block*-$P2VP_{75k}$	THF	0.41	0.0127	1.0 :2.0:3.0…	49.49nm
PS_{102k}-*block*-$P2VP_{97k}$	THF	0.49	0.00800	1.0：3.0：4.0…	78.53nm
PS_{25k}-*block*-$P2VP_{25k}$	THF	0.50	0.01707	1.0：3.06…	36.81nm
$PS_{8.2k}$-*block*-$P2VP_{8.3k}$	THF	0.50	0.03841	1.0：…	16.36nm

From the curves obtained with THF, peaks positions are carefully identified (see Table III. 8 and Figure III. 14). The period sizes of PS_{102k}-*block*-$P2VP_{97k}$, PS_{25k}-*block*-$P2VP_{25k}$ and $PS_{8.2k}$-*block*-$P2VP_{8.3k}$ are listed in Table III. 8.

Depending on the publication[13], the lamellar period can be shown to relate to the total polymerization degree as follow Equation 3- 10. Where $\bar{a}$ is average segment size

of monomer, were found by segment size of monomer polystyrene $a_{PS} = 0.67\,nm$[14], poly(2-vinylpyridine)$a_{P2VP} = 0.71\,nm$[15] and their respective volume fractions f_{PS} and $1 - f_{PS}$(Equation 3- 11).

Equation 3- 10
$$d = \bar{a}N^{2/3}2\sqrt[3]{\frac{1}{3}\left(\frac{\chi}{6}\right)^{1/2}}$$

Equation 3- 11
$$\bar{a} = \sqrt{f_{PS}a_{PS}^2 + (1 - f_{PS})a_{P2VP}^2}$$

N is the degree of polymerization (see Table III. 6) and χ is the Flory-Huggins interaction parameter. In this case $\bar{a} = 0.69\,nm$, $\chi = 0.18$ at room temperature[16,17].

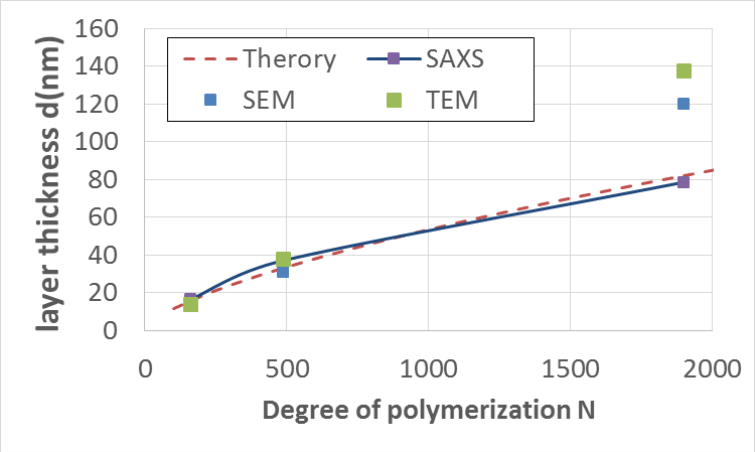

Figure III. 15 Period size thickness under different measurements and theory

Table III. 9 Period size under different measurements and theory

Polymer	N	d(nm) TEM	d(nm) SEM	d(nm) SAXS	d(nm) Theory
PS_{102k}-*block*-$P2VP_{97k}$	1899	137.6	120	78.53	81.80
PS_{25k}-*block*-$P2VP_{25k}$	487	37.74	31	37	33.02
$PS_{8.2k}$-*block*-$P2VP_{8.3k}$	161	13.66	13.8	16.36	15.76

For block copolymers with volume fraction approximately equal to 0.5, the morphologies are lamellar phases based on SAXS (Figure III. 14) and electron microscopy images (see Figure III. 11 and Figure III. 12)(PS_{102k}-*block*-$P2VP_{97k}$ PS_{25k}-*block*-$P2VP_{25k}$ and $PS_{8.2k}$-*block*-$P2VP_{8.3k}$). As shown in the plot Figure III. 15, the period measured by SAXS is very consistent with the theory Equation 3- 10, while TEM and SEM results are consistent only for the smaller diblock. This is very likely due to the fact that the presence of the gold increases significantly the measured dimensions for the longest copolymer films.

In conclusion, we have obtained several lamellar phases with PS-b-P2VP of different total polymerization degrees, when the blocks are equally long (f_{P2VP}≈0.5). These phases present lamellar period over a large size range, so that we can produce lamellar films of controlled period between 15nm and 78nm.

III.3 Controlling period thickness of lamellar phase by homopolymer addition

As we discussed in III.2, different polymerization degrees give different period thickness. PS_{102k}-*block*-$P2VP_{97k}$ gives 78nm, PS_{25k}-*block*-$P2VP_{25k}$ gives 37nm, $PS_{8.2k}$-*block*-$P2VP_{8.3k}$ gives 16nm. Additional and finer modulation of the lamellar period could be desirable in our systems.

For this, we studied the mixture of homopolymer of poly (2-vinylpyridine) into PS-*block*-P2VP to increase the layer thickness of P2VP, which will be helpful for fine-tuning of the layer thickness (see Figure III. 16) and may also affect the gold growth in the systems.

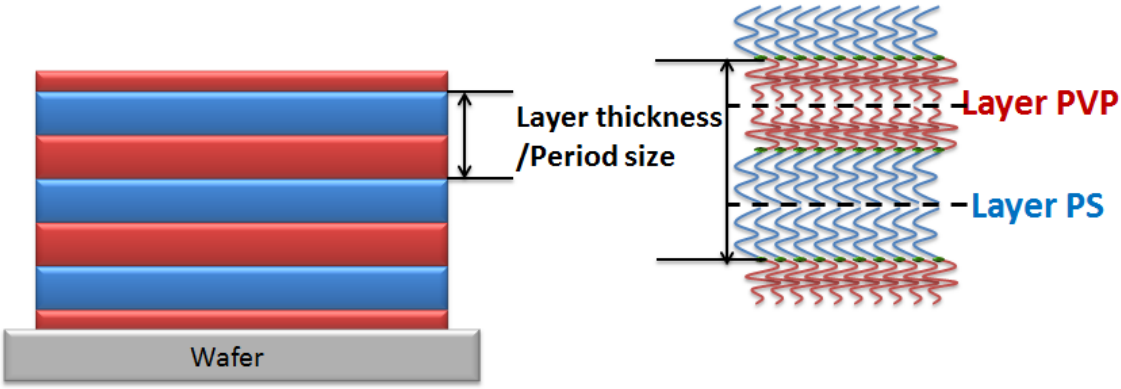

Figure III. 16 the definition for layer thickness: 1 layer PVP + 1 layer PS.

III.3.1 Experimental

Material

PS_{25k}-*block*-$P2VP_{25k}$ (PDI: 1.12) and Poly (2-vinylpyridine) (P2VP, M_n=4500, PDI: 1.04).

Polymer solution

P2VP was mixed at 5.0 weight%, 10.0 weight% and 15.0 weight% in PS_{25k}-*block*-$P2VP_{25k}$, and then the polymers were generally dissolved in THF to yield 15.0 weight% 6.0 weight% and 3.0 weight% solutions and were stirred overnight at room temperature to ensure complete solution.

Samples for SAXS were prepared in the same way as we described in III.2.1" Samples for SAXS".

Samples for SEM were prepared in the same way as we described in III.2.1 "Samples for electron microscope", except for 55µl 3.0 weight% and 6.0 weight% solutions are spin-coated on silicon wafer only and the spin time is 30seconds with the spin speed of 4500 rpm/s, 3 sec of acceleration time and deceleration time.

III.3.2 Results

Results of SEM

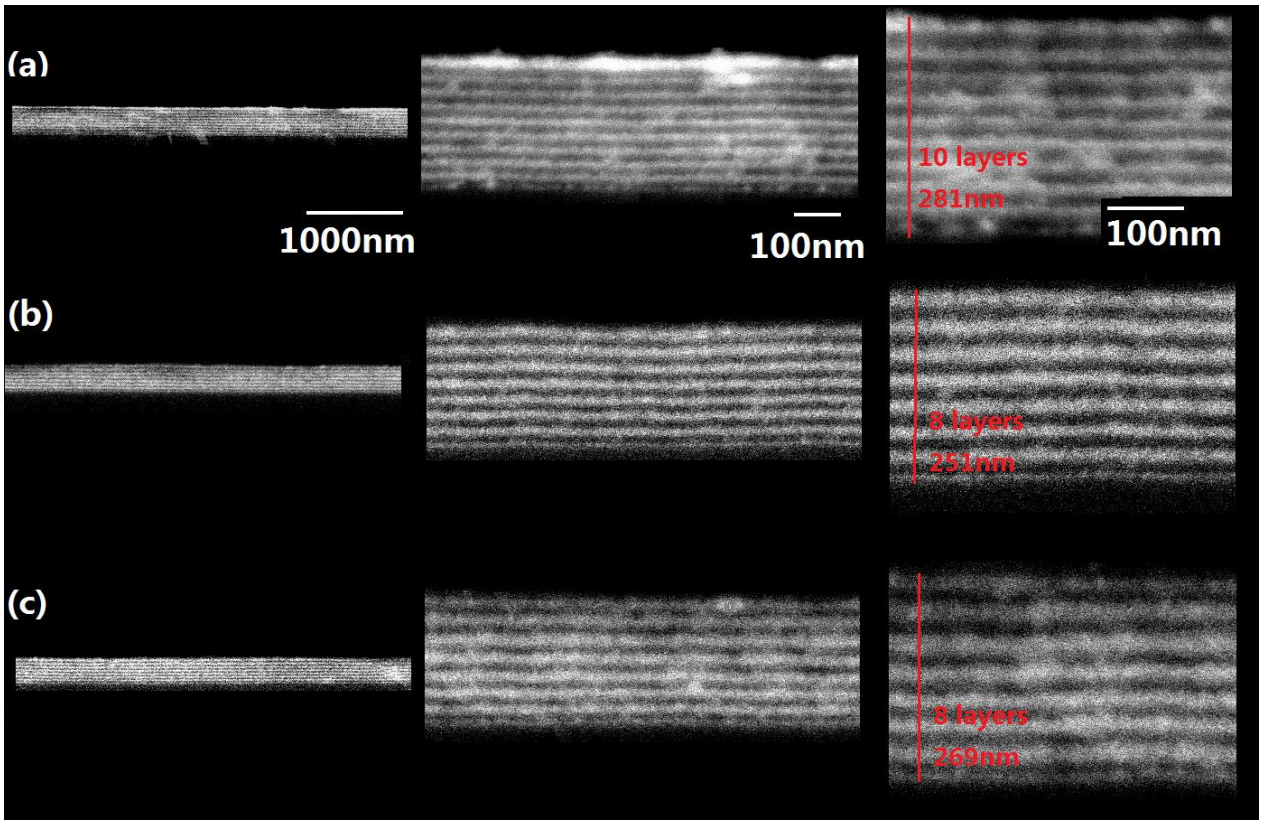

Figure III. 17 Cross-sections of different P2VP fraction mixtures of polymers under SEM in BSEI. (a) 0 w.t. % P2VP in polymers, and 10 layers thickness is 281nm, so 1layer is 28.1nm; (a) 5 w.t. % P2VP in polymers, and 8 layers thickness is 251nm, so 1layer is 31.4nm; (a) 10 w.t. % P2VP in polymers, and 8 layers thickness is 269nm, so 1layer is 33.6nm.

From the SEM images Figure III. 17, we can see that as the concentration of P2VP increasing from 0 wt% to 5wt% to 10 wt%, the bilayer thickness is obvious increasing from 28.1nm to 31.4nm to 33.6nm (measured from SEM images). Since the resolution for SEM is not enough for thickness less than 10nm, we have performed SAXS.

Results of SAXS

Based on the same analysis process of III.2.2"SAXS", Figure III. 18 shows the final curves of different concentration of P2VP. As the weight fraction of P2VP grows from 50.0 % to 57.5 %(0wt% added P2VP to 15wt% added P2VP), the q_0 peaks shifts to smaller values, which indicates an increase of the bilayer thickness in the lamellar phase. If the fraction of P2VP increases to 65 %(30 wt% added P2VP), the lamellar morphology is lost.

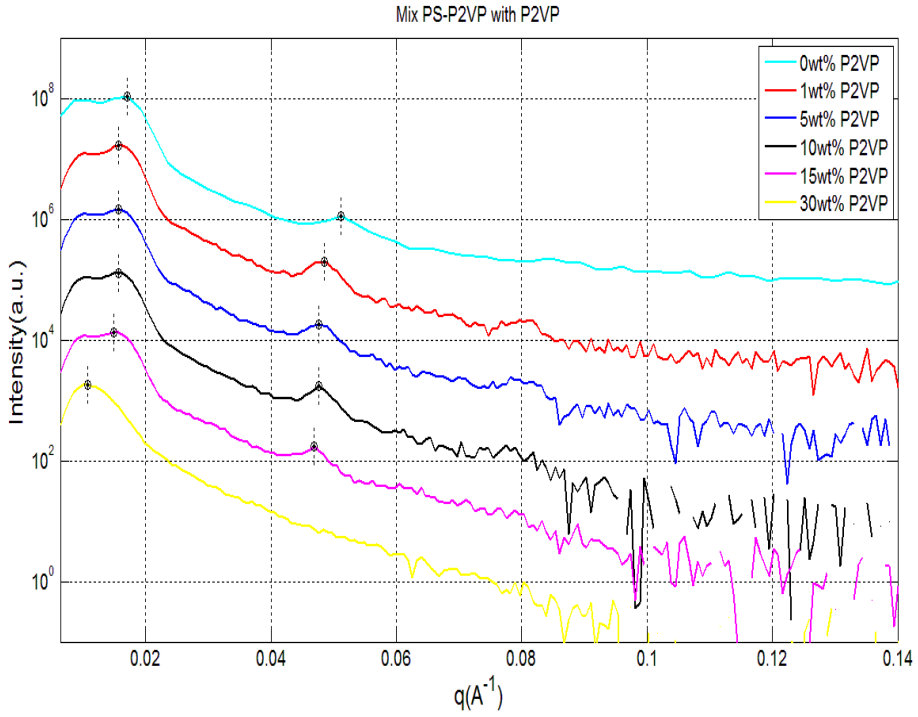

Figure III. 18 SAXS results of the mixture of PS-block-P2VP with P2VP in various concentrations in semi-log coordinates. The curves are vertically shifted for clarity.

The layer thickness calculated from q_0 is listed in Table III. 10. It shows the period size of all the results. Compared with the layer thickness measured from SEM, As the P2VP weight fraction increases, both SAXS and SEM methods indicate an increase of the bilayer thickness following a similar trend.

Table III. 10 Peak positions and the period size

Concentration of P2VP in mixture	Morphology	P2VP weight fraction	q_0 (A^{-1})	Period size Based on SAXS(nm)	Period size based on SEM(nm)
0	lamellar	0.500	0.01686	37.27	28.1
1.0	lamellar	0.505	0.01617	38.86	-
5.0	lamellar	0.525	0.01587	39.59	31.4
10.0	lamellar	0.550	0.01587	39.59	33.6
15.0	lamellar	0.575	0.01563	40.20	-
30.0	No	0.650	-	-	-

Figure III. 19 shows the period size as function of P2VP fraction in mixture. The range of variation of the period size is very limited (3nm), which is probably due to an incomplete mixture of the homopolymer in the diblock nanostructure.

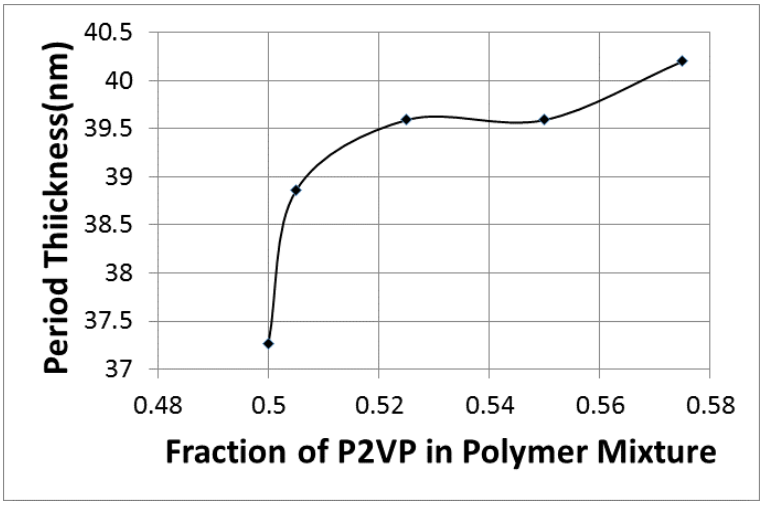

Figure III. 19 Period size as function of the weight fraction of P2VP in the polymer mixtures

As a conclusion, the PS-P2VP diblock copolymers can be organized and aligned in lamellar structures on large areas by thermal annealing. By controlling the concentration of the polymer solution before spin coating, the film thickness can be well controlled between 30nm and 800nm. The bilayer thickness in the films can be controlled by the polymerization degree of the symmetric diblock copolymers, and is a subwavelength size ranging from 17nm to 70nm.

References

1. Hall, D. B., Underhill, P. & Torkelson, J. M. Spin coating of thin and ultrathin polymer films. *Polym. Eng. Sci.* **38,** 2039–2045 (1998).
2. Stange, T. G., Mathew, R., Evans, D. F. & Hendrickson, W. A. Scanning tunneling microscopy and atomic force microscopy characterization of polystyrene spin-coated onto silicon surfaces. *Langmuir* **8,** 920–926 (1992).
3. Kingsley, R. E. & Cole, N. L. Preparation of cultured mammalian cells for transmission and scanning electron microscopy using Aclar film. *Microsc. Res. Tech.* **10,** 77–85 (1988).
4. Taguchi, G. *Introduction to quality engineering: designing quality into products and processes*. (1986).
5. Roy, R. K. *Design of experiments using the Taguchi approach: 16 steps to product and process improvement*. (John Wiley & Sons, 2001).
6. Roy, R. K. A primer on the Taguchi method, 1990. *New York* (1990).
7. Allen, T. T. *Introduction to engineering statistics and six sigma: statistical quality control and design of experiments and systems*. (Springer Science & Business Media, 2006).
8. Corazza, M. *et al.* Comparison of ultramicrotomy and focused-ion-beam for the preparation of TEM and STEM cross section of organic solar cells. *Appl. Surf. Sci.* **389,** 462–468 (2016).
9. Spatz, J. P., Möller, M., Noeske, M., Behm, R. J. & Pietralla, M. Nanomosaic surfaces by lateral phase separation of a diblock copolymer. *Macromolecules* **30,** 3874–3880 (1997).
10. Sohn, B. H. & Seo, B. H. Fabrication of the multilayered nanostructure of alternating polymers and gold nanoparticles with thin films of self-assembling diblock copolymers. *Chem. Mater.* **13,** 1752–1757 (2001).
11. Heier, J., Kramer, E. J., Walheim, S. & Krausch, G. Thin diblock copolymer films on chemically heterogeneous surfaces. *Macromolecules* **30,** 6610–6614 (1997).
12. Arichi, S., Matsuura, H., Tanimoto, Y. & Murata, H. Studies of poly-2-vinylpyridine. ii. solubilities in various solvents. *Bull. Chem. Soc. Jpn.* **39,** 434–439 (1966).

13. Papadakis, C. M., Almdal, K., Mortensen, K. & Posselt, D. A small-angle scattering study of the bulk structure of a symmetric diblock copolymer system. *J. Phys. II* **7,** 1829–1854 (1997).

14. Ballard, D. G. H., Wignall, G. D. & Schelten, J. Measurement of molecular dimensions of polystyrene chains in the bulk polymer by low angle neutron diffraction. *Eur. Polym. J.* **9,** 965–969 (1973).

15. Matsushita, Y. *et al.* Preparation and Characterization of Poly (2-vinylpyridine) with Narrow Molecular Weight Distributions. *Polym. J.* **18,** 361–366 (1986).

16. Dai, K. H. & Kramer, E. J. Determining the temperature-dependent Flory interaction parameter for strongly immiscible polymers from block copolymer segregation measurements. *Polymer* **35,** 157–161 (1994).

17. Hammond, M. R., Cochran, E., Fredrickson, G. H. & Kramer, E. J. Temperature dependence of order, disorder, and defects in laterally confined diblock copolymer cylinder monolayers. *Macromolecules* **38,** 6575–6585 (2005).

Chapter IV Metal loading process

Introduction

Our goal is to fabricate the target nanostructured multilayers (Figure IV. 1) consisting of alternate nanocomposite layers and polymer layers. We already know how to obtain controllable and aligned lamellar structures (see Chapter III), and we now want to produce similar structures with metallic particles inside some of the layers.

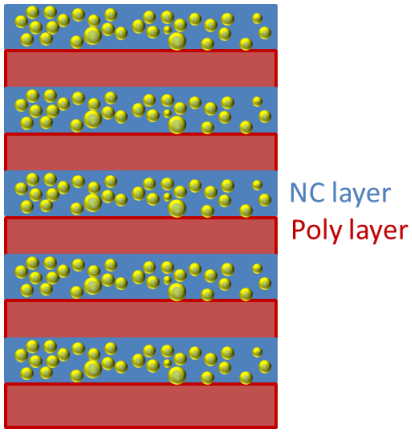

Figure IV. 1 Target structure. NC layer stands for polymer with metallic nanoparticles. Poly layer stands for layer consisting of pure polymer.

After the work of Clémence Tallet (PhD student Year 2010-2013)[1], we decided to study *in situ* synthesis processes, because the introduction of pre-formed nanoparticles in such lamellar polymer structures is often restricted to small nanoparticle sizes and small quantities. Figure IV. 2 shows, as an example, the nanostructure of a PS-PMMA blend with gold Nps (A 0.05 volume % and B 0.58 volume %) covered with a small poly(styrene) ligand.

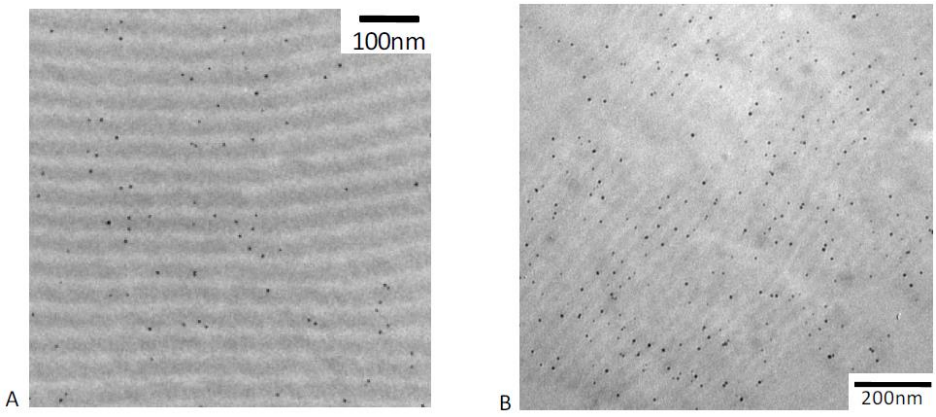

Figure IV. 2 PS-PMMA blend with Au-PS; A volume fraction of Au is 0.05%;B volume fraction of Au is 0.58% [1]

There are two main *in situ* methods we can use. The first one is called one-step method in this chapter: it consists in first blending in solution the gold precursor and the diblock copolymers and then use the self-assembly properties of diblock copolymers to achieve the lamellar nanostructure with nanocomposite and polymer layers. The second one is called the impregnation process: it start from the lamellar

structure template based on self-assembled diblock copolymers (see Chapter III), impregnate metallic particles inside one of the block domains and then produce the target nanocomposite structures.

In this chapter, we are going to discuss these two methods and find an efficient way to reach the target structure.

IV.1 One-step method

IV.1.1 Introduction

In the one-step process, we mix the Au precursor with the diblock copolymers in solution before spin-coating. In the mixed solution the gold ions from $HAu(Cl)_4$ will form gold(Ⅲ) complexes with pyridine[2].

$$Au(Cl)_4^- + Pyridine \longrightarrow Au(Pyridine)(Cl)_3 + Cl^-$$

After the annealing process (solvent or thermal annealing), we may obtain a nanocomposite structure with lamellar structures. In this study, chloroauric acid ($HAuCl_4 \bullet xH_2O$) is used as the Au precursor.

IV.1.2 Experimental

Material

The same as we described in chapter III 3.1.1.2 “material”. Hydrogen tetrachloroaurate(III) hydrate($HAuCl_4 \bullet xH_2O$) is purchased from Alfa Aesar were used without any further purification.

Film preparation

In order to obtain well dispersed mixture of gold precursor and polymer solution, we dissolved the copolymer and the gold precursor separately and then mix them together.

Two different polymer solutions were prepared: PS_{25k}-P_2VP_{25k} and PS_{34k}-P_2VP_{18k} were dissolved in toluene to yield respectively 6.0 weight% and 8.0 weight% solution, and stirred overnight at room temperature to ensure complete solution.

For the gold precursor solution, $HAuCl_4 \cdot xH_2O$ was dissolved in ethanol to yield 3.0 weight% solution.

Two mixed solutions were prepared:

1) 1 volume of gold precursor solution mixed with 6.4 volumes of PS_{25k}-*block*-$P2VP_{25k}$ solution;

2) 1 volume gold precursor solution mixed with 4.4 volumes of PS_{34k}-*block*-$P2VP_{18k}$ solution.

All the mixed solutions were stirred overnight in room temperature and protected from the light, to obtain well-dissolved solutions and were then spin-coated onto silicon wafers. Spin time is 30seconds with the spin speed of 5000 rpm/s, 3 seconds of acceleration time and deceleration time.

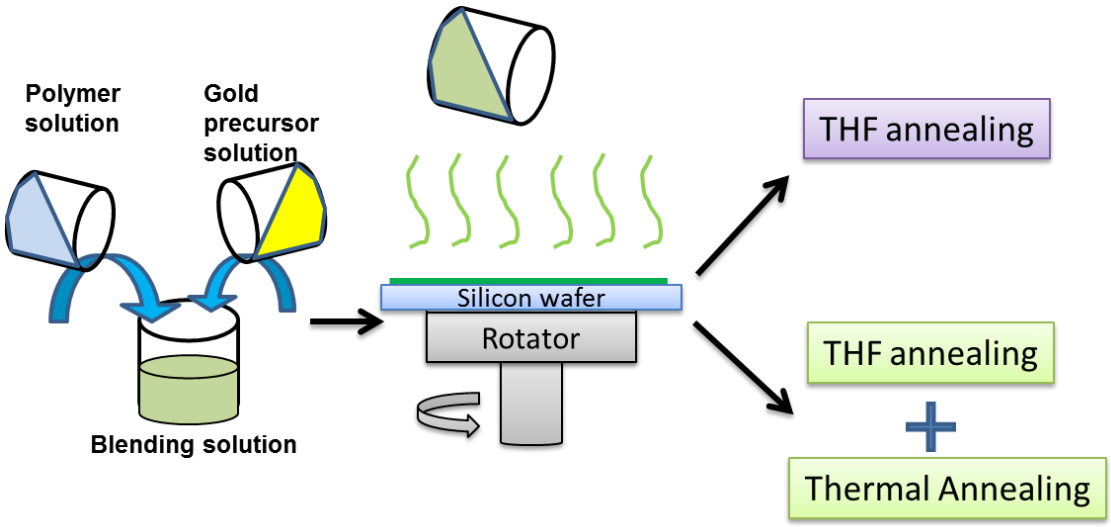

Figure IV. 3 Schematic illustration of the one-step method for Au loading in the films. Mix polymer solution and gold precursor solution to obtain mixed solution. Deposit the mixed solution on silicon wafer by spin coating. Following the deposition, two different annealing processes were used: solvent annealing only or solvent annealing followed by thermal annealing.

After the film coating, two different annealing processes were used:

1) Solvent annealing (8h in THF and then dried in room temperature) to obtain lamellar phase.

2) Solvent annealing (8h in THF and then dried in room temperature) followed by thermal annealing (180℃ in a vacuum oven for 10 hours).

In addition, the solvent annealing was usually followed by one day of slow drying in air. Subsequent removal of any residual solvent is carried out under vacuum for an additional minimum of 4 hours.

Table IV. 1 samples preparation conditions by the one-step method

Samples	PS_m-block-$P2VP_n$ Mn (m-n)	Solvent annealing (In THF)	Thermal annealing (180ºC in vacuum)
OT1	25k-25k	8h	0
OT2	25k-25k	8h	10h
OT3	34k-18k	8h	0
OT4	34k-18k	8h	10h

The prepared samples are listed in Table IV. 1 samples preparation conditions by the one-step method.

Sample observations

The upper surface of the samples was observed by optical microscopy at room temperature. For side view of samples, the films on silicon wafer were broken into half manually and observed by SEM.

IV.1.3 Results

Figure IV. 4 shows the surface of sample OT2 under optical microscopy after spin-coating (a), after solvent annealing (b), and after thermal annealing(c). From the images we can see that after the solvent annealing, the surface of the sample shows globular structures with dark colors, which are preserved after thermal annealing, while the colors become lighter, which may be caused by a reflection effect of Au(0).

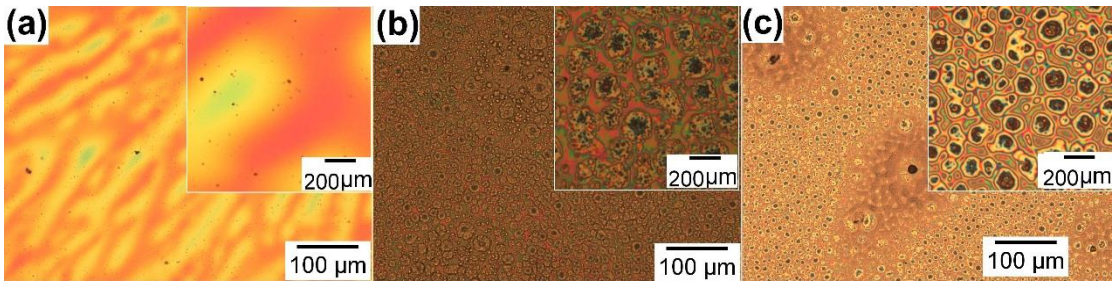

Figure IV. 4 The top view of sample OT2 under microscopy. (a) After spin-coating. (b) After solvent annealing. (c) After thermal annealing.

The side view of the samples was observed by SEM under low and high magnifications, as shown in Figure IV. 5 and Figure IV. 6. In the samples prepared without thermal annealing (a) and (c), there are no visible gold domains inside the films. On the contrary, after thermal annealing (b) and (d), we can see that Au nanoparticles synthesized successfully. The thermal annealing seems necessary for the reduction of the gold salt, whereas when the preparation is limited to a solvent annealing, no reduction apparently occurs. For both 25k-25k copolymer samples (a) and (b), we can detect indications of the aligned lamellar structure both in BSEI and SEI, indicating that the solvent annealing is efficient in the structure alignment. In the case of the 34k-18k copolymer samples (c) and (d), elongated structures are visible, but with no obvious alignment and it is difficult to conclude that these structures are the P2VP cylindrical domains. In thermally annealed samples, the gold nanoparticles are in a very limited amount and do not appear to have any order.

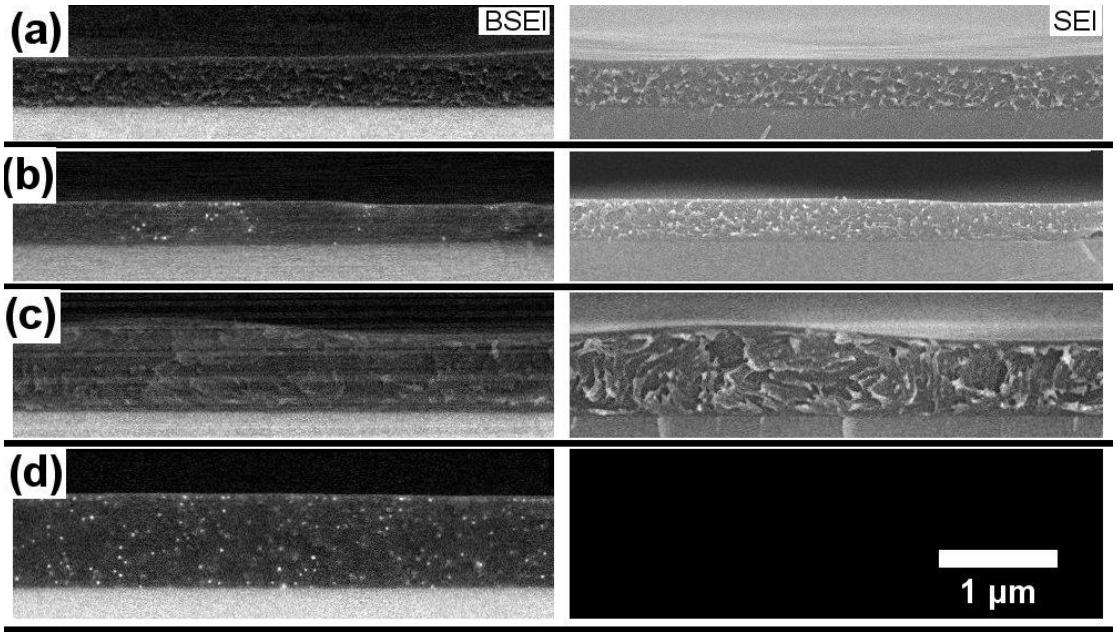

Figure IV. 5 Side view of samples (a) OT1 (Lamellar/Solvent annealed), (b) OT2 (Lamellar/Solvent+thermal annealed), (c) OT3 (Cylindrical/Solvent annealed), (d) OT4 (Cylindrical/Solvent +thermal annealed), under SEM in low magnification. Left images are BSEI while the right images are SEI. Under BSEI images, white parts correspond to gold domains.

In conclusion, this one-step method is not efficient in fabricating the nanocomposite lamellar structures. So we consider using lamellar structures of polymer as the templates and loading gold afterwards.

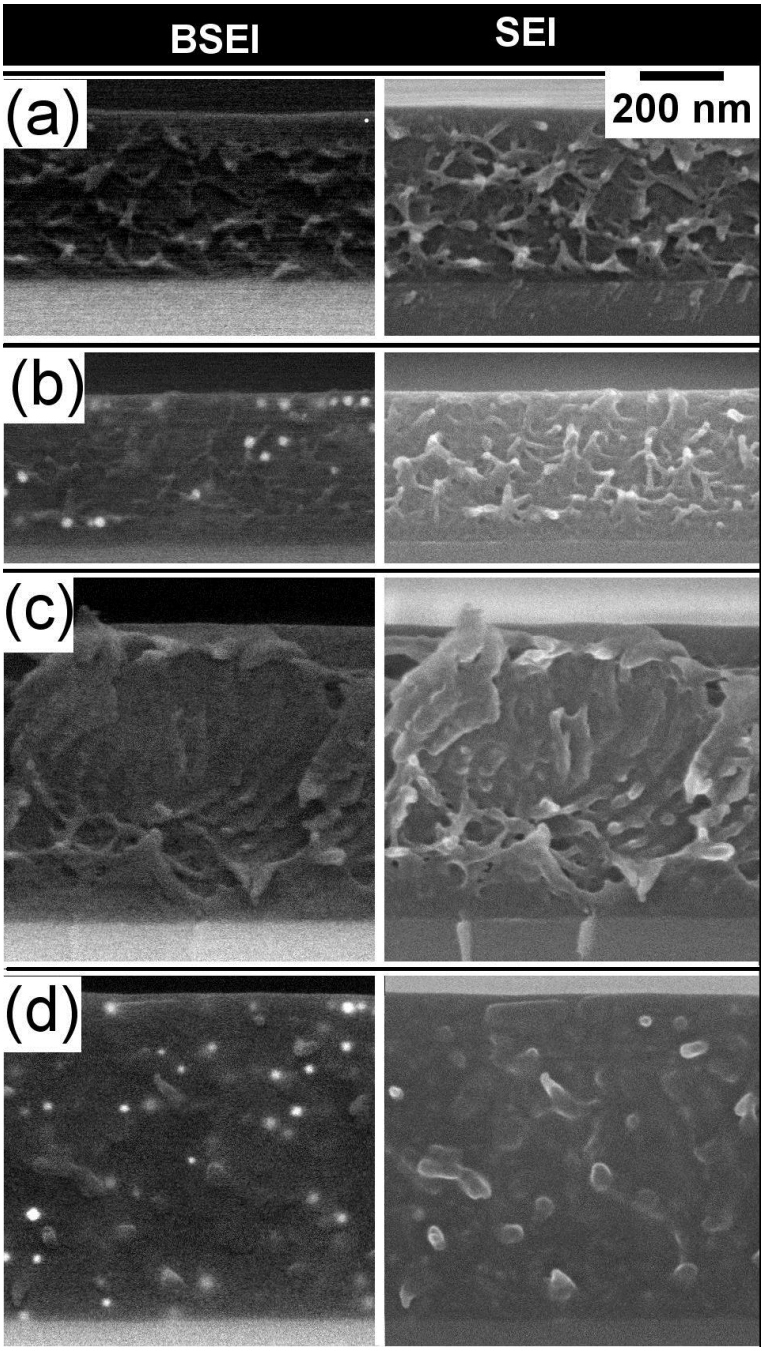

Figure IV. 6 Side views of samples (a) OT1, (b) OT2, (c) OT3, (d) OT4, under SEM in high magnification. Left images are BSEI while the right images are SEI. Under BSEI images, white parts correspond to gold domains.

IV.2 Impregnation process

IV.2.1 Introduction

As we discussed in Chapter III, the nano-scale lamellar phase produced by PS-P2VP copolymers can be well controlled. Various thicknesses of films (from 100nm-700nm) can be realized by different concentrations of the polymer solution before spin coating. In the meantime, the bilayer thickness within the lamellar structures can be controlled by using different polymerization degrees of the block copolymers. Once the lamellar structure is obtained and aligned, we plan to use selective solvent effects in order to introduce metallic entities into the structure directly, while confining them in the P2VP domains, in a well-controlled manner. Such selective swelling of block copolymer lamellar phases was used for the introduction of metal salts by Sang-Hyun Yun et al.[1] and B. H. Sohn et al.[2] who studied the conductivity of anisotropy films, and by B. Maxit et al.[3] for the introduction of small inorganic nanoparticles.

IV.2.2 Experiment

Material used in this study is the same as described in IV.1.2 ”Material”. Silver nitrate ($AgNO_3$) purchased from Sigma-Aldrich was used without any further purification. The diblock copolymers poly(styrene)-*block*-poly(vinylpyridine) (PS-*block*-P2VP) used are listed in Table IV. 2.

Table IV. 2 Diblock copolymers used in this chapter

Polymer PSMn-block-PVPMn	Mw/Mn (PDI)	P2VP fraction (%)	Layer thickness d0 (nm)
PS102k-block-P2VP97k	1.12	0.49	75.5
PS25k-block-P2VP25k	1.06	0.50	37.2
PS8.2k-block-P2VP8.3k	1.08	0.50	17.0
PS25k-block-P4VP25k	1.15	0.50	/

Film preparation

PS_{25k}-$P2VP_{25k}$ copolymers were dissolved in toluene to yield 0.8 weight%, 1.5 weight%, 3.0 weight%, 6.0 weight% and 10.0 weight% solutions and stirred overnight at room temperature to ensure complete dissolution.

The spin-coating was accomplished by dropping 55 µL of the polymer solution onto 1 cm^2-silicon wafers and spin it at 5000 rpm with acc/dec time 3s/3s for 30 s at room temperature. This gave homogenous films.

Following the deposition, a thermal annealing at 180° in vacuum (15 hours for samples on silicon wafers, 2 hours for samples coated on Aclar substrates) was used to generate well-defined lamellar structure.

Au loading process

After we obtained the aligned and organized lamellar phases, we proceed with the following process:

1) We immersed the film in 3.0 wt% $HAuCl_4$ solution in ethanol for 5 minutes following by a gentle rinsing of deionized water several times.

2) The films loaded with $HAuCl_4$ were then immersed into 0.65 wt% $NaBH_4$ solution in water for 30 sec.

We repeat the cycle comprising steps 1) and 2) for N times (N is integrate from 0 to 30) to increase the concentration of Au NPs. Figure IV. 7 shows the process of Au loading.

Ag loading process

We used a similar process for loading silver within the films, but we had to change the solvent of the first step, because silver nitrate is not soluble in ethanol. So we tried two different solvents to introduce the silver precursor in the films, water and a mixture water/ethanol (1/1 in volume). Starting from the previously aligned and organized lamellar phases, we followed the following process:

1) We immersed the film in 3.0 wt% $AgNO_3$ solution in water or in water/ethanol (1/1 in volume) for 5 minutes and then rinsed it with deionized water several times.

2) The films with loaded $AgNO_3$ were then immersed into 0.65 wt% $NaBH_4$ solution in water for 30 sec.

We repeated step 1) and 2) for N times (N is integrate from 0 to 15) to increase the concentration of Ag NPs.Figure IV. 7

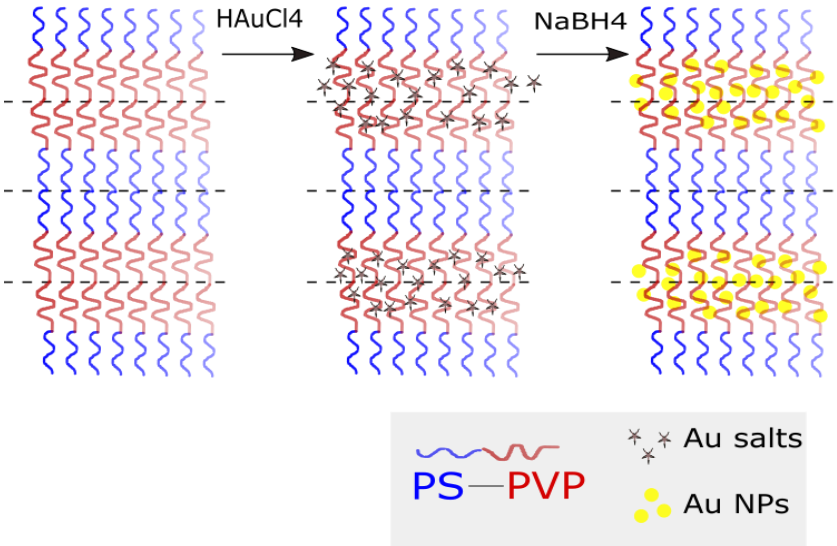

Figure IV. 7 Schematic illustration of the in-situ gold loading process. A film with organized lamellar phase was immersed into a 3 wt% $HAuCl_4$ ethanol solution, and Au salts bind with the amine functions in the PVP domains; then the film loaded with Au salt is immersed into a 0.65 wt% aqueous $NaBH_4$ solution to reduce the Au salts into Au NPs. We repeat the process for N times (N is integrate from 0 to 45) to increase the concentration of Au in the PVP domains.

Measurements

The surface topography of samples was imaged with optical microscopy (OLYMPUS BX51-P polarizing microscope) at room temperature.

The samples were studied by variable angle spectroscopic ellipsometry (VASE), the experimental details are in Chapter II.1. We use the configuration of UVISEL II with AIO=55º, 65º and 75º.

For side views of the samples, 1) the films on silicon wafer were broken into half manually and observed by SEM; 2) the films on Aclar substrates were prepared as described in the previous chapter 'Ultramicrotomy technique' in III.2.1. The films were embedding in epoxy and cut into 60nm thin sections using a diamond knife. The sections were floated on deionized water, picked up by TEM grids and observed in a TEM.

After all the measurements, samples were dissolved in toluene to disperse the resulting Au NPs, which were then observed by TEM and SAXS.

SAXS correction

The solutions with dissolved thin (ca. 300nm) and thick (ca. 700nm) films of various values of N (N=0, 5, 10, 20 and 30, N=0 stands for pure polymer used for treatment of the SAXS data) were placed in capillaries and were set directly in the beam in the SAXS sample chamber. The intensity is accumulated for 4h.

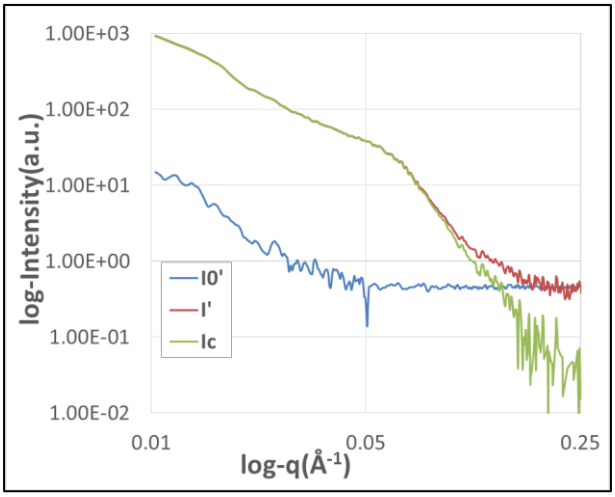

Figure IV. 8 An example SAXS data correction on thickness of film 300nm and value of N=20. I_0' stands for the polymer data without gold, I' stands for experiment after background correction, and I_c stands for the correction data from pure polymers.

The description of SAXS principle was given in Chapter II 2.2. Before analyzing the scattered intensities obtained after azimuthal integration of the detector 2D spectra, we corrected the data for background scattering following the method detailed in III.2.2. Based on Equation 3-9, the background B is obtained from the slope of a linear fitting of $I(q) \times q^4$ versus q^4 plot in the high q region.

The recorded scattering pattern after background correction then contains the scattering from three different objects in the suspensions: the neat gold nanoparticles, gold nanoparticles attached with polymers and single polymer chains. In the case of the film with N=0, the suspension contains only the polymer. We subtracted the intensity scattered by the suspension N=0 to all the other data, in order to remove most of the polymer signal. We then neglected the remaining polymer signal, and analyzed the SAXS data with a model of neat gold nanoparticles only, because they present a much larger electronic density than the solvated polymer chains. We also assumed that the particles are all spheres and that their size distribution can be described by a Gaussian function (Equation 4- 2). These are approximations, which should provide a simple access to the order of size of the formed nanoparticles. The analyzed data is

Equation 4- 1 $$I_c = I' - I_0'$$

where $I' = I_{sample} - B_{sample}$ is the background-corrected intensity for the sample N≠0 and $I_0' = I_{polym} - B_{polym}$ is the background-corrected intensity for the pure polymer solution N=0. For example, Figure IV. 8 shows the SAXS data after correction with background and pure polymer suspension. We can see that the polymer scattering is two orders of magnitude smaller that the sample scattering, which is dominated by the gold NPs, for the small wavevectors ($0.2<q<1nm^{-1}$). The polymer signal becomes significant at larger q ($q>1nm^{-1}$) when the nanoparticles scattering vanishes. All the SASX data were corrected to I_c.

IV.2.3 Results and Discussion

IV.2.3.1 Films with gold nanoparticles

As we discussed in the previous chapter, the P2VP blocks are preferred at the interface with the substrate while the PS blocks are preferred at the interface with air, which leads to an asymmetric configuration of the lamellar phase film (see Chapter I.3). If the final film thickness after annealing is not exactly equal to nd_0 or $(n+1/2)d_0$ (n is positive integrate and d_0 is the thickness of the bilayers), it is not possible to obtain a flat surface and holes or islands form on the free surface with step heights of d_0. Therefore, observation by optical microscopy or AFM of holes or islands formation on the top of the film is a good indication of a multilayered structure of parallel lamellae in the film[4].

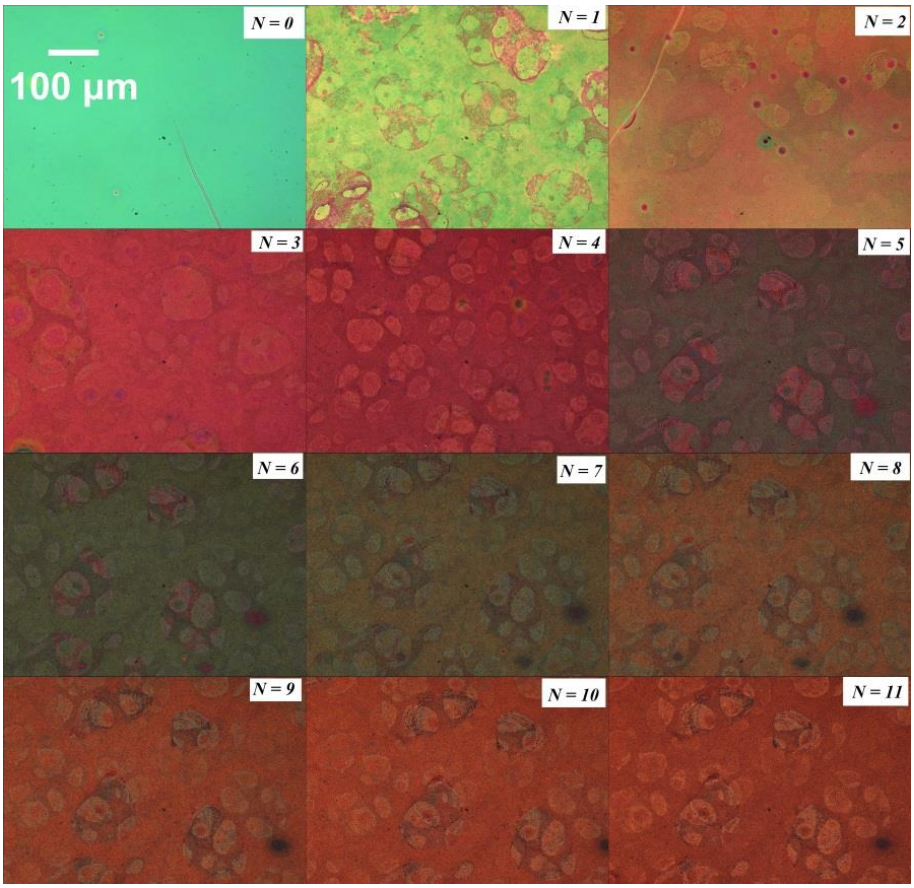

Figure IV. 9 Topography of films PS_{25K}-$P2VP_{25K}$ observed by optical microscope with an increasing number of impregnation cycles N. N=0 is the film after spin-coating and before annealing. The increasing purple color of the film is related to the localized surface plasmon resonance of the nucleated gold nanoparticles

Figure IV. 9 shows the film for N=0 after spin-coating and before annealing, and we can see a homogenous film deposited on silicon wafer. After thermal annealing, the film is impregnated with gold one time (Figure IV. 9 N=1), and the images show islands and holes formation on the topography of the film, which suggests that the film is the parallel lamellae morphology. One of the advantages of this infiltration procedure is that we can slowly increase, in a controlled way, the volume fraction of introduced nanoparticles, by repeating the double dipping process N times. As we can see on the Figure IV. 9, each cycle increases the purple color of the film, which is related to the localized surface plasmon resonance of the nucleated gold nanoparticles. When the cycle number increases, the film keeps the islands and holes on the free surface, which means that this gold loading process does not perturb significantly the structure of the films.

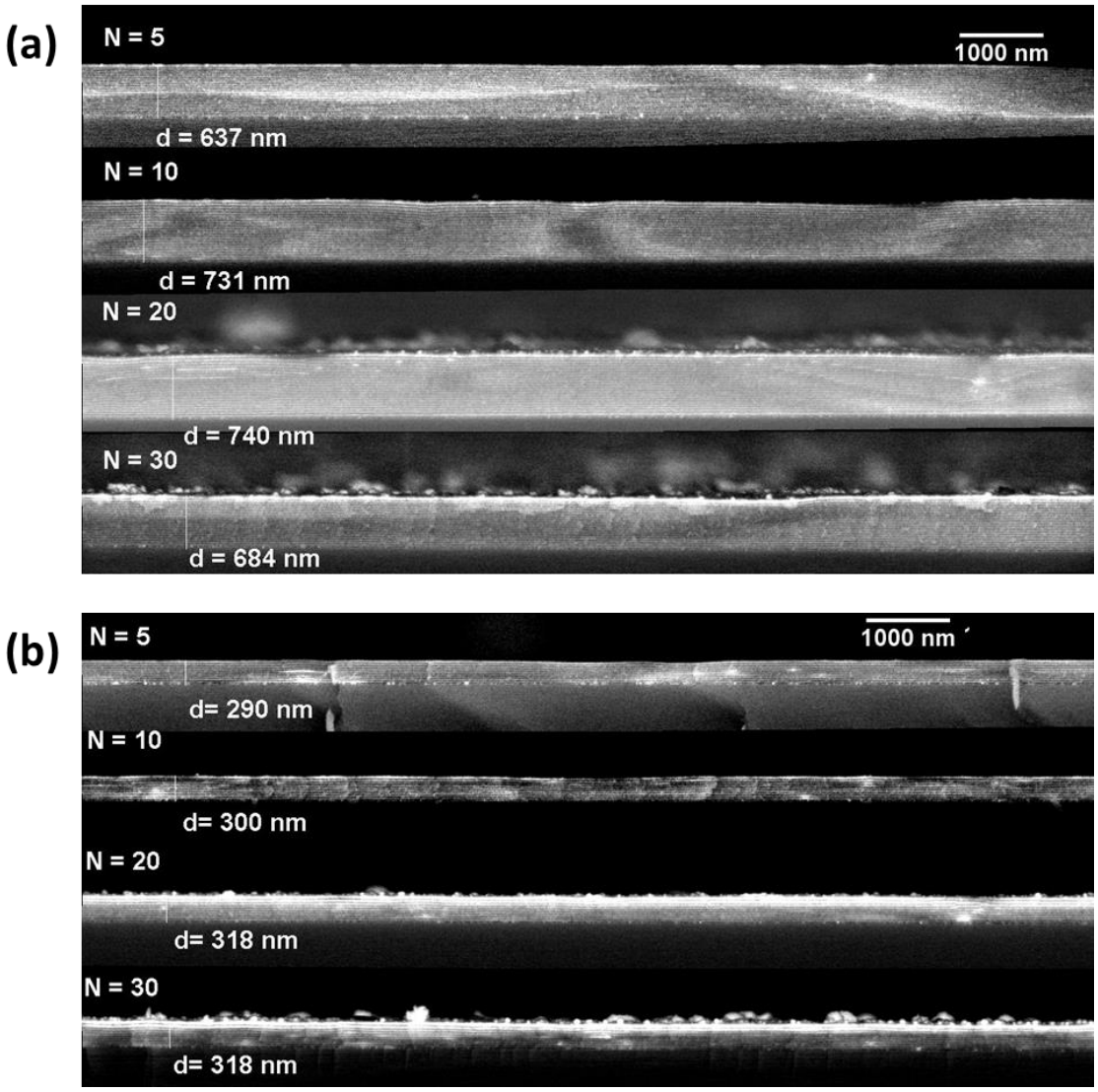

Figure IV. 10 Low-magnification SEM BSEI images of (a) thick (~700nm) and (b) thin (~300nm) films at different values of N.

After the gold nanoparticle formation at various values of N, the films were imagined in side-view SEM (under low magnification Figure IV. 10 and under high magnification Figure IV. 11). We studied films of two different thicknesses ca. 650nm and ca. 300nm. We can see that homogenous PS-*block*-P2VP films with lamellar structures are formed with a half-layer of the PVP block at the substrate interface and a half layer of the PS block at the air interface[5]. As we discussed in Chapter II, the light parts in the SEM micrographs are metallic rich domains and the dark parts are pure polymer domains, because the SEM images are formed by the signal of backscattered electrons. Under low magnification Figure IV. 10(a) and (b), we can see that the gold nanoparticles are well selectively introduced into the P2VP layers and that the nanocomposites present a well-aligned lamellar structure in large areas for both thick and thin films.

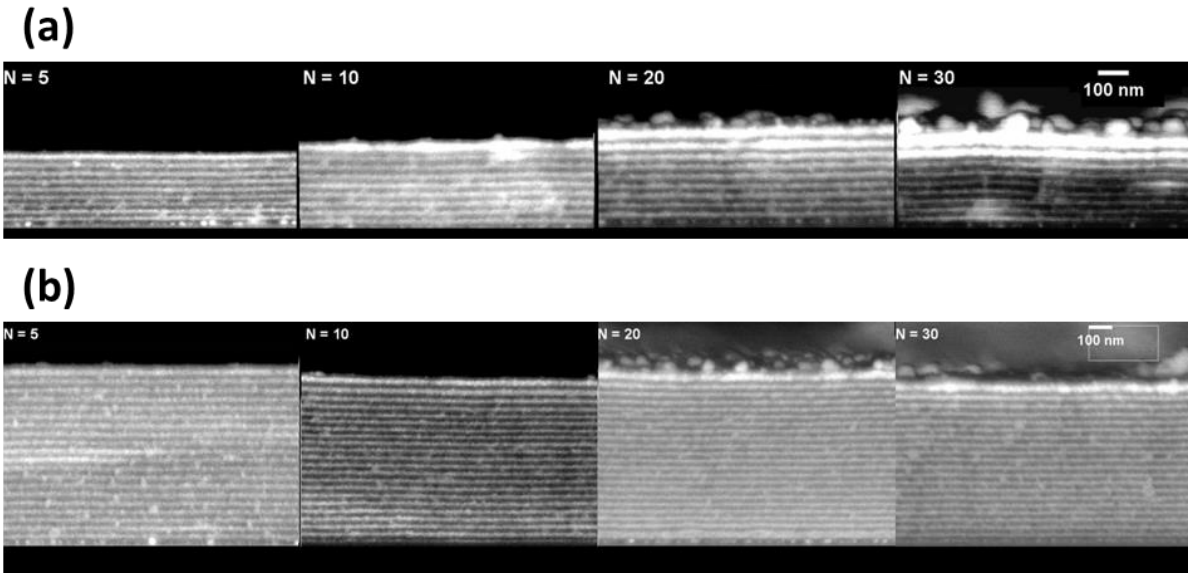

Figure IV. 11 High magnification SEM BSEI micrographs of the section of (a) thick (~700nm) and (b) thin (~300nm) films in different values of N.

From the high magnification images in Figure IV. 11, we can see that the gold nanoparticles are well selectively introduced both in thin and thick films, along the whole film depth. This indicates that the gold precursors $AuCl_4^-$ were reduced to gold nanoparticles in a homogeneous manner within the P2VP layers by aqueous solutions and that both the gold precursors $AuCl_4^-$ and the reducing agents $NaBH_4$ molecules penetrate in a homogeneous manner within the multilayer stack[5]. The reactants can pass through the stack using two possible mechanisms: (1) the reactants access the P2VP domains from the edges of the films (2) the reactants access from the top of the films by permeation through the different layers and/or through defects. There is no direct evidence of the possibility (1) and the homogeneity of the distribution of gold nanoparticles in each layer for the whole film, including on very large lateral scales, tends to favor rather the possibility (2). Indeed, if the access of reactant was coming from the sides of the film, we would expect to see some laterally graded composition of the layers due to the diffusion of gold from border to center. This is not seen even at low concentration of gold (N=5) or high concentration of gold (N=30). We then tend to consider that the reactants diffuse from the top, which means they have to permeate through the unfavorable PS[6] layers, sometimes in large numbers like in the examples of the Figure IV. 11(a) (almost 10 bilayers, $D=9.5d_0$) and (b) (almost 12 bilayers, $D=11.5d_0$). As displayed on the micrographs, the PS layers appear to have no obvious holes, defects or inhomogeneity, even on large scale images. We thus conclude that

the PS does not block the penetration of reactants. This is in agreement with the conclusion of others studies in the literature[6].

Concentrated gold nanoparticles in the top two layers are found to form on the surface of the films after 20 cycles of impregnation in both thin and thick films. We can thus propose that the reactants penetrate from the top of the films. From the homogeneity of film in the perpendicular direction to substrate, PS and P2VP domains did not block the penetration of reactants (ethanol swells P2VP and can well penetrate into films[6]).

A significant increase of gold in the top two layers, indicating that loading is going from the top and that PS layers tend to hinder it, was observed in some of the samples.

We can thus propose that the reactants in this loading process could be diffusing through all PS and PVP layers. More studies are going to be discussed related to this in the next chapter.

IV.2.3.2 Au nanoparticles in the films

We dissolved in toluene the final films containing loaded gold nanoparticles with different values of N in order to “kinetically” study the gold nanoparticles inside the layers. The obtained suspensions were then studied by SAXS and TEM (see Figure IV. 12).

TEM micrographs of the gold particles extracted from the films after different values of N were analyzed using the software ImageJ (see Figure IV. 13). We extracted the distribution of the diameters of the particles in the image and drew a histogram (with a step size bin=2nm, and a count of between 100 and 200 nanoparticles). The fits of these histograms with Gaussian distribution functions (Equation 4- 2) are displayed on the Figure IV. 14.

Equation 4- 2

$$f(2r,\mu,\sigma) = \frac{1}{\sqrt{2\pi}\sigma} e^{-\frac{(2r-\mu)^2}{2\sigma^2}}$$

Where r is the radius of the gold nanoparticles (2r is the diameter), μ is the mean diameter and the σ is the standard deviation.

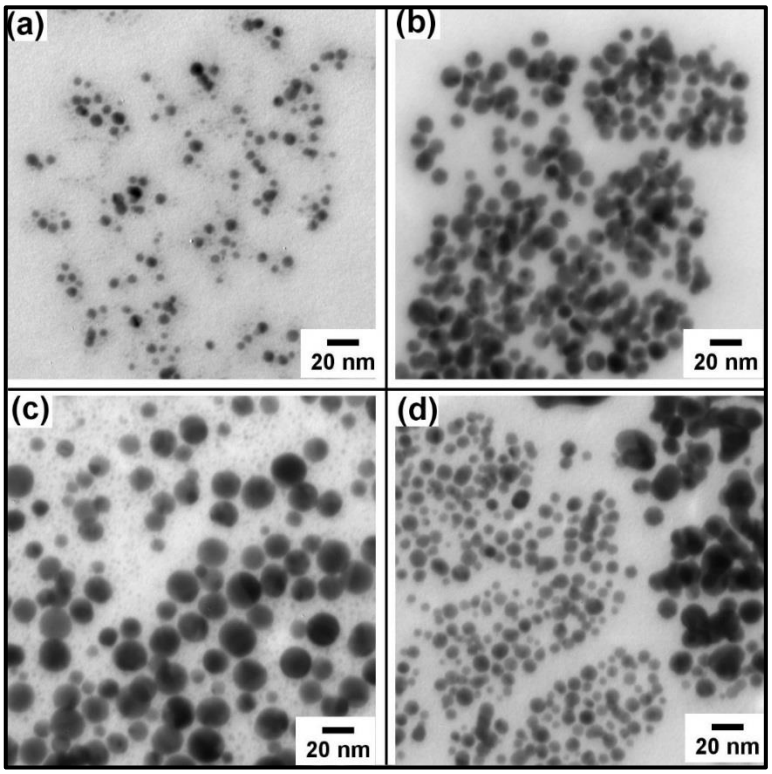

Figure IV. 12 TEM micrographs of the gold nanoparticles extracted from the gold loaded films with the values of (a) N=5 (b) N=10 (c) N=20 and (d) N=30.

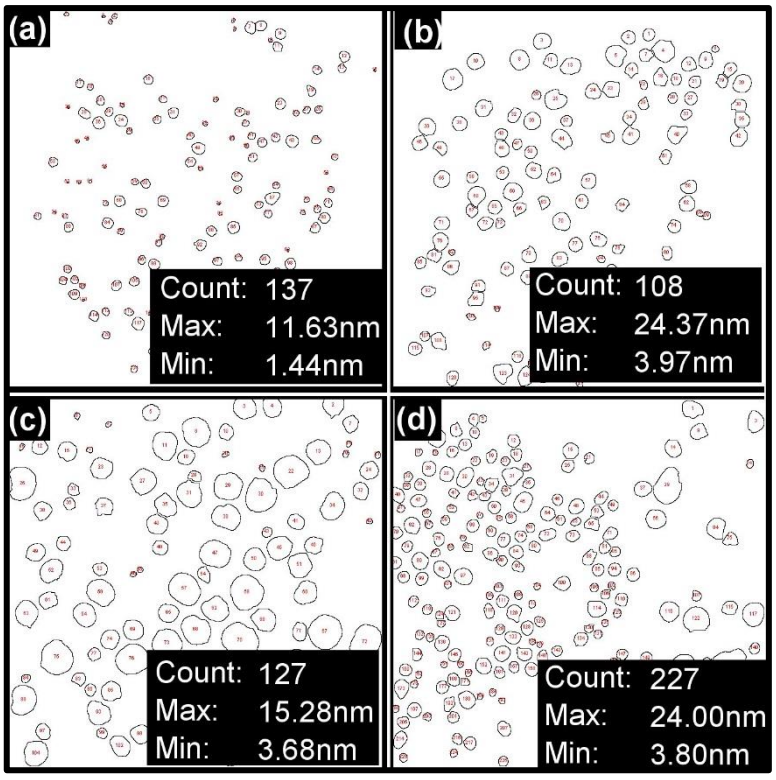

Figure IV. 13 ImageJ analyses of the micrographs of nanoparticles (Figure IV. 12) of (a) N=5, (b) N=10, (c) N=20 and (d) N=30. Insets indicate the count number of particles ≥100, and Max and Min stand for the maximum and minimum values of particles diameters.

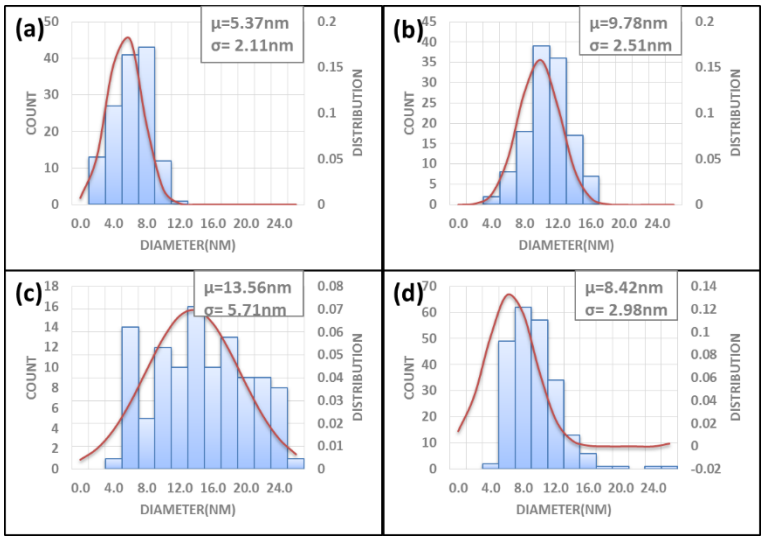

Figure IV. 14 Histograms the size distributions of the gold particles observed on TEM images . Bin=2nm. The count stands for the number of particles analyzed. Red lines are the fitted Gaussian distrubution with the mean radii μ and the standard deviations σ.

From the diameter distribution of gold nanoparticles, we can see that the diameter of the gold nanoparticles is well controlled and increases from 5 nm to 10 nm as N increases from 5 to 20. For N=30, we observe more inhomogeneous particles (see Figure IV. 12(d) and Figure IV. 13(d)), and we suspect that some of the bigger observed objects come from the uncontrolled gold deposition on the surface of the films (see irregular particles on surface from N=20 and N=30 in Figure IV. 11), making a proper analysis difficult. In conclusion, the nanoparticles size can be well controlled around 10 nm.

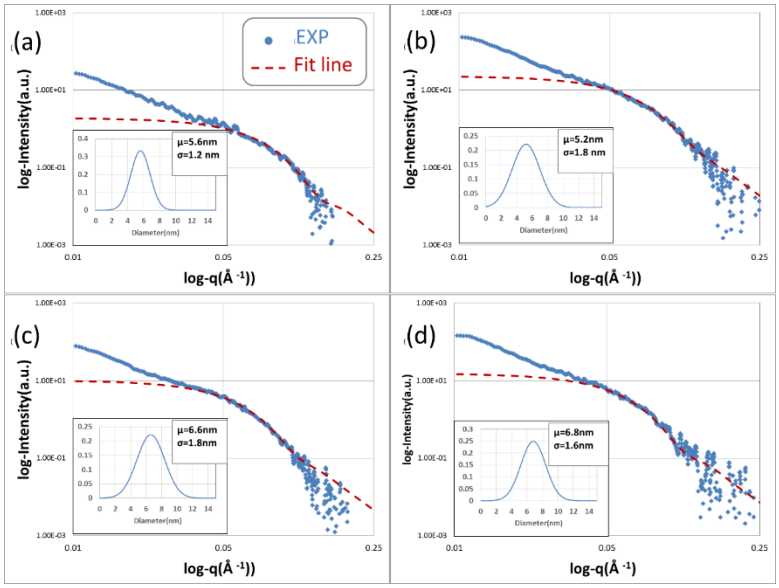

Figure IV. 15 Experimental SAXS data I_c (blue dots) and fitting results (red dash lines) for the particles suspensions extracted from thin (a)(c) and thick (b)(d) films, for the value of N=5 (a)(b)

and N=10 (c)(d). Insets are the diameter Gaussian distributions used in the fitting lines. μ and σ are the mean diameter and standard deviation of the distribution, respectively.

We complemented the TEM images analyses in order to access a more statistical measurement. For this, we analyzed the same nanoparticles suspensions by SAXS to obtain the global view of the size of the nanoparticles and their distributions. Figure IV. 15 and Figure IV. 16 show the experimental results and the fitting by a form factor of spheres modulated by a Gaussian distribution of sizes, for various values of N (5, 10, 20, 30) and two different film thicknesses ca. 300nm Figure IV. 11(b) and 700nm Figure IV. 11(a).

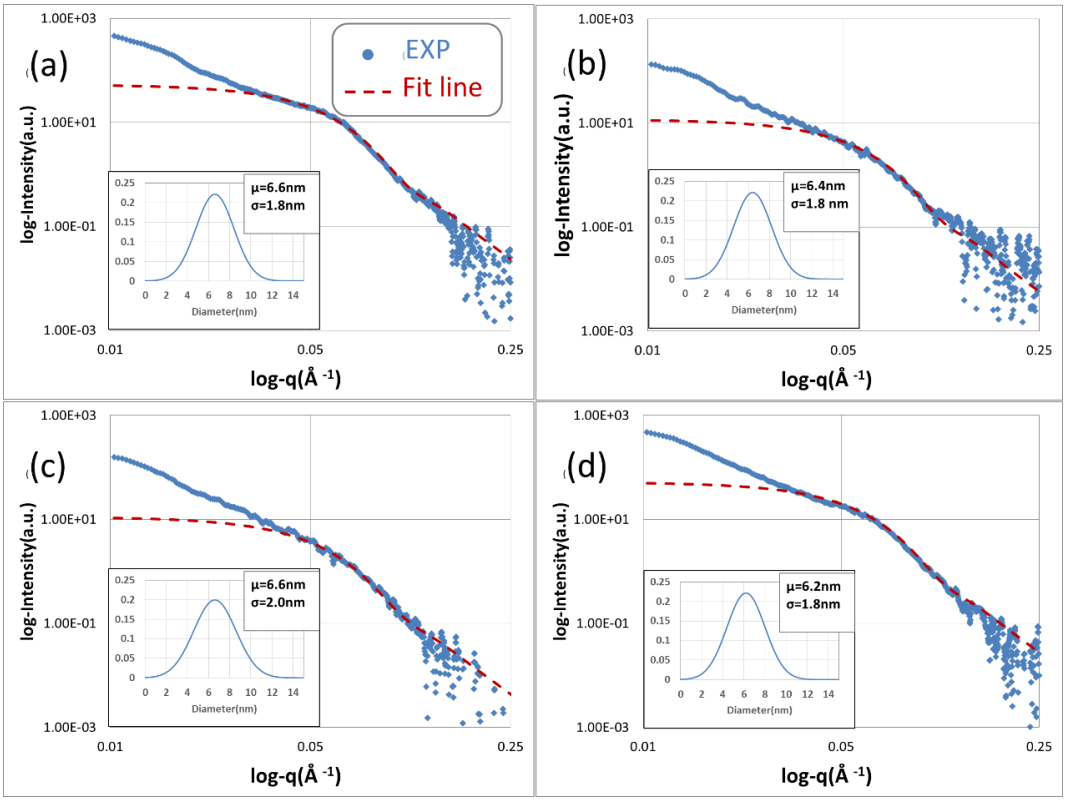

Figure IV. 16 Experimental SAXS data I_c (blue dots) and fitting results (red dash lines) for the particles suspensions extracted from thin(a)(c) and thick(b)(d) films in the value of N=20 (a)(b) and N=30 (c)(d). Insets are the diameter Gaussian distributions used in the fitting lines. μ and σ are the mean diameter and standard deviation of the distribution, respectively.

Comparing the nanoparticles in thin (a) and thick (b) (or (c) and (d)) films for various values of N, we can see that the thickness of the film has no influence on the nanoparticles sizes and distributions. When N=5 (Figure IV. 15(a) and (b)), the mean value of gold nanoparticles diameter μ=5.2nm and the standard deviation σ=1.4. When N=10 (Figure IV. 15(c) and (d)) μ=5.4nm and the standard deviation σ=2.4. When N=20 (Figure IV. 16 (a) and (b)), μ=6.8nm and the standard deviation σ=1.6. When

N=30 (Figure IV. 16(c) and (d)), μ=6.2nm and the standard deviation σ=1.8. As the value of N increases, the nanoparticles size increases but is limited to 7nm, which confirmed also by the results of TEM (see Figure IV. 12), showing that the nanoparticles size increases but is limited to 20nm.

From the plot of the gold nanoparticles size, measured by TEM and SAXS, as a function of the N value (see Figure IV. 17), we can see that the difference thicknesses (400nm difference) of the films have no influence in the size of gold nanoparticles under this gold loading method. The size of gold nanoparticle is increased as the impregnation process continues and could be confined to ca.8 nm, which is a good size to obtain a nanoparticle plasmon resonance. Even though both of the measurements give a large error bar, we can thus propose that gold nanoparticles size can be well controlled by the bilayer thickness in the film ~15nm. The process appears to be the following: the several first cycles of impregnation deposit small nanoparticles in the P2VP layers, which then act as seeds of gold and the following loading cycles are used for growing the gold NPs.

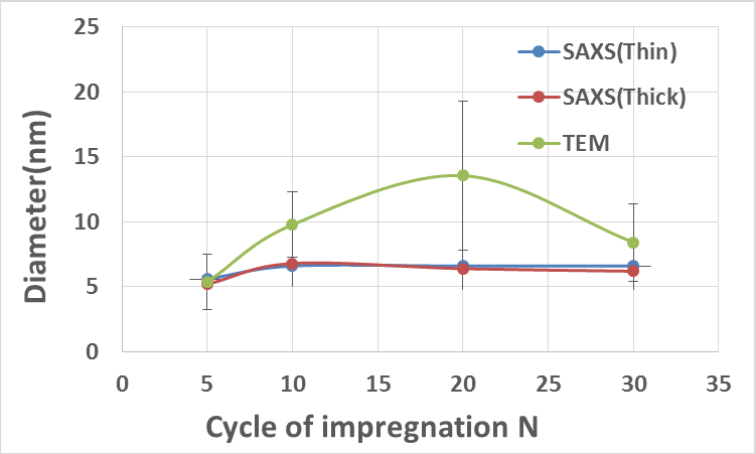

Figure IV. 17 Comparison of the mean nanoparticles diameter as a function of N, as obtained from TEM and SAXS.

IV.2.3.3 Optical properties of the Au loaded films

The films were “kinetically” measured by spectroscopic ellipsometry with the gradual increase of N. N=0 stands for the structured film without any gold particles inside. Considering the film and the silicon wafer as an effective medium, we consider the pseudo-epsilon <ε> (see Figure IV. 18) from the ellipsometry data. Note that <ε> is not the real permittivity of the films, but it gives a first idea to understand the film structures.

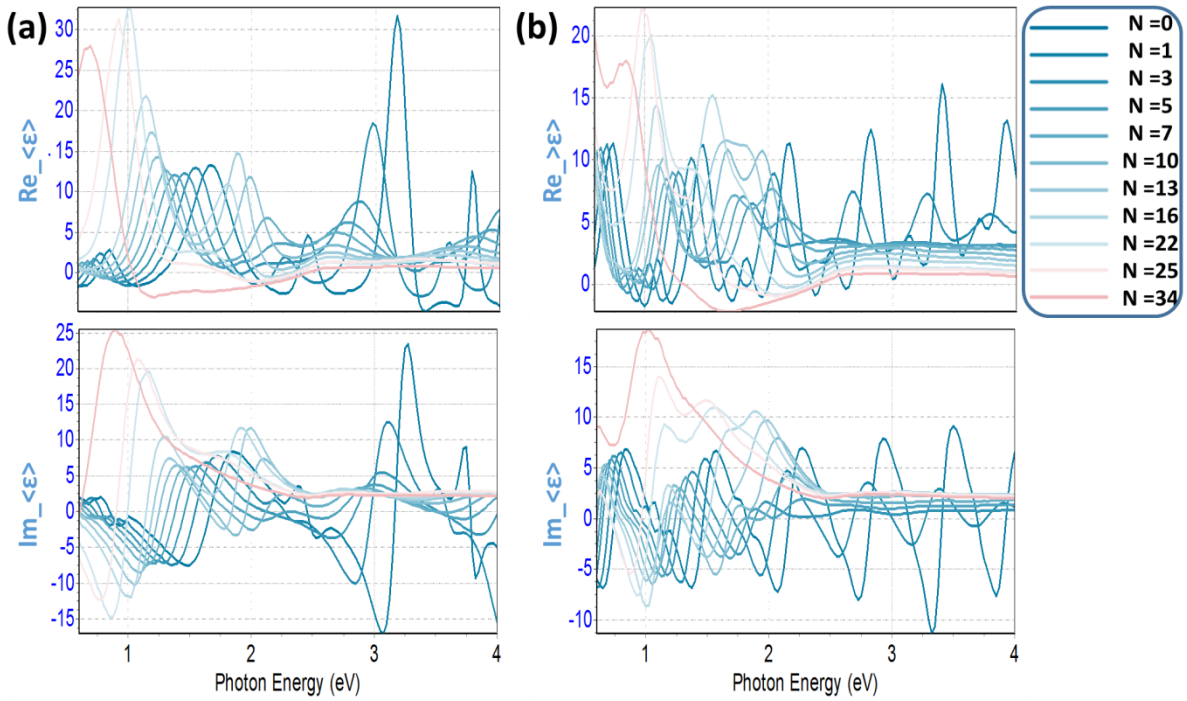

Figure IV. 18 Real (upper plots) and imaginary (lower plots) parts of <ε> measured at the angle of incidence 65º, as a function of the photon energy for gradually increasing values of the number N of gold loading cycles (from N=0 to 34). (a) shows the thin films, with thickness ca. 300 nm while (b) shows the thick films, with thickness ca.700nm.

As seen on the Figure IV. 18 the pseudo-permittivity <ε> measured on films without gold, N=0, present fringes regularly spaced in the photon energy scale and closer to one another for the thicker films, which we interpret as interference fringes related to the film thickness. We can see that as the value of N increases, the fringes present a red shift and the absorption becomes stronger in the energy range 0.9eV-2.01 eV (λ ranging from 616.8 nm to 1377 nm) which is caused by the gaining of gold in the films. The red shift can either be caused by an increase of thickness or by a change in the optical index due to the gaining of gold. From the Figure IV. 11, we can see that the thickness increase as N increases is limited. So the shift of the <ε> fringes is more probably caused by the increase of volume fraction of gold nanoparticles. It was shown earlier that a single layer of such disordered nanocomposite of nanoparticles and polymer presents a plasmon resonance due to the metallic nanoparticles[7] and that the resonance amplitude increases as the gold volume fraction in the nanocomposite increases. As the resonance deepens, the system will ultimately reach ε<0 in some frequency range: in fact, the Maxwell Garnett Effective Medium Approximation (MG-EMA), although not truthfully applicable for such high fractions, suggests this can occur for gold volume fractions beyond approximately 25%. An

accurate measurement of the volume fraction of gold nanoparticle is not easy, so we use this “kinetically” loading process to give another access to approach the volume fraction of accumulated gold. We are going to describe two types of measurements we performed for the measurement of the volume fraction of gold nanoparticles in IV.3.

IV.2.3.4 Films with silver nanoparticles

Structures

The structure of the silver films is little different from the gold ones due to the solvent used for the impregnation of the precursors. We cannot use the same reaction condition because silver nitrate is not soluble in ethanol. So we used 2 different solvent to dissolve the silver precursor, water and a mixture water/ethanol (1/1 in volume).

The well-aligned copolymer films were immersed in solutions of silver precursor either in water or in water/ethanol (1/1 in volume), whereas the solvent for gold precursor was ethanol.

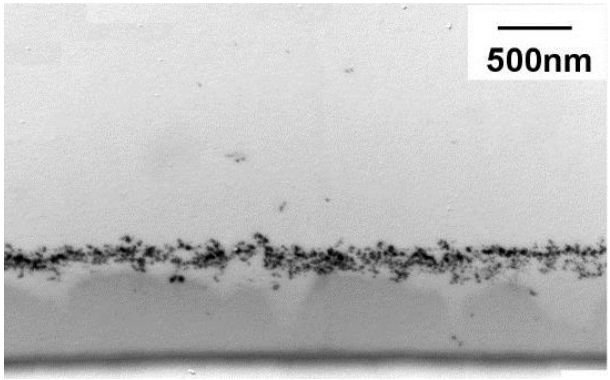

Figure IV. 19 Cross-section of lamellar structure loaded by silver nitrate in water solution with N=5.

From the side-section TEM image of ultramicrotomed films with N=5 cycles, Figure IV. 19, we can see that when the loading process is made in water the silver precursor cannot penetrate the films and accumulate at the surface.

From the side-section SEM micrographs (Figure IV. 20) of films with N=20 cycles, we can see that silver nanoparticles were selectively synthesized in the P2VP domains, and that the structure of well-aligned multilayers was preserved. In the case of water solvent (Figure IV. 20 (a)), the reactant could apparently not penetrate the whole film and the silver synthesis was limited to the top 4 bilayers. Confirming the observations made on the film on Aclar observed by TEM Figure IV. 19(a), we thus propose that the silver precursor dissolved in water cannot penetrate the bilayers and that the silver particles present in the top 4 layers resulted from the penetration of precursors through defects in the films. In the water/ethanol case, the silver precursors diffused in the whole films, which indicates that the reactant permeate through both the PS and the P2VP layers. So the solvent use for the impregnation of the metallic precursor is the

key factor for the diffusion and the metal loading. Note however, that the silver nanoparticles appear significantly more disordered and polydisperse than what we obtained with gold, which means that an optimization study would be necessary to obtain nicer films.

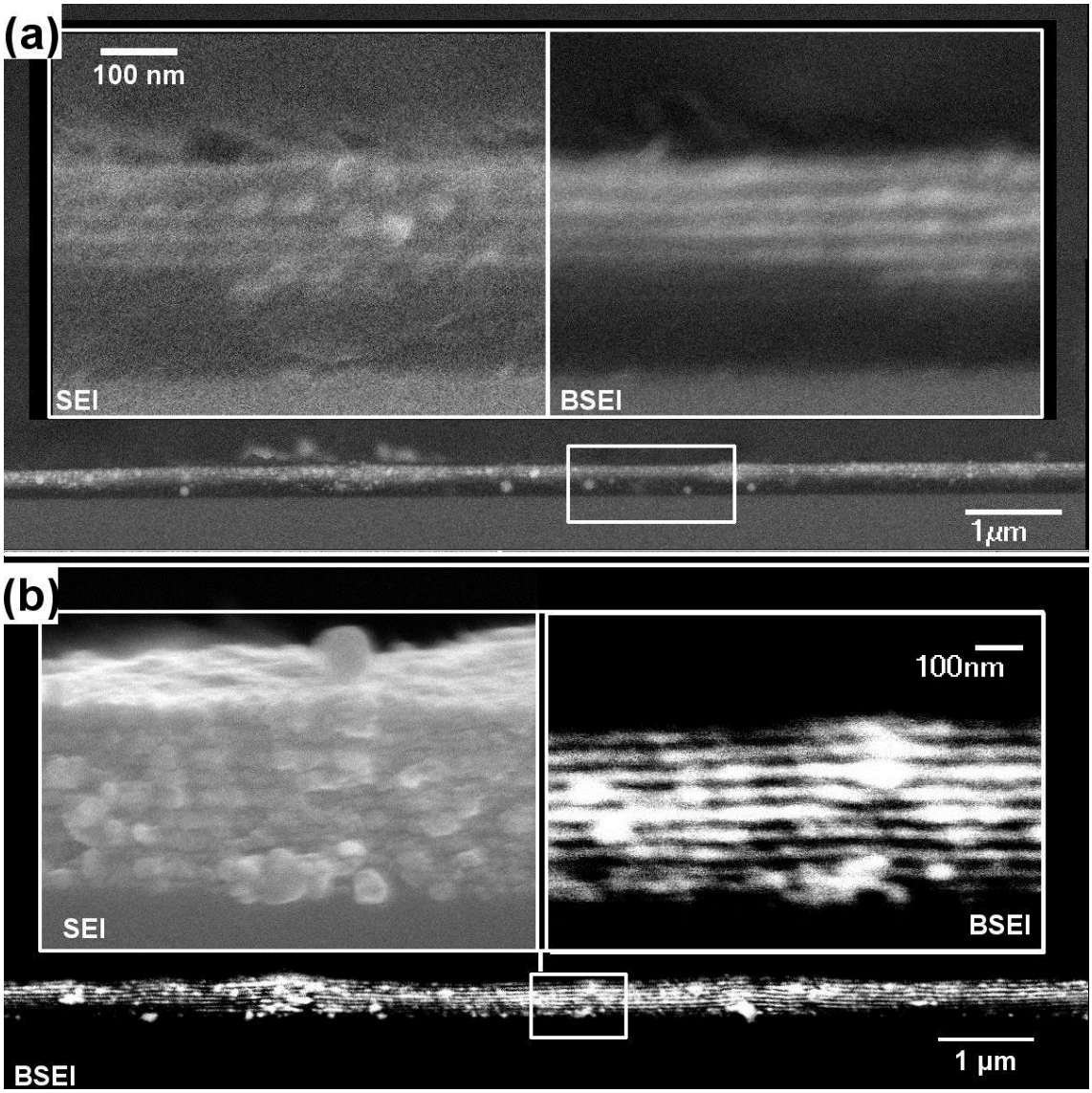

Figure IV. 20 High and low magnification SEM SEI and BSEI images of cross-sections of silver loaded films by precusor solution in (a) water and (b) water/ethanol(1/1 in volume) with N=20.

As we discussed in the previous section, the results of silver loading confirmed the conclusion that the reactants are diffusing though the bilayers from the top. Ethanol[2,6] plays an important role in this diffusion, because it is a selective solvent for P2VP. In a previous study[6] of the penetration of solvents in multilayers, it was shown that when the solvent is selective for one block, the other block will retard the diffusion of the solvent. In addition, we can see from the results evidenced on the Figure IV.

20(a), that even if the solvent can also pass through the defects in the stack, there is no efficient penetration if the solvent is not a good solvent for at least one of the blocks.

In order to get a selective loading and a good penetration of the precursor, we will keep ethanol as the solvent of the precursors in the further study (in particular for the reducing agent optimization study).

Optical responses of the Ag loaded films

The films were “kinetically” measured by spectroscopic ellipsometry, with the gradual increase of N. N=0 stands for the structured film without any particles inside. Considering the film and the silicon wafer as an effective medium, we plot the pseudo-epsilon <ε> (see Figure IV. 21). Note that <ε> is not the real permittivity of the films, but it gives a first idea to understand the film response.

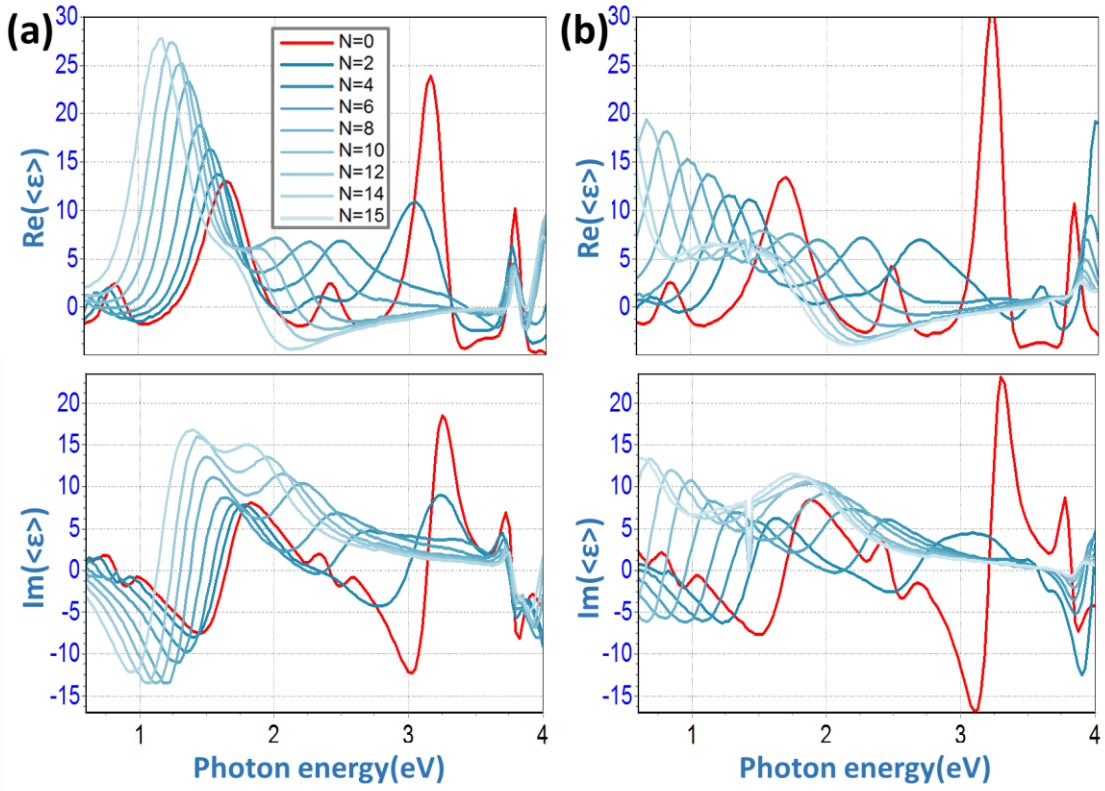

Figure IV. 21 Real (upper plots) and imaginary (lower plots) parts of pseudo permittivity <ε> as a function of photon energy for different values of silver loading cycles N (from 0 to 15). (a) shows the silver precursor loaded in water system while (b) shows the water/ethanol(1/1 in volume) system.

Starting from the film without silver, N=0, we observe fringes, which we interpret as interferences related to the film thickness. As the value of N increases (the

concentration of silver in the films increases), the curve fringes present a red shift and the absorption becomes stronger on the frequency range 1.8eV-2.73eV (λ ranging from 455nm to 690nm) which is likely caused by the plasmon resonance due to the gaining of silver in the films. Figure IV. 21(a) corresponding to the film with only 4 layers of nanocomposite (see Figure IV. 20(a)) shows gradual increase of the amplitude and the shift of the curve fringes, which indicates the gaining of silver nanoparticles either in quantity or size. Figure IV. 21(b) corresponding to the film with a multilayer of nanocomposite spreading over the whole film (see Figure IV. 20(b)) present an increase in the amplitude and shift of the curves, which is quite abrupt as soon as N=1, in the frequency region around 3eV, which indicates the gaining of silver nanoparticles. For N≥11, the curves do not evolve anymore, which probably indicates a saturation of the silver in the layers. The films produced with silver precursor loaded by two different solvent systems show significantly different signals. This may be caused by both the difference in size or dispersion of the silver particles in the two systems (smaller in water and larger in water/ethanol) and by the difference in the location of the silver NPs in the multilayers.

IV.3 Study of the volume fraction of Au Nps in the P2VP layers

IV.3.1 Introduction

As we explained (Chapter II), the multilayer templates is fabricated in a controlled way, and gold nanoparticles are selectively synthesized inside the P2VP layers (Chapter IV.2). The extraction of accurate optical responses from the spectroscopic ellipsometry data, which will come in Chapter VI, critically relies on the precise knowledge of the sample structure, and in particular, the gold loading. The quantities of gold nanoparticles in the layers are quite small, which is difficult to approach by conventional measurement methods. In this part, we are going to use a Quartz Crystal Microbalance as a measurement tool to ‘kinetically’ study the volume fraction of Au upon loading in the films.

IV.3.1.1 Introduction of QCM-D

Quartz Crystal Microbalance with Dissipation monitoring (QCM-D)[8] is an extremely sensitive sensor capable of measuring mass changes in the nanogram

range. It provides novel information regarding structural (viscoelastic) properties of adsorbed layers. In the past decade, a lot of QCM[5,9] studies were applied to solution-surface interface systems.

This technique is based on the piezoelectricity of quartz crystal. Piezoelectric effect (Figure IV. 22) is a property of certain materials. When a piezoelectric material is placed under mechanical stress, the center of the positive and negative charges in the material shifts, which results in an induced electric field. Reversely, when a piezoelectricity material is placed under an external electrical field, it causes either stretching or compression of the material.

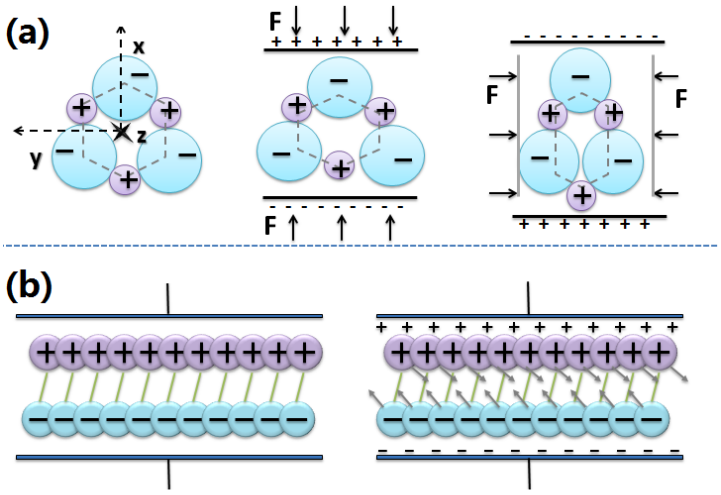

Figure IV. 22 Schematic illustration of piezoelectricity effect. (a) Piezoelectric effect: induced electric field caused by mechanical stress (b) reverse piezoelectric effect: compression or stretching caused by external electric field.

If we apply an alternating voltage to the quartz crystal, it will induce mechanical oscillations. When the frequency of the induced oscillations is equal to the natural frequency of the quartz crystal, we have a stable resonance. Any change of the crystal system will induce the change of the resonance frequency. Many studies[10–12] have studied the relation between the change of mass of the crystal system and the change of frequency in operation in vacuum, air, or liquid. The first method is established by Sauerbrey[13], in the year 1959. Then Nomura and Okuhara[10] modify the relation and relate the frequency and mass change in a liquid, where viscosity and dissipation effects can take place. The relation in Newtonian fluids was set up by Kanazawa and Gordon.

When one face of a quartz crystal is in contact with a liquid, its resonance frequency f and dissipation D values are affected by the liquid density and viscosity. If the coated film is a pure elastic mass bound tightly to the QCM surface, the Sauerbrey equation Equation 4- 3 is applicable[8]. In this study, the samples are rigid, distributed as an even film and sufficiently thin, which allows us to use the classical Sauerbrey relation. We are going to discuss the technique details in the following paragraph.

Equation 4- 3

$$\Delta f = -\frac{2\Delta m f^2}{A\sqrt{\mu\rho_q}}$$

Where

Δf is the measured resonant frequency decrease (Hz)

f is the intrinsic crystal frequency

Δm is the elastic mass change (g)

A is the electrode area (cm^2)

ρ_q is the density of quartz (2.65 g/cm^3)

μ is the crystal shear modulus (2.95 x 10^{11} dyn/cm^2)

IV.3.1.2 Rigid film

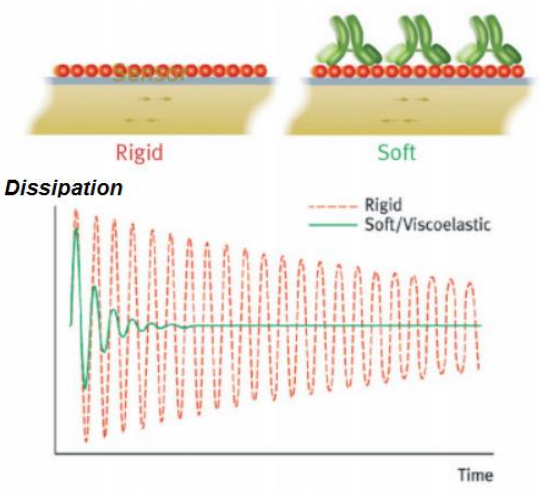

Figure IV. 23 Diagram illustrates the difference in the oscillation generated by a rigid (red) and soft (green) molecular layer on the sensor crystal (from biolinscientific company technical note).

In order to choose a good model to calculate the mass loading, we need to find out if the film is rigid or viscoelastic. Dissipation is the value for distinguishing the film

between rigid and viscoelastic. When the driving voltage to the sensor is switched off, the energy from the oscillating crystal dissipates and one can calculate:

Equation 4- 4 $$D = E_{lost}/(2\pi E_{stored})$$

where E_{lost} is the energy lost during one oscillation cycle and E_{stored} is the total energy stored in the oscillator. The Figure IV. 23 shows schematically the oscillations for a viscoelastic (green) and rigid (red) film when the driving voltage is turned off.

The amount of dissipation is extracted from the experimental measurements and will be displayed in the Experimental part. We will then see that the dissipation is not significant in our measurements and that the films can be considered as rigid.

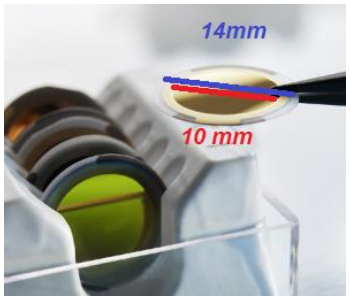

Figure IV. 24 Q-sensor with coated silica (from biolinscientific)

IV.3.2 Experimental

The quartz sensors (Q-sensor) coated by silicon dioxide (SiO_2) with diameter 14mm and thickness 0.3mm were used in all experiments. They have a fundamental frequency of 4.95MHz±50kHz and were purchased from Biolin Scientific. Note that the diameter of the bare surface is 10 mm because the films were coated in the center of sensor (See Figure IV. 24).

IV.3.2.1 Preparation of films on silicon wafer and quartz sensor

PS_{25k}-*block*-$P2VP_{25k}$ was dissolved in THF to yield 1.5 weight%, 3.0 weight% and 6.0 weight% solutions stirred overnight at room temperature to ensure complete dissolution. Two different substrates, silicon wafer and Q-sensor (Figure IV. 26), were used in the experiments for comparison purposes. 60µl of three different copolymer solutions were spin-coated on the substrates to form films of three different thicknesses (see Table IV. 3). The spin time is 30 seconds with the spin speed of 4000rpm, 3 seconds of acceleration time and deceleration time. Then a thermal annealing (180^o in vacuum for 15 hours) was used to generate well-defined and aligned lamellar structure.

After annealing, the block copolymer films are ready for the gold loading study. The synthesis of gold nanoparticles was carried out according to the chemical reduction method using hydrogen tetrachloroaurate(III) hydrate (dissolved in ethanol) as the precursor and sodium borohydride (dissolved in water with concentration of 0.65weight %) as the reducing agent. Here is the chemical reaction[14]:

$$Au(Cl)_4^- + Pyridine \longrightarrow Au(Pyridine)(Cl)_3 + Cl^-$$

$$4HAuCl_4 + 3NaBH_4 \longrightarrow 4Au + 6H_2 + 3NaCl + 3BCl_3 + 4HCl$$

The homogeneity and roughness of the samples were examined by Atomic Force Microscope (AFM) imaging carried out under ambient conditions. The volume fraction of gold nanoparticles in the PVP layer of the samples on silicon wafer was investigated by spectroscopic ellipsometry after different numbers of gold loading cycles, and the samples on Q-sensor were subjected to the gold loading cycles within the QCM device, as will be explained below.

Table IV. 3 samples used in the experiments

Wafer	Concentration of polymer solution	Thickness of the film
Silicon wafer	1.5 weight %	59.4 nm
	3.0 weight %	100.7 nm
	6.0 weight %	272.3 nm
Q-sensor	1.5 weight %	52.0 nm
	3.0 weight %	120.6 nm

IV.3.2.2 Spectroscopic Ellipsometry measurements

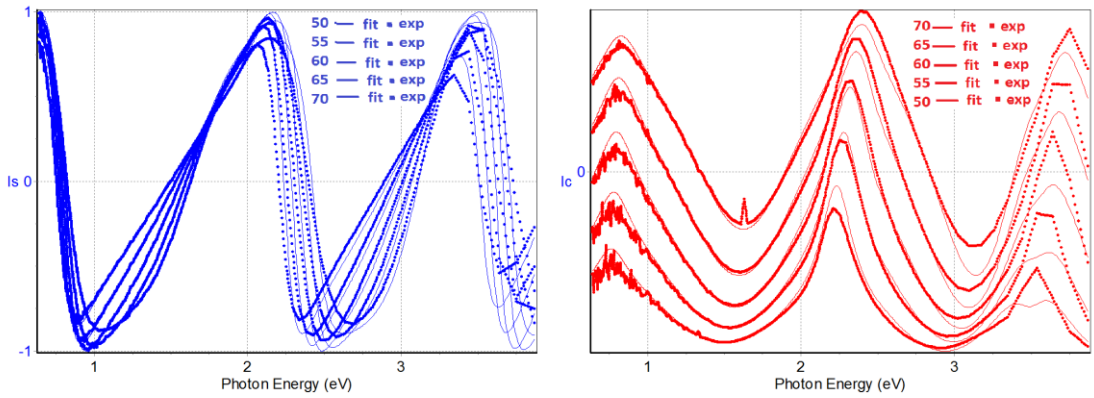

Figure IV. 25 Primary VASE data of the film with 5 cycles of gold loading process (N=5). Left I_s as function of photon energy in 5 angles of incidence. Right I_c as function of photon energy in 5 angles of incidence.

The films on silicon wafers are (i) immersed into 3.0weight% $HAuCl_4$-ethanol for 5 min and then rinsed with deionized water several times (ii) then dipped into 0.65weight% $NaBH_4$-H_2O solution for 30sec to reduce the precursors to Au nanoparticles, (iii) then measured by spectroscopic ellipsometry (SE). We repeat the cycle (i)(ii)(iii) for N times

(N is between 1 and 10). The “kinetic” VASE information was thus obtained by recording the full spectra in-between each gold loading cycle (step (i) and (ii)).

Five values of the incidence angle AOI=50º, 55º, 60º, 65º and 70º were used and analyzed simultaneously. The VASE data, for one studied film at N=5, are shown on the Figure IV. 25, where the ellipsometric parameters I_s and I_c are plotted for angles of incidence AOI=50º, 55º, 60º, 65º and 70º. The analysis of such data will be given in the following paragraph IV.3.3.

IV.3.2.3 QCM-D measurements

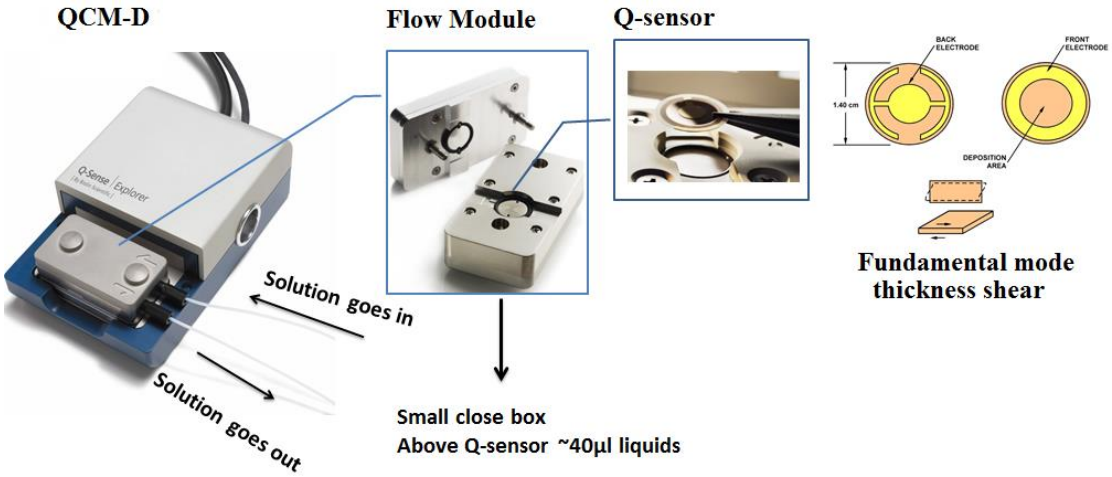

Figure IV. 26 Illustration of QCM-D and Q-sensor. The Q-sensors we used consists of a quartz disk with metallic electrodes on both sides. Once alternating voltage is applied, the crystal vibrates in its fundamental thickness shear mode.

QCM-D measurements were performed with the Q-SENSE EXPLORER system equipped with flow module from Biolin Scientific. The original data extracted from the measurements are the different frequency harmonics and the dissipation. Changes in the resonance frequency are related to changes in the attached mass, and the dissipation, D, is related to frictional (viscous) losses in the adsorbed layer or at the interface between the layer and the liquid. The measurements were performed in a liquid environment at a temperature of 25℃ in exchange mode (the ambient solvent of sample can be changed during the experiment by a tube). The resonance frequency and the dissipation were measured at several harmonics simultaneously. Liquid was delivered with the help of a peristaltic pump (ISM935C from Ismatec, Switzerland) with a flow rate of 0.2 ml/min. The experiments are completed in 2 steps (i) A freshly dried

Q-sensor covered with a lamellar copolymer film was installed in the QCM cell (see Figure IV. 26). The measurement started in water to obtain a stable baseline.

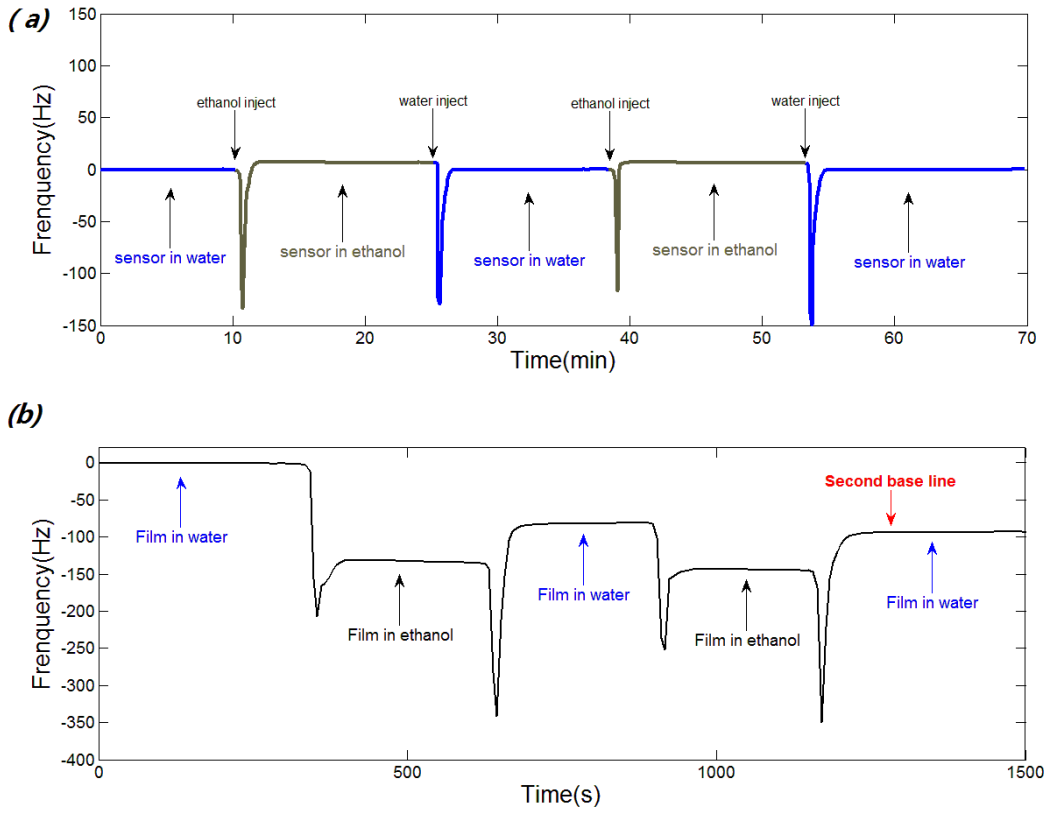

Figure IV. 27 Study of solvent exchange influence on the resonance frequency. (a) Primary QCM measurements on bared sensor, and (b) on sensor with thin film without gold. For the bare sensor, the frequency in water always came back to original position. For the sensor with thin film, the frequency in water has a slight change for the first solvent exchange and is stable afterwards.

A first experiment showed that the exchange of solvent (from water to ethanol or ethanol to water) has no influence on a bare wafer: the resonance frequency is slightly modified, in a reversible manner (Figure IV. 27 (a)). In the case of the copolymer films, changing the ambient solvent from water to ethanol induces a change of resonance frequency, which we interpret as due to an increased swelling of the PVP domains in ethanol, which is not completely reversible when water and ethanol are exchanged again. We suppose that constraints in the collapsed conformation of the PVP chains in water relax irreversibly in ethanol. Once the sample underwent twice the exchange of solvent, the frequency changes become reversible. Hence, the frequency of the sensor in the third solvent change of water could be treated as the proper (“second”)

baseline for the measurement, which then involves introduction of gold (see Figure IV. 27(b)).

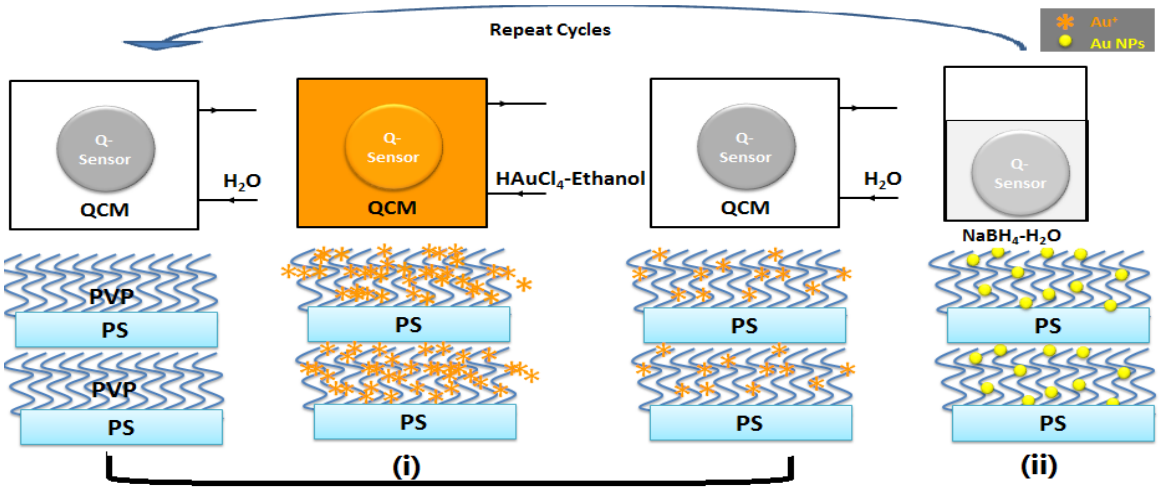

Figure IV. 28 Schematic illustration of full process of QCM measurement including inside QCM device (i) and outside QCM device (ii). Step (i) Measurement inside the QCM-D cell. The measurement starts in water, then HAuCl4-ethanol is flushed, then water is flushed to rinse the Au^{3+} which is not bound with pyridine in the PVP layers. Step (ii) Reducing step outside the QCM-D cell. The sensor is immersed in the reducing agent solution to obtain gold nanoparticles. Repeat step (i)(ii) for N times.

After stabilization of the second baseline, we can consider that the solvent effects are reversible, and we can start the gold loading study. A certain concentration of $HAuCl_4$ in ethanol (1.0 weight%, 3.0 weight% and 6.0weight %) was flushed inside the cell and kept in contact with the film for 20mins. Then water was flushed for 10mins and kept for 20mins. Then the film-bearing sensor was taken out of the QCM and exposed to a reducing solution (0.65 weight% $NaBH_4$ in H_2O) outside the QCM-D device in order to synthesis the gold nanoparticles. The reason for not performing the reduction step inside the device is that the reaction between $HAuCl_4$ and $NaBH_4$ produce H_2 bubbles, which dramatically changes the surrounding of sensor and the frequency of resonance and could not be handled reproducibly. We then repeated these steps for N times (N≤10) to increase the gold loading. In fact, the QCM-D measurements are related to the mass increase in gold salt and not in gold nanoparticles. In order to access the final gold quantity, we assume that all the gold salt deposited in the PVP layers is then reduced to gold nanoparticles by $NaBH_4$. After the reduction step, the film-bearing Q-sensor is introduced again in the device to proceed with more cycles of gold loading.

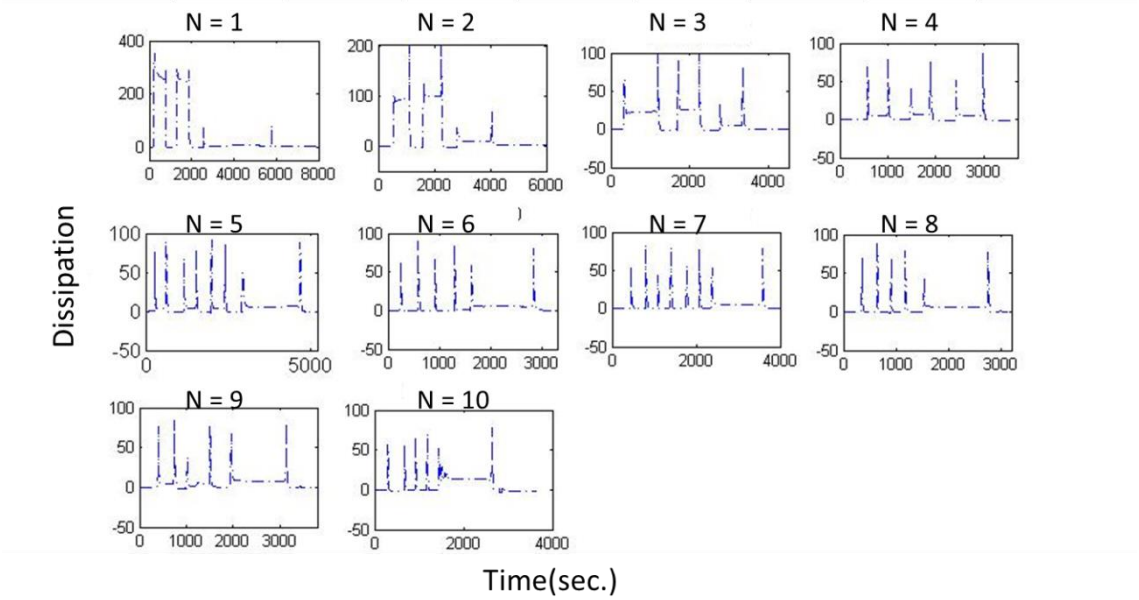

Figure IV. 29 Example of the dissipations measured for films at various N until N=10.

The Figure IV. 29 displays a representative example of measured dissipation as a function of the time during the experiment, at various impregnation cycle numbers N. We can see that the dissipation significantly departs from zero only during the first two flushes with solvent exchanges, and before gold salt is introduced and frequency changes are actually determined. We thus concluded that there is no significant dissipation and that the films can be considered as rigid. Moreover, the films are sufficiently thin (thickness of quartz crystal is 0.3mm >> thickness of films ca. 100 nm), and we can finally use the Sauerbrey relation to calculate the mass changes in the PVP layers.

The determination of the gold nanoparticles mass was carried out using the Sauerbrey model[2]. The change of frequency of the oscillating sensor is proportional to the change in the adsorbed mass by the relation:

Equation 4- 5
$$\frac{\Delta f}{n} = -\frac{2f^2}{A\sqrt{\mu\rho_q}}\Delta m$$

Equation 4- 6
$$\Delta m = -C\frac{\Delta f}{n}$$

Where,

Δf measured resonant frequency decrease (Hz)

f the intrinsic crystal frequency (4.95MHz±50kHz)

Δm the elastic mass change (g)

A the electrode area (d=10mm, A=0.785cm^2)

ρ_q the density of quartz (2.65 g/cm^3)

μ shear modulus (AT-cut crystal 2.95 x 10^{11} dyn/cm^2)

C the mass sensitivity constant (in this case C is 13.8g/Hz)

Here, the gained mass noted as Δm_{Au}, is consisting of Au and Cl in the molar ratio 1:3, based on the reaction between $HAuCl_4$ and pyridine[14]. Table IV. 4 shows the basic information of the films. The mass change of Au can then be calculated by the change of frequency, and the volume fraction of Au in the composite layers can be obtained by the linear Equation 4- 7 and Equation 4- 8.

Equation 4- 7 $$Volume\ fraction_{Au} = \frac{2*\Delta m_{Au}}{A*d*\rho_{Au}} \text{ where } \Delta m_{Au} = \frac{M_{Au}}{M_{Au}+3M_{Cl}}\Delta m$$

Equation 4- 8 $$Volume\ fraction_{Au} = 6.374 * 10^{-5} * \Delta f$$

Table IV. 4 Parameters used in the calculations for the film with 160nm thickness

Parameters of foreign weight		Parameter of Film	
Molecular Mass of Au (M_{Au})	196.97	Thickness	160nm
Molecular Mass of Cl (M_{Cl})	35.45	Area	0.785 cm^2
Mass fraction of Au in layer	64.94%	Volume of film	1.25663x10^{-5}cm^3
Density of gold	19.9 g/cm^3	Volume of PVP	0.62319x10^{-5}cm^3

IV.3.3 Results

The results of the thin film with 58nm thickness are not stable, this may be caused by the unevenly distribution of polymer on wafers due to the super too small thickness (2-3 bilayers). So in this section, we are going to present the results of film with thickness around 160nm.

IV.3.3.1 Results of ellipsometry measurements

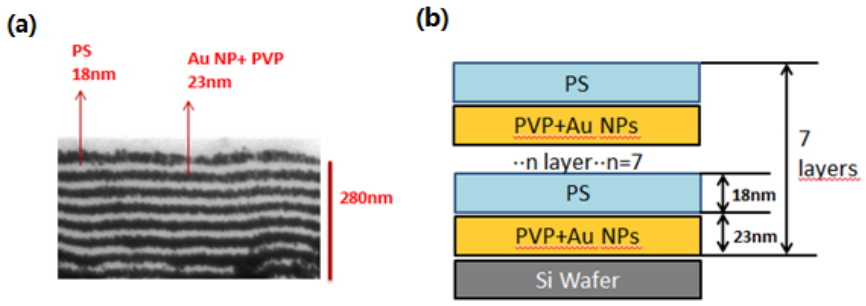

Figure IV. 30 The ellipsometric model used (b) is built based on the information from the thin-section TEM image (a). PS stands for layer of polystyrene and PVP+Au NPs stands for layer of nanocomposite composed of gold nanoparticles and poly(2-vinylpyridine).

The data were analyzed using the DeltaPsi2 software from Horiba Scientific. SE data measured on the bare silicon substrate were analyzed using the Si and SiO_2 tabulated dielectric functions and yielded a thickness value (2.0 nm) for the native silica layer on the surface, which was fixed in the further analysis. The model (Figure IV. 30 (b)) we used is a multilayer stack using the information on layers number and thicknesses from the thin section TEM images (with an example displayed in the Figure IV. 30(a)). We assume that the layers of gold-polymer nanocomposite can be described as effective media by the Maxwell-Garnett formula (see Chapter II.1, Equation 2- 9) and the volume fraction f of Au nanoparticles is the only unknown parameter in the model. The fitting procedure was carried out both on the whole measurement wavelength range (320nm-1934nm) and also restricted to the UV range (320nm-400nm).

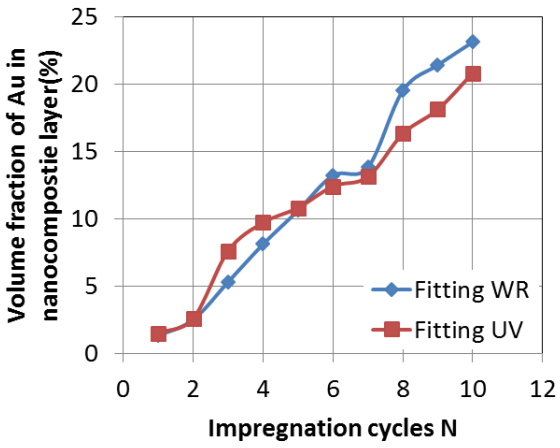

Figure IV. 31 Volume fraction of Au nanoparticles in the composite layers as function of the impregnation cycles number.

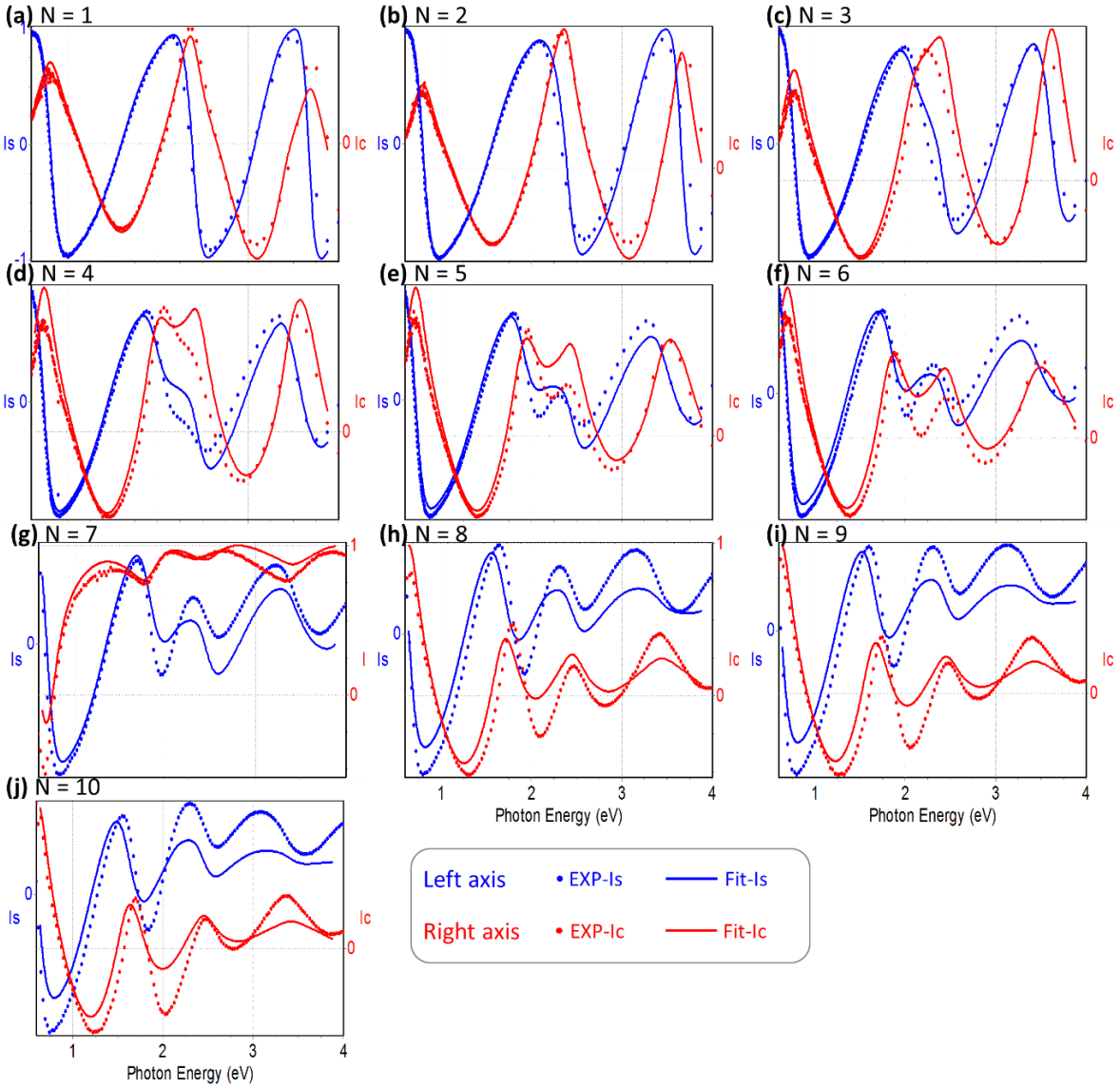

Figure IV. 32 (a)-(j) are the plots of ellipsometry data Is and Ic as a function of the photon energy for different values of the number N of cycles in the impregnation process. They are examples at the AOI=65° of the SE data and fitting results from model (Figure IV. 30(b)). EXP stands for experimental data and Fit stands for fitting lines.

As the Figure IV. 32(a)-(j) shows, the fitting lines agree well with the VASE data for N smaller than N=4 but are not in good agreement with the experimental data after N=5. In particular, as the value of N increase, the fits do not adjust well the plasmon resonance domain (between 1.5 and 3eV). This is most likely due to the fact that even at low concentration of NPs, some coupling exists in such disordered nanocomposites, as was shown earlier[15]. An improved effective medium model can then be used. But it did not improve the fitting significantly, and the extracted Au volume fraction was found very similar. Another way of avoiding this problem is to fit only on the UV range, where the absorption of gold is related to the interband transition and does not relate much

to the shape and structure of the gold domains. Also here, we found very similar value of gold volume fraction.

On the I_s and I_c plots of the Figure IV. 32, we observe that the initial large interference fringes for N=0 are attenuated as the film is loaded with Au particles (increasing N), which is due to the absorption associated with the plasmon resonance of the gold nanoparticles. Figure IV. 31 shows the volume fraction of gold nanoparticles extracted from SE data using the fits presented above. In order to confirm the data, the results from another technique QCM-D are compared in the following.

IV.3.3.2 Results of QCM-D

Using the QCM-D procedure described in IV.3.2, kinetic measurements were performed in order to determine the mechanism of gold impregnation, in particular to determine the mass loading and volume fraction of particles introduced by each cycle of impregnation.

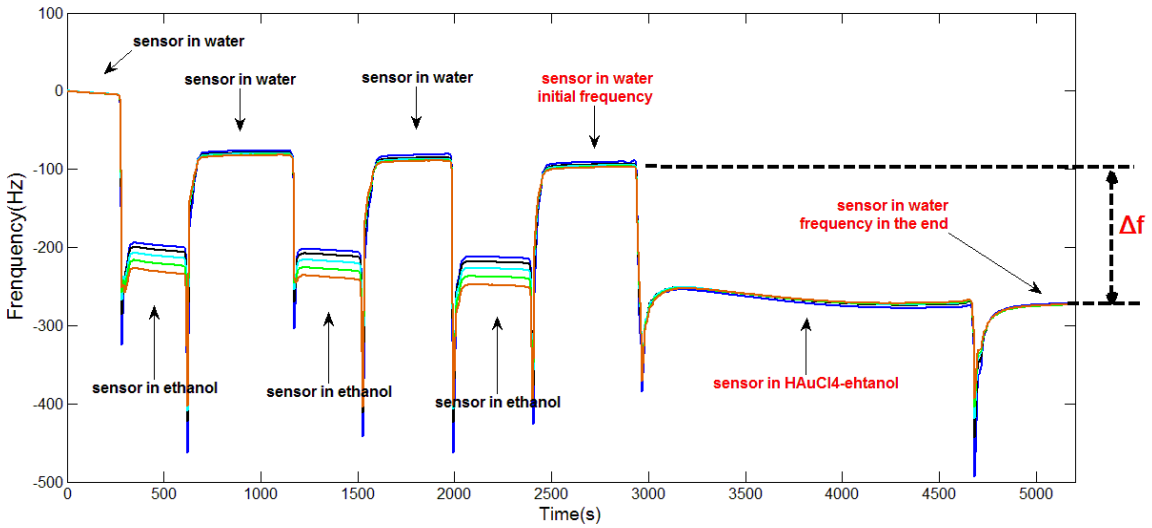

Figure IV. 33 Primary QCM measurement for N=5, the solution $HAuCl_4$-ethanol is 3.0 weight%, expressed as the relative frequency for the fifth overtone vs time. The measurement starts in water. Solvent exchange between water and ethanol was performed twice to eliminate the frequency changes due to the PVP swelling. Then the frequency in water is the initial frequency. Gold salt in ethanol is flushed for 20min and then rinsed by water until the measured frequency reached stabilization. Δf stands for the change of frequency caused by the change of mass.

Figure IV. 33 shows an example of the primary QCM measurement (N=5 in 3.0 weight% solution of $HAuCl_4$ in ethanol). The change of frequency Δf, is measured

between the sensor in water after two solvent exchanges and the sensor in water after the gold salt loading.

The measurement was started in water, a considerable decrease of frequency was observed after the first manipulation of solvent exchange, which is attributed to the swelling of the PVP layers in ethanol. After the second manipulation of solvent change, the relative frequency always came back to its original value, which could be treated as the initial frequency. When the solution $HAuCl_4$-ethanol of 3.0weight% concentration was pumped and in contact with the film for 20mins, a significant decrease in the relative frequency was observed, which confirmed an efficient deposition of gold salt in the film. After being rinsed by water, the film stayed in water and the final frequency was read. The difference between this final frequency and the original one is caused by the mass of gold salt loading.

As we discussed in 4.3.2 the gained mass consists of Au and Cl in the ratio 1:3 based on the reaction between $HAuCl_4$ and pyridine. Based on the Equation 4- 6- Equation 4- 8, the change of mass is calculated for the different samples (see Figure IV. 34).

Figure IV. 34(a) shows the cumulative gold mass gain in the film (thickness 160nm) as function of the number of impregnation cycles in three different concentrations of gold salt in ethanol solution (1.0 weight%, 3.0 weight%, and 6.0 weight %) with a flow rate of 0.2 ml/min. The dash lines are the differential gold gains for each cycle of impregnation process. The first impregnation cycles lead to the adsorption of large quantities of gold, and the differential gained mass of gold then decreases as the number of impregnation cycle increases. After 5 cycles, the differential gain of gold mass remains constant. We can recall the results of IV.2.3.2, showing that the diameter of the gold NPs is increasing as the number of impregnation cycles increases (Figure IV. 17). We can then suggest that the PVP layers get loaded with many gold seeds during the first impregnation cycles, and then the seeds grow bigger during the later impregnation process. We also studied the influence of the $HAuCl_4$ concentration in the ethanol solution used for the impregnation. From the results, during the first cycle of the process, the gold gain values are 6.97µg, 6.97µg and 6.68µg for the 1.0, 3.0, 6.0 weight% solutions, respectively, and the differential gain of gold remain almost similar afterwards. In conclusion, the gold loading is independent of the concentration

of the Au salt solution for the studied range, and the key factor for the gold loading seems to be the capture capacity of the PVP layers.

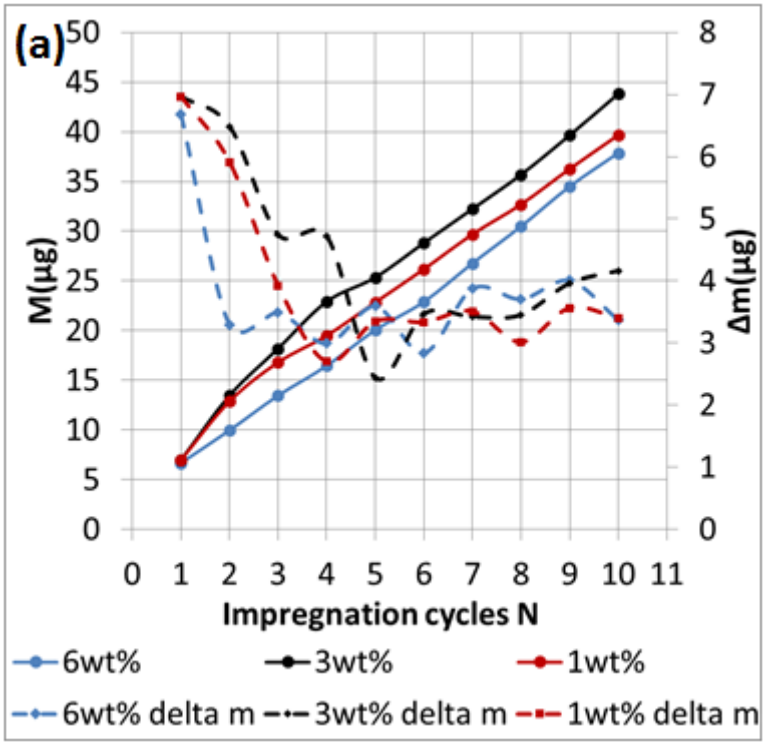

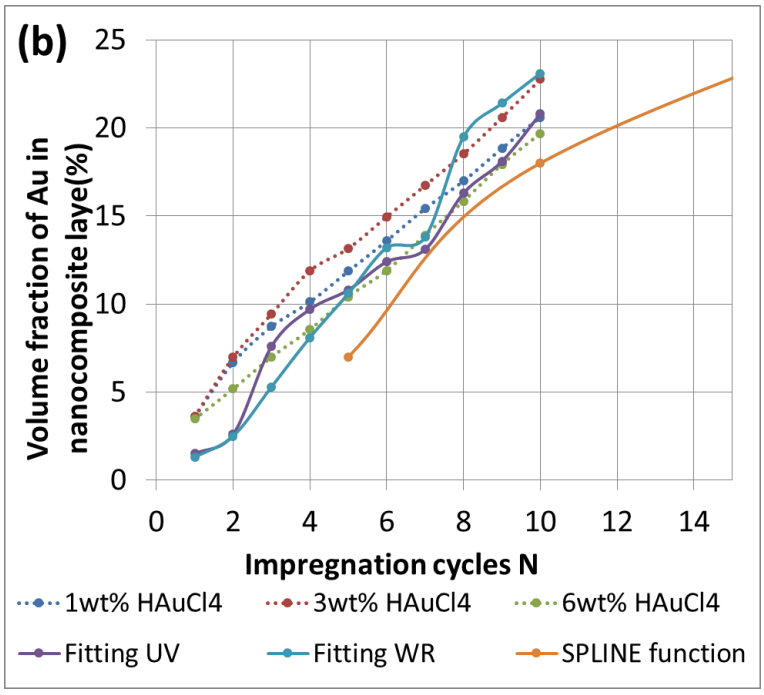

Figure IV. 34 (a) is the plot of the cumulative gold mass gaining (left axis) and differential gold mass gaining for each impregnation cycle (right axis) as function of the number of impregnation cycles obtained in various gold ionic concentration of $HAuCl_4$ on the film of thickness 160nm with flow rate of 0.2 ml/min. The dash lines show that (i) the first impregnation cycles adsorb large quantities of gold, and the gold gaining then decreases; (ii) the first loading mass obtained from various concentration of gold salt solution are similar; (iii) after 5 cycles of loading process

the mass of gold loading for each process cycle is constant. (b) is the plot of the volume fraction of Au in PVP layer as function of impregnation cycles, measured by QCM (dash lines) and SE (solid lines, analyzed with different model), which shows the good agreement between QCM results and SE results.

The solid lines are the cumulative loading of gold in the film mass. The gained mass of gold keeps increasing with the number of cycles and did not reach a maximum. As the gold amount increases not only in the PVP layers but also on the surface of films (see AFM images Figure IV. 36), after 10 cycles of impregnation, our measurements do not make it possible to distinguish between a mass gaining in the layers and a mass gaining on surface. We noticed that for N>10, the QCM-D signal presents an increased dissipation, which could be related at least in part to the gold particles accumulating on the surface. A more complex analysis mode could maybe be used to distinguish the amount of gold inside and above the films.

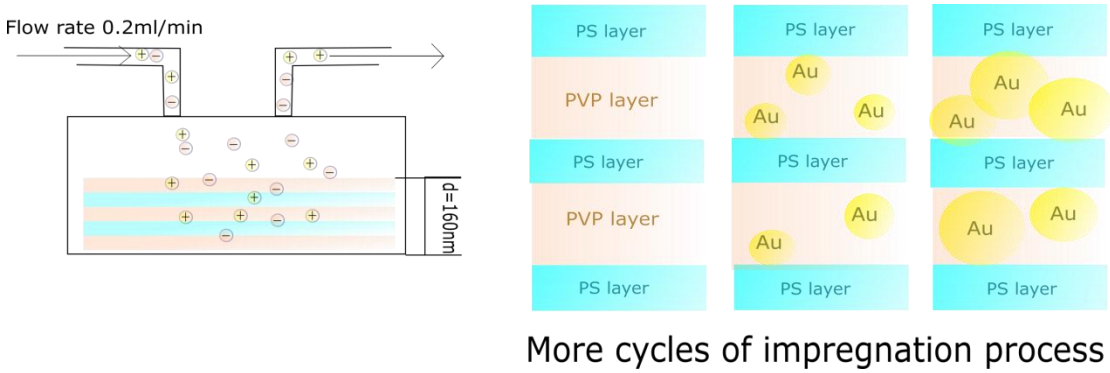

Figure IV. 35 Schematic illustration of the gold loading process. The left part is the flow of gold salt solution in the QCM cell, the gold salts stay in the PVP layer. The right part shows the mechanism of the gold loading, gold nanoparticles with small diameter are obtained in the first several cycles of the impregnation process, and then the mass gaining is caused by the growth of the nanoparticlesdiameter.

In conclusion, we deposited a homogeneous film on the Q-sensor. The concentration of gold precursor solution HAuCl4 has no influence on the cumulative loading of gold, the increasing lines are similar. After 5 impregnation cycles, the gold loading mass for each cycle is constant, taking a value of ca. 3µg. We can thus reach volume fractions of 10% (resp. 20%) with 5 (resp. 10) cycles of impregnation.

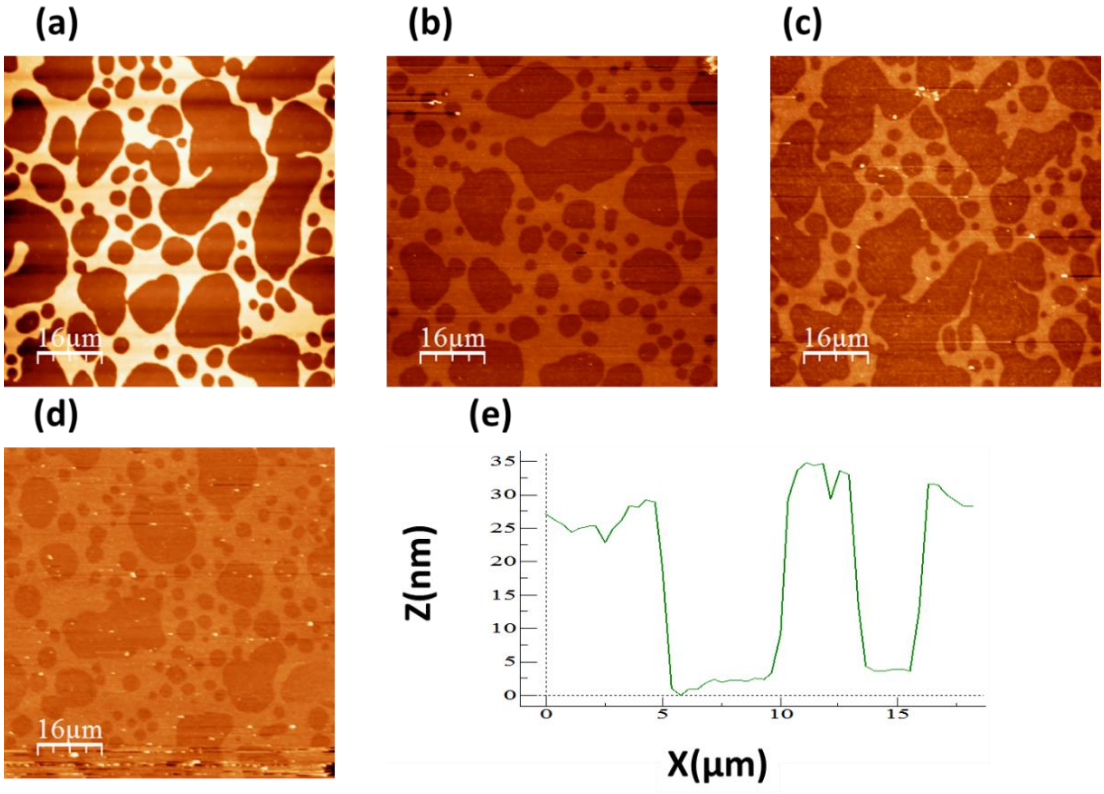

Figure IV. 36 AFM images on the surface of the Q-sensor. (a)(b)(c)(d) are AFM images of the surface of the sensor after 0 cycle of impregnation process, 5 cycles, 7 cycles, and 10 cycles respectively. The bright dots are Au nanoparticles, whose quantity increases as the process cycle number increases. (e) is a thickness profile along part of image (a) displayed to show that the difference in thickness is 25nm (close to a half bilayer thickness) between light and dark domains on the images.

Conclusions

In this chapter, we studied two methods for fabricating multilayer nanocomposites. The one-step method is not efficient to load gold nanoparticles in multilayer structures, while the impregnation process can load gold nanoparticles inside PVP layer effectively, which also works for silver nanoparticles impregnation.

In the impregnation process, the reactants could be diffusing through all PS and PVP layers. However, if the solvent of the metallic precursor change from ethanol to water, there is no penetration of the reactants in the films. So we are going to keep the solvent of gold precursor to be ethanol in the later studies.

The impregnation process used for silver nanoparticles loading need to be improved. In order to achieve structures as good as the one with gold nanoparticles, the reducing step needs to be optimized.

Furthermore, the observation of same reduction condition in various value of N suggests that the loading of the precursor could reach near-equilibrium: one $HAuCl_4$ per pyridine unit[16]. As the value of N increase, the size of the gold nanoparticles increases *in situ*.

According to the study of the gold nanoparticles inside films by SAXS and TEM, the gold nanoparticles inside film are nanospheres with diameter of $\pm$8nm. The diameter of nanoparticles is independent of thicknesses of the films and value of N (N>5). The several first cycles of impregnation deposit small nanoparticles in the P2VP layers, which then act as seeds of gold and the following loading cycles used for growing the gold NPs.

After study the volume fraction of gold with QCM-D and SE, we obtained results with a good agreement. The concentration of gold precursor solution $HAuCl_4$ has no influence on the cumulative loading of gold. After 5 impregnation cycles, the gold loading mass for each cycle is constant, taking a value of ca. 3µg. We can reach volume fractions of 10% (resp. 20%) with 5 (resp. 10) cycles of impregnation.

References

1. Yun, S.-H. *et al.* Electrically anisotropic thin films consisting of polymeric and metallic nanolayers from self-assembled lamellae of diblock copolymers. *Langmuir* **21,** 3625–3628 (2005).
2. Sohn, B. H. & Seo, B. H. Fabrication of the multilayered nanostructure of alternating polymers and gold nanoparticles with thin films of self-assembling diblock copolymers. *Chem. Mater.* **13,** 1752–1757 (2001).
3. Maxit, B., Bendejacq, D. & Ponsinet, V. Facile formulation of high density well-ordered nanoparticle–copolymer nanocomposites. *Soft Matter* **8,** 1317–1320 (2012).
4. Peters, R. D., Yang, X. M., Kim, T. K., Sohn, B. H. & Nealey, P. F. Using self-assembled monolayers exposed to X-rays to control the wetting behavior of thin

films of diblock copolymers. *Langmuir* **16,** 4625–4631 (2000).

5. Atashbar, M. Z., Bejcek, B., Vijh, A. & Singamaneni, S. QCM biosensor with ultra thin polymer film. *Sensors Actuators B Chem.* **107,** 945–951 (2005).
6. Lin, H., Steyerl, A., Satija, S. K., Karim, A. & Russell, T. P. Solvent penetration into ordered thin films of diblock copolymers. *Macromolecules* **28,** 1470–1474 (1995).
7. Vieaud, J. Propriétés optiques effectives de films composites de polymère et de nanoparticules d'or. (Thèse, Université Bordeaux 1, 2011).
8. Marx, K. A. Quartz crystal microbalance: a useful tool for studying thin polymer films and complex biomolecular systems at the solution− surface interface. *Biomacromolecules* **4,** 1099–1120 (2003).
9. Suematsu, S., Oura, Y., Tsujimoto, H., Kanno, H. & Naoi, K. Conducting polymer films of cross-linked structure and their QCM analysis. *Electrochim. Acta* **45,** 3813–3821 (2000).
10. Nomura, T. & Okuhara, M. Frequency shifts of piezoelectric quartz crystals immersed in organic liquids. *Anal. Chim. Acta* **142,** 281–284 (1982).
11. Keiji Kanazawa, K. & Gordon, J. G. The oscillation frequency of a quartz resonator in contact with liquid. *Anal. Chim. Acta* **175,** 99–105 (1985).
12. Kubiak, K., Adamczyk, Z. & Oćwieja, M. Kinetics of Silver Nanoparticle Deposition at PAH Monolayers: Reference QCM Results. *Langmuir* **31,** 2988–2996 (2015).
13. Sauerbrey, G. The use of quartz oscillators for weighing thin films and for microweighing. *Zeitschrift für Phys.* **155,** 206–222 (1959).
14. Mironov, I. V & Tsvelodub, L. D. Equilibria of the Substitution of Pyridine, 2, 2'-Bipyridyl, and 1, 10-Phenanthroline for Cl^- in $AuCl_4^-$ in Aqueous Solution. *Russ. J. Inorg. Chem. C/C ZHURNAL Neorg. KHIMII* **46,** 143–148 (2001).
15. Vieaud, J. *et al.* Effective medium description of plasmonic couplings in disordered polymer and gold nanoparticle composites. *Thin Solid Films* **603,** 452–464 (2016).
16. Förster, S. & Antonietti, M. Amphiphilic block copolymers in structure-controlled nanomaterial hybrids. *Adv. Mater.* **10,** 195–217 (1998).

Chapter Ⅴ Optimization of the films made by the impregnation process

Introduction

As we mentioned in the last chapter, the Au NPs are well introduced into the PVP layer of the lamellar phase. However, irregular Au NPs are also synthesized on the top of the upper surface of the films for high values of N, and the first two layers are thicker than the other layers (Figure V. 1). These structural irregularities are susceptible to influence the optical properties of the films, and we have studied the possibility of avoiding them.

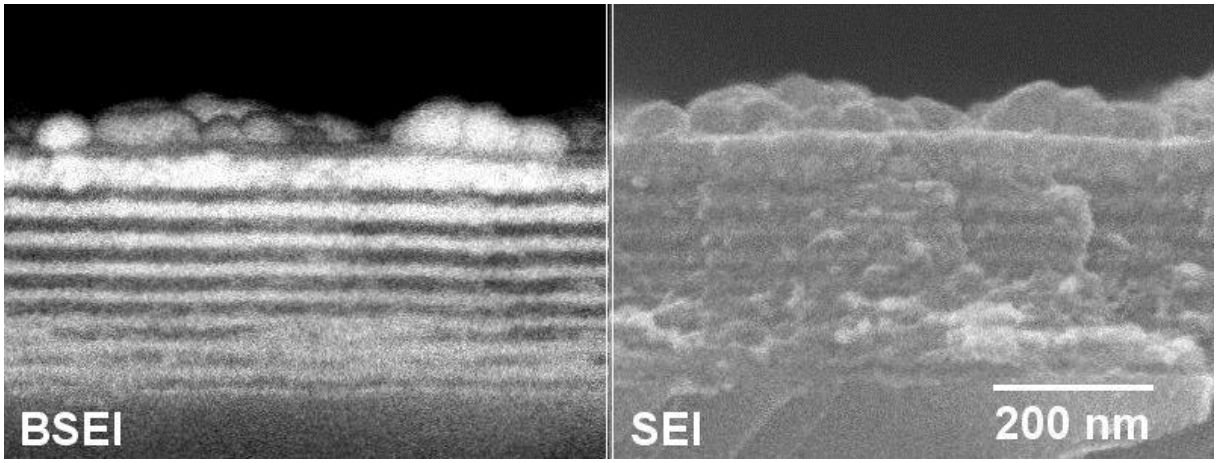

Figure V. 1 Cross-section of the film under SEM in SEI (secondary electron image) and BSEI (backscattered electron image). The sample was fabricated by PS_{25000}-block-$P2VP_{25000}$ and repeat the loading process for N=30.

This goal leads us to try to understand the processes of impregnation and reduction. In this chapter, we are going to study and optimize the Au NPs synthesis process and try different ways to fix the irregular particles on surface. In particular, we will study how the reduction process depends on the choice of solvent and reducing agent.

V.1 Impregnation process improvement

V.1.1 Influence of solvent of the reduction step

V.1.1.1 Introduction

In the step of impregnation of the film by the gold salts, described in Chapter IV, two steps are used: first we immerse the film in a gold precursor solution and then we immerse the film in a reducing agent solution, which involves two different solvents,

ethanol for the gold salt and water for the reducing agent. In order to know the influence of the solvents, we plan to change the solvent of the reducing agent and study the film structure and Au nanoparticles shape and size in the films. We are not going to change the solvent of the gold because some studies[1,2] and our study in Chapter IV show that the affinity of the gold salts with the PVP layers is due to the gold salt penetration from the top of the film and the solvent plays an important role in this step. In 1995, H. Lin et al[3] studied the penetration of solvent in ordered thin films and showed that there was no penetration of the solvent into the underlying multilayered structure if the solvent is poor to one of the block. So the manipulation of solvent in this step is ineffective. Thus, in this section we are going to focus on the solvent manipulation in the reducing step.

Ellipsometric modeling used in this section

As we mentioned the in V.1.1.2, we repeat the loading process for several cycle in order to increase the Au NPs amount. Simultaneously, the samples were analyzed by spectroscopic ellipsometry (SE) at each cycle. We analyze the data in two different models, shown in Figure V. 2.

Model 1 (Figure V. 2(a)) assumes the whole sample including substrate as an effective bulk media. So we extracted an apparent and not real permittivity, we will call it pseudo-permittivity and write it as ‹ε›. Although this ellipsometric model does not provide access to the anisotropic effective permittivity of the material, it gives primary “kinetic” information on the evolution of the resonance caused by the progressive gain of Au NPs.

Model 2 (Figure V. 2(b) and (d))is built based on the detailed film nanostructure obtained from the section SEM images, as schematized in the Figure V. 2(c) for the water system or (e) for the water/ethanol system. The materials PS and PVP are described by New Amorphous dispersion relation (details are described in ChapterII.1.4).

PS stands for pure polystyrene and NC for the nanocomposite composed of gold nanoparticles and poly(2-vinylpyridine). The thickness of the PS and NC layers are written as d_{PS} and d_{NC}, respectively. Half thickness layers of PS and NC are present at the sample/air interface and sample/substrate interface, respectively. Two different effective medium approximations are used to describe the optical constants of the nanocomposite layers (NC layers) consisting of dispersion of gold NPs in PVP. They

are the Maxwell-Garnett model (MG) and the Bruggeman model (EMA), which were already introduced in the ChapterII.1.

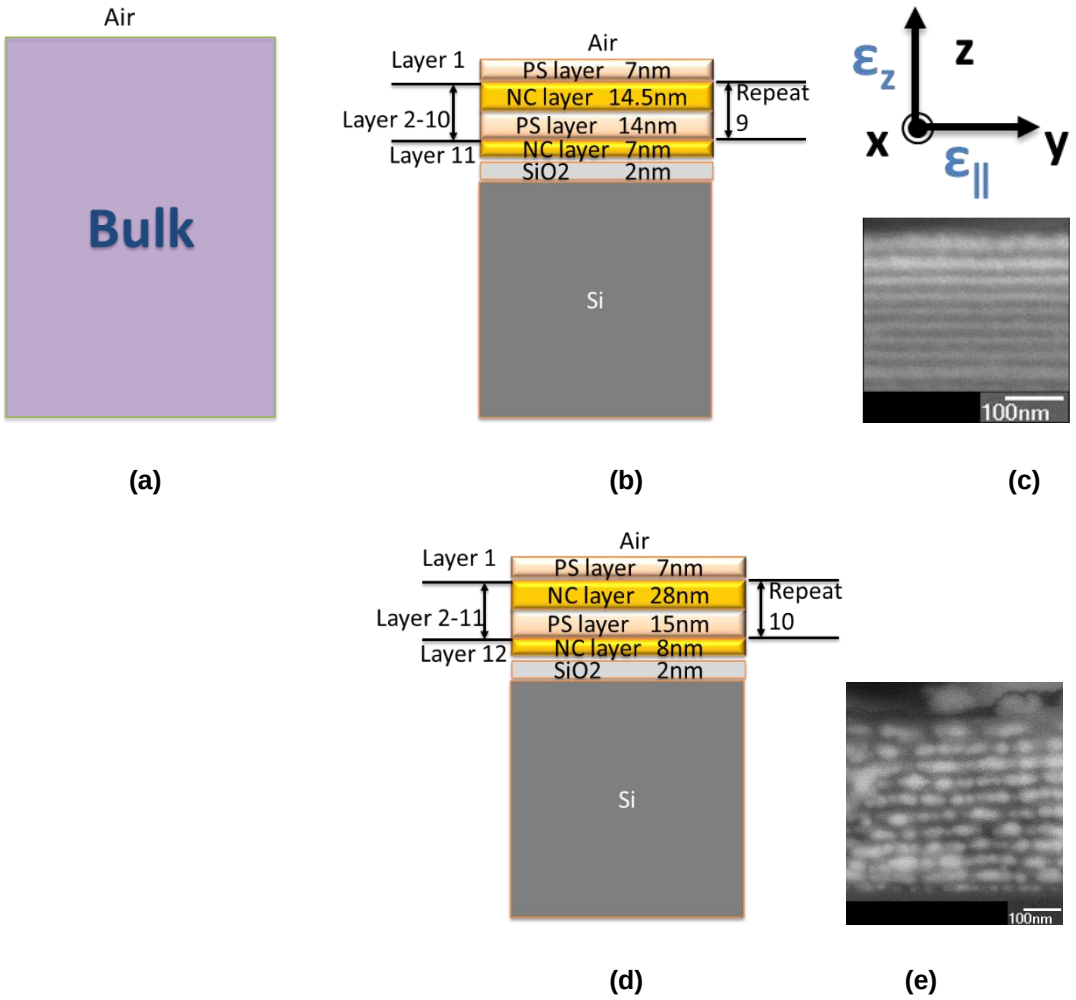

Figure V. 2 the models used for analsis.(a) model 1, the whole film and silicon wafer are assumed as an effective media bulk. (b) (d) are model 2 for film fabricated in water system and water/ethanol system, respectively. They are built based on the detailed film nanostructure obtained from the cross-section SEM images, as schematized in (c) for water system and (e) for water/ethanol system. PS stands for pure polystyrene and NC for the nanocomposite composed of gold nanoparticles and poly (2- vinylpyridine), of varying composition when N increases. The trihedral in (c) indicates the ordinary ((x,y) or //) and extraordinary (z) directions. The ε is separated into $\varepsilon_{//}$ and ε_z.

Let us recall that the MG model is based on the Clausius-Mossotti relationship which describes the dielectric function of a set of dilute polarizable spheres homogeneously immerged in a host medium. This model defines the dielectric function ε_{MG} of the effective medium according to the following formula

Equation 5- 1 $$\varepsilon_{MG} = \varepsilon_1 \frac{\varepsilon_2(1+2f)+2\varepsilon_1(1-f)}{\varepsilon_2(1-f)+\varepsilon_1(2+f)}$$

With the dielectric constant of spherical particles ε_2 immerged in a host medium whose dielectric constant is ε_1. f is the volume fraction of the spheres in the matrix. It is only valid for low volume of particles.

In EMA model, the different components of the mixture are treated equivalently, without preliminary assumption on the relative proportions. This model is self-consistent: the mixture of the different materials forms the host medium, which means that the dielectric function of the host medium is the EMA-Bruggeman dielectric function. In this model the number of phases can exceed 2. The dielectric functions of the different materials are ε_i (with i=1,2,3,…) with corresponding volume fractions f_i. The dielectric functions verify the equation:

Equation 5- 2 $$\sum_i f_i \frac{\varepsilon_i - \varepsilon_{EMA}}{\varepsilon_i + 2\varepsilon_{EMA}} = 0$$

In this chapter, two phases are present, the metallic particles of volume fraction f_1 and the polymer matrix, f_2=1-f_1.The dielectric function of the effective medium fulfills the following equation:

Equation 5- 3 $$-2{\varepsilon_{EMA}}^2 + [3f_1(\varepsilon_1 - \varepsilon_2) + 2\varepsilon_2 - \varepsilon_1]\varepsilon_{EMA} + \varepsilon_1\varepsilon_2 = 0$$

with ε_1 the dielectric constant of the gold NPs and $\varepsilon_2$that of the PVP matrix.

The permittivity ε_{NC} of the NC layers is determined by fitting the Model 2 to the SE data using the Deltapsi2 software and using either a Maxwell-Garnett or a Bruggeman effective medium as full fit. This fitting procedure allows to extract $\varepsilon_{NC}(\lambda)$ for the different values of N.

Once the NC layers are modeled, the next step in the modeling is to include these NC layers in the multilayer structure, alternating with pure PS layers of known thickness and permittivity. This is done by considering the effective permittivity of a periodic stack of infinite thin layers, which gives access to the anisotropic effective permittivity of the lamellar material.

The optical properties of the uniaxial effective medium $\varepsilon_{//}(\lambda)=\varepsilon_{//}'(\lambda)+ i\ \varepsilon_{//}''(\lambda)$ and $\varepsilon_z(\lambda) + \varepsilon_z'(\lambda) + i\ \varepsilon_z''(\lambda)$ can be written[4–6] in Equation 5- 4 and Equation 5- 5. In these equations, the thickness of PS and NC layer, noted as d_{PS} and d_{NC} respectively, as usually observed in lamellar block copolymer thin films. The permittivity of PS layer,

noted as ε_{PS} can be found in the Figure II. 7(b) and the Table II. 1 of Chapter II.1.4. The permittivity of NC layer, noted as ε_{NC} is extracted by the fitting model mentioned previous paragraph.

Equation 5- 4
$$\varepsilon_{||} = \left(\frac{d_{NC}}{d_{NC}+d_{PS}}\right)\varepsilon_{NC} + \left(\frac{d_{PS}}{d_{NC}+d_{PS}}\right)\varepsilon_{PS}$$

Equation 5- 5
$$\frac{1}{\varepsilon_z} = \left(\frac{d_{NC}}{d_{NC}+d_{PS}}\right)\frac{1}{\varepsilon_{NC}} + \left(\frac{d_{PS}}{d_{NC}+d_{PS}}\right)\frac{1}{\varepsilon_{PS}}$$

V.1.1.2 Experiment

Film preparation:

The PS_{25k}-$P2VP_{25k}$ was dissolved in toluene at 6.0 wt %. The polymer solutions were stirred overnight and spin-coated onto cleaned wafers. Spin time is 30seconds with the spin speed of 5000 rpm/s, 3 seconds of acceleration time and deceleration time. Self-assembly of the lamellar structure in the films were obtained by thermal annealing (180ºC in oven with vacuum) for 15 h or longer.

Au loading process

After we obtained the aligned and organized lamellar phases, 1) we immersed the film in 3.0 wt% $HAuCl_4$ solution in ethanol for 5 minutes following by a rinsing of deionized water several times. 2) Afterward, the films with $HAuCl_4$ loading were immersed into different $NaBH_4$ 0.65 wt% solution in water, mixture of water and ethanol in volume of 1/5, or methanol for 30 sec. We repeat step 1) and 2) for N times of cycles (N is integrate from 0 to 30) to increase the concentration of Au NPs.

Measurement

The samples were measured by variable angle spectroscopic ellipsometry (VASE), the details are in Chapter II.1.3. We use the configuration of UVISEL II with AIO=55º, 65º and 75º.

For cross-sectional view of the samples, the films on silicon wafers were broken in half manually and observed by SEM.

After all the measurements, samples were dissolved in toluene to disperse the resulting Au NPs, and then observe them by TEM.

V.1.1.3 Results

Structures

As we discussed in Chapter III, the PS and PVP domains separate into a lamellar phase after thermal annealing. As the film is then dipped into the gold salt solution, the solvent brings the gold salt into the PVP layers. Figure V. 3 shows the side view of the samples prepared with $NaBH_4$ in 3 different solvent, in water, water/ethanol=1/5 in volume, and methanol. In the SEM images, the white part is corresponds to the gold-rich areas and dark parts correspond to the pure polymer domains (PS). The loading process goes well in the aqueous system (Figure V. 3 upper). The gold NPs are well introduced into the PVP layers and appear homogenously distributed. In the water/ethanol system (Figure V. 3 middle), the thickness of film is increased and the gold salts were reduced to gold within the PVP layers. However, the film is inhomogeneous and gold particles are obviously bigger than the ones in the aqueous system. In methanol (Figure V. 3 (a) below), only a few gold particles were synthesized.

From Figure V. 4 (a), compared to the samples fabricated in water and methanol, we can see that the thickness of the film dipped in the water/ethanol solution increases significantly by almost 200 nm, which is likely due to the swelling of the PVP chains in ethanol. Concerning the water/ethanol system, since there is a large amount of solvent in the layers, several effects can be predicted: (1) a large amount of reducing agent $NaBH_4$ enter the layers (2) more particles grow with little bound to PVP. As we mentioned in Chapter I, gold nanoparticle also bind with hydroxyl, even though the ligand is weaker than the one with amnion.(3) since ethanol can easily penetrate multi layers, the particles bound with ethanol have more mobility in the layers. All of these results in the larger gold particles in the layers and the increase of the layer thickness.

Figure V. 4 (b) and (c) show the TEM images of Au particles in the samples after the film has been dissolved and resulting NPs have been recovered on TEM grid, and the distribution of particles in histograms, respectively. In Figure V. 4 (b) and (c), we can see that the Au particles in the film which is reduced in water are spheres of diameters ranging from 1 to 15nm. In the case of the film reduced in water/ethanol, the Au are irregular and their sizes range from 1 to 230nm. Finally, the few Au particles in the film which is reduced in methanol are spheres of diameter ranging from 4 to 46 nm.

The Au NPs synthesis in water system works very well, the loading and reduction processes preserve the self-assembled block copolymers lamellar structure, and the

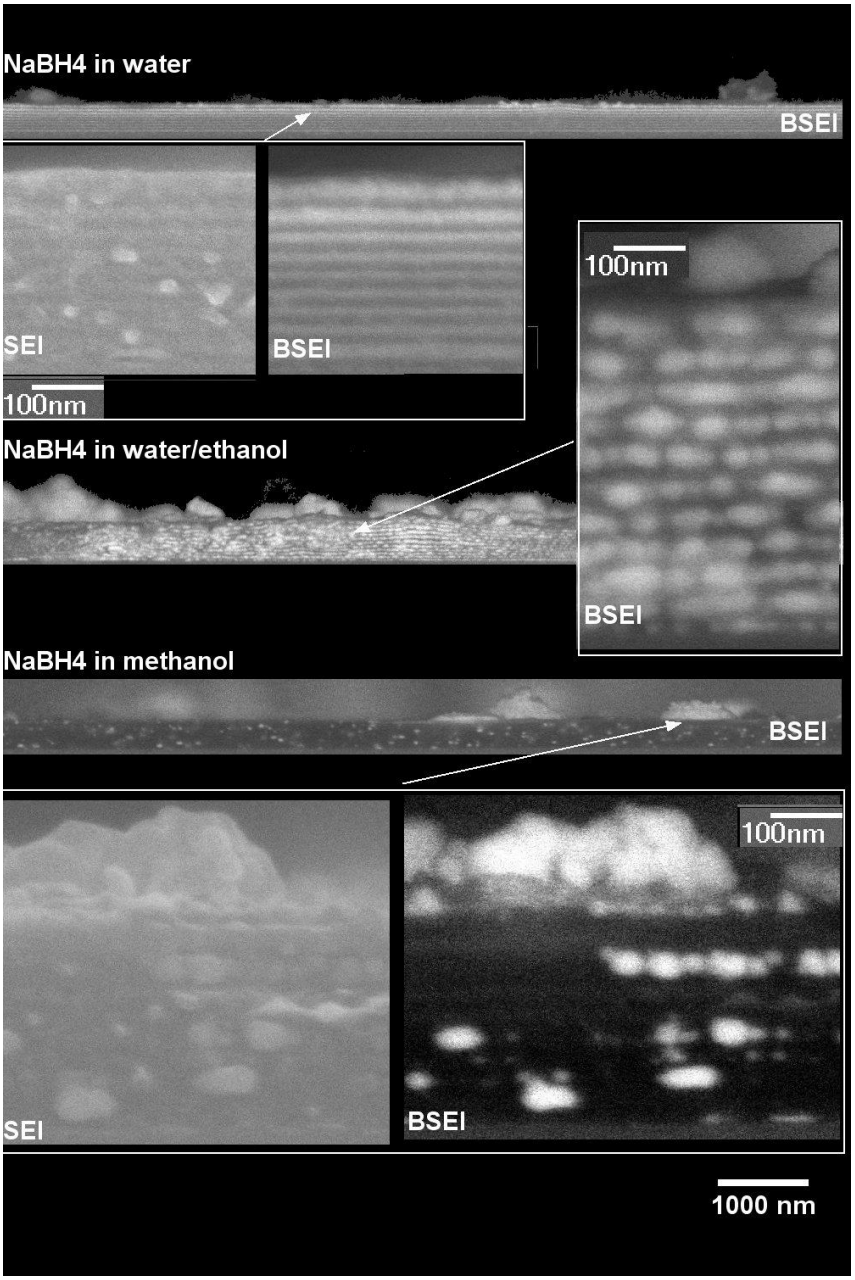

Figure V. 3 SEM images of samples cross-section fabricated in different solvent (N=20): water, water/ethanol=1/5(volume) and methanol.

Au NPs shape (sphere) and size (around 10 nm) are well controlled. In the water/ethanol system, the loading process preserves the self-assembled lamellar structure expect for the nanocomposite layer thickness (the thickness increases), and most of the gold particles in the layers are aggregated. We can thus propose that the aggregation could be manipulated by the proportion of ethanol and water. This gives us a possibility to study the optical response caused by the couplings between the

metallic particles. In the methanol system, the lamellar structure is well kept but the in-situ synthesis is not working well. However, the gold particles in the layers grow bigger than in the water system. It gives us another possibility to increase the size of gold particles.

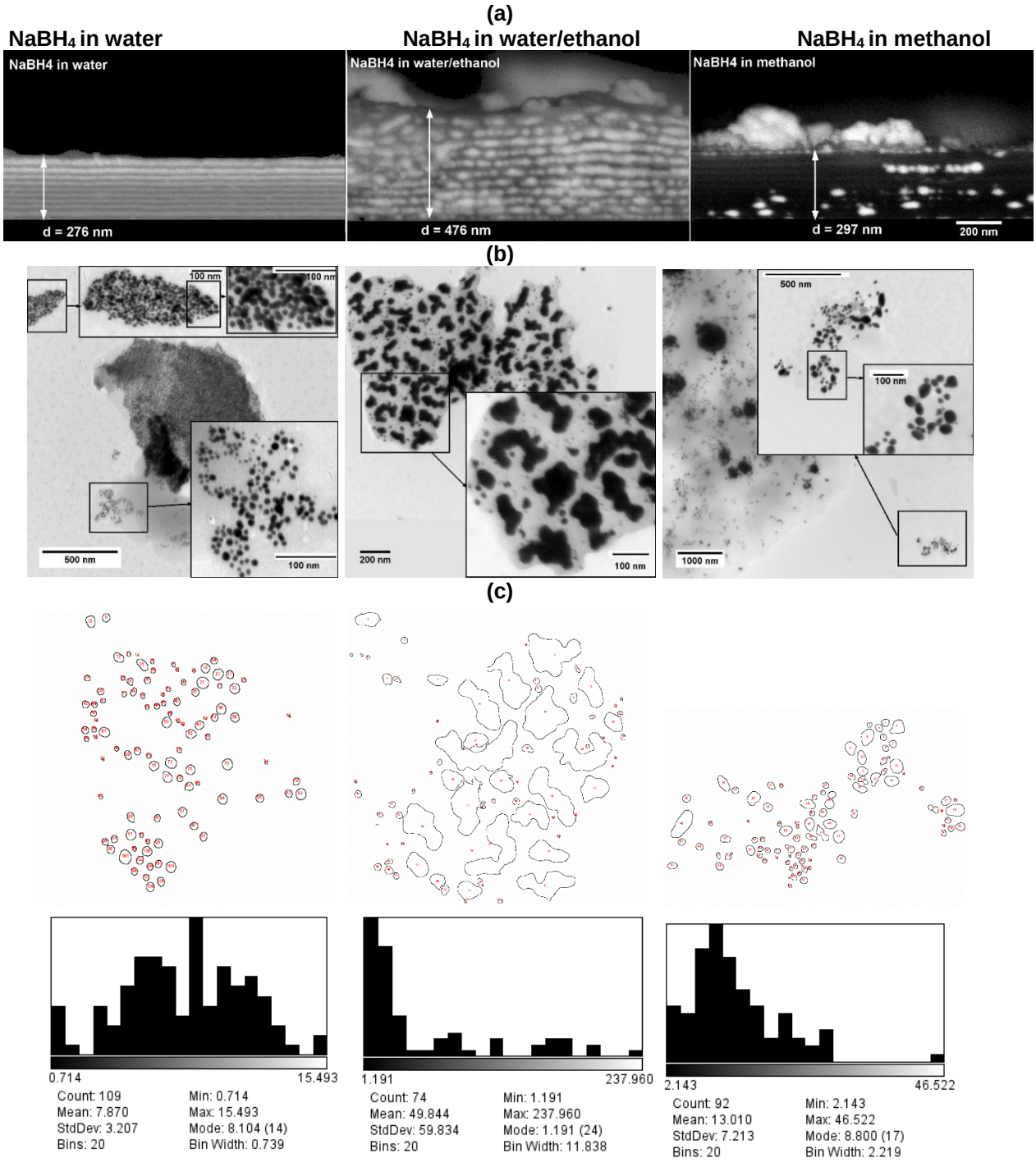

Figure V. 4 (a) SEM images of samples cross-section in high resolution. (b) TEM images of Au NPs in samples synthesis in-situ in 3 different solvent (c) the distribution of particles in histograms. Bin=20.

Results of optical properties

Results of Model 1

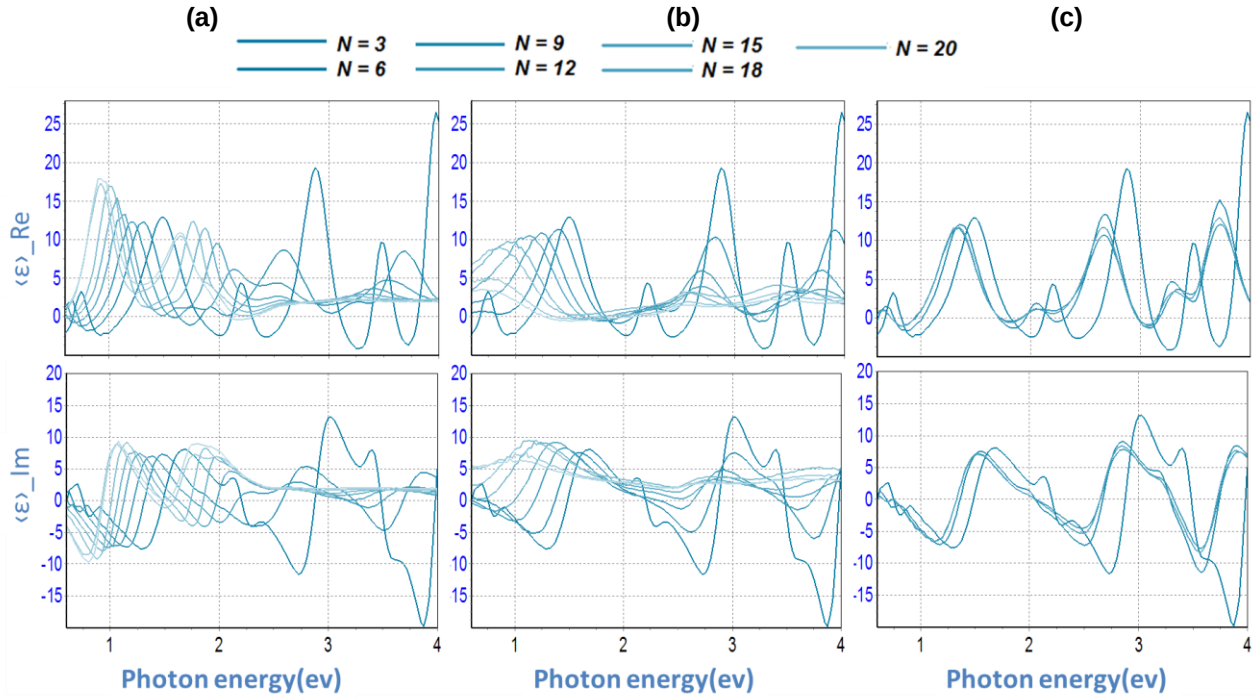

Figure V. 5 Results of model 1. Real (upper plot) and imaginary (lower plot) parts of the pseudo-dielectric function ‹ε› of the whole sample from the SE study for different values of N=3, 6, 9, 12, 15, 18 and 20. As the values of N increase, the colour of the line decrease gradually. (a) (b) (c) are Au salts reduced in water system, water/ethanol=1/5 (in volume) system and methanol, respectively; The resonance amplitude varies as N increases, due to the increasing introduction of plasmonic NPs.

Figure V. 5 shows the primary results of model 1, they are plots of real (upper plot) and imaginary (lower plot) parts of the apparent dielectric function ‹ε› of the whole sample as function of the photon energy. The reaction in the water system (Figure V. 5 (a)) and water/ethanol system (Figure V. 5 (b)) are efficient. Indeed, as the value of N increases, the fringes of real and imaginary part of ‹ε› present a red shift. As we know, interference effects for a film of thickness d will lead to fringes with extrema at wavelengths verifying $2nd = m\lambda$, where, m is an integer or half integer, $\boldsymbol{n} = n + ik$ is the refraction index of the film, k is the extinction coefficient. From the SEM images shown previously, we can see that the change of film thickness is very limited, so the progressive red shift of the fringes for an increasing value of N can be attributed to a change of refractive index of the film. In this case, the change of n is mostly caused by the increase of the Au NPs volume. Between photon energy 1.8 and 2.5ev (corresponding to the wavelength ranging from 689 to 496 nm), the real parts (upper

plot) of ‹ε› decreases as the value of N increases and the imaginary (lower plot) parts of ‹ε› decreases at the same time. This is caused by dissipative effect of the Au NPs resonance. The signal damping in UV range and amplification in IR range are observed in the water system, and the damping in the whole wavelength range is observed in the water/ethanol system. They occur following the gain of Au NPs volume, which is step by step. On the contrary, the reaction in the methanol system (Figure V. 5(c)) is not efficient. And from the shift of ‹ε›, we can see that all the reaction is finished in the first step. As the value of N increases, Re (‹ε›) does not evolve much after the first cycle. The gold NPs shown in left of Figure V. 4 (c) and (d) are synthesized in the first cycle of impregnation process.

Results of Model 2

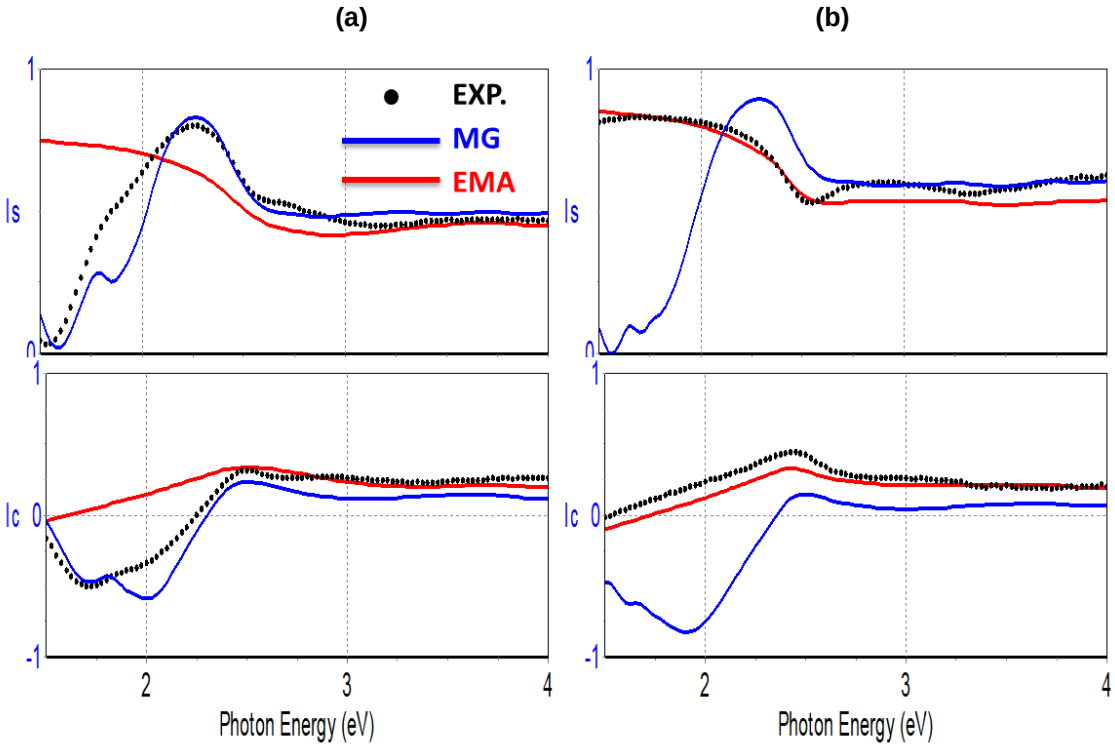

Figure V. 6 Plots of Is and Ic as a function of the photon energy in different fitting models. Black dots stand for experimental data (EXP.), red lines and blue lines stand for fitting results of effective medium described by Maxwell-Garnett model (MG) and Bruggeman model (EMA), respectively. (a) Fitting result of the sample with Au fabricated in water system N=20. It shows a good agreement of EXP. in water system and MG fitting. It means the Au NPs in layer are non-coupling spherical gold nanoparticles. (b) Fitting result of the sample with Au fabricated in water/ethanol system N=20. It shows a goodl agreement of EMA fitting and EXP. in water/ethanol system. It indicates the Au NPs in layer are large or aggregated.

As we illustrate in 'Ellipsometric modeling', the MG and EMA models stands for two different dispersion state of the Au NPs in the layer. The MG model stands for dilute non-coupling spheres while the EMA stands for random mixture of polymer and Au. From the Figure V. 6, it appears that the fitting of MG works better in the water system and that of EMA works better in the water/ethanol system. The Au NPs in the layer reduced in water correspond better to non-coupling spheres while in the water/ethanol system, the produced gold correspond better to large Au domains, which can be confirmed by the TEM image in the Figure V. 2. At the photon energy from 1.7eV to 1.8eV (λ~729nm to 690nm), the data of water system (Figure V. 6(a)) present a peak which is not exactly fitted by MG model. This is probably because the MG model considers monodisperse and perfectly spherical gold inclusions. In the sample, the Au NPs, although well defined, present a significant polydispersity, as is confirmed by the TEM results showed in the left image of Figure V. 4 (c).

For the following simulation of water system, the NC layer is described by MG model. On the contrary, the simulation of the water/ethanol system is done with the NC layer described by the EMA model.

The real and imaginary parts of ε_{NC} of the NC layers in the lamellar stack extracted from the SE study with Model 2(Figure V. 2(b) & (d)) are presented in the Figure V. 7 for different values of N=6, 15 and 20.

When pushing the Maxwell-Garnett effective medium approximation (MG-EMA) to higher N, a degraded agreement is naturally expected: it remains nevertheless reasonably good especially below 2.1 eV (above 580nm). These partial agreements provide rough estimates of the loading concentration in gold: we find in the water system N=6 to correspond to a MG-extracted value of f=7%, and N=15 and N=20 to *approximately f=23%* and *f=40%*, respectively. And in the water/ethanol system N=6 to correspond to an EMA-extracted value of *f=6%,* and N=15 and N=20 to approximately f=28% and f=47%, respectively. As the Au NPs loading (f_{Au}) increases in the NC layers, the real part of ε_{NC} of NC layer corresponding to the Maxwell-Garnett effective medium (Figure V. 7 (a) upper plot) takes large values in the IR range, while the real part of ε_{NC} extracted from NC layer corresponding to the EMA-Bruggeman effective medium (Figure V. 7(a) lower plot) decreases in the IR energy range. Also, the imaginary part increases in the IR wavelength energy range. Figure V. 7(b) shows the comparison of the extracted ε_{NC} for the two different Au particles in the NC layers. For

the small Au NPs (the water system, solid line), ε_{NC} presents a stronger resonance, whereas for the large NPs (water/ethanol system, dashed line) ε_{NC} presents only a small and spectrally broad (for N=6) or no (for N=15 and 20) resonant behavior, and has a shape close to that of bulk gold.

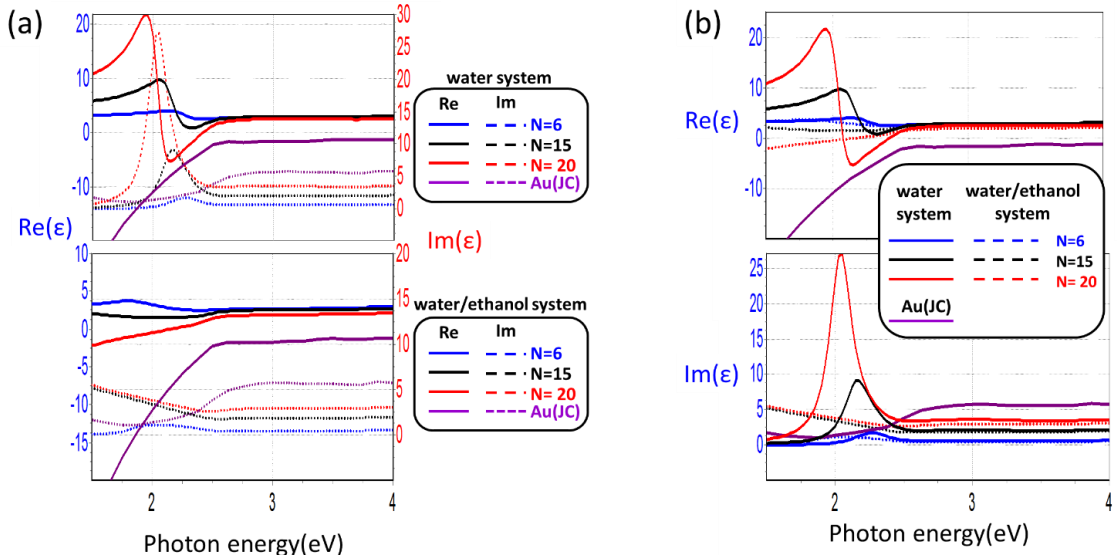

Figure V. 7 (a) Real (Re, solid line) and imaginary (Im, dash line) parts of ε_{NC} of the NC layers in the lamellar stack, as extracted from the SE study for different values of N between 6 and 20. The Au NPs reduction process is done in water system (upper plot) and water/ethanol system (lower plot); (b) Comparison of the two systems. Real (upper plot) and imaginary (lower plot) parts of the dielectric function ε_{NC} of the NC layers in the lamellar stack. The resonance amplitude varies as N increases, due to the increasing introduction of plasmonic NPs. Au(JC) stands for experimental data of gold bulk from publication [7].

Following the second step of Model 1, the dielectric constants of the uniaxial effective medium are first determined using the optical properties of the fitted Au loaded polymer layers (NC) and the PS layer, through Equation 5- 4 and Equation 5- 5. The resulting effective optical properties are showed in Figure V. 8. $\varepsilon_{//}$ and ε_z are the components of the permittivity tensor parallel and perpendicular to the substrate plane.

Figure V. 8 shows the comparison real part (Re) and imaginary part (Im) components $\varepsilon_{//}(\lambda)$ and $\varepsilon_z(\lambda)$ extracted for N=6, 15 and 20 between the sphere gold nanoparticles and gold bulk. As is shown on the solid lines of Figure V. 8, for the gold NPs fabricated in water system(MG-extracted), the dielectric functions $\varepsilon_{//}$ and ε_z both present a resonance at the a photon energy of 2.1 eV (or alternatively the wavelength λ=580 nm), close to the plasmon resonance of the gold nanoparticles. However, the resonance amplitudes of the two components significantly differ. In the case of ε_z, the

amplitude of the resonance increases only slightly with the value of N. By contrast, the resonance of $\varepsilon_{//}$ is increases strongly with N, and it reaches regime of negative $\varepsilon_{//}$ at or beyond N=20. As a result, strong artificial anisotropies with different characteristics are found across the spectrum.

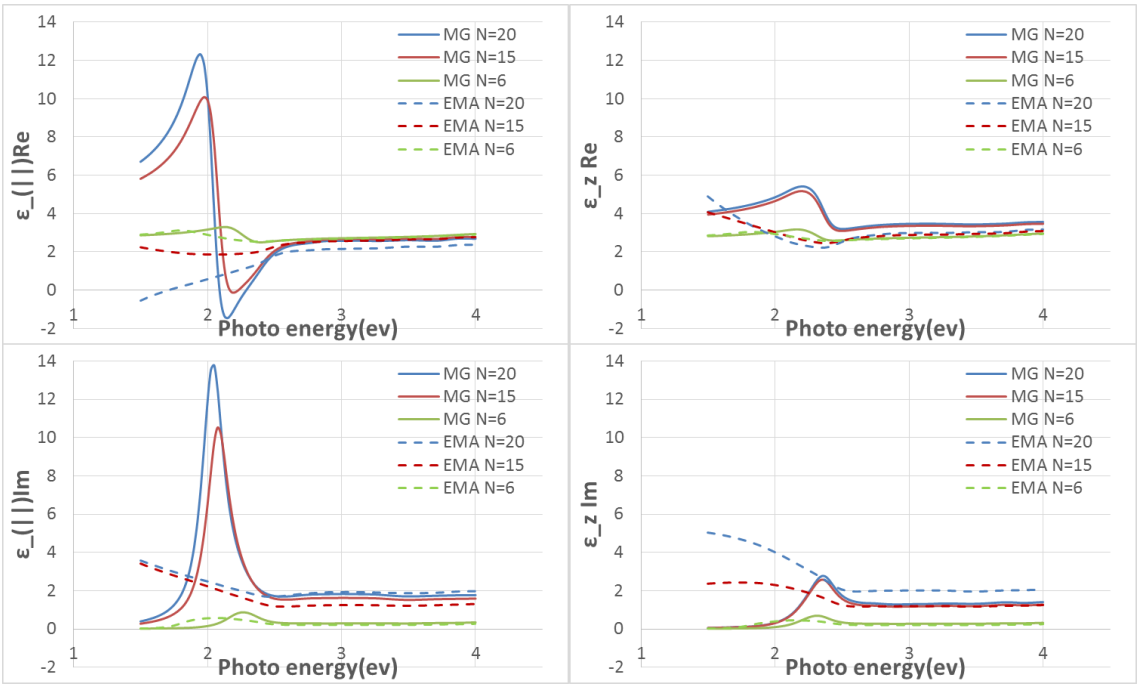

Figure V. 8 Real (upper plots) and imaginary (lower plots) parts of the components $\varepsilon_{//}$ (left) and ε_z (right) of the lamellar nanoplasmonic thin films fabricated in water system (solid line) and water/ethanol system (dash line), as computed using Eqs. (4) and (5) from the Model 2 SE extractions for different values of N 6, 15 and 20 (solid lines: MG-extracted f_{Au} between 7% and 40%; dash lines: EMA-extracted f_{Au} between 7% and 47%). The resonance amplitude varies as N increases in MG-extracted, due to the increasing volume fraction of introduced plasmonic nanoparticles.

As is shown on the dash lines of Figure V. 8, for gold fabricated in water/ethanol system (EMA-extracted), the Au inside the NC layers are large objects with some similitudes with bulk Au. The NC material is not resonant, and the multilayer structure is not well defined enough to present a layer resonance.

We can compare the 2 different forms of Au particles in the layers, if the Au NPs are spheres in NC layer without coupling, a stronger resonance around 580nm can be observed. As shown in Figure V. 8, Re($\varepsilon_{//}$) (continuous lines) has a strong resonance around a photon energy of 2.1eV (or alternatively the wavelength λ=580 nm), while the resonance of Re(ε_z) are weaker. If the Au NPs in the NC layers are bigger than 60nm or aggregated into thin gold layers, the resonance perpendicular to the substrate Re(ε_z)

can be stronger and the parallel Re($\varepsilon_{//}$) becomes weaker, which can be seen also in dashed lines of Figure V. 8. However the resonance of Re(ε_z) is not significant in our case, this is because the volume fraction of gold in NC layers is not high enough and the gold nanoparticles are polydisperse. We can suppose that a more significant difference between Re($\varepsilon_{//}$) and Re(ε_z) could be observed if more gold particles were aggregated into nearly gold layers.

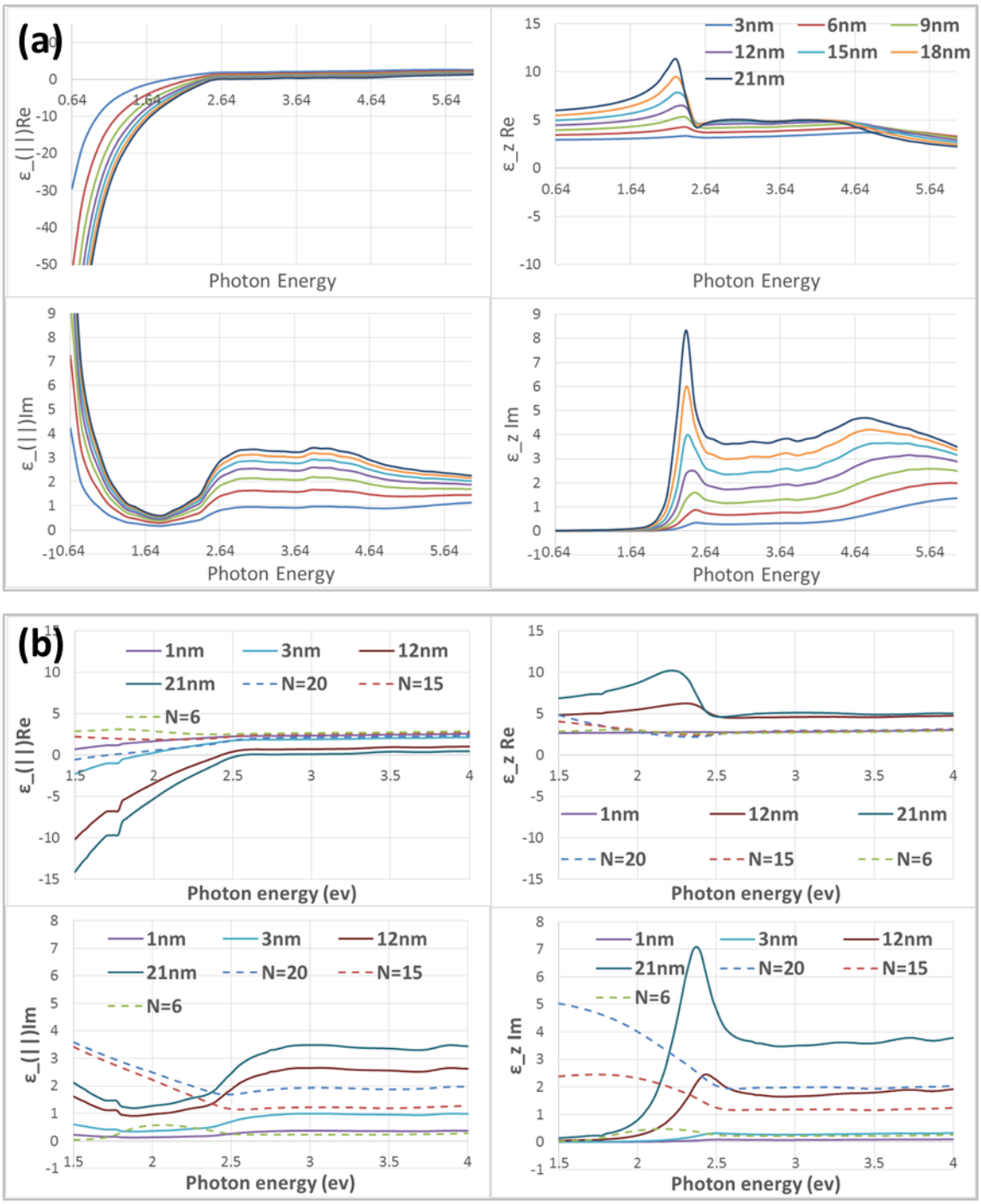

Figure V. 9 (a) Real (upper plots) and imaginary (lower plots) parts of the components $\varepsilon_{//}$ (left) and ε_z (right) of the lamellar nanocomposite thin film consisting of infinite alternative 15 nm PS layer and Au layer in different thickness(from 1nm to 21nm)

(b) Comparison of real (upper plots) and imaginary (lower plots) parts of the components $\varepsilon_{//}$ (left) and ε_z (right) of the lamellar nanocomposite thin film consistings of infinite alternative 15 nm PS layer and Au layer in different thickness (from 1nm to 21nm, solid lines) and thin films fabricated in water/ethanol system in different value of N (N=6, 15, 20, dash lines)

In order to know the difference between pure gold/polymer multilayer system and the gold nanocomposite prepared in water/ethanol system, we set a model with infinite alternative layers of pure PS, of thickness 15 nm and pure gold of thickness d_{Au} (from 1nm to 21nm). Then we simulate the real and imaginary parts of the components $\varepsilon_{//}$ and ε_z of the lamellar thin films showed in Figure V. 9(a).

The *in-situ* synthesis of Au NPs produces a better defined nanostructure when the reduction step is done in aqueous system. A tuning of the proportion of ethanol and water in the solvent of the reduction step could lead to different structures or couplings of Au particles, which can induce a modulation of the optical properties of the materials.

V.1.2 Influence of reducing agent

V.1.2.1 Introduction

In order to better understand how the mechanisms of the Au NPs synthesis in the PVP layers, we varied the reducing agent in the reduction step. It is known that different reducing agents produce different shape and size of Au NPs via the reduction of $HAuCl_4$[8–10]. In this study, sodium borohydride ($NaBH_4$), trisodium citrate (Na_3Ct) and L-ascorbic acid (AA) are used as reducing agent.

V.1.2.2 Experiment

Material

The following materials were obtained from Aldrich: auric acid ($HAuCl_4 \cdot xH_2O$), trisodium citrate (Na_3Ct), sodium borohydride ($NaBH_4$), L-ascorbic acid (AA). All chemicals and solvents were used without further purification.

($NaBH_4$) **(Na_3Ct)** **(AA)**

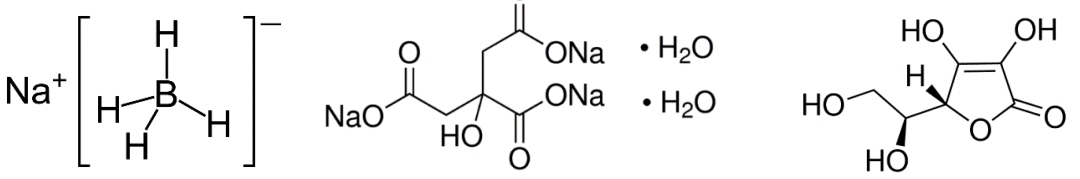

Sodium borohydride **Trisodium citrate** **L-ascorbic acid**

Film preparation is the same as described in V.1.1.2 “Film preparation”.

Gold loading process

After we obtained the aligned and organized lamellar phases, 1) we immersed the films in 3.0 wt% ethanol solution of $HAuCl_4$ for 5 minutes following by a rinsing of deionized water several times. 2) Afterward, the films with loaded $HAuCl_4$ were immersed into different 0.65 wt% aqueous solution of $NaBH_4$, Na_3Ct or AA for 30 sec. We repeat step 1) and 2) for N cycles (N is integrate from 0 to 20) to increase the concentration of Au NPs.

In the case of Na_3Ct, step 2) was processed both in room temperature and at 70ºC, in order to check the effect of temperature.

In the case of AA, the step 2) was processed both in neat AA solution, and in a AA solution with pH adjusted to pH=11 by NaOH addition, and thermal annealing (180ºC in vacuum for 2hours) after all the loading process.

Measurement

The samples were studied by VASE using the configuration of UVISEL II with AOI=55º, 65º and 75º.

For cross-sectional views of the samples, the films on silicon wafer were broken in half manually and observed by SEM.

After all the measurements, samples were dissolved in toluene to disperse the resulting Au NPs, and then observe them by TEM.

V.1.2.3 Results

Structures

As we mentioned before, In the BSEI SEM images, white parts is corresponds to the gold-rich areas and dark parts correspond to the pure polymer domains (PS). Figure V. 10(a) shows the SEM image side view of the sample prepared by Na_3Ct at room temperature and at 70 ºC. Figure V. 10(b) shows the side view of the samples prepared by AA at room temperature. We can see that Au NPs are synthesized on surface of samples instead of inside the layers. We can thus propose that the reaction between the gold salt and organic reducing agents (Na_3Ct and AA) works, but that the

reducing agent may not penetrate through the layers. We tried a sample prepared (Figure V. 10(c)) by AA at room temperature and heating the samples at 180 ºC for 15h at the end of the loading process. We can see from Figure V. 10(c), that after this annealing, gold was formed both on the surface and inside the layers. Therefore, Au salts are present inside the layers and are reduced at elevated temperature. We can thus propose that Au salts can penetrate through the layers[2], but the reducing agent AA can not. The reason why most of the gold stay at the bottom of the film, may be caused by the reorganization of the block-copolymers under the thermal annealing, which tends to expel the Au NPs leading them to be aggregated. The Au shape is also changed by the elevated temperature. Figure V. 10(c) shows the low-magnification and high-magnification TEM images of Au particles in the sample reduced by AA with thermal annealing. The TEM images presents different shapes of synthesized Au NPs, like sphere, cylinder, equilateral triangle (side length is 94 nm) and regular hexagon (side length is 55nm). The observed cylinder length ranges from 30nm to 230nm, and width is 30nm. Although the shape and size of the gold particles are various, they are hard to control. Still, it also gives us a possibility to synthesize *in situ* different shapes and sizes of Au NPs inside the layers by manipulating the temperature. Since non-spherical noble-metal nanoparticles typically exhibit more than one surface plasmon resonance mode, the wavelength of which is strongly dependent on their sizes and shapes, this could give access to a modulation of the optical properties of the nanocomposites.

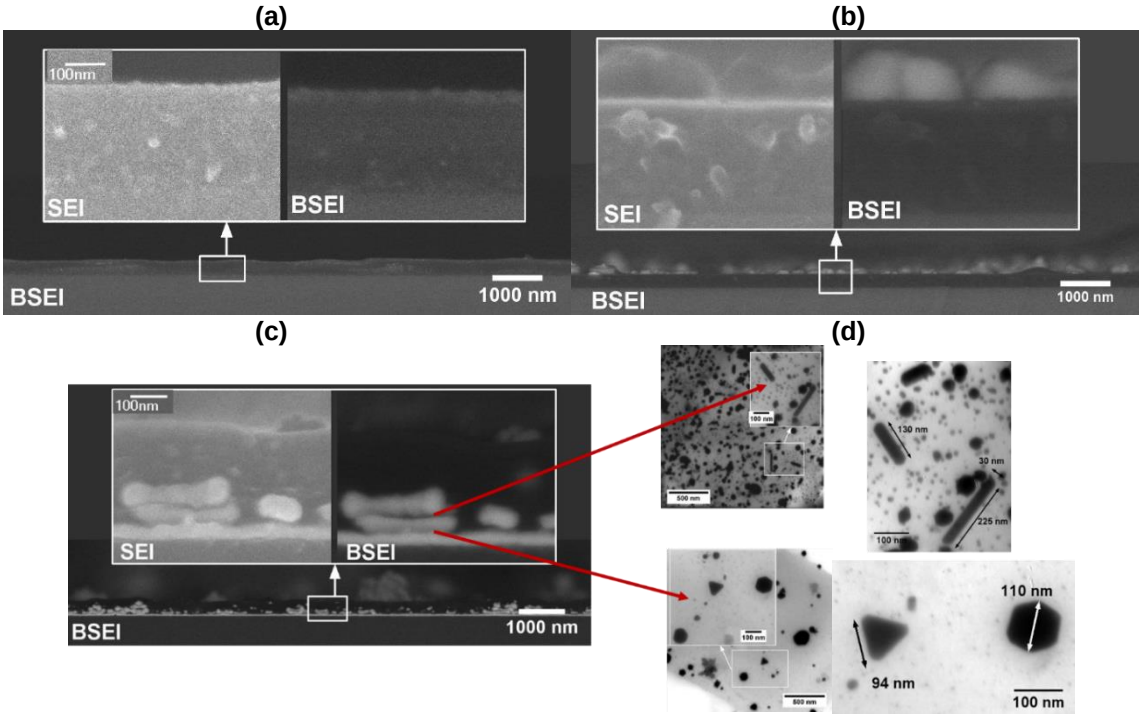

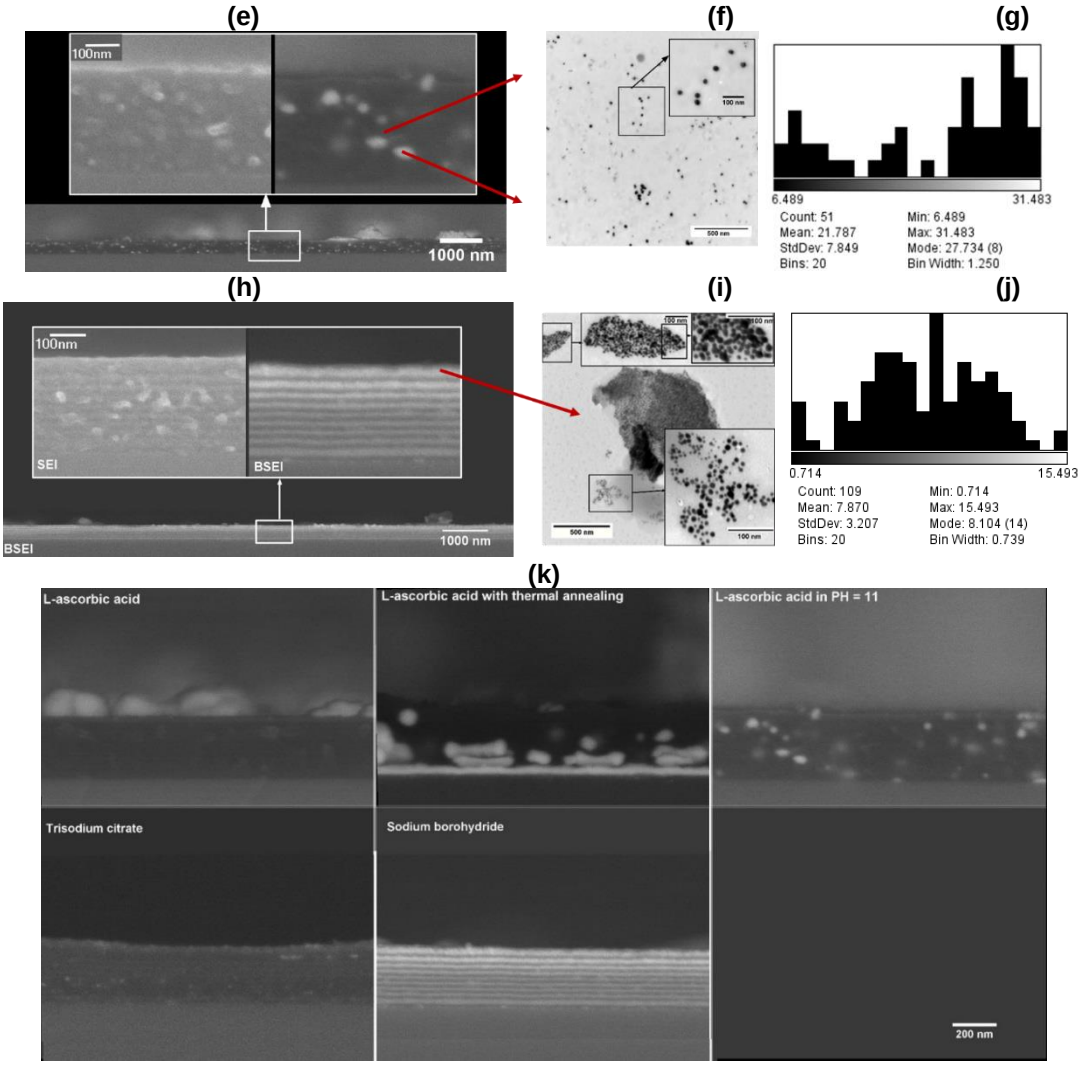

Figure V. 10 (a), (b), (c), (e) and (h) are SEM images in SEI (secondary electron image) and BSEI(backscattered electrons image). The bottom of each images shows a large view of the film at low magnification, the upper 2 images are zooms of the same place from white squares in SEI and BSEI. In SEI, we can see the film topography. In BSEI, white part is metallic and dark part is polymer. (a) SEM images of the sample reduced by Na_3Ct (N=8) in SEI and BSEI. (b) SEM images of sample reduced by AA (N=8) in SEI and BSEI. (a) and (b) show gold NPs formed on surface of the film but not inside the layers. (c) SEM images of sample reduced by AA (N=11) and thermal annealing (180 ºC in vacuum) in the last step. A lot of Au NPs have been produced and stay at the bottom of the film. The Au NPs observed by TEM are shown in (d). Various size and shape (sphere, triangle and cylinder) of Au NPs were synthesized. (e) SEM images of sample reduced by AA in pH=11. A few gold NPs were synthesized in the layers. The Au NPs observed by TEM are shown in (f) and they are spheres. The distribution of Au particles in histograms is shown in (g). Au NPs are polydisperse, the particle diameters range from 6 to-31nm, and there are two main sizes of particles, small ones are around 8nm, big ones are around 27nm. (h) SEM images of sample reduced by $NaBH_4$ N=20. Gold NPs were well introduced in the layers. The Au NPs observed by TEM are shown in (i) and they are spheres. The distribution of Au particles in histograms is showed in (j). Au NPs are polydisperse, the particles diameters range from 0.7 to 15nm, and the diameter of most particles is around 8nm. (k) Comparison of all samples under

BSEI SEM images. They have same structures before loading gold. The thicknesses of all the films are similar.

Sample prepared by AA in base solution (pH=11) is shown in Figure V. 10(e), (f) and (g). Figure V. 10 (e), (f) and (g) shows the SEM images of the samples, the TEM images of Au particles in the samples after the film has been dissolved and resulting NPs recovered on TEM grid, and the distribution of particle sizes in histograms, respectively. We can see that a few gold particles were synthesized inside layer and they are spheres with diameter sizes range from 6nm to 31nm. The distribution of Au particle sizes in histograms is shown in (g) and indicates that Au NPs are polydisperse, with particles the diameter ranging from 6nm to 31nm, and there are two main sizes of particles, small ones are around 8nm, big ones are around 27nm.The big particles size is bigger than the layer thickness (20nm), which indicates the damage of the lamellar structure.

The sample prepared by $NaBH_4$ is shown in Figure V. 10(h), (i) and (j). Figure V. 10(h), (i) and (j) show the SEM images of the sample, TEM images of Au NPs in the sample, and the distribution of particle sizes in histograms based on TEM images, respectively. We can see that gold particles were well synthesized and introduced inside the layers and they are spheres of diameters ranging from 1nm to 15nm. It means $NaBH_4$ can penetrate through the layers and get into contact with the gold salt.

We can compare the SEM images (Figure V. 10(k)) of samples prepared by AA with and without thermal annealing in the last step. We believe that the gold precursor are well loaded in the PVP layers. From the surface of the sample prepared by Na_3Ct (Figure V. 10 (a)) and AA (Figure V. 10(b)), there are gold NPs formed on surface. It means the gold salt can be reduced by the organic reducing agent. Therefore, the absence of reduction inside the layers is rather caused by the fact that the organic reducing agent cannot penetrate the layers to reduce Au salt inside samples rather than a low reducing ability.

Comparing the results of samples reduced by different reducing agents (Figure V. 10(k)), we can see that $NaBH_4$ is more efficient than Na_3Ct and AA. $NaBH_4$ (molecular weight 37.83 g/mol) has lower molecular weight, which gives it more mobility through the porosity of the polymer layers. On the contrary, the organic reducing agents, Na_3Ct (molecular weight 294.10 g/mol) and AA (molecular weight 176.12 g/mol) have larger

molecular weight and seems less capable of penetrating the polymer layers. This tends to confirm that the reducing agent permeates from the surface to the bottom of the film.

Results of optical properties

In order to trail the “kinetic” loading process, we measured the samples by SE at N=0, 3, 6, 9, 12, 15, 18 and 20. For samples prepared in Na_3Ct and AA (N=0, 3, 6, 7, 8), we measured only at N=0, 3, 6, 7 and 8, because as the value of N increased after 3, the measurement curves did not change anymore.

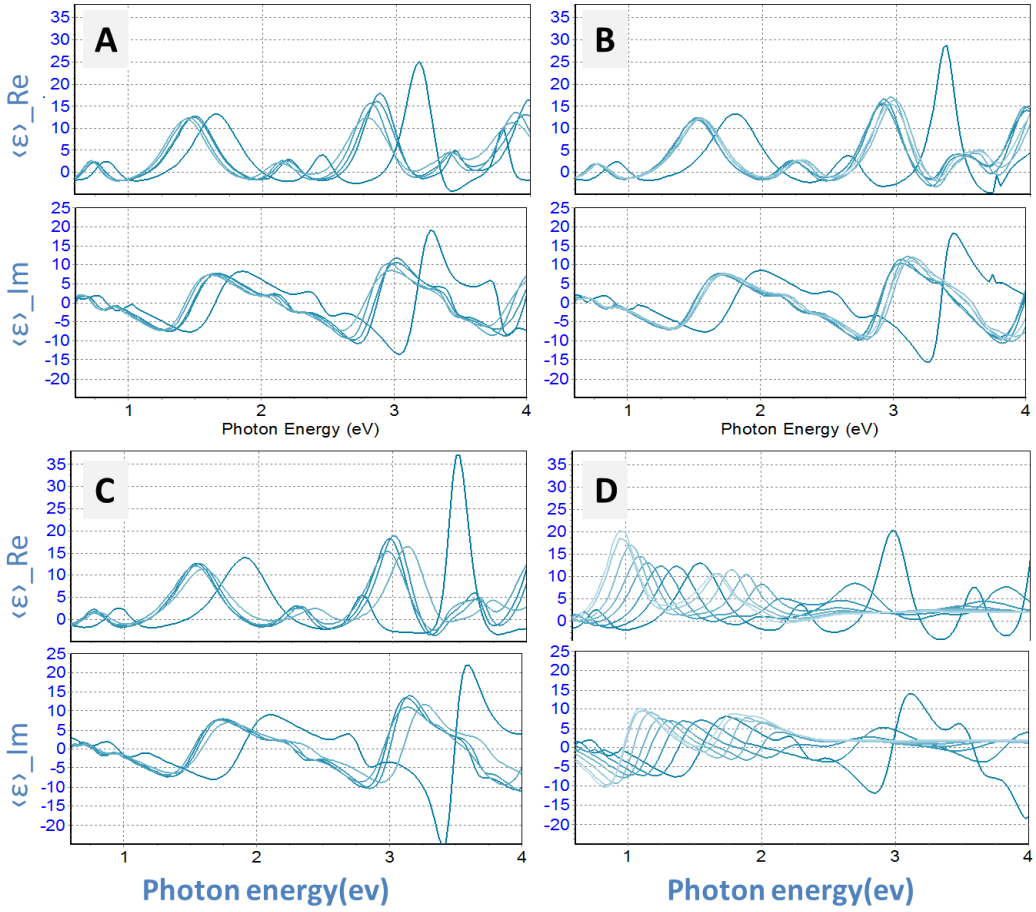

Figure V. 11 Real (Re, solid line) and imaginary (Im, dash line) parts of ‹ε› for different values of N between 0 and 20. The different colors of indicate different values of N. As the values of N increases, the line becomes gradually lighter. (A) gold salt reduced by Na_3Ct at room temperature and at 70 °C for values of N=0, 3, 6, 7, 8. (B) gold salt reduced by AA for values of N=0, 2, 6, 7, 8. (C) gold salt reduced by AA in condition of pH=11 for values of N=0, 3, 6, 9, 11. From the change of curves in plots (A) (B) and (C), it appears that the reactions were finished at the first loading process. No further reaction occurred after the first step. The fringes shift between N=0 and N=2 is caused by the increase of the film thickness or gold NPs deposition on the film surface. (D) gold salt reduced by $NaBH_4$ for values of N=0, 3, 6, 9, 12, 15, 18 and 20. The resonance amplitude varies as N increases, due to the increasing introduction of plasmonic NPs.

In this part, Model 1 (Figure V. 2(a)) is used to study the SE data. It assumes the whole sample including substrate as an effective bulk media. Although this ellipsometric model does not provide access to the anisotropic effective permittivity of the material, it gives primary “kinetic” information on the evolution of the resonance caused by the progressive gain of Au NPs. Figure V. 11 shows the real part and imaginary part of the pseudo-permittivity ‹ε› of the samples. Figure V. 11 A, B and C show that for samples prepared with organic reducing agents Na_3Ct or AA, the reactions were finished after the first loading process. Due to the increasing of film thickness and Au particles inside layer (reduced by AA in pH=11, Figure V. 10(e) (f) (g)) and on surface (reduced by Na_3Ct, Figure V. 10 (a) and AA, Figure V. 10 (b)), red shift of the fringes happened, but only at the first impregnation process. In the previous results from SEM and TEM, there are several particles in the layer of sample reduced by AA in pH=11, which is not obvious from the SE results. This is due to the low concentration of Au particles because the reducing process works only at the first step.

V.2 Removal irregular Au NPs on surface of films with high N

As we discussed in V.1, the best condition we found for the reducing step in the gold loading process is the use of an aqueous solution of sodium borohydride. This method works efficiently, but uncontrolled gold NPs are gradually deposited on the top of the film surface, for large N values, as well as inside the layers. In addition, the first two layers from the surface are sometimes loaded with more gold particles than the other layers. In order to avoid such inhomogeneous distribution of Au NPs in the layers and erase the irregular particles on the surface, two different techniques following the loading Au NPs process have been studied and will be presented here: 1. Reorganizing block copolymer by thermal annealing; and 2. Etching Au NPs by chemicals.

V.2.1 Thermal annealing after Au loading process

V.2.1.1 Introduction

As we know, block copolymers have the ability to spontaneously form periodic morphologies with controllable length scales. The self-assembly of block copolymers can be achieved through annealing the block copolymers thin film in a suitable environment, either at elevated temperature using thermal annealing[11–13],or by solvent

annealing[14–16]. Because solvent annealing is more difficult to control, we have started with thermal annealing. Thermal annealing (a temperature higher than the glass transition temperature) will give the copolymer a chance to move freely and reorganize the lamellar structure, which may “absorb” the Au NPs from surface to layers.

V.2.1.2 Experiment

Film preparation follows the same process as described in V.1.1.2, with 0.65 wt% reducing agent $NaBH_4$ and AA in H_2O.

Gold loading process

After we obtain the aligned and organized lamellar phases, 1) we immersed the films in 3.0 wt% $HAuCl_4$ solution in ethanol for 5 minutes followed by a rinsing of deionized water several times. 2) Afterward, the films with loaded $HAuCl_4$ were immersed into different 0.65 wt% aqueous solutions of $NaBH_4$ for 30 sec.

We repeat step 1) and 2) for N times of cycles (N is integrate from 0 to 30) to increase the concentration of Au NPs. This is noted as *Normal Process*.

We repeat step 1) and 2) for N times of cycles (N is integrate from 0 to 30) to increase the concentration of Au NPs. In additional, thermal annealing (180 ºC in vacuum for 2hours) was applied on samples after every 5 cycles of step 1) and 2) until N=30. This is noted as *Annealing Process*.

Measurement

The samples were observed by VASE using the configuration of UVISEL II with AOI=55º, 65º and 75º. For cross-sectional view of samples, the films on silicon wafer were broken in half manually and observed by SEM.

V.2.1.3 Results

Structures

As showed in Figure V. 12, the thermal annealing is an efficient method to remove the surface Au nanoparticles and rearrange the Au nanoparticles inside layers. The thermal annealing process for every 5 cycles preserves the self-assembled lamellar structure but not the arrangement of Au NPs in the layers. In order to understand the changes of this rearrangement, the SE data will be explained in the following paragraph.

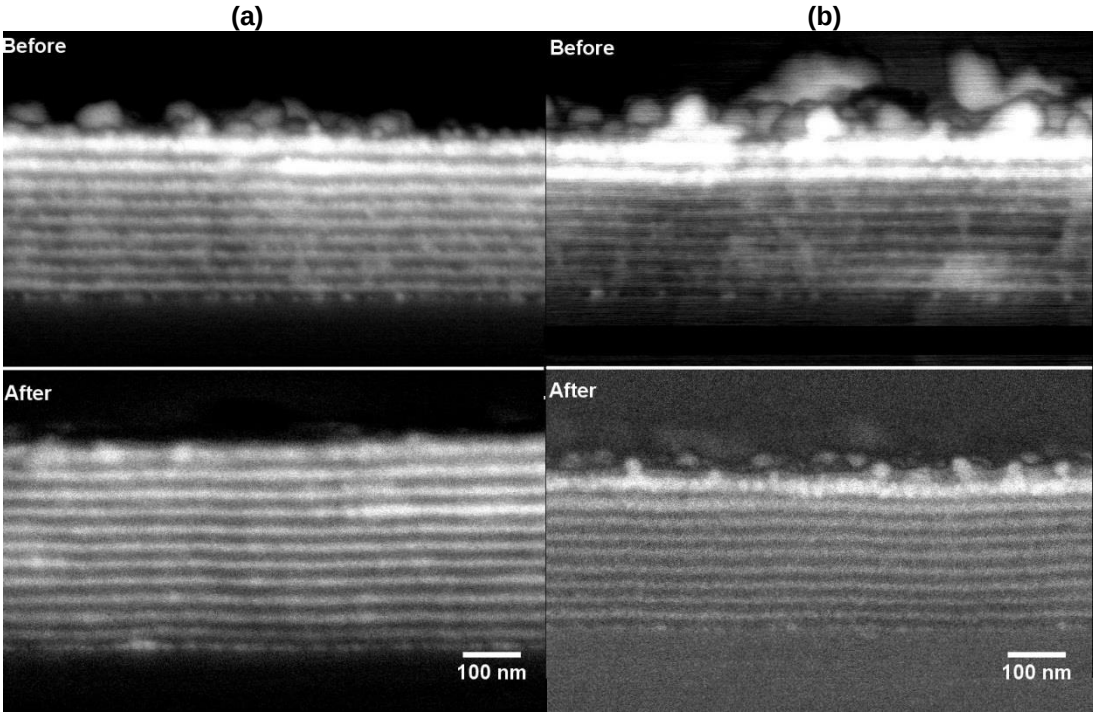

Figure V. 12 SEM images of (a) N=20 (b) N=30. Before means gold loading follow the Normal Process. After means gold loading follow the Annealing Process.

Results of optical properties

We measured the samples prepared by *Annealing Process* by SE at N=0, 5, 5(after thermal annealing), 10, 10 (after thermal annealing), 15, 15(after thermal annealing), 20, 20(after thermal annealing), 25, 25(after thermal annealing) and 30, 30(after thermal annealing), while the samples prepared by *Normal Process* at N=0, 5, 10, 15, 20, 25, 30.

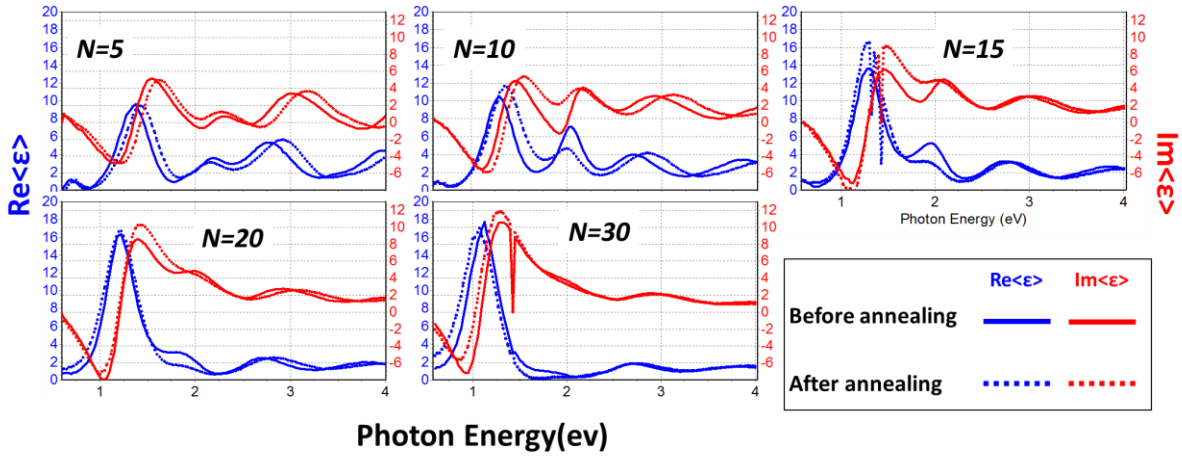

Figure V. 13 Comparing of the pseudo-permittivity <ε> before and after thermal annealing in N=5, 10, 15, 20 and 25. Continuous lines (dash lines) are before (after) annealing, while blue (red) lines are the real (imaginary) part of <ε>

In this part, Model 1 (Figure V. 2(a)) is used to analyze the SE data. It assumes the whole sample including substrate as an effective bulk media. Although this ellipsometric model does not provide access to the anisotropic effective permittivity of the material, it gives primary “kinetic” information on the evolution of the resonance caused by the progressive gain of Au NPs.

The Figure V. 13 compares the pseudo-permittivities <ε> of samples prepared by *Annealing Process*, before and after thermal annealing for different values of N. We can see that as the value of N increases, the fringes of <ε> in the UV range from 2.5eV to 4.0eV (λ~496nm to 310nm) are damped. This is due to the interband absorption of the gold particles. As the value of N increases the difference between the optical responses before and after annealing becomes smaller. In particular the peak around 2.1eV(λ~590nm) caused by the resonance of the gold NPs, increases after annealing at N=5 and then decreases after N=10. We can thus propose that during the annealing process at N=5, the shape or size of gold nanoparticles changed and then the annealing process have limited influence on the gold nanoparticles when N>5.

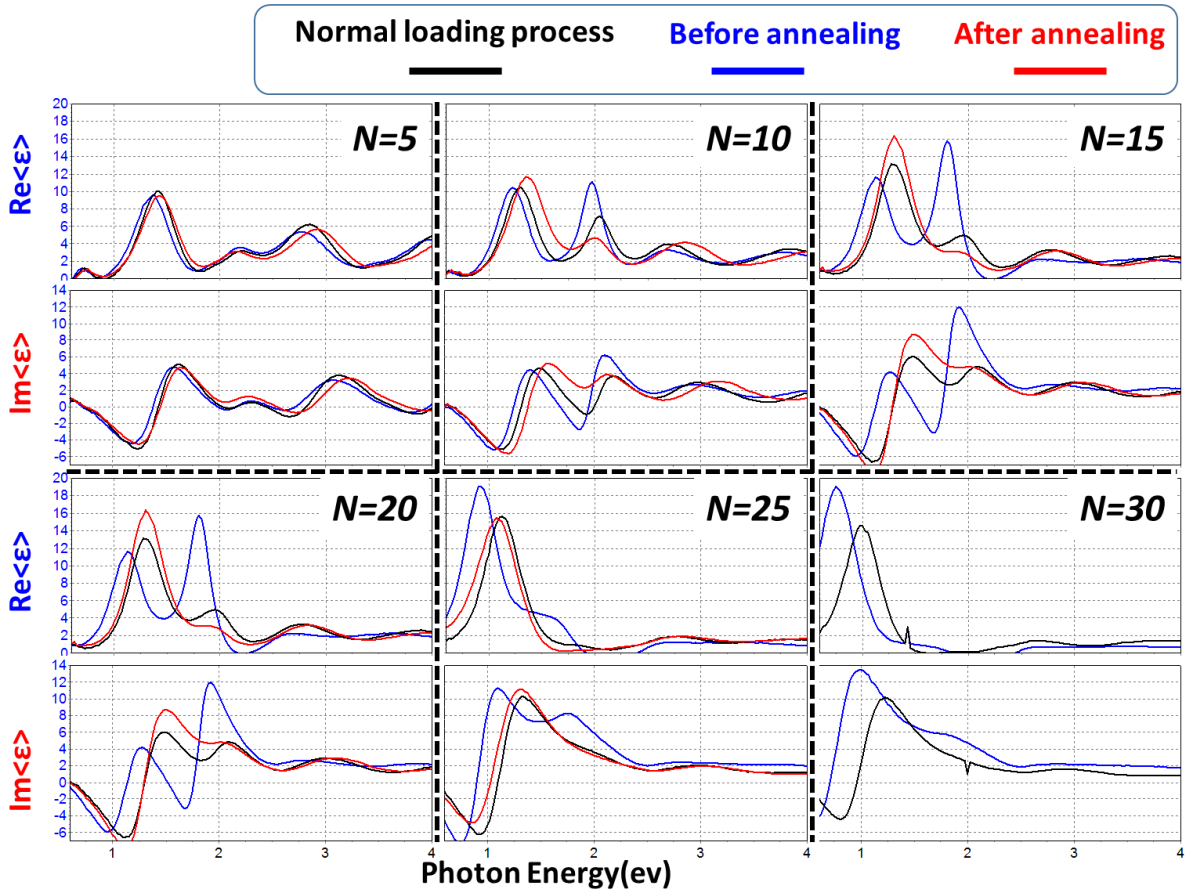

Figure V. 14 Comparison of samples prepared in Normal process(lines in blue) and Annealing process(lines in black and red) for N=5, 10, 15, 20, 25 and 30.

The Figure V. 14 compares the pseudo-permittivity <ε> of samples prepared by *Annealing Process* and *Normal process*. We observe a lost of fringes in the UV range for the both processes. At N=5, little difference is observed. A significant difference between the two processes is observed at the photon energy ranging from 2.1eV to 1.8eV (λ~590nm to 688nm) when N≥10. We can see that as the value of N increases, Re(<ε>) and Im(<ε>) of samples prepared by *Normal process* increase until N=20 while a decrease of the peak is observed in the samples prepared by *Annealing Process.* At N=25, in the case of *Normal process* the peak caused by resonance of gold NPs can still observed but become wider and smaller, which maybe due to the irregular particles deposited on the film surface; while in the case of *Annealing Process*, the resonance caused by gold NPs.is hardly visible in measured the signal. At N=30, both processes lost the resonance.

In conclusion, the *Annealing Process* can efficiently remove irregular particles on the film surface. However, the optical responses are impacted because the annealing also modifies the NPs inside the films. Therefore, the *Annealing Process* such as we studied is not a satisfying modification process.

V.2.2 Etching Au NPs on surface

V.2.2.1 Introduction

As we discussed in V.2.1, even though the *Annealing Process* can remove the irregular surface gold nanoparticles efficiently, the structure of gold nanoparticles inside the layers is changed and the optical responses are impaired because the resonance of the Au NPs is mostly lost. Thus, we are going to etch Au NPs by chemicals directly to preserve the gold nanoparticles inside the layers.

Three different chemicals are used here: 11-mercaptoundecanoic acid (11-MUA), aqua regia and potassium iodide.

V.2.2.2 11-MUA

Introduction

11-mercaptoundecanoic acid (11-MUA)[17,18] is a well-known gold-capping and reducing agent, which contains an organosulfur compound thiol–SH. With metal ions, thiolates behave as ligands to form transition metal thiolate complexes. The structure formula of 11- MUA is shown below Figure V. 15.

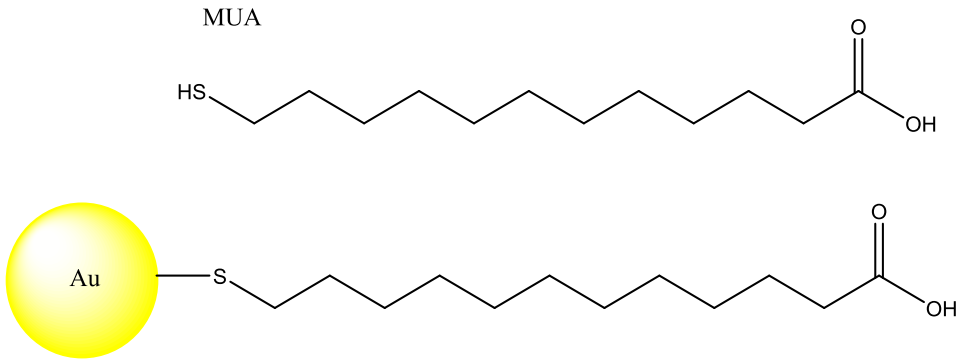

Figure V. 15 The structure formula of 11- MUA

11-MUA has a carboxyl group, which deprotonated at high pH.[19] When 11-MUA is used as ligand for gold nanoparticles, the charge of the carboxylic group induces an electrostatic repulsion, which stabilizes the nanoparticles in water.

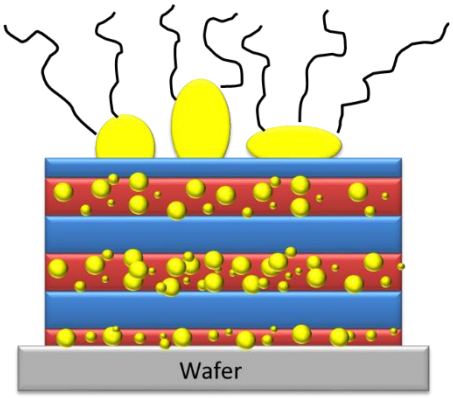

Figure V. 16 Schematic of the removal of surface Au NPs by 11-MUA. Red part is nanocomposite layer of Au and PVP, blue part is PS, yellow part is gold, and black lines are 11-MUA.

In this study, we plan to use the properties of 11-MUA and attach it to the gold nanoparticles on the surface of the film. Due to its large molecular weight, 11- MUA cannot easily penetrate in the polymer films. Therefore, the removal of the particles may happen only on the surface without collapsing the lamellar structures and the Au nanoparticles inside the layers may be preserved, as Figure V. 16 shows.

Experiment

The film preparation follows the same process as described in Chapter V.1.1.2.

Au loading process:

After we obtained the aligned and organized lamellar phases, 1) we immersed the film in 3.0 wt% $HAuCl_4$ solution in ethanol of for 5 minutes followed by a rinsing with

deionized water several times. 2) Afterwards, the film with loaded $HAuCl_4$ was immersed into an aqueous solution of 0.65 wt% sodium borohydride for 30 sec. We repeat step 1) and 2) for N times of cycles(N >=30).

MUA solution preparation:

5 mg 11-MUA, 1 mg NaOH were dissolved in 5 ml distilled water.

Removal process:

The sample was immersed in MUA solution and put in an ultrasonic bath for 5-8 mins.

Measurement:

The films on silicon wafer were broke in halfmanually and observed by SEM.

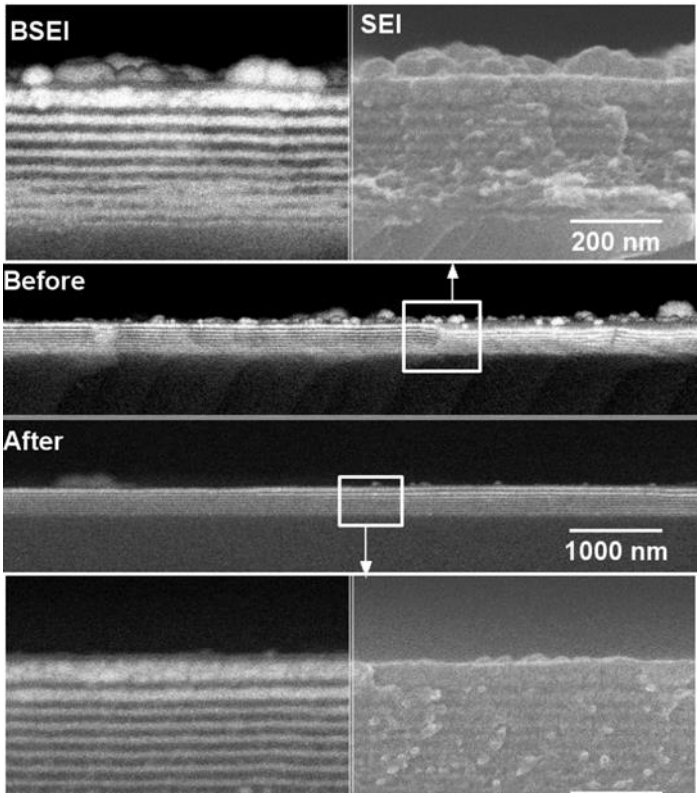

Figure V. 17 SEM images of samples before and after treatment by 11-MUA with ultrasons. The middle 2two images are low-magnification BSEI images. The upper two images are the zoom of part of sample before treatement by 11-MUA in white square under high-magnification in SEI and BSEI, respectively. Lower two images are the zoom of part of sample after treated by 11-MUA in white square under high-magnification in SEI and BSEI, respectively.

Results

Because the reducing agents penetrate from the surface as we discussed in Chapter V.1, the *in situ* synthesis of Au NPs in PVP layers is inhomogeneous, especially the first two layers from the top are sometimes denser than the others. They contain more gold NPs than the other layers as we discussed previous. Since 11-MUA barely penetrates the film, the gold removal can only happen on the top surface and not inside the layers. This seems confirmed by our observations, as in Figure V. 17, we can see that the irregular gold nanoparticles on the surface are well removed by MUA treatment, and that the first two layers from the top still contain more Au NPs than the other layers, and the structure of the film did not collapse.

There is, however, a possibility that this treatment damaged the film. Figure V. 18 shows a thicker film treated in the same conditions, which was damaged by the ultrasons. We would need to control the time and frequency of ultrasonic treatment, depending on different polymer composition and film thickness in order to avoid the creation of defects on films.

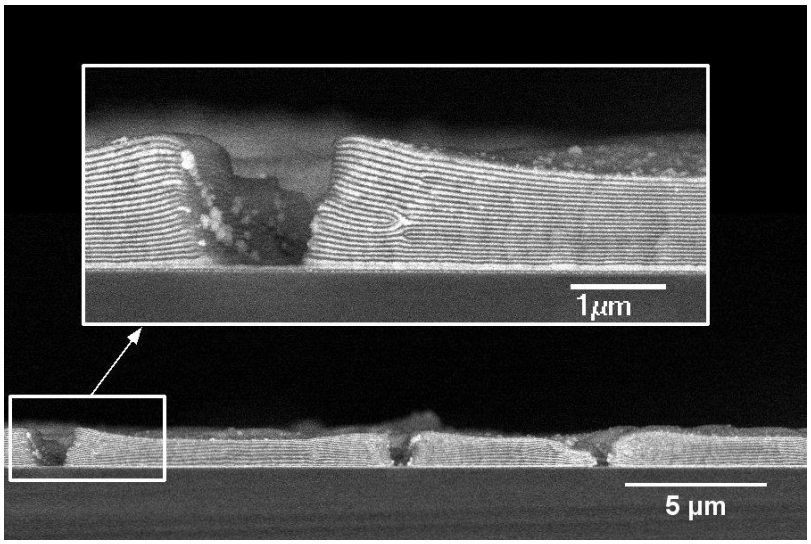

Figure V. 18 Defects caused by ultrasons after treatment by 11-MUA.

11-MUA is efficient for removing the gold NPs on the film surface. However, the time and frequency of ultrasons needs to be adjusted depending on different film polymer and thickness. Besides, the first two layers still need to be fixed. We considered to using wet etching to remove Au on the surface and in the first two layers. This study is going to be explained in the coming sections.

V.2.2.3 Aqua regia

Introduction

As we know, the traditional medium for dissolving gold is aqua regia. It is a mixture of three parts of concentrated hydrochloric to one part of concentrated nitric acid. The reactions involved are as follows[20]:

$$2HNO_3 + 6HCl \rightarrow 2NO + 4H_2O + 3Cl_2$$

$$2Au + 9HCl + 3HNO_3 \rightarrow 2AuCl_3 + 3NOCl + 6H_2O$$

$$3HCl + HNO_3 \rightarrow Cl_2 + NOCl + 2H_2O$$

The last reaction is reversible. If the aqua regia solution is diluted with water, then chlorine and nitrosyl chloride recombine to form hydrochloric acid and nitric acid. From the SEM images of films (see Figure V. 1), we can see that the size of the gold NPs on the surface is around 200 nm. The initial idea is that Aqua regia could dissolve the naked Au NPs on surface and the Au in layers could be protected by polymers. Since

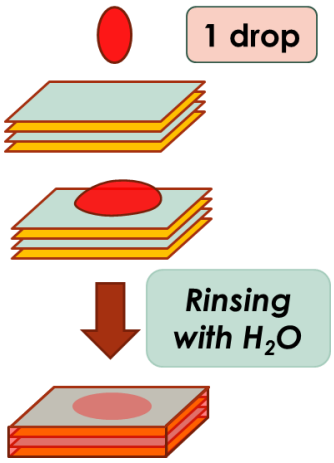

Figure V. 19 schematic removal process

the reaction is fast and the reactant aggressive, aqua regia should stay only shortly on the film.

Experiment

"Film preparation" and "Au loading process" are same as V.2.2.1.

Aqua regia preparation:

Add 1 part concentrated nitric acid HNO_3 to 3 parts concentrated hydrochloric acid HCl with slow pouring inside of the acid fume hood. The appearance of an orange/red solution color and gas bubbles is an indication that the reaction is progressing. Aqua regia-is prepared immediately before use.

Removal process:

Put 1 drop of aqua regia solution on the samples and rinsing with distilled water instantly. And repeat this process for 2, 4 and 6 times in order to get a better surface. Figure V. 19 shows the schematic removal process.

Measurement:

For cross-sectional view of samples, the films on silicon wafer were broke in half manually and observed by SEM.

The surface were observed by Optical Microscope (OM).

Results

Aqua regia is aggressive and the reaction with gold is fast. Our observations after 6 times of removal process (see Figure V. 20(a)) show that not only the gold NPs on the surface but also in the layers of the sample, were removed. We then reduced the treatment cycles to 4 times (see Figure V. 20 (b)) and 2 times (see Figure V. 20(c)). The gold NPs on the surface became smaller and the Au NPs in the first top two layers are similar to the NPs in the other layers.

This method can remove gold NPs efficiently, but there are two main problems: First one is shown in Figure V. 20(d): if there are many defects in the film, the gold NPs in the layers will be rinsed to the bottom and will aggregate. The second problem is shown in Figure V. 20(e): because the fast reaction between aqua regia and Au, we

used drops instead of immersing the films in aqua regia and the reagent concentration on the surface is therefore inhomogeneous. As we can see in optical microscope image, this causes the different colors on the surface, corresponding to different concentration of Au NPs in the layers.

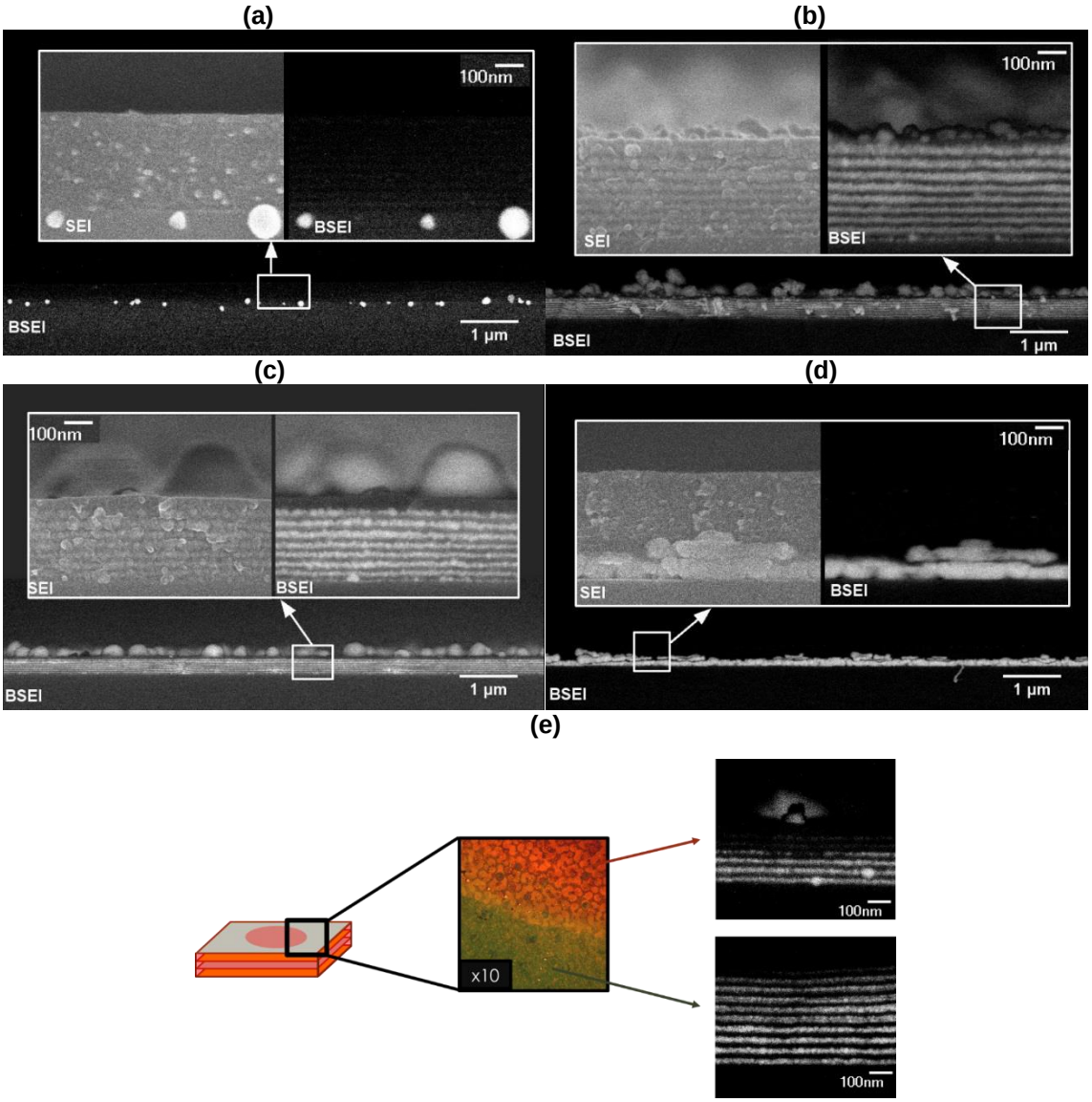

Figure V. 20 (a) (b) and (c) are SEM images of cross-section of films treated by aqua regia in 6 cycles, 4 cycles and 2 cycles, respectively. (d) Film with defects after treatment by aqua regia in 2 cycles. (e) Schematic of inhomogeneous treatment by aqua regia. The middle image is under optical microscope. Right images are SEM micrographs of sections corresponding to different surface color.

In order to fix the problem, we plan to use another milder etching agent and we chose potassium iodide. The following section will present this study.

V.2.2.4 Potassium iodide KI-I_2

Experiment

"Material", "Film preparation", and "Au loading process" are the same as V.2.2.1.

Potassium iodide solution preparation:

Add 4 g of Potassium Iodide KI, 1 g of Iodine I_2 and 40 ml distilled water in a glass container. Then stir until all the solid is dissolved in water.

Removal process:

Put 1 drop of KI-I_2 solution on the samples and rinsing with distilled water instantly. And repeat this process for 2, and 4 times in order to get a better surface. Figure V. 19 shows the schematic removal process. Or immerse the sample in the KI-I_2 solution for 10 seconds and rinsing with distilled water instantly.

Measurement:

For side view of the samples, the films on silicon wafer were broke in half manually and observed by SEM.

Results

As we mentioned in the Chapter II.3, SEI is secondary electron image and BSEI is backscattered electrons image. In SEI, we could see the topography of the film. In BSEI, white part is metallic and dark part is polymer. So in order to fully understand the structure of film, we should compare SEI and BESI images. Figure V. 21 (a) (b) and (c) show the side view SEM images of the samples treated by KI-I_2 for 4 drops, 2 drops and immersed for 10 sec. We can see that after treatment with 4 drops, there are some "black holes" in the film, which are not real holes: In SEI, we can see that the polymers and the lamellar phase are present, but in BSEI appears like a hole. Comparing the SEI and BSEI images, we can see that this "black hole" is actually polymer without gold, which results from the fact that the etchant solution permeates through the polymer film and removes the Au NPs in the layers.

The treatment with 2 drops Figure V. 21(b) removes the irregular Au NPs on surface and preserves the Au NPs inside the layers. The treatment with 10 sec immersing Figure V. 21(c) removes the Au NPs on the surface as well as in the first 2 layers. As we explained previously, comparing the SEI and BSEI images, we can see

that the film seen by SEI appears “thicker” than seen by BSEI. In the first two layers, all the Au NPs were removed by the KI-I_2 solution. The first two layers are still a lamellar phase consisting of pure polymer PS and PVP layers. This is why they appear black under BSEI.

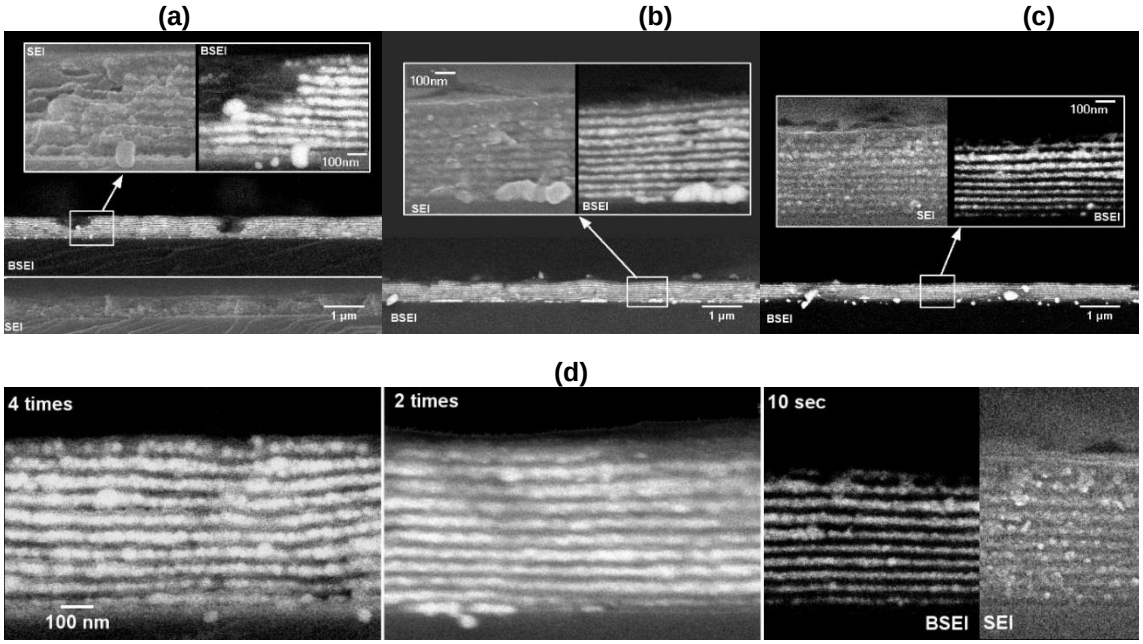

Figure V. 21 (a) (b) and (c) are SEM images of side views of the films after treatment by 4 drops of KI-I_2 solution, 2 drops of KI-I_2 solution and 10 seconds immersing in KI-I_2 solution, respectively. The bottom of each images show large view of the films at lower magnification, the upper two images are zooms of the same place from white squares in SEI and BSEI. In SEI, we could see the film topography. (d) is the comparison of different level of treatment.

Figure V. 21(d) shows the comparison of three different treatments by the KI-I_2 solution. The etching reaction with KI-I_2 goes soft and controllable. The reaction with drops leads to inhomogeneous surfaces like in the case of aqua regia. The immersion method is more homogeneous. We can propose, as a conclusion, that the immersion with shorter time and lower concentration of KI-I_2 could be a better method to remove Au NPs on surface and optimizing the Au distribution in the layers.

As a conclusion, the solvent used for the introduction of the reducing agent is important for the gold loading method and can tune the structure of the gold nanoparticles. When the value of N is high, irregular particles are present on the film surface, and we showed that they can be removed by an etching solution or a thermal annealing step.

References

1. Shen, H., Zhang, L. & Eisenberg, A. Multiple pH-induced morphological changes in aggregates of polystyrene-block-poly (4-vinylpyridine) in DMF/H2O mixtures. *J. Am. Chem. Soc.* **121,** 2728–2740 (1999).
2. Sohn, B. H. & Seo, B. H. Fabrication of the multilayered nanostructure of alternating polymers and gold nanoparticles with thin films of self-assembling diblock copolymers. *Chem. Mater.* **13,** 1752–1757 (2001).
3. Lin, H., Steyerl, A., Satija, S. K., Karim, A. & Russell, T. P. Solvent penetration into ordered thin films of diblock copolymers. *Macromolecules* **28,** 1470–1474 (1995).
4. Centeno, E. & Moreau, A. Effective properties of superstructured hyperbolic metamaterials: How to beat the diffraction limit at large focal distance. *Phys. Rev. B* **92,** 45404 (2015).
5. Belov, P. A. & Hao, Y. Subwavelength imaging at optical frequencies using a transmission device formed by a periodic layered metal-dielectric structure operating in the canalization regime. *Phys. Rev. B* **73,** 113110 (2006).
6. Kang, X.-B., Tan, W. & Wang, Z.-G. Validity of effective medium theory for metal-dielectric lamellar gratings. *Opt. Commun.* **284,** 4237–4242 (2011).
7. Johnson, P. B. & Christy, R.-W. Optical constants of the noble metals. *Phys. Rev. B* **6,** 4370 (1972).
8. Frens, G. Controlled nucleation for the regulation of the particle size in monodisperse gold suspensions. *Nature* **241,** 20–22 (1973).
9. Pong, B.-K. *et al.* New insights on the nanoparticle growth mechanism in the citrate reduction of gold (III) salt: formation of the Au nanowire intermediate and its nonlinear optical properties. *J. Phys. Chem. C* **111,** 6281–6287 (2007).
10. Grzelczak, M., Pérez-Juste, J., Mulvaney, P. & Liz-Marzán, L. M. Shape control in gold nanoparticle synthesis. *Chem. Soc. Rev.* **37,** 1783–1791 (2008).
11. Han, E. *et al.* Perpendicular orientation of domains in cylinder-forming block copolymer thick films by controlled interfacial interactions. *Macromolecules* **42,** 4896–4901 (2009).
12. Albert, J. N. L. & Epps, T. H. Self-assembly of block copolymer thin films. *Mater.*

Today **13,** 24–33 (2010).

13. Xiao, S., Yang, X., Edwards, E. W., La, Y.-H. & Nealey, P. F. Graphoepitaxy of cylinder-forming block copolymers for use as templates to pattern magnetic metal dot arrays. *Nanotechnology* **16,** S324 (2005).
14. Giermanska, J., Sekar, S., Ly, I. & Chapel, J.-P. Influence of the formulation pathway on the growth of polyelectrolyte multilayer films. *Colloids Surfaces A Physicochem. Eng. Asp.* **509,** 666–674 (2016).
15. Ghoshal, T. *et al.* Morphological evolution of lamellar forming polystyrene-block-poly(4-vinylpyridine) copolymers under solvent annealing. *Soft Matter* **12,** 5429–5437 (2016).
16. Malassis, L. *et al.* Bottom-up Fabrication and Optical Characterization of Dense Films of Meta-Atoms Made of Core–Shell Plasmonic Nanoparticles. *Langmuir* **29,** 1551–1561 (2013).
17. Laaksonen, T., Ahonen, P., Johans, C. & Kontturi, K. Stability and Electrostatics of Mercaptoundecanoic Acid- Capped Gold Nanoparticles with Varying Counterion Size. *ChemPhysChem* **7,** 2143–2149 (2006).
18. Smalley, J. F., Chalfant, K., Feldberg, S. W., Nahir, T. M. & Bowden, E. F. An indirect laser-induced temperature jump determination of the surface p K a of 11-mercaptoundecanoic acid monolayers self-assembled on gold. *J. Phys. Chem. B* **103,** 1676–1685 (1999).
19. Su, C.-H., Wu, P.-L. & Yeh, C.-S. pH dependence of interparticle coupling for gold nanoparticle assemblies formation: Electrostatic attraction and hydrogen bonding. *Bull. Chem. Soc. Jpn.* **77,** 189–193 (2004).
20. Sheng, P. P. & Etsell, T. H. Recovery of gold from computer circuit board scrap using aqua regia. *Waste Manag. Res.* **25,** 380–383 (2007).

Chapter VI Optical properties

Introduction

As we discussed in the Chapter III “film fabrication”, Chapter IV “gold loading process” and Chapter V “film structure optimization”, we produced our target nanostructures with well controlled film thickness, bilayer thickness, volume fraction of gold nanoparticles in the PVP layers, shape and size of the gold nanoparticles. Once the fabrication and structural characterization steps are completed, we would like to choose several typical films to study their optical properties and the relation between structure and optical responses.

In this chapter, we are focusing on the question of how the structure influences the optical properties. However, with our self-assembled nanostructures, presenting some degree of disorder, it is often difficult to find a good model to analyze the experimental data. In this chapter, we are going to study the SE data by several models to understand the relations between optical properties and structure parameters.

VI.1 Ellipsometric modelling

In order to extract the effective optical properties of the studied films from the SE data, two different models were built (see Figure VI. 1).

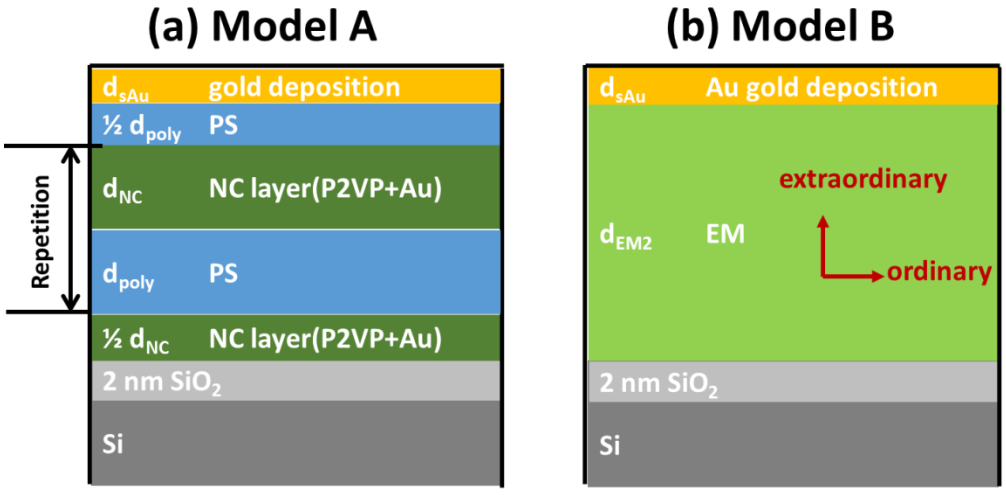

Figure VI. 1 Models used for analyzing the SE data. (a) Model A is a complete multilayer stack, using the SEM information on number and thicknesses of all the layers (b) Model B assumes the film is a uniaxial anisotropic layer. PS stands for pure polystyrene and NC for the nanocomposite composed of gold nanoparticles and poly (2-vinylpyridine. The “kinetic” SE data are analyzed so as to extract the N-independent dimensions d_{NC},d_{PS},d_{EM2}, and the N-dependent parameters,

which are the thickness d_{SAu} and dielectric function of the upper gold layer, and the dielectric functions of the polymer-gold nanocomposite effective media NC, and EM2

VI.1.1 Model A

The first model in Figure VI. 1(a) is built using the information on the layer number and thicknesses, appropriate interface layers and number of bilayer repetitions inferred from the SEM images, as is already mentioned in the Chapter V.1. In this model, the thickness of the individual layers are d_{PS}, d_{NC}, where the bottom and top half-layer thickness are fixed to $d_{PS}/2$ and $d_{NC}/2$, respectively, as usually observed in lamellar block copolymer thin films. An additional homogeneous layer of thickness d_{SAu} is added in the model, to account for the uncontrolled gold deposit layer. The optical properties of the PS layer are fixed to those of the Woolam database. The permittivity ε_{NC} of the NC layers is determined by fitting the Model A to the SE data using the BSPLINE function available in the Complete Ease software and using a Maxwell-Garnett Effective medium as an initial guess. This fitting procedure allows to extract $\varepsilon_{NC}(\lambda)$ for the different values of N.

Equation 6- 1
$$\varepsilon_{MG} = \varepsilon_{PS-P2VP}\frac{\varepsilon_{Au}(1+2f)+2\varepsilon_{PS-P2VP}(1-f)}{\varepsilon_{Au}(1-f)+\varepsilon_{PS-P2VP}(2+f)}$$

The unknown, which will be extracted from the fit of model A to the experimental data, is the permittivity $\varepsilon_{NC}(\lambda)$ of the NC layers. Once this function is determined, the optical properties of the uniaxial effective medium $\varepsilon_{//}(\lambda)=\varepsilon_{//}'(\lambda)+ i\ \varepsilon_{//}''(\lambda)$ and $\varepsilon_z(\lambda) + \varepsilon_z'(\lambda) + i\ \varepsilon_z''(\lambda)$ can be calculated, using the relation[1–3] as follows:

Equation 6- 2
$$\varepsilon_{//} = \left(\frac{d_{NC}}{d_{NC}+d_{PS}}\right)\varepsilon_{NC} + \left(\frac{d_{PS}}{d_{NC}+d_{PS}}\right)\varepsilon_{PS}$$

Equation 6- 3
$$\frac{1}{\varepsilon_z} = \left(\frac{d_{NC}}{d_{NC}+d_{PS}}\right)\frac{1}{\varepsilon_{NC}} + \left(\frac{d_{PS}}{d_{NC}+d_{PS}}\right)\frac{1}{\varepsilon_{PS}}$$

ε_{NC} is the only unknown factor in Equation 6- 2 and Equation 6- 3. To obtain ε_{NC}, we assume the NC layer can be described by a mixture of polymer (ε_m listed Figure VI. 2) and Au NPs (ε_{Au} listed Figure VI. 2). The mixture is following the Maxwell-Garnett Effective Medium Approximation (Equation 6- 1, detailed in Chapter II.1.3). The permittivity of gold nanoparticles and polymers used in this section is shown in Figure VI. 2.

In order to access the anisotropic effective permittivity of the lamellar material, we then apply an effective medium approximation to the perfect periodic lattice of Model A. It is well known that the transfer matrix for the superlattice, $M_{SL}=(M_{PS}\times M_{NC})^m$ may be replaced by the transfer matrix[22] of an effective uniaxial layer ($M_{uniaxial}$) if the number of repetitions is large, and $\frac{2\pi}{\lambda_o}n_{PS}d_{PS} \ll 1$ and $\frac{2\pi}{\lambda_o}n_{NC}d_{NC} \ll 1$, where n_{PS} and n_{NC} are optical indices of PS and NC, respectively, the latter being a function of N.

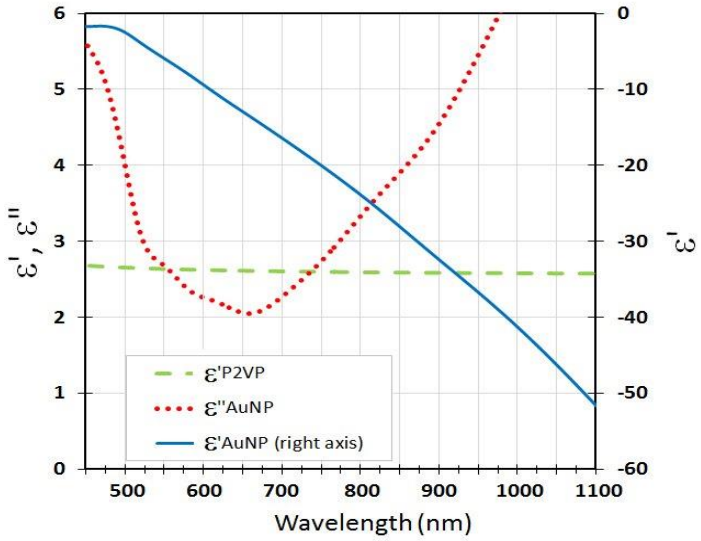

Figure VI. 2 Permittivity of the nanoparticle gold $\varepsilon_{Au}=\varepsilon_{AuNP}' + i\,\varepsilon_{AuNP}''$ and of the polymer $\varepsilon_m=\varepsilon_{P2VP}'$ as used in the Maxwell-Garnett model presented in the analysis of the NC layer properties. The gold permittivity is obtained by a well-described modification from the Johnson & Christy tabulated data in order to take into account finite size effects in the nanoparticles[4], while the polymer permittivity was obtained independently.

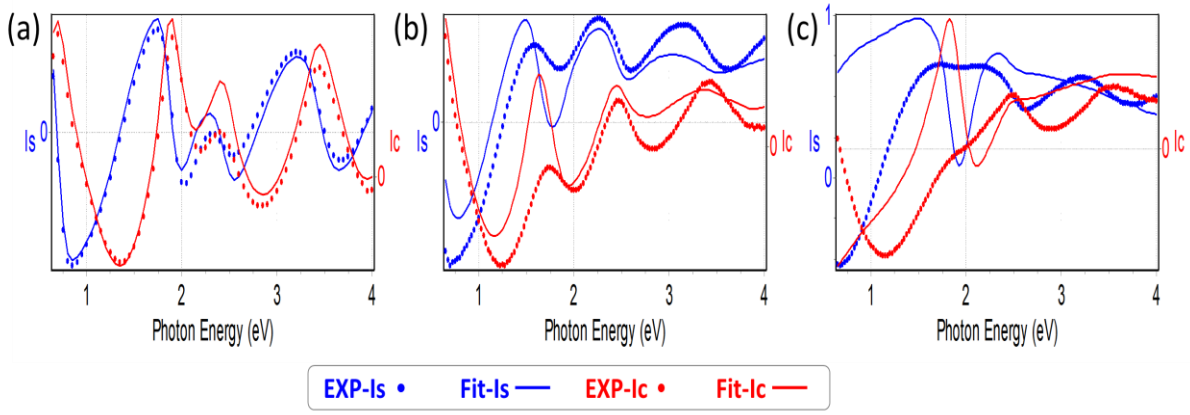

Figure VI. 3 Three examples of the fitting lines (continuous lines) and experimental data (dots) for different values of N, (a) N=5 (b) N=20 (c) N=30.

Finally, Model A first allows us to extract ε_{NC} from the experimental VASE data, from which we then calculate $\varepsilon_{//}$ and ε_z, using Equation 6- 2 and Equation 6- 3.

This model works efficient to extract $\varepsilon_{//}$ and ε_z of the films, but not well in the high volume fraction of gold nanoparticles. Figure VI. 3 show the fitting lines using the multilayer model for values of N=5(a), 20(b) and 30(c). We can see that at N=20, the model is not good enough especially in the gold plasmon resonance region ca. 1.9eV to 2.2eV (λ 625nm to 563nm). So we propose another simpler model of Figure VI. 1(b).

Spline function is defined as piecewise polynomials of degree n and used as approximating functions in mathematics and numerical analysis. The definition[5] is shown in Equation 6- 4 and Equation 6- 5.

Equation 6- 4 $$y = S(x) = P_i(x) = a_i + b_i x + c_i x^2 + d_i x^3$$

$\xi_{i-1} \le x \le \xi_i$ and $\xi_0 = -\infty;\ \xi_{m+1} = \infty$

Equation 6- 5 $$P_i^{\,k}\left(\xi_i\right) = P_{i+1}^{\,k}\left(\xi_i\right); k = 0, 1, 2; j = 1,2, \cdots, m$$

Where, $P_i^{\,k}$ denotes the *k*th derivative of the *j*th polynomial piece. n is the degree of the spline function. m is the number of knots. ξ_j is the positions of the knots. The free coefficients of the spline function is m+n+1. Each polynomial piece has n+1 coefficients, and the continuity conditions introduce n bands per knot, leaving (m+1)(n+1)-mn=M+N+1 free coefficients. Is an example of fitting process. The data treatments follow this rules.

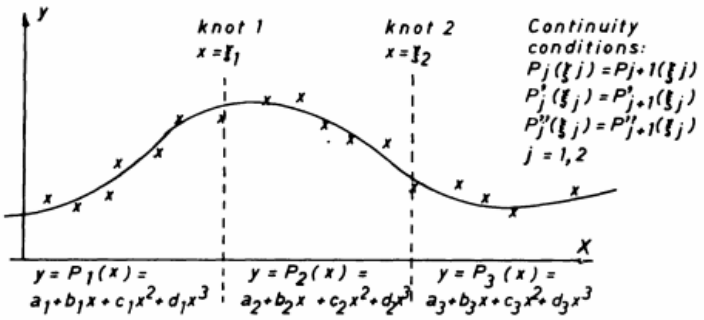

Figure VI. 4 spline function(solid curve) with two knots, fitted to data points(crosses)

Any spline function[6] of given degree can be expressed as a linear combination of B-spline. B-splines have knots that are equidistant from each other. B-splines can be used for curve-fitting because they creates smooth curves.

VI.1.2 Model B

The second model is a direct uniaxial effective medium approach. As demonstrated by the SEM images, the films are structurally uniaxial and homogeneous and we can define their dielectric permittivity tensor with the ordinary (parallel to the substrate, $\varepsilon_{ord}=\varepsilon_{//}$) and extraordinary (normal to the substrate, $\varepsilon_{extraord}=\varepsilon_z$)

VI.1.2.1 Model B-1

The Model B-1 (Figure VI. 1(b)) is a direct uniaxial effective medium approach (compared to the indirect approach using the fitted lamellar stack) in which we use the super-lattice results as initial guesses. It combines the surrounding half layers, i.e. the bottom $d_{NC}/2$ and top layer $d_{PS}/2$ into the effective uniaxial layer, in order to account for the whole self-assembled diblock copolymer film. The uniaxial permittivity ($\varepsilon_{//}$, ε_z) of the medium EM2 is determined by fitting the Model B-1 to the SE data using the BSPLINE function available in the Complete Ease software and using the results of Model A as an initial guess. This fitting procedure allows to extract $\varepsilon_{//}(\lambda)$ and $\varepsilon_z(\lambda)$ for the different values of N.

VI.1.2.1 Model B-2

We assume that the film is a uniaxial anisotropic film. Shown in Figure VI. 1(b), it consists of the $\varepsilon_{//}(\lambda)$ (for ordinary) and $\varepsilon_z(\lambda)$ (for extraordinary). In order to construct the components $\varepsilon_{//}(\lambda)$ and $\varepsilon_z(\lambda)$, we can point out that, if $\varepsilon_{NC}(\lambda)$ follows a Maxwell-Garnett variation (equation 6-3), and $\varepsilon_{PS}(\lambda)$ is a constant on most of the wavelength range, then equations 6-1 and 6-2 will lead to functions $\varepsilon_{//}(\lambda)$ and $\varepsilon_z(\lambda)$, which present also a Maxwell-Garnett variation, with amplitudes slightly varying with the gold volume fraction for $\varepsilon_{//}(\lambda)$ and strongly varying with the gold volume fraction for $\varepsilon_z(\lambda)$. Therefore, in this model, $\varepsilon_z(\lambda)$ is described by a mixture of polymer and gold, with a Maxwell-Garnett Effective Medium Approximation (see Figure VI. 5) and a gold volume fraction f fixed to 5 %(see Equation 6-1).

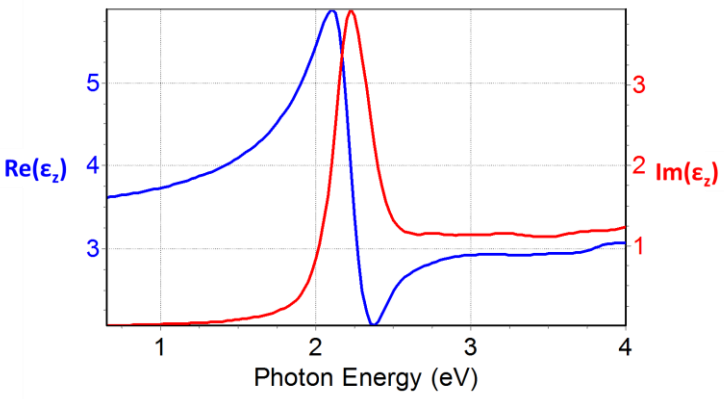

Figure VI. 5 $\varepsilon_z(\lambda)$ used in Model B

As we detailed in the Chapter II.1, PS-P2VP is described by the New Amorphous dispersion relation (see Equation 2-8) with the parameter n_∞=1.507, $\omega_g = 3.833eV$, $f_j = 0.055eV$, $\omega_j = 5.397eV$ and $\Gamma_j = 0.593eV$. The permittivity of gold nanoparticles[7] and PS-P2VP are shown in Figure VI. 6.

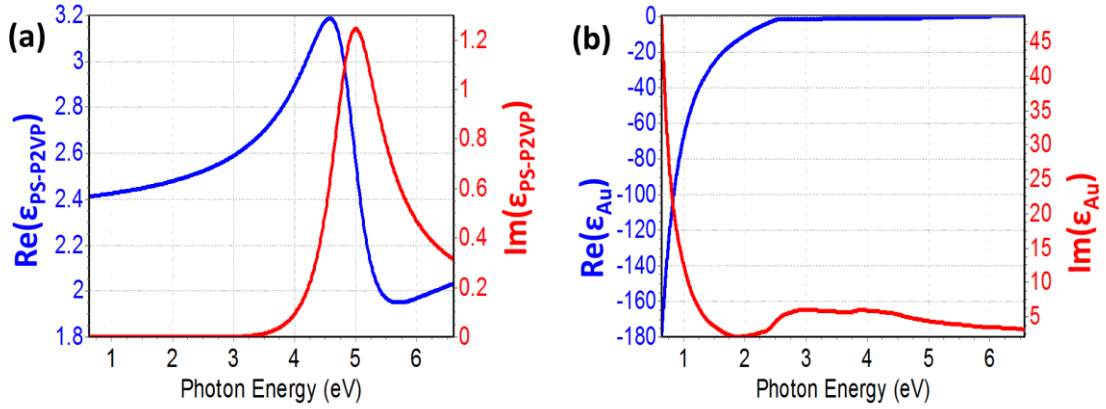

Figure VI. 6 the permittivity of (a) PS-P2VP and (b) gold nanoparticles used in model.

For $\varepsilon_{//}(\lambda)$, two different approaches are used. The first one is to also model this component as that of a mixture of polymer and gold, with a Maxwell-Garnett Effective Medium Approximation (see Equation 6- 1), noted as ε_{MG}. It consists of PS-P2VP and gold nanoparticles with the volume fraction of gold used as the fitting variable.

The second approach used is the Tauc Lorentz[8] dispersion function of the appropriate effective medium with one oscillator (details see Equation 2-10 and 2-11 of Chapter II.1.3), noted as ε_{TL}. Recall from Chapter II.1 Tauc Lorentz[8] (see Equation 2- 10) and oscillators[9] dielectric functions (see Equation 2- 11) are the following:

Equation 2- 10 $\varepsilon = \varepsilon_1 + i\varepsilon_2$ where:

$$\varepsilon_1 = \frac{2}{\pi} \cdot P \cdot \int_{E_g}^{\infty} \frac{\xi \cdot \varepsilon_2(\xi)}{\xi^2 - E^2} d\xi$$

$$\varepsilon_2 = \begin{cases} \frac{1}{E} \cdot \frac{A \cdot E_0 \cdot C \cdot (E - E_g)^2}{(E^2 - E_0^2)^2 + C^2 \cdot E^2} & , E > E_g \\ 0 & , E \leq E_g \end{cases}$$

- E is photon energy;

- E_g is the optical band gap;

- E_0 is the peak central energy;

- C is the broadening term of the peak;

- P is the Cauchy principal value containing the residues of the integral at poles located on lower half of the complex plane and along the real axis.

Equation 2- 11 $$\varepsilon = \frac{f_j \omega_{0j}^2}{\omega_{0j}^2 - \omega^2 + i\gamma_j \omega}$$

With ω_{oj} the resonance frequency, f_j an amplitude factor and γ_j the dissipation term.

In the Maxwell-Garnett Effective Medium Approximation, the resonance position of gold is fixed to a certain position, which leads to disagreement with the experimental data for some samples. However ε_{MG} give us an initial guess of the volume fraction of gold inside layers. The dielectric function constructed with a Tauc Lorentz[8] function plus one oscillator is more flexible in the resonance position, which may give a better approach.

The data were analyzed using the DeltaPsi2 software from Horiba Scientific.

VI.2 Dimensions and optical properties

As we discussed in the previous chapters, we produce well controlled lamellar structures with film thickness from ca. 100nm to 700nm and lamellar period from ca.17nm to 70 nm.

VI.2.1 Influence of the film thickness

VI.2.1.1 Samples structure

The studied samples were all fabricated from poly(styrene)-*block*-poly(2-vinylpyridine) (M_n 25000-25000, PDI 1.06), with lamellar period of 30nm. The description of the fabrication can be found in the Chapter III.1.1.2 and the film thicknesses were measured by SEM and SE (spectroscopic ellipsometry). The number of impregnation cycles are written as N. Note the thickness measurement extracted from SE is carried out before gold impregnation process, when the film is not organized yet, while the values from SEM are measured after gold impregnation process. Also, the SE measurement is an average value on a large area of the sample, while the measurements done on the SEM images are very local.

We show here the comparison of the results obtained on films of PS-b-P2VP 25k-25k of two different thicknesses. We repeated the loading process for N=10 cycles

(see detail of loading process in Chapter IV.2.2), and the volume fraction of gold in the PVP layers can be estimated at ca. 20 %(measurement details given in Chapter IV.3.3).

Table VI. 1 Samples used for analyzing the effect of the film thickness

Samples	D1	D2
Thickness (SE)	287 nm	671 nm
Thickness (SEM)	287.1 nm	655.1 nm

The structure of the samples is shown on the side images obtained by SEM BSEI mode (see Chapter II.3) in the Figure VI. 7.

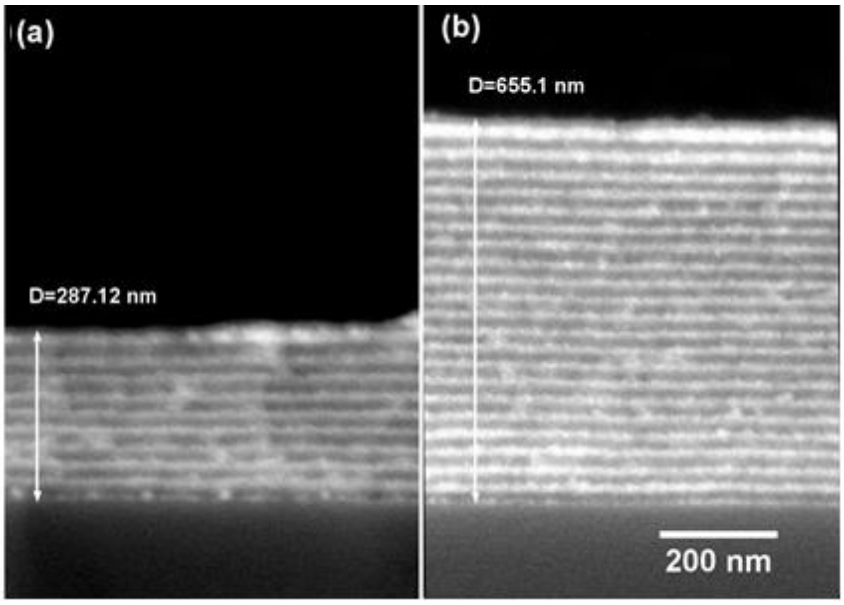

Figure VI. 7. BSEI SEM images of films of PS-b-P2VP 25k-25k after N=10 gold impregnation cycles (a) D1 with thickness 287.1 nm (b) D2 with thickness 655.1 nm

VI.2.1.2 Optical responses

We start by plotting the pseudo permittivity <ε> of the films. The pseudo permittivities <ε> are shown in Figure VI. 8(a) shows the pseudo permittivities for the samples without gold nanoparticles(N=0), which present the regular fringes related to the thickness of the film: their spectral separation is smaller when the thickness is larger. When the films are loaded with gold (N=10), the fringes are damped in the UV range due to the intraband absorption of gold. Moreover, their amplitude is also strongly modified around 2.1 eV (λ ~ 590 nm), which is caused by the surface plasmon resonance of the gold nanoparticles.

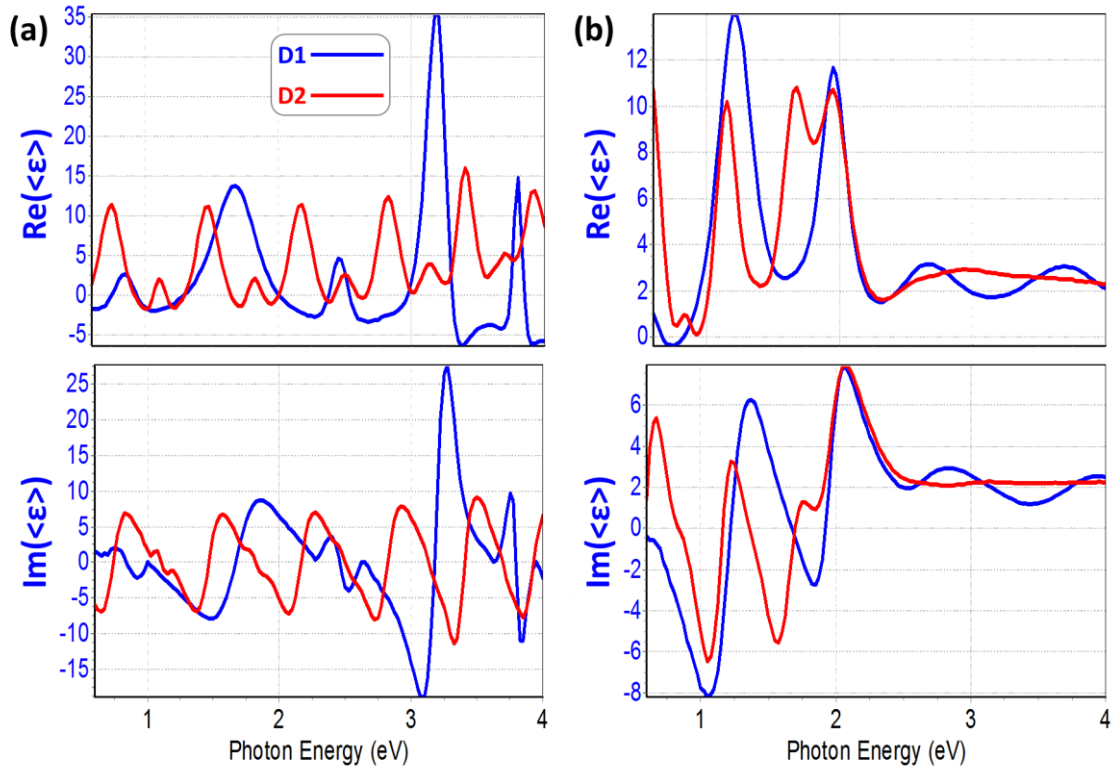

Figure VI. 8 Real (upper plots) and imaginary (lower plots) part of the pseudo permittivity <ε> extracted from the ellipsometry data (a) N=0 and (b) N=10. The ellipsometry data are measured at AOI 65°. The thicknesses of D1 and D2 are 287 nm and 655 nm, respectively.

For the films D1 and D2 with N=5 and 10, we fitted the ellipsometry data by the uniaxial layer Model B-2, using a fixed MG function for the extraordinary permittiviy ε_z and adjusting the ordinary direction permittivity of uniaxial layer $\varepsilon_{//}$. For ε_z we use a MG function with f=5.0%. For $\varepsilon_{//}$, the first approximation is (MG) Maxwell-Garnett Effective Medium: the permittivity of $\varepsilon_{//}$ is noted as ε_{MG} in this approach. The second approximation (TL) is a Tauc Lorentz function with an additional oscillator: the permittivity of $\varepsilon_{//}$ is noted as $\varepsilon_{TL.}$ in this case. The fitting is shown in Figure VI. 9, both of the fitting are works good, which tend to confirm the anisotropy of our system. When comparing the two different fittings in Figure VI. 9, we see that the TC-fitting (in red) adjusts better the plasmon spectral range (between2.0 and 2.5eV). This is due to the larger flexibility of the TC fitting, in which both the spectral position and the amplitude of the resonance can be varied.

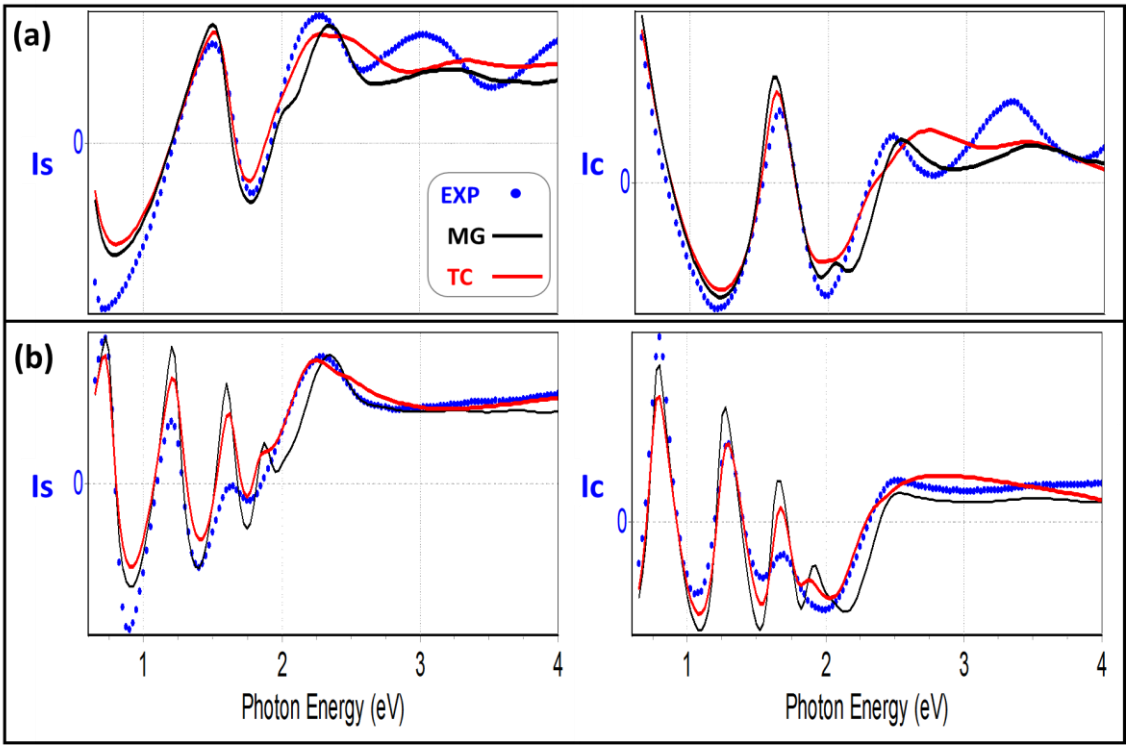

Figure VI. 9 Fitting with the Model B-2 of the ellipsometric data Is (left plots) and Ic(right plots) versus to photon energy (eV). The experimental data (EXP) are in blue, $\varepsilon_{//}$ described by Maxwell-Garnett approximation media (MG) are in black, and by Tauc Lorentz with one oscillator are in red. The ellipsometry data are measured at AOI 65°. The thicknesses of (a) D1 and (b) D2 are 287 nm and 655 nm, respectively.

For ε_{MG}, the fitting results are shown in Table VI. 2 and Figure VI. 10(a). From Equation 6- 1, f, the volume fraction of gold inside films is the only fitting parameter in this case. We can see that in the low value of N=5, the thicker film takes more gold, 5.8% in the film D1 with thickness of 287nm and 9.8% in the film D2 with thickness of 655nm. While in the high value of N=10, there is no difference in the thin and thick films, 16.4% in film D1 with thickness of 287 nm and 17.33% in film D2 with thickness of 655nm. From Figure VI. 10(a), we can see that the change of film thickness from 287nm to 655nm have no influence in the properties of the films. The MG model gives the same spectral position for the absorption and, which is not exactly in agreement with the resonance observed in the experimental data. This is the limitation of the use of the MG approach, which could be improved by the TL fit.

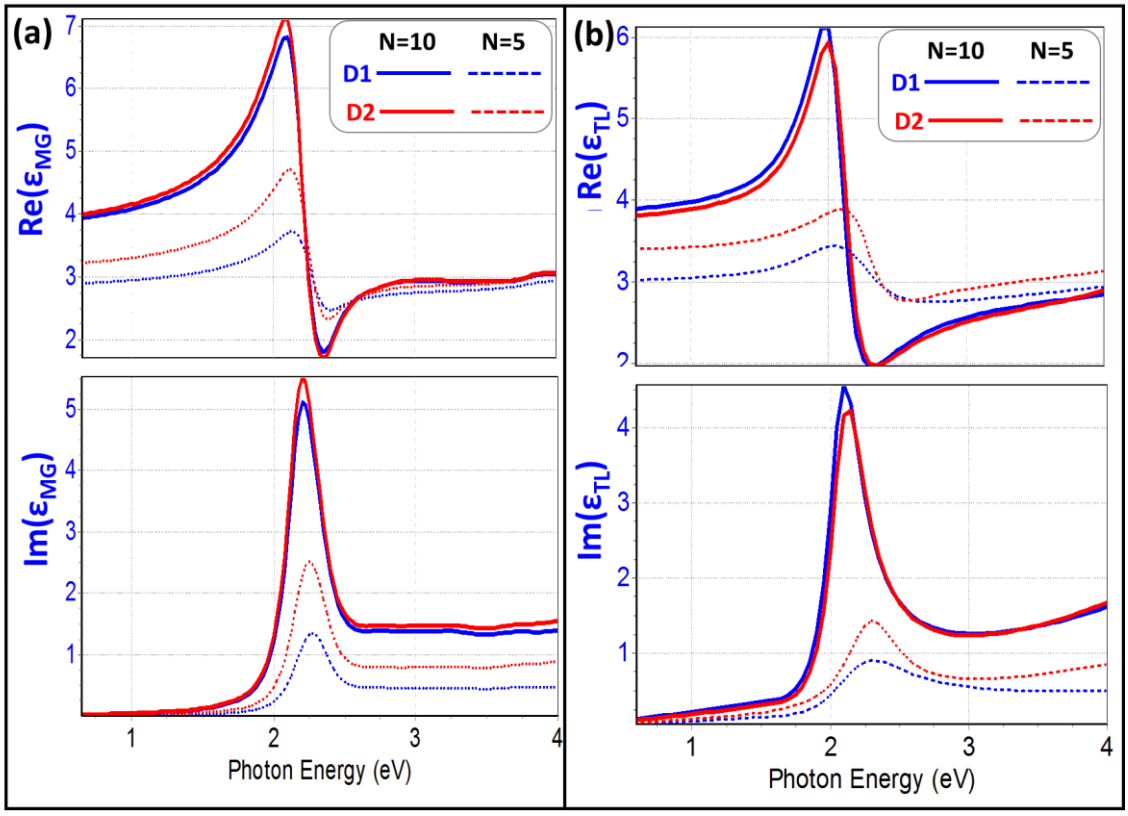

Figure VI. 10 Real (upper plots) and imaginary (lower plots) parts of the permittivity $\varepsilon_{//}$ extracted from the ellipsometry data using the Model B-2. The uniaxial media is described by (a) Maxwell-Garnett Effective Medium Approximation and (b) Tauc Lorentz dispersion formula with one oscillator. The ellipsometry data are measured at AOI 65°. The thicknesses of D1 and D2 are 287 nm and 655 nm, respectively.

Table VI. 2 Volume fraction of gold used in Maxwell-Garnett Effective Medium Approximation Parameters. The thicknesses of D1 and D2 are 287 nm and 655 nm, respectively.

	D1	D2
N=5	5.8%	9.8%
N=10	16.37%	17.33%

With the second fit ε_{TL}, the fitting results are listed in Table VI. 3 and Figure VI. 10(b). We can see that as the thickness of sample increases the energy position of the peak of absorption E are similar (2.09eV and 2.08eV). From Figure VI. 10, for N=5, as the thickness of layer increase, the resonance become stronger at 2.1eV (λ~590nm), while the position of resonance trends to the same when N=10. This results in a good agreement with MG fitting. From the $\varepsilon_{//}(\lambda)$ (both ε_{MG} Figure VI. 10(a) and ε_{TL} Figure VI. 10(b)) of D1 and D2 are almost overlapped, the thickness of film has little influence on the optical properties.

Table VI. 3 Tauc Lorentz and oscillator (Equation 2-10 and Equation 2-11) parameters found through the fit of the ellipsometry data for the samples with N=5 and 10. The thicknesses of D1 and D2 are 287 nm and 655 nm, respectively.

	D1		D2	
	N=5	N=10	N=5	N=10
ε_∞	3.370	4.670	4.190	5.420
E_g	1.600	1.550	1.260	1.510
A	5.200	20.000	2.410	16.940
E	2.210	2.090	2.280	2.080
C	0.640	0.370	0.450	0.320
f	-0.530	-1.300	-0.990	-1.950
ω_0	6.430	5.160	6.300	6.130
γ	-7.950	-3.010	-5.080	-3.640

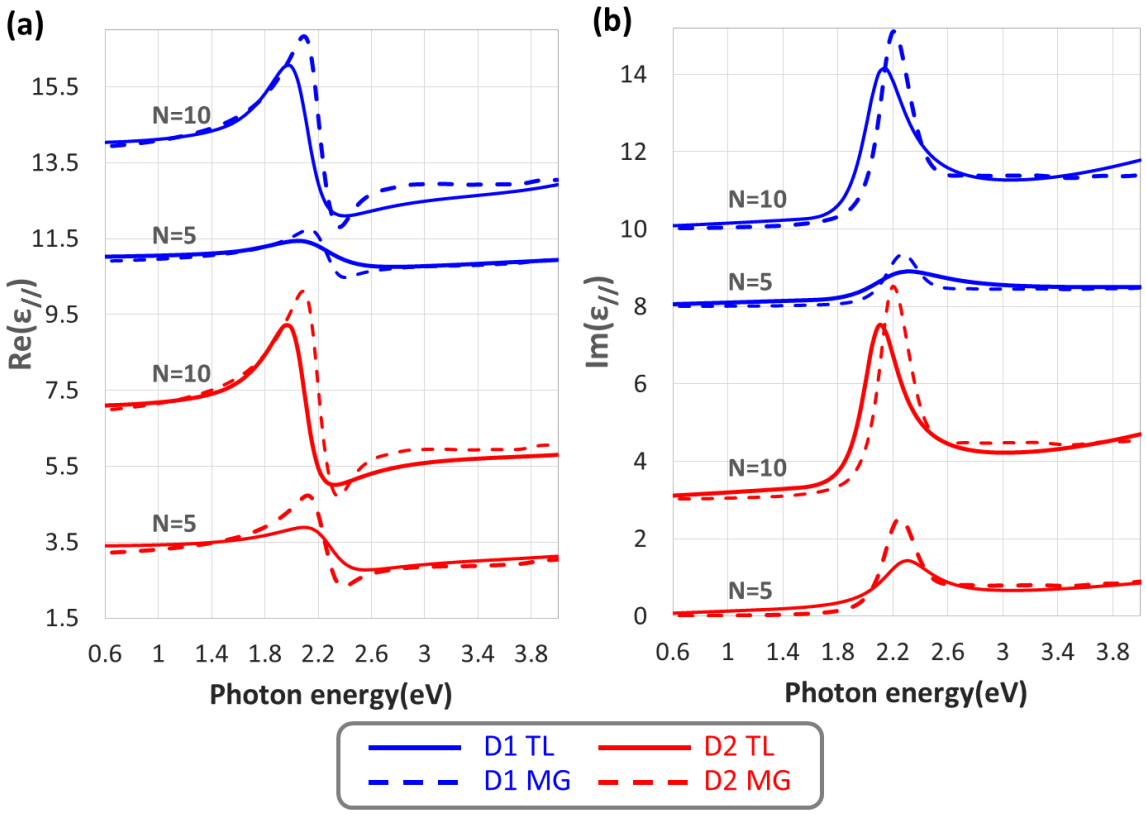

Figure VI. 11 Comparison of the real (a) and imaginary (b) parts of the ordinary permittivity ε// extracted from the ellipsometry data using the Model B-2. The media for ordinary direction is described by Maxwell-Garnett Effective Medium Approximation (MG dash lines) and Tauc Lorentz dispersion formula with one oscillator (TL continuous lines). The film thicknesses of D1 and D2 are 287 nm and 655 nm, respectively. The value of N stands for the number of gold loading process cycles. The curves are vertically shifted for clarity.

The Figure VI. 11 compares the $\varepsilon_{//}$ extracted from the two used fits. With the TL function, the plasmon resonce spectral position and width are fixed, while the MG function restricts these features. As we discussed in previous chapters, our fabrication method provides gold nanoparticles with some polydispersity and packed in a dense and disordered way in the NC layers, which may lead to wide and red-shifted plasmon peaks. At this point, the TL fitting appears more appropriate in this system. TL fitting results show that as the value of N increases, the plasmon resonance position has a red shift.

In conclusion, both of the fitting indicate that the results of the gold loading process we used do not depend on the thickness of the film in the studied range. With the increase of the N value, there might be a small influence of thickness on the films. Also, the optical properties analysis can be done in the same way for different film thicknesses.

VI.2.2 Influence of the lamellar period

VI.2.2.1 Samples structure

As was detailed in Chapter III.2, using different molar masses of symmetrical PS-b-P2VP diblock copolymers, we can obtain lamellar films with different lamellar periods between 17 nm and 80 nm. The lamellar period extracted by SAXS is obtained on bulk samples without gold.

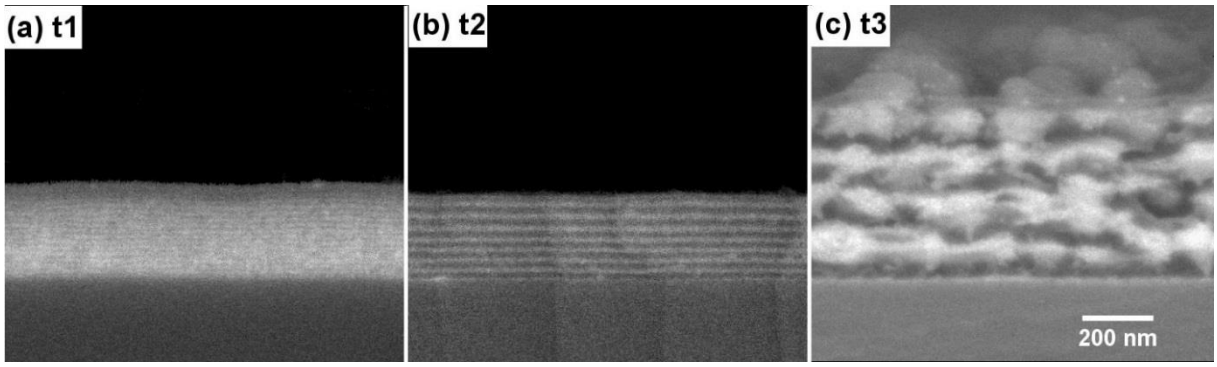

Figure VI. 12 BSEI SEM images of films of PS-b-P2VP 25k-25k after N=10 gold impregnation cycles with layer thicknesses (a) t1 16.4 nm (b)t2 31 nm (c)t3 78.5 nm

The SEM BSEI micrographs in the Figure VI. 12 show the structure of the samples after 10 gold impregnation cycles. The structure of the sample t1, from the copolymer PS-b-P2VP 102k-97k is not as regular as the two other samples, but we can still identify a lamellar organization and count the number of layers. These lamellar

samples were shown to have interesting plasmonic response leading to plasmon-induced Brewster extinction[23]. For the copolymer PS-b-P2VP 8.2k-8.3k, the image indicates a nice lamellar order, but the SEM resolution does not allow counting the number of layers.

Table VI. 4 Characteristics of the samples with different lamellar period.

Samples	t1	t2	t3
Lamellar period (SAXS)	16.4nm	36.8nm	78.5nm
Lamellar period (SEM)	//	31 nm (7 layers)	120 nm (4 layers)
Thickness (SE)	213 nm	225 nm	507 nm
Thickness (SEM)	265.4 nm	242.6 nm	519.6 nm

VI.2.2.2 Optical responses

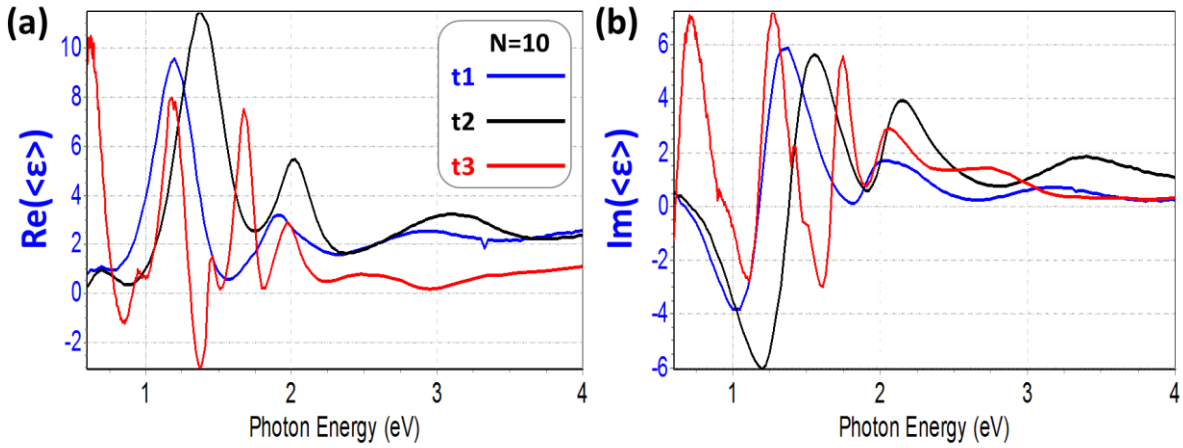

Figure VI. 13 Real (a) and imaginary (b) part of the pseudo permittivity <ε> extracted from the ellipsometry data using the Model A. The ellipsometry data are measured at AOI 65°. The layer thicknesses of t1, t2 and t3 are 16.4 nm, 31 nm and 78.5 nm, respectively.

We start by plotting the pseudo permittivity <ε> of the individual film. The pseudo permittivities <ε> are shown in Figure VI. 13. For the sample t3, the separation of the fringes is due to the difference thickness of film, t1 and t2 are ca.250nm, while t3 is 520nm (seeTable VI. 4). As we concluded in the previous section, the film thickness has negligible influence on optical analysis. We can suppose that the difference in thickness will have no effect on our analysis. The fringes are damped in the UV range in the presence of gold, due to the intraband absorption of gold. Moreover, their amplitude around 2.1 eV (λ~590 nm) is markedly modified as N increases, which is due to the plasmon resonance of the gold nanoparticles. However, it is difficult to extract more information from the pseudo-permittivities.

As for the film thickness analysis, we extract the ordinary direction permittivity of uniaxial layer $\varepsilon_{//}$ by Model B-2 with a fixed ε_z (Figure VI. 5) of extraordinary direction from t1, t2 and t3 when N=5 and 10. The ordinary permittivity $\varepsilon_{//}$.is modeled either by a (MG) Maxwell-Garnett Effective Medium (the permittivity $\varepsilon_{//}$ is noted ε_{MG} or by a (TL) is Tauc Lorentz with one oscillator (the permittivity $\varepsilon_{//}$ is noted $\varepsilon_{TL.}$ in this case). The fittings are shown in Figure VI. 14, and both of the fitting are good. When comparing the two different fittings in Figure VI. 14, we can see that the MG fitting (in black) adjusts less well the experimental data, especially in the spectral range pf the plasmon resonance of the gold NPs, while the TL fitting (in red) adjusts better the data. As we said earlier, with the TL function, the plasmon resonance spectral position and width are not fixed, unlike with the MG function. In the sample t3 (Figure VI. 14(c)), the fitting lines are not very good, which is probably related to the unwell defined film (see Figure VI. 12(c)).

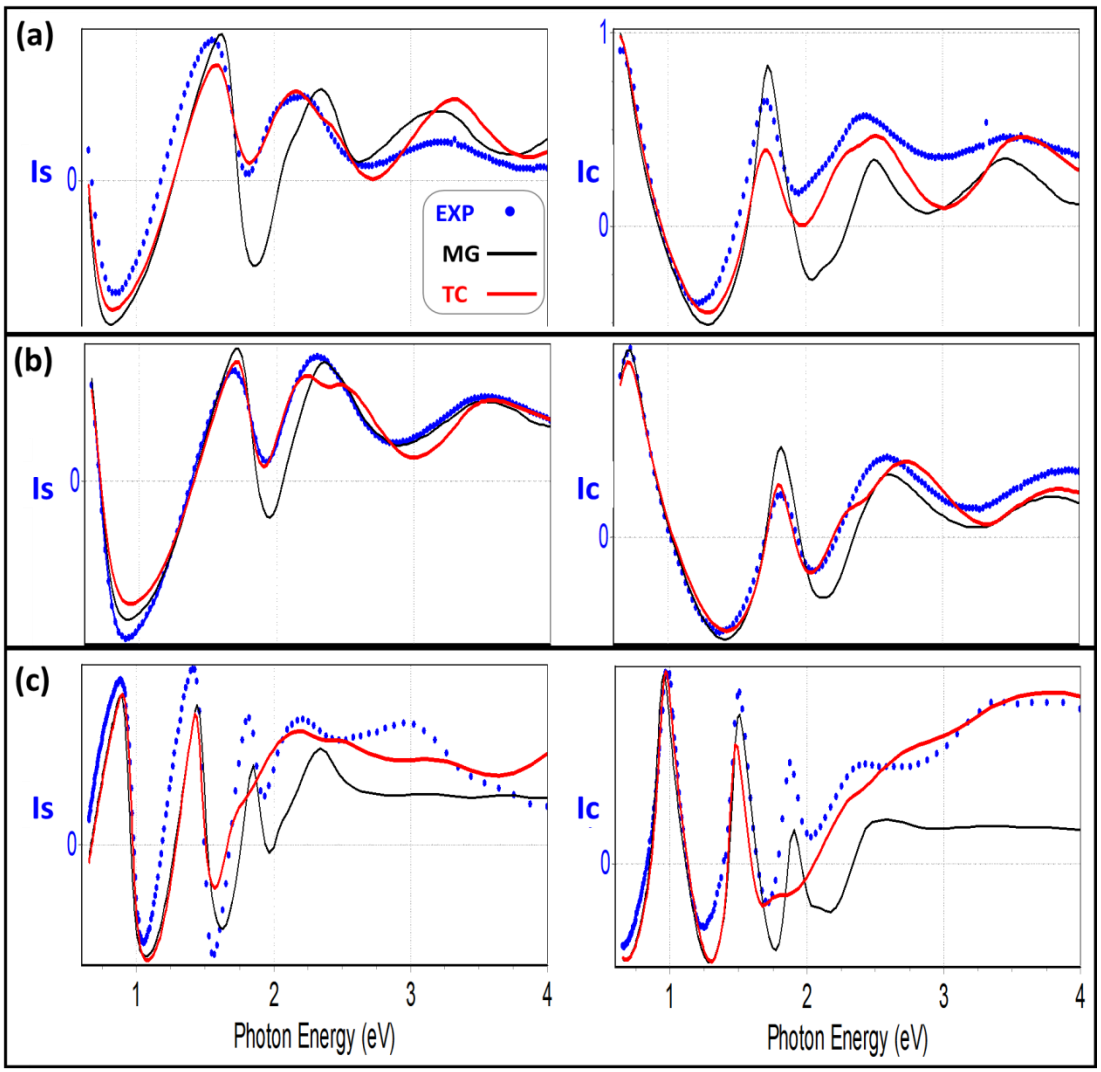

Figure VI. 14 Fitting results of Model B-2 for Is (left plots) and Ic (right plots) versus the photon energy (eV). The experimental data (EXP) are in blue, fitting $\varepsilon_{//}$ described by Maxwell-Garnett approximation media (MG) is in black, and fitting by Tauc Lorentz with one oscillator is in red.

The ellipsometry data are measured at AOI 65°. The bilayer thicknesses of (a) t1, (b) t2 and (c) t3 are 16.4nm, 31nm and 78.5nm, respectively.

For the $\varepsilon_{//}$, the fitting results of MG are shown in Table VI. 5 and Figure VI. 15(a). From Equation 6- 1, f, the volume fraction of gold inside the films is the only fitting parameter in this case. We can see that for that both values of N=5 and N=10, when the bilayer thickness increase, the films have a slightly higher uptake of gold. When N=5, 6.2 % and 7.3 % are present in t1 and t2, whose bilayer thickness are 16.4nm and 31 nm. While as the bilayer thickness continuous to increase, the structure is not well defined and the amplitude around gold plasmon resonance is not as good as t2. Furthermore, the MG gives the same position of absorption, which is not exact in the experimental data. This is the limitation of the usage of the MG approach, which is improved by the TL fit.

Table VI. 5 Volume fraction of gold used in Maxwell-Garnett Effective Medium Approximation Parameters. The bilayer thicknesses of t1, t2 and t3 are 16.4 nm, 31 nm and 78.5 nm, respectively.

	t1	t2	t3
N=5	6.2%	7.4%	5.1%
N=10	10.9%	13.72%	12.7%

Table VI. 6 Parameters used in Tauc Lorentz and one oscillator (Equation 2-10 and Equation 2-11). The bilayer thicknesses of t1, t2 and t3 are 16.4 nm, 31 nm and 78.5 nm, respectively.

	t1		t2		t3	
	N=5	N=10	N=5	N=10	N=5	N=10
ε_∞	3.37	8.71	3.53	4.68	2.74	14.30
E_g	1.78	1.16	1.86	1.59	1.68	1.31
A	8.06	3.90	20.57	16.70	14.63	13.25
E	2.40	2.03	2.03	2.07	2.19	1.92
C	0.50	0.43	0.30	0.36	0.69	0.52
f	-0.53	-5.67	-0.59	-1.41	-0.34	-11.53
ω_0	5.39	16.21	5.43	6.42	4.66	13.08
γ	-1.48	-7.61	-4.57	-4.36	-0.61	-0.54

The second approximation (TL) is a function Tauc Lorentz with one oscillator (the permittivity $\varepsilon_{//}$ is noted $\varepsilon_{TL.}$ in this case), the fitting results are listed in Table VI. 6 and plotted in Figure VI. 15(b). We can see that as the bilayer thickness of the samples

increases from 16nm to 31nm, both in N=5 and N=10, the plasmon resonance is stronger around 2.1eV (λ~590nm) and the position of resonance varies only a little. With the increase of volume fraction of gold (comparing N=5 and N=10), all the samples show a red shift of the resonance position, which is also observed in the samples D1 and D2.

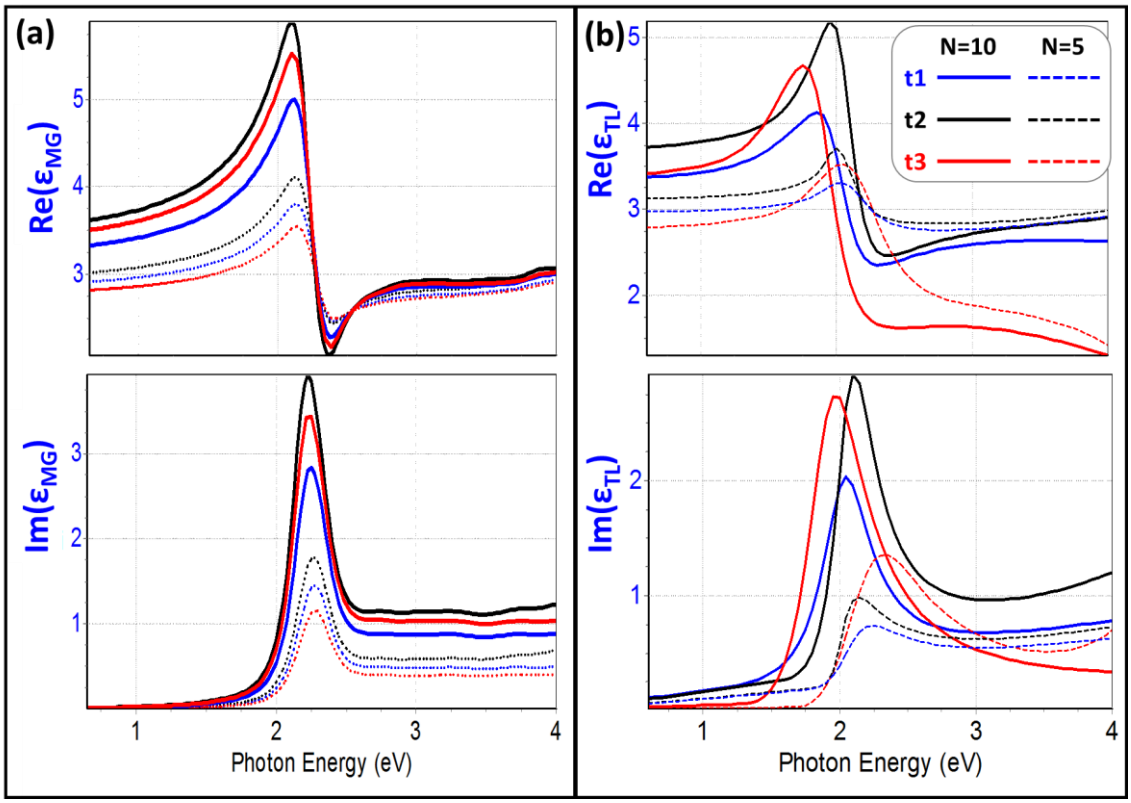

Figure VI. 15 Real (upper plots) and imaginary (lower plots) parts of the permittivity ε// extracted from the ellipsometry data using the Model B-2. The uniaxial media is described by (a) Maxwell-Garnett Effective Medium Approximation and (b) Tauc Lorentz dispersion formula with one oscillator. The ellipsometry data are measured at AOI 65°. The bilayer thicknesses of t1, t2 and t3 are 16.4 nm, 31 nm and 78.5 nm, respectively.

The comparison of the $\varepsilon_{//}$ extracted from both modeling functions, is seen on the Figure VI. 16. From N=5 to N=10, the volume fraction of gold increases, which leads to a stronger amplitude ranging from 1.9eV to 2.3 eV (λ ranging from 539nm to 620nm) in $\varepsilon_{//}$, and the red shift of the position in ε_{TL}. The ε_{MG} presents a fixed resonance position at 2.3eV (λ=540nm), while with ε_{TL} the position of the gold plasmon resonance varies a little, and the absorption peak is wider than ε_{MG}. As we discussed in previous chapters, our fabrication method provides gold nanoparticles with some polydispersity and packed in a dense and disordered way in the NC layers, which may lead to wide and red-shifted plasmon peak due to inter particle couplings. At this point, the TL fitting

seems more appropriate in this system. TL fitting results show that as the value of N increases, the plasmon resonance position does not shift significantly. The absorption position for t1, t2 and t3 with bilayer thickness 17nm, 31nm and 78nm are at 2.05eV, 2.15eV and 1.95 eV. Therefore, the different bilayer thickness can lead to only slightly different wavelengths of plasmon resonance.

In conclusion, both fittings with MG and TL models indicate that as the bilayer thickness increases, a slightly higher uptake of gold occurs. However, once the bilayer thickness is too large (70nm), the nanostructure of the film is not well defined and leads to a lower amplitude of the resonance. The sample with layer thickness 31nm gives the strongest resonance.

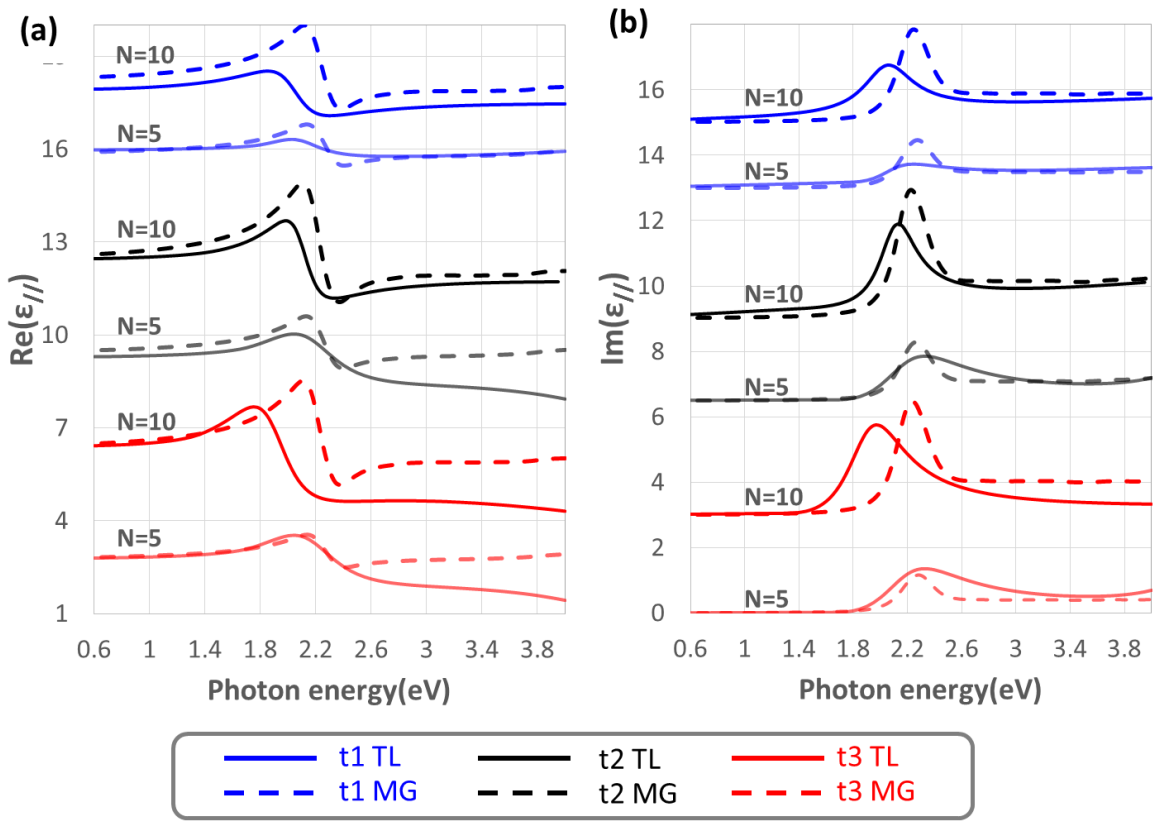

Figure VI. 16 Comparison of Real (a) and imaginary (b) parts of the permittivity $\varepsilon_{//}$ extracted from the ellipsometry data using the Model B-2. The media for ordinary direction is described by Maxwell-Garnett Effective Medium Approximation (MG dash lines) and Tauc Lorentz dispersion formula with one oscillator (TL continuous lines). The bilayer thicknesses of t1, t2 and t3 are 16.4 nm, 31 nm and 78.5 nm, respectively. The value of N stands for the number of gold loading process cycles. The curves are vertically shifted for clarity.

VI.3 Different metallic particles and optical properties

As we discussed in Chapter IV, we can introduce gold or silver nanoparticles inside the lamellar films. Also the size and shape of the gold nanoparticles can be modified by the choice of the solvent for the reducing step and/or the addition of a thermal annealing step, as was explained in Chapter V. We present here our study of how these parameters affect the optical properties.

VI.3.1 Gold and silver nanoparticles

VI.3.1.1 Samples structure

The samples were all fabricated based on poly(styrene)-*block*-poly(2-vinylpyridine) (M_n25000-25000, PDI 1.06) copolymers, with lamellar period ca.30nm. The fabrication description can be found in the Chapter III.1.1.2. The film thicknesses were 288 ± 2 nm measured by SE carried out before the gold impregnation process. The metal loading process was performed as described in the Chapter IV.2.2: in short, in the gold loading case (samples are named Au), the film-bearing wafer is dipped into an Au salt (HAuCl4) solution and then into a reducing agent (NaBH4) water solution. In the silver case loading case, the film-bearing wafer is dipped into an Ag salt ($AgNO_3$) solution and then into a reducing agent ($NaBH_4$) water solution (the sample is named Ag1) or water/ethanol solution (the sample is named Ag2). We repeat the gold/silver loading processes for N cycles (N from 0 to 15). In the case of gold, we know that N=5 and N=10 correspond to a volume fraction of gold in the PVP layers of ca. 10% and ca. 20 %, respectively, according to the QCM study(see Chapter IV.3.3).

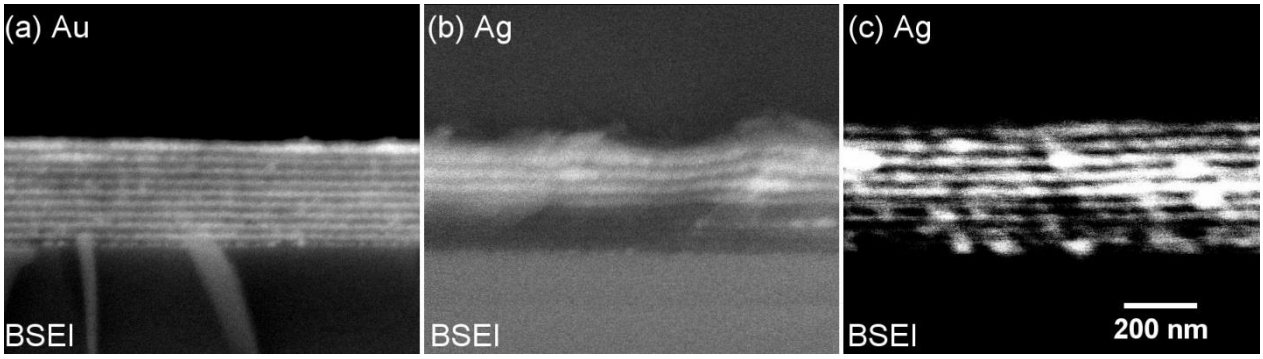

Figure VI. 17 BSEI SEM images of films of PS-b-P2VP 25k-25k after N=10 gold impregnation cycles (a) gold nanoparticles in P2VP layers (b) silver nanoparticles in the first 4 P2VP layers from top (c) silver nanoparticles in P2VP layers

The structures of the samples are shown on the side images obtained by SEM in BSEI mode (see Chapter II.3) in the Figure VI. 17. The samples Au (Figure VI. 17(a)) and Ag2 (Figure VI. 17(c)) are composed of 9 bilayers (PS) + (NC), while the sample Ag1 (Figure VI. 17(b)) is composed of 4 bilayers (PS) + (NC), because we do not consider the lower part of the film where Ag did not penetrate.

VI.3.1.2 Optical responses

We start by plotting the pseudo permittivity <ε> of each film. The pseudo permittivities <ε> are shown in Figure VI. 18 and Figure VI. 19.

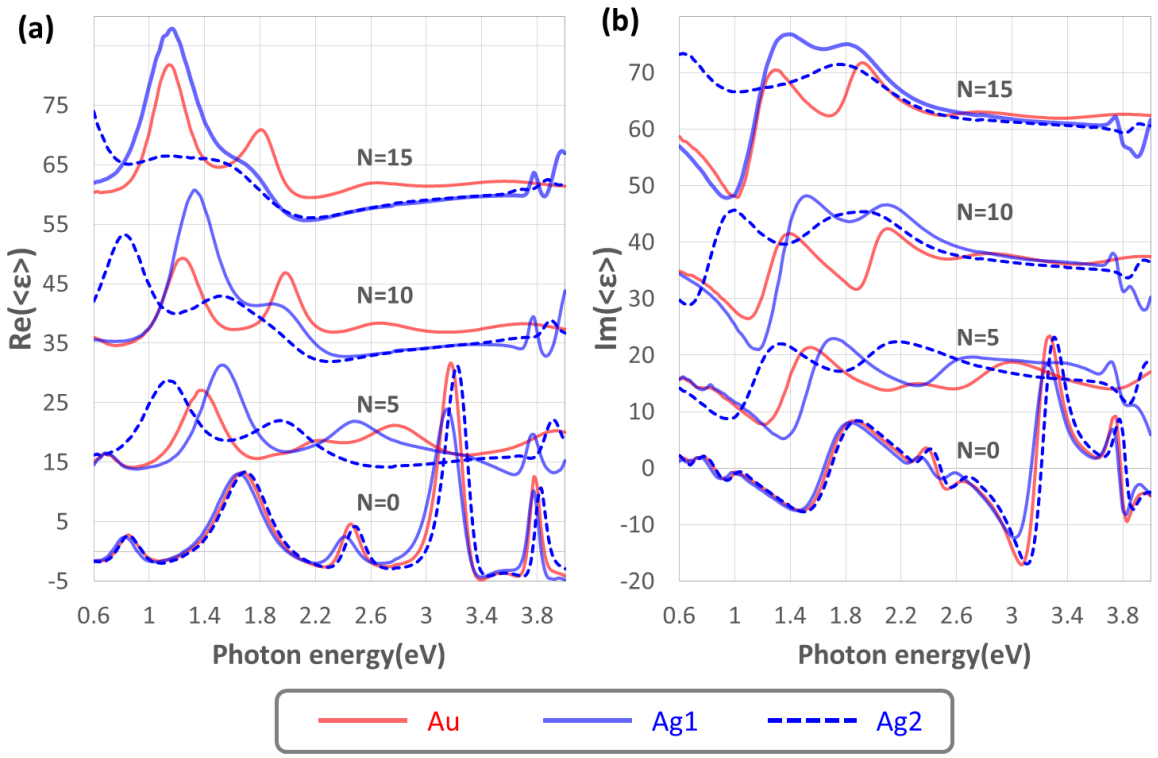

Figure VI. 18 Real (a) and imaginary (b) parts of the pseudo permittivity <ε> from the ellipsometry data. The ellipsometry data are measured at AOI 65°. N stands for the number of the impregnation cycles for loading process. Au stands for sample with gold NPs (Figure VI. 17(a)), Ag1 stands for sample with silver NPs in top 4 layers (Figure VI. 17(b)), and Ag2 stands for sample with silver NPs in the whole film (Figure VI. 17(c)). The curves are vertically shifted for clarity.

Before the metal loading process, the three samples Au, Ag1 and Ag2 were started in the same conditions and in Figure VI. 18, when N=0 the curves of the three samples Au, Ag1 and Ag2 overlapped. As the value of N increases, the fringes in UV range damped due to the absorption by the metallic particles. Between the 1.8eV and 2.1eV, the samples with both gold and silver have strong absorption. In the case of gold, we can identify an absorption peak, which is caused by the gold nanoparticles

plasmon resonance at 2.1eV. On the other hand, the samples with Ag shows a board absorption in the whole visible range. From the micrographs of Ag1 and Ag2 shown in Figure VI. 17, we can see that the silver particles in Ag2 are much bigger and more polydisperse than the ones in Ag1: these large and polydisperse silver particles cause strong and borad absorption, as can be observed in the figures. As the value of N increases, these phenomena occur more significant. We can see that in Figure VI. 18, the dash blue line is almost flat in the whole visible wavelength range.

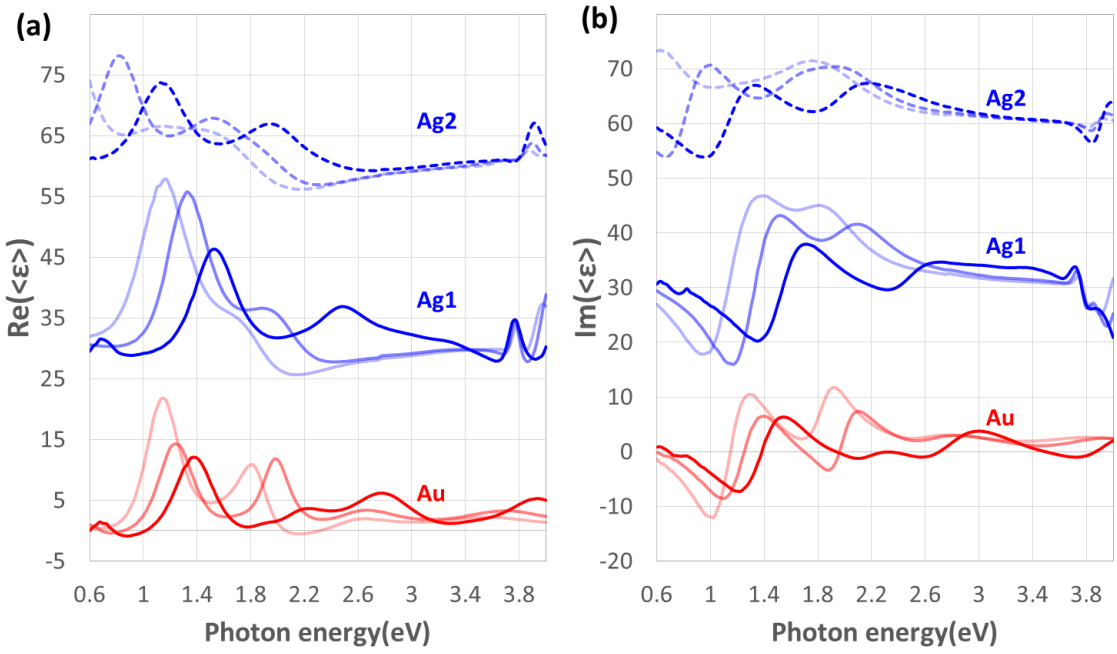

Figure VI. 19 Real (a) and imaginary (b) parts of the pseudo permittivity <ε> from the ellipsometry data. The ellipsometry data are measured at AOI 65°. The different impregnation cycles for loading metal N=5, N=10 and N=15 are shown in the figure with gradually lighter colors. Au stands for the sample with gold NPs (Figure VI. 17(a)), Ag1 stands for sample with silver NPs in the top 4 layers (Figure VI. 17(b)), and Ag2 stands for the sample with silver NPs in the whole film (Figure VI. 17(c)). The curves are vertically shifted for clarity.

As the value of N increases, we can see from Figure VI. 19 that the curves of Au, Ag1 and Ag2 change gradually, which indicates that the metallic particles are loading little by little. In the case of the sample with gold, the resonance caused by the Au nanoparticles ca. 2 eV(λ~620nm) are stronger and have a red shift as the value of N increase. In the case of Ag1 and Ag2, the absorption is stronger as the value of N increases. A significant difference in optical response is observed between Ag1 and Ag2.

However, the models we mentioned in VI.1 do not fit well the experimental data (see Figure VI. 20). To access the permittivity of the samples with silver, we would need a better model of analysis.

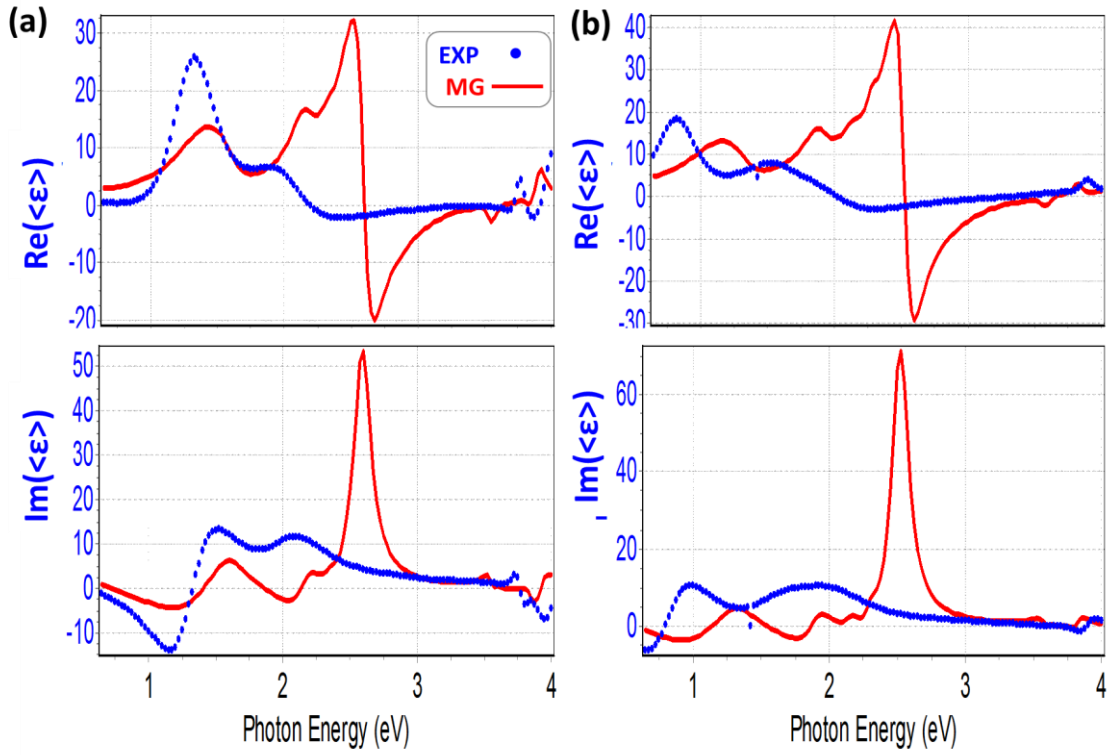

Figure VI. 20 Real (upper plots) and imaginary (lower plots) parts of the pseudo permittivity <ε> of (a) samples Ag1 and (b) Ag2. EXP stands for the ellipsometry data (blue dots) and MG stands for the fitting lines of Model B-2 (red curves). We extract the ordinary direction permittivity of uniaxial layer $\varepsilon_{//}$ by Model B-2 with the fixed extraordinary component ε_z (Figure VI. 5) and the $\varepsilon_{//}$ is the approximation of Maxwell-Garnett Effective Medium. The ellipsometry data are measured at AOI 65°. The number of impregnation cycles for metal loading is N=10. Ag1 stands for the sample with silver NPs in the top 4 layers (Figure VI. 17(b)), and Ag2 stands for the sample with silver NPs in the whole film (Figure VI. 17(c)).

In conclusion, different metallic particles of Au and Ag in lamellar structure give different optical responses. The structures with silver NPs show stronger absorption than the one with gold. To analysis the detail of the different responses, we need a better fabrication method to reach a better dispersion and homogeneity of the silver NPs in the films and a better model for analysis.

VI.3.2 Gold nanoparticles shape

VI.3.2.1 Influence of the shape of the gold nanoparticles

A step of thermal annealing[10,11] can change the shape of gold nanoparticles inside the layers. As we mentioned in the Chapter V.1.2, once the thermal annealing process was introduced at the end of the gold loading process, significant changes of gold nanoparticles shape were observed (Figure VI. 21). However, the shape of the gold nanoparticles inside the layers is very diverse, including spheres, prism, and cylinders, which induces a broadening of the resonance and a loss of interesting properties. Our results suggest that the shape of the nanoparticles can probably be controlled by the temperature of the annealing process, and this could be studied in the future.

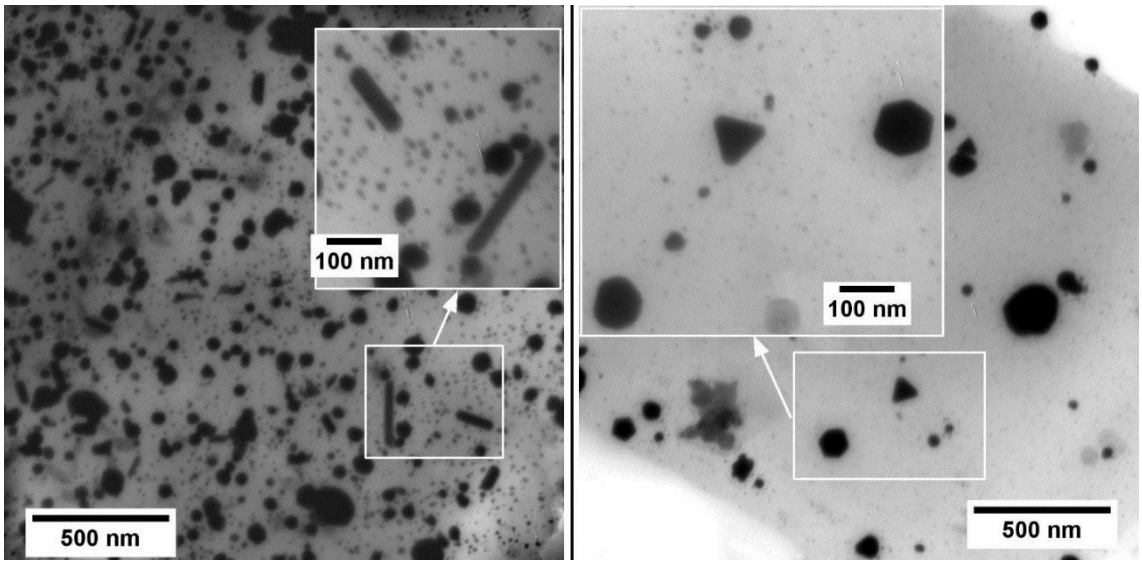

Figure VI. 21 Gold particles in the film fabricated with impregnation process (N=10) with an annealing process after N=5 and N=10.

We can see from Figure VI. 22 that the samples non annealed (N=0) and annealed (AN=0) before gold incorporation give the same optical response (blue lines). After 10 cycles of impregnation (black lines), a broad peak appears at photon energy of 2eV (λ=620 nm), which we attribute to the plasmon resonance of the gold nanoparticles , but it is lower in the annealed film (black dash line) than in the film without annealing (normal gold loading process, black solid line). As the gold loading goes up to 20 cycles of impregnation (red lines), the resonance is increased for the film without annealing (red solid line) and shifted to a photon energy of 1.65eV (λ=750 nm), while it has completely disappeared for the film with annealing process (red dash lines), which is probably due to the fact that the gold nanoparticles fuse and become much less well

defined during the annealing. Also, the size of gold nanoparticles becomes larger, which is another reason for the red shift of the resonance.

However, the model B-2 in Figure VI. 1(b) does not work perfectly, because gold nanoparticles in the film have various shape and high polydispersity, which makes the optical responses complex and difficult to fit.

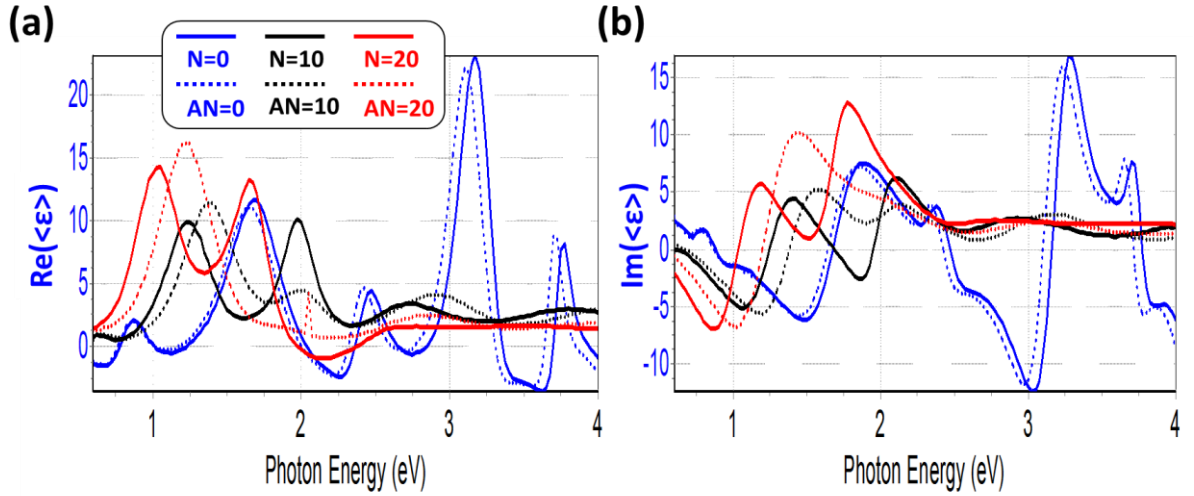

Figure VI. 22 Real (a) and imaginary (b) parts of the pseudo permittivity <ε> from the ellipsometry data using the Model A. The ellipsometry data are measured at AOI 65°. N stands for the normal loading process, while AN stands for the gold loading process with thermal annealing every 5 cycles. And the value after N and AN means the number of cycles of loading processes.

VI.3.2.2 Ellipsoidal gold nanoparticles

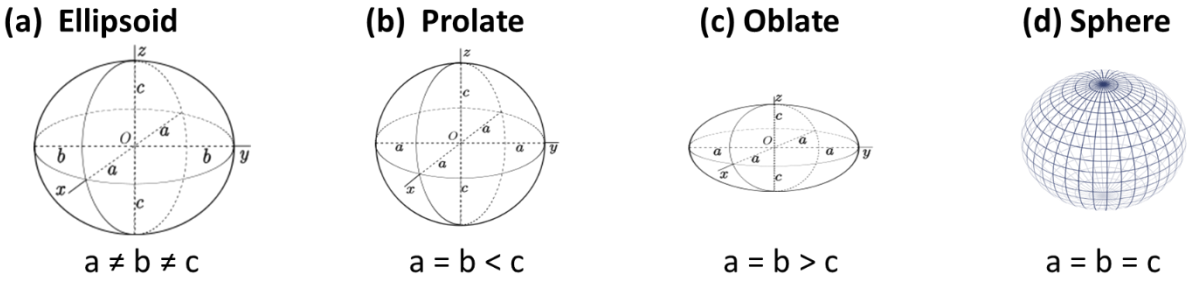

Figure VI. 23 Type of ellipsoid corresponds to semi-principal axes a, b, and c.

We saw in the previous paragraphs that when we fit the SE data, the resonance spectral position and width does not always correspond to what is predicted by a simple MG model of spherical gold nanoparticles in a polymer matrix. We know, from the previous work of Kévin Ehrhardt[12] and Julien Vieaud[13], that this could be due to either non-spherical shape of the nanoparticles, or interparticle couplings, which can be

modeled by non-spherical polarizabilities of the gold NPs. In this section, we are going to give simulations of the SE signal for lamellar nanocomposites with various shapes of ellipsoid.

Ellipsoid is a closed quadratic surface that is a three dimensional analogue of an ellipse (see Figure VI. 23), where a_1, a_2 and a_3 are called the semi-principal axes (see Equation 6- 6).

Equation 6- 6
$$\frac{x^2}{{a_1}^2}+\frac{y^2}{{a_2}^2}+\frac{z^2}{{a_3}^2}=1$$

a_1, a_2 and a_3 correspond to the semi-major axis and semi-minor axis of the appropriate ellipses (see Figure VI. 23). Sphere is a particular case when $a_1=a_2=a_3$, while when $a_1=a_2<a_3$ ($a_1=a_2>a_3$) it is called prolate (oblate). Of course there will be some cases of $a\neq b\neq c\neq a$, we are going to discuss the simple cases with a revolution symmetry: sphere, prolate and oblate in this section.

The depolarization factors N_i in ellipsoid is shown in Figure VI. 24. It can be calculated by

Equation 6- 7
$$N_i=\frac{a_1a_2a_3}{2}\int_0^\infty\frac{dq}{(a_i{}^2+q)f(q)}$$

Where $f(q)=\sqrt{({a_1}^2+q)({a_2}^2+q)({a_3}^2+q)}$

The depolarization factors have the following properties $N_1+N_2+N_3=1$. If $N_1=N_2=1/3$ the particle is a sphere.

In the two particular cases of ellipsoids, prolate ($a_1>a_2=a_3$) and oblate ($a_1=a_2<a_3$), their depolarization factors are described in Equation 6- 8 and Equation 6- 9, respectively.

Equation 6- 8
$$N_1=\frac{1-e^2}{e^2}\left[-1+\frac{1}{2e}ln\left(\frac{1+e}{1-e}\right)\right]$$

Where the excentricity e is defined by

$$e^2=1-\frac{{a_2}^2}{{a_1}^2}$$

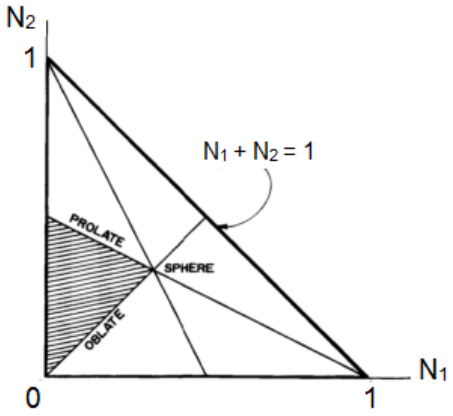

Figure VI. 24 the shape of the ellipsoids as a function of the depolarization factors N_1 and N_2. The gray area corresponds to the case $N_1 < N_2 < N_3$. The spheres are located on the central point of the triangle, the intersection of the different line segments (figure from Bohren and Huffman[21]).

Equation 6- 9 $$N_1 = \frac{g(e)}{2e^2}\left[\frac{\pi}{2} - arctan(g(e))\right] - \frac{g^2(e)}{2}$$

Where $g(e) = \sqrt{\frac{1-e^2}{e^2}}$ and $e^2 = 1 - \frac{{a_3}^2}{{a_1}^2}$

The polarizability of a nanoparticle relates the dipolar moment **p**, which the NP will acquire when submitted to an electric field E, to the field: **p**=α**E**. The polarizability of an ellipsoid is different depending on the direction of the field, shown as following matrix:

$$\bar{\bar{\alpha}} = \begin{pmatrix} \alpha_x & 0 & 0 \\ 0 & \alpha_y & 0 \\ 0 & 0 & \alpha_z \end{pmatrix}$$

By definition, the depolarization factor Ni is a geometrical factor in which the complexity of the geometrical calculation is hidden. The polarizability can then be expressed with a simple expression

$$\alpha_i = V\frac{\varepsilon_p - \varepsilon_h}{\varepsilon_h + N_i(\varepsilon_p - \varepsilon_h)}$$

Where N_i is the depolarization in the direction i.

The model (see Figure VI. 25) used for simulation is based on the structure we fabricated by PS-P2VP with layer thickness 20 nm. The material PS and P2VP can be described by New amorphous with the parameters listed in Table VI. 7. The model considers a lamellar stack, as shown in the Figure VI. 25 with nanocomposite layers described as effective medium consistsing of mixture of P2VP with 20% in volume fraction of the non-aligned ellipsoidal gold nanoparticles following Maxwell-Garnett theory. The gold nanoparticle used in the model are in Figure VI. 2. The only variable parameter in the simulation is the shape of ellipsoid with N_1 (see Figure VI. 24).

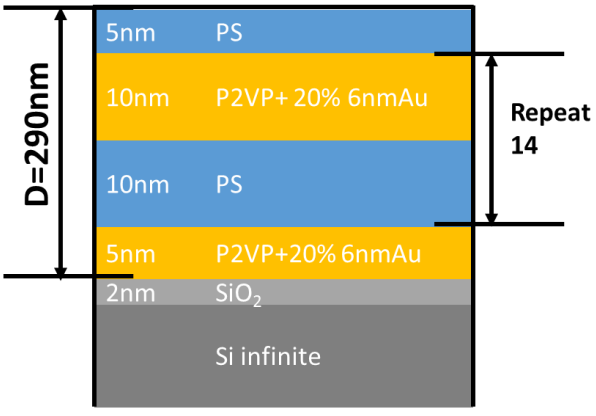

Figure VI. 25 model used for simulation

When we assume the whole samples as a bulk material including silicon wafer and all the layers, the pseudo-permittivity <ε> was simulated by the DeltaPsi software and is plotted in Figure VI. 26 (note not the real permittivity). It gives primary indications

on the optical responses from various ellipsoid particles. As the value of depolarization factor approaches 1/3, the value face sphere, the peak caused by the resonance of gold at 1.925 eV to 2.1 eV (λ ranging from 644.1 nm to 590.3 nm) is the strongest. Once the shape of particles tends to be oblate or prolate, the peak has a red shift and the resonance becomes weaker.

Table VI. 7 Parameters of PS and P2VP used in New amorphous equations

Parameters	n_∞	ω_g	f_j	ω_j	Γ_j
PS	1.541	3.713	0.124	5.408	1.728
P2VP	1.460	2.059	0.017	6.922	0.608

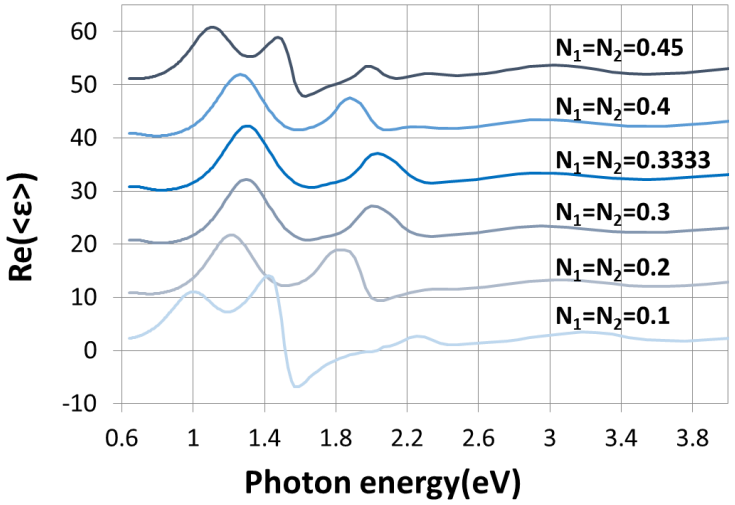

Figure VI. 26 the real part of <ε> in various value of depolarization factor N_1, whose values correspond to the shape of the ellipsoid in Figure VI. 24. The curves are vertically shifted for clarity.

Using ellipsoidal particles in the model did not, however, improve much the fits obtained in our systems, compared to a TL fit as presented before.

VI.4 Effect of the volume fraction of gold particles on the optical properties

As we discussed in VI.2, we know that the film thickness have negligible influence on the optical properties and the film with bilayer thickness 31nm have the strongest resonance for a given number N of impregnation cycles. We also know that the volume

fraction of gold particles plays an important role in optical responses based on previous analysis. In order to study the complete optical properties and determine if we can access hyperbolic metamaterials, we chose a lamellar nanocomposite structures of 12~14 layers with characteristic size ca. 30 nm and various volume fraction of gold to discuss the possibility of the sample to have hyperbolic properties[14,15], based on the following features: the material presents a high degree of order and a uniaxial symmetry with the lamellar phase in parallel alignment, it has a characteristic size 30 nm<< 500 nm (wavelength of gold NPs resonance) and combines a gold nanoparticles response (ε<0) and a polymer layer response (ε>0). In this section, we are going to study the volume fraction of gold nanoparticles influences the optical properties and also demonstrate that the studied system achieves the hyperbolic metamaterial regime.

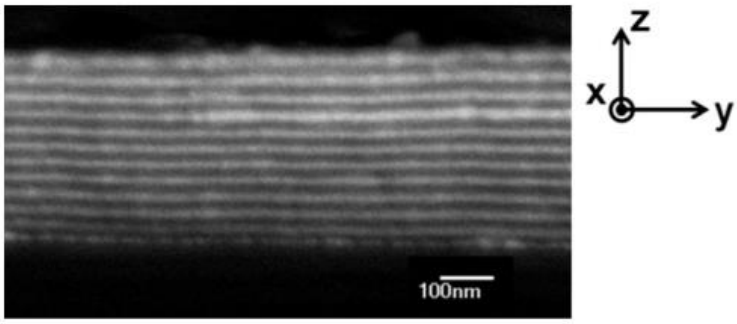

Figure VI. 27 Backscattering scanning electron microscopy side-view image (SEM) of a 370 nm-thick film of alternating layers of poly(styrene) (PS, appearing black) and Au nanoparticles: P2VP nanocomposite (NC, appearing white). The lower and upper black domains of the micrograph are the substrate and the air, respectively. The trihedral indicates the ordinary ((x,y) or //) and extraordinary (z) directions.

VI.4.1 Structure details and measurement

The studied samples were fabricated by poly(styrene)-*block*-poly(2-vinylpyridine) (M_n25000-25000, PDI 1.06), with lamellar period ca.30nm. The fabrication description can be found in the Chapter III.1.1.2. The film thicknesses were measured by SE (spectroscopic ellipsometry) before gold loading. The film-bearing wafer is dipped into an Au salt (HAuCl4) solution and then into a reducing agent ($NaBH_4$) solution. We repeat the gold loading process for N cycles (N from 0 to 30 see Chapter IV.2.2). In the case of gold, we know that when N=5 and N=10, these correspond to a volume fraction of gold in the PVP layers of ca. 10% and ca. 20 % according to the QCM study (see Chapter IV.3.3).

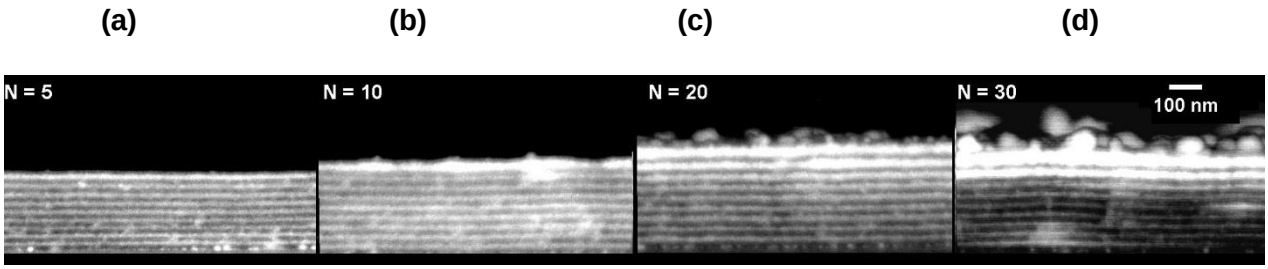

Figure VI. 28 Backscattering scanning electron microscopy side-view image (SEM) of the 265 nm-thick film of alternating layers of pure polymer (PS, appearing black) and of Au nanoparticles:P2VP nanocomposite (NC, appearing white), for a number of cycles of gold impregnation and reduction of N=5 (a), 10 (b), 20 (c), 30 (d).

A structure of alternating pure PS and (NC) (Au nanoparticle plus P2VP nanocomposite) layers is produced and measured by SEM (Figure VI. 28) in different values of N=5, 10, 20 and 30. Optical studies of the film were performed at different steps along the fabrication process by SE, so that the same film was investigated for different values of N, which we will refer to in the following as “kinetic” measurements.

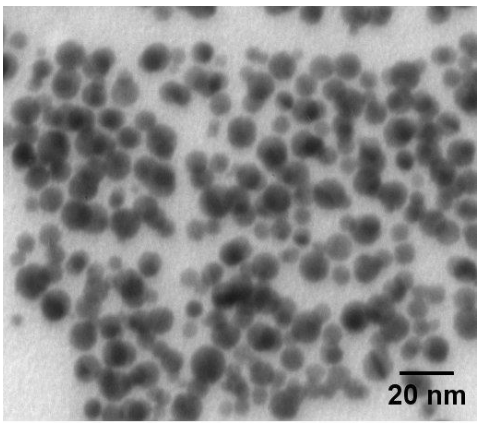

Figure VI. 29 Transmission electron microscopy (TEM) image obtained with a grid on which was deposited a drop of the dispersion obtained by full dissolution of a film, at the step N=20 of the fabrication process, in a good solvent of the diblock copolymer. The image evidences gold nanoparticles of mean diameter 7 nm. Note that this observation technique being destructive, it was performed on different samples than the ones studied by SEM and VASE.

The nanoparticles inside films were analysis by TEM and SAXS. Both techniques measured a dispersion obtained through the full dissolution of the samples in a good solvent of the diblock copolymer at the end of the fabrication process (detail see Chapter VI.2.3.2). Results show that the NC layers are composed of individual gold nanoparticles (NPs) of relatively homogeneous size (diameter D ~ 7±2 nm). Figure VI. 29 shows an example of the results obtained by TEM in the case of N=25. We can

therefore infer that such 7 nm-gold NPs are dispersed with no specific order and surrounded by a P2VP matrix in NC layers.

VI.4.2 Optical responses

Let us now present and discuss the optical parameters that were extracted from the ellipsometric study for the fabricated nanostructures[24]. This part of analysis was done in collaboration with Morten Kildemo, from the Norwegian University of Science and Technology (NTNU), in Trondheim, using the analysis software called Complete Ease from J.A. Woolam Company using spline function.

VI.4.2.1 Primary results

The “kinetic” VASE information was obtained by recording the full spectra every five gold loading cycles. This turns out to be very important information about the stacked structure as it is progressively evolving upon increased gold absorption in the layers.

From Figure VI. 30, we can see for the initial lamellar structure (before infiltration, N=0), periodic oscillations typical of interferences driven by reflections at the air/film and film/substrate interfaces, as both PS and P2VP polymers are transparent in the studied energy range. As N is increased, the extrema shift toward lower energies and the fringe spectral separation decreases indicating an evolution possibly combining an increase in the total film thickness and a change in the effective dielectric function of the NC (Au nanoparticles:P2VP) layers. Moreover, their amplitude decreases markedly as

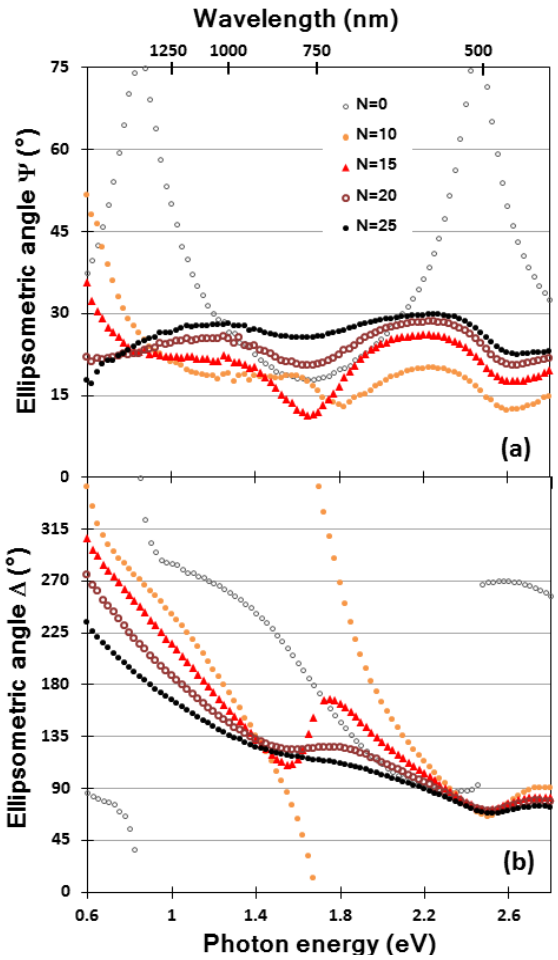

Figure VI. 30 Evolution of the measured ellipsometric angles Ψ and Δ as a function of the photon energy for an angle of incidence of θ_o=65° and different values of N between 0 and 25. The spectroscopic features are damped as N increases, due to the increasing absorption of the film

the volume fraction of Au increases and the absorption of light by the LSPR and interband transitions in Au nanoparticles becomes dominant. Nevertheless, the interference features are damped but not rubbed out after successive infiltrations, showing that light does still travel through the film thickness and that the material remains at least partially transparent in this spectral range.

VI.4.2.2 Nanocomposite (NC) layers

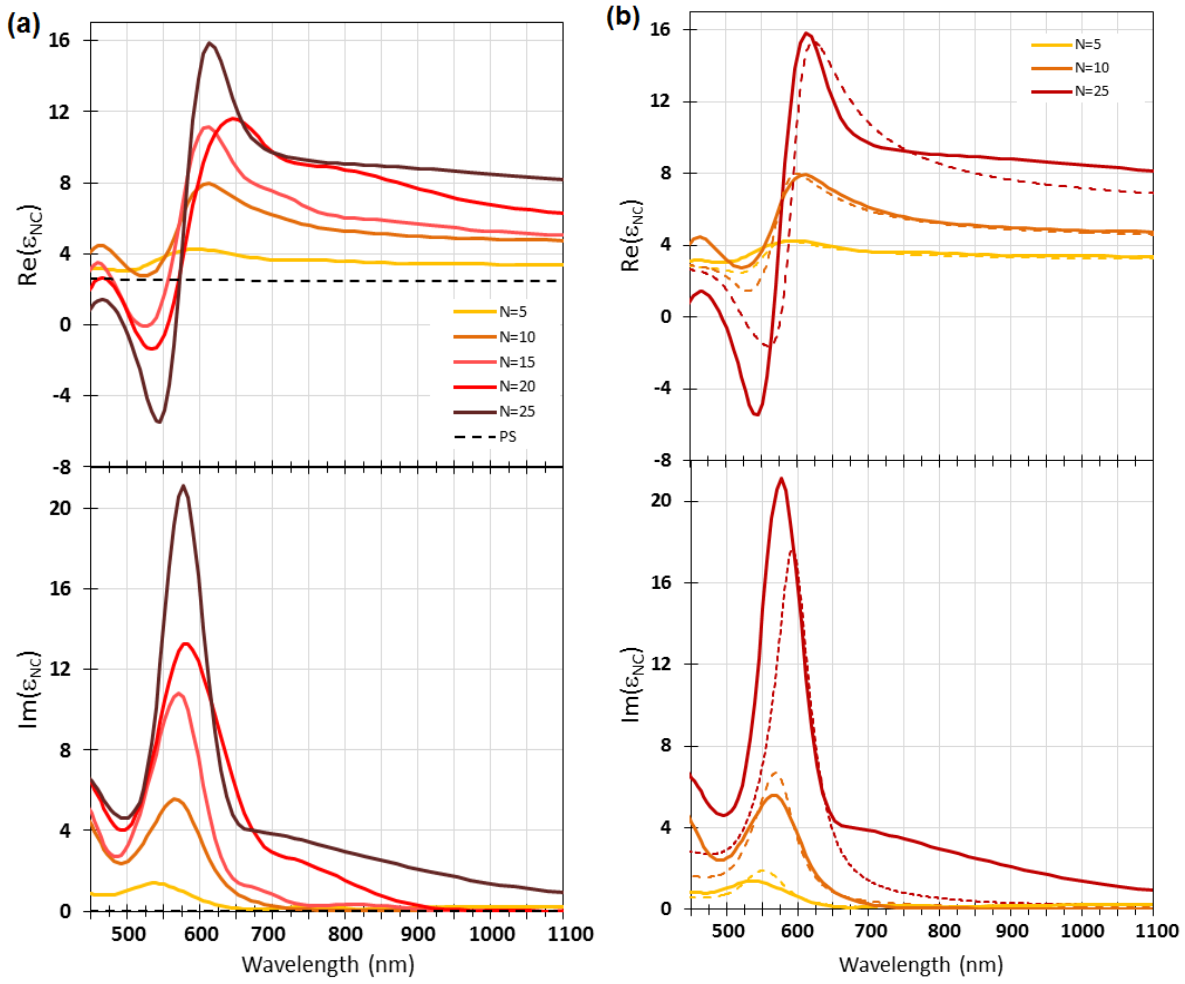

Figure VI. 31 (a)Real (upper plot) and imaginary (lower plot) parts of the dielectric function ε_{NC} of the NC layers in the lamellar stack, as extracted from the SE study for different values of N between 5 and 25. The dotted line is the dielectric function used for the PS layer, with $Im(\varepsilon_{PS})=0$. The resonance amplitude varies as N increases, due to the increasing introduction of plasmonic NPs.

We start by extracting the optical properties of the individual NC layers with model A (Figure VI. 1(a)) by making up the lamellar stack. From SEM images, we fully characterize the structure of the studied multistack films. As can be seen on an example for N=5(Figure VI. 28), the film is composed of 9 bilayers of (PS) + (NC),

where the thickness of (PS) and (NC) $d_{poly}=d_{NC}$=14nm, with an additional (NC) layer of 6 nm along the substrate surface and an additional (PS) layer of 6 nm along the air. The additional homogeneous layer of thickness d_{SAu} in the model A is to account for the uncontrolled gold deposit layer on top of films. The thickness of this Au pollution layer (d_{SAu}) was found to increase from 4 nm at N=5, to 20 nm at N=25, which is in agreement with the SEM observations. In fact, for N ≤ 15, the results show very little variation when removing the top layer from the model (d_{SAu}=0), confirming its presence is negligible.

The resulting dielectric functions are consistent with what can be expected for a disordered composite of spherical inclusions within a homogeneous matrix. In fact, such composite can be described, at least at small gold volume fraction by the Maxwell-Garnett effective medium function[16] (Equation 6- 1). The Figure VI. 31(b) shows how the extracted values of ε_{NC} compare with those of ε_{MG}, calculated using Equation 6- 1 and a dielectric function for gold modified from the Johnson & Christy tabulated data[4,7] in order to take into account finite size effects, which we used before.

For small N ≤ 5 (small gold fraction), the agreement is very good on all the red part of the spectrum, for wavelengths above the resonance value at ~580 nm, and satisfying at lower wavelengths (Figure VI. 31(b)).

When pushing the Maxwell-Garnett effective medium approximation (MG-EMA) to higher N, a degraded agreement is naturally expected: it remains nevertheless reasonably good especially for wavelengths above 580 nm. These partial agreements provide rough estimates of the loading concentration in gold: we find N=5 to correspond to a MG-extracted value of f=7%, and N=10 and N=25 to approximately f=18% and f=31%, respectively. It is in good agreement with the QCM results on similar systems (see the Chapter IV.3.3).

Finally, the resulting dielectric function $\varepsilon_{NC}(\lambda)=\varepsilon_{NC}'(\lambda)+ i\ \varepsilon_{NC}''(\lambda)$ for the NC layers in the superlattice, from N=5 to N=30, are shown on Figure VI. 31(a). The optical properties of the Au-loaded polymer NC layer are dominated by a resonance at λ=580 nm, close to that expected [13] for the plasmon resonance of the gold NPs present in the NC layers, with an amplitude increasing with the number of loading cycles N, as expected. In particular, the NC medium presents a pseudo-metallic behavior beyond N=15 with ε_{NC}'< 0 on a large wavelength range, of width 80 nm for N=25 and 50 nm

for N=20. This “pseudo-metal” behavior being resonant in nature is associated with a significant level of losses as can also be seen on Figure VI. 31(a).

VI.4.2.3 Uniaxial effective medium

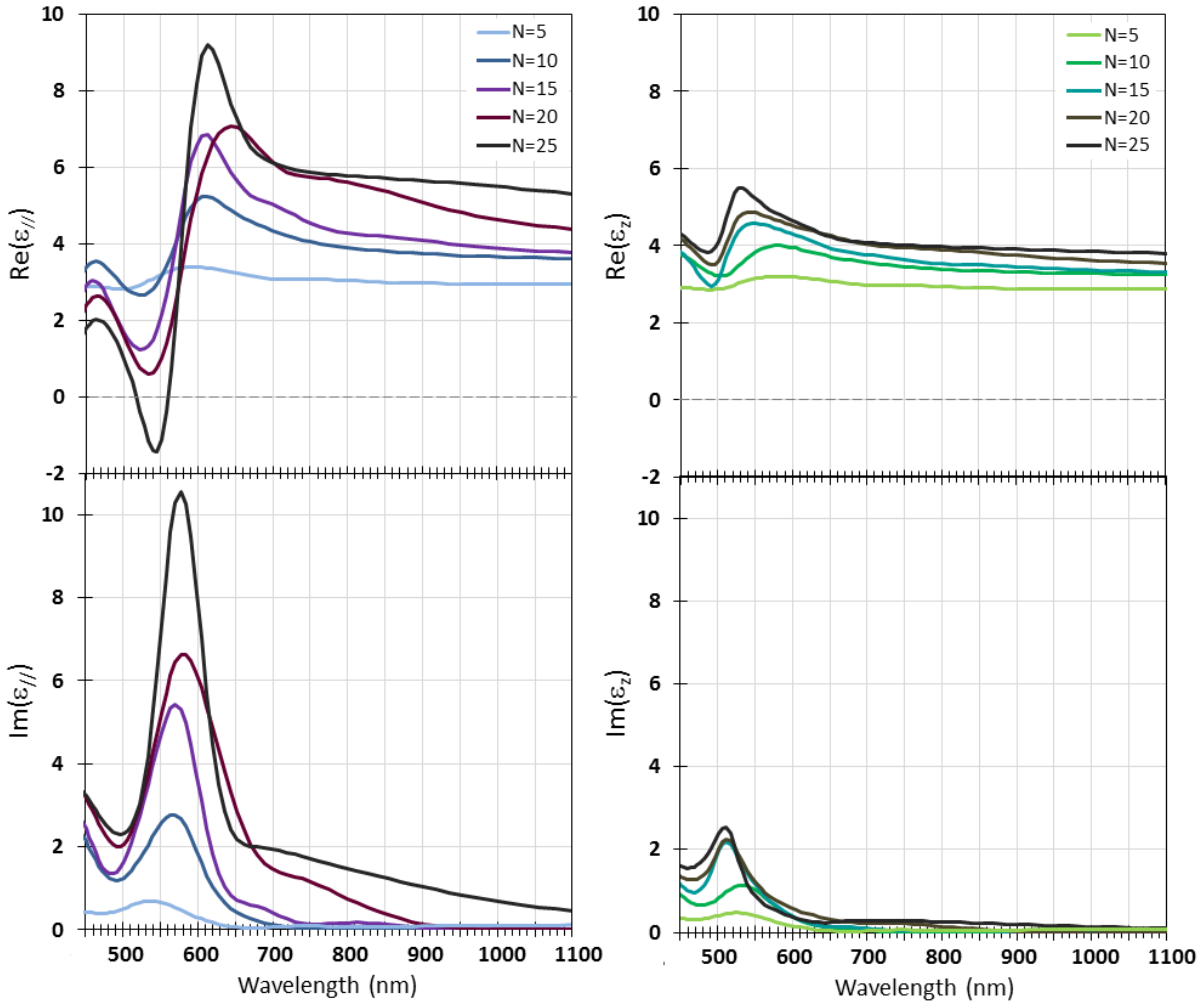

Figure VI. 32 Real (upper plots) and imaginary (lower plots) parts of the components ε// (left) and εz (right) of the lamellar nanoplasmonic thin films, as computed using Equation 6- 2 and Equation 6- 3 from the Model A SE extractions for different values of N between 5 and 25 (MG-extracted f between 7% and 31%,). The resonance amplitude varies as N increases, due to the increasing volume fraction of introduced plasmonic nanoparticles.

Following the second step of Model A, the dielectric constants of the uniaxial effective medium $\varepsilon_{//}(\lambda)=\varepsilon_{//}'(\lambda) + \varepsilon_{//}''(\lambda)$ and $\varepsilon_z(\lambda)=\varepsilon_z'(\lambda) + i\,\varepsilon_z''(\lambda)$ are first determined using the optical properties of the fitted Au loaded polymer layers (NC) and the PS layer, through Equation 6- 2 and Equation 6- 3.The resulting effective optical properties are shown inFigure VI. 32.

The analysis of the SE data through direct inversion as a uniaxial effective medium (Model B-1) leads to a similar or better goodness-of-fit, compared to Model A. Figure VI. 33 shows the comparison between the components $\varepsilon_{//}$' (λ) extracted for N=15, N=20 and N=25 using Models A and Model B-1. Both models were found to give highly similar results, within the experimental accuracy, in particular for $\varepsilon_{//}$, although ε_z shows a little more variation between the models. The agreement between the extractions of the two models substantiates the main result of this experimental study showing that the dielectric functions $\varepsilon_{//}$ and ε_z have opposite signs in a finite wavelength range.

As is shown on the Figure VI. 32, the dielectric functions $\varepsilon_{//}$ and ε_z both present a resonance at the wavelength λ=580 nm (or alternatively a photon energy of 2.1 eV), close to the plasmon resonance of the gold nanoparticles. However, the resonance amplitudes of the two components significantly differ. In the case of ε_z, this amplitude is limited and varies only little with the value of N, in direct relation with the amount of gold nanoparticles in the nanostructure. By contrast, the resonance of $\varepsilon_{//}$ is stronger and its amplitude significantly increases with N, reaching a regime of negative values beyond N=20. As a result, strong artificial anisotropies with different characteristics are found across the spectrum.

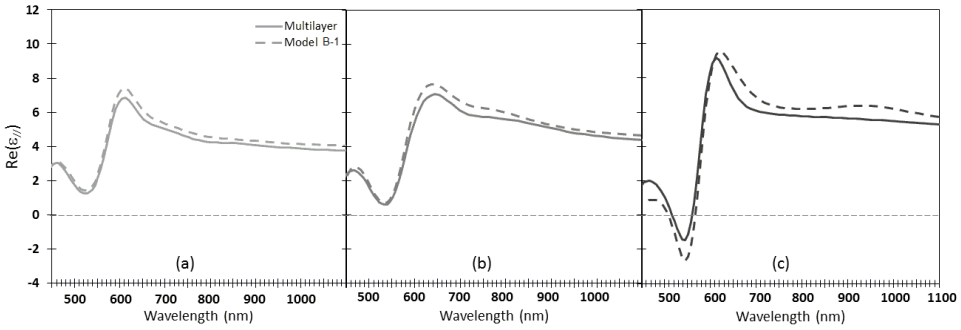

Figure VI. 33 Comparison between the real part of the ordinary components in the cases of the multilayer (Model A, continuous lines) and uniaxial model (Model B-1, dashed lines) for N=15 (a), N=20 (b) and N=25 (c).

Finally note that attempting to combine the top Au deposit layer (of thickness d_{SAu}) into the effective uniaxial medium smears its properties and does not produce negative $\varepsilon_{//}$, in contrast with the analyses based on the two used models. Therefore, future studies will aim at lifting off the uncontrolled detrimental gold deposit top layer. In the current analysis, it is regarded as an experimental artifact whose analysis needs to be isolated from the analysis of the targeted nanostructure below it.

VI.4.2.4 Hyperbolic dispersion relation

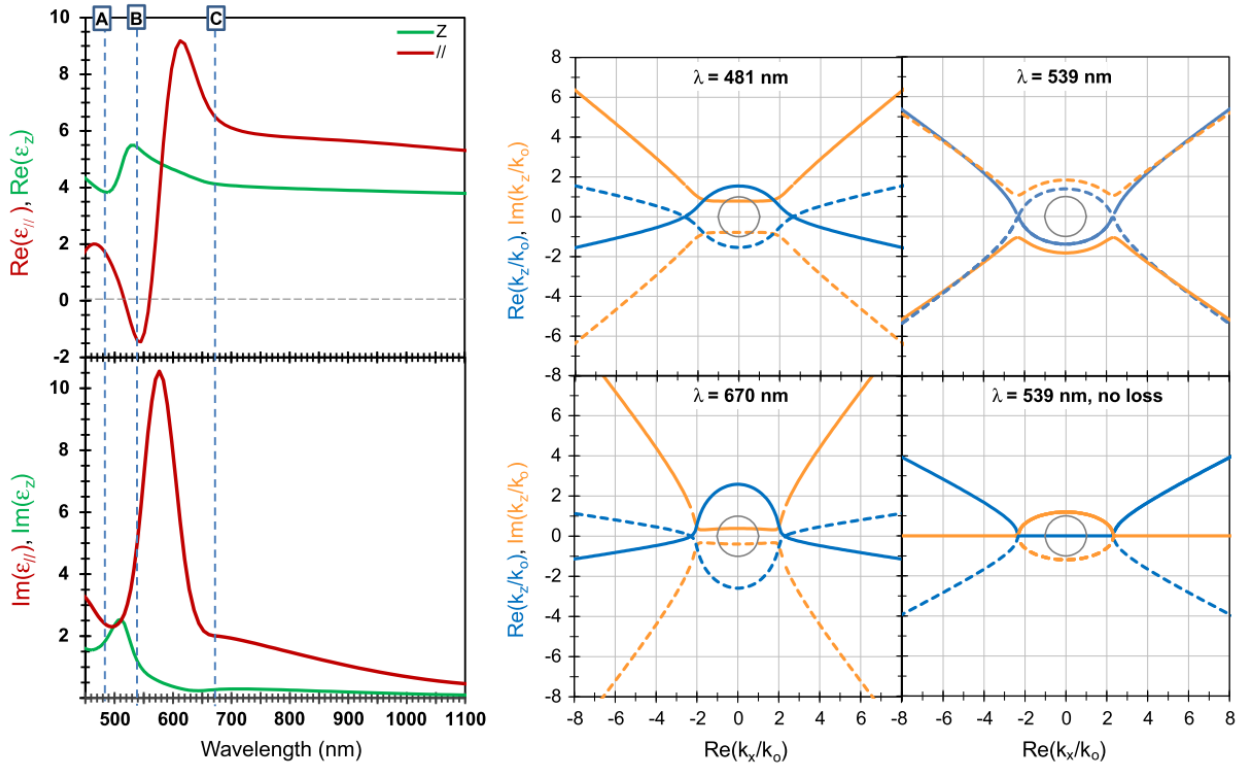

Figure VI. 34 Left: Parallel (red continuous line) and perpendicular (green dotted line) components of the uniaxial dielectric function of the lamellar nanoplasmonic stack for N=25 (f=30% in the NC layers). The vertical blue dashed lines indicate the three conditions (A: λ=481 nm; B: λ=539 nm; C: λ=670 nm) chosen for the calculation of the dispersion relations, which are displayed in the right part. Right: Dispersion relation at k_y=0, showing the real (blue lines) and imaginary (orange lines) parts of the k_z component of the wave-vectors in the material as a function of the k_x component. Thick continuous and dashed lines correspond to opposite solutions of Equation 1-22. The thin black continuous circle corresponds to the wavevectors propagating in air $k_x^2 + k_z^2 = k_o^2$, shown for reference. The plot labeled D, shown for reference, is a fictional hyperbolic case without losses: at λ=539 nm, ε//' and εz' are set to the values for case B, whereas ε//" and εz" are set to zero.

We consider three regions of strong anisotropy denoted A: $\varepsilon_z' > \varepsilon_{//}' > 0$ (for example λ=481nm), B: $\varepsilon_{//}' < 0 < \varepsilon_z'$ (λ=539 nm) and C: $\varepsilon_{//}' > \varepsilon_z' > 0$ (λ=670 nm) indicated on Figure VI. 34, which displays the values of $\varepsilon_{//}$ and ε_z for N=25 (corresponding to a MG-extracted f=31%). The iso-frequency dispersion diagrams of the constitutive material can be produced using the experimental dielectric functions and are also shown on Figure VI. 34. For each frequency ω considered (or equivalently, excitation wavelength), two wave-vector ranges can be distinguished $|k_x| < k_x^*|$ and $|k_x| > k_x^*$, with

Equation 6- 10 $k_x^* = k_o\sqrt{\frac{\varepsilon_z'^2+\varepsilon_z''^2}{\varepsilon_z'}}$ *and* $k_o^2 = \varepsilon_o\mu_o\omega^2$

Cases A and C present typical elliptical dispersion diagrams,when both ε//' and εz' are positive: one can observe, for small values of $|k_x|$ ($|k_x| < k_x^*$), two symmetrical elliptical branches where the real part of kz is significantly larger than the imaginary part, typical of an attenuated propagation. For larger $|k_x|$ ($|k_x| > k_x^*$), hyperbolic branches are observed, which are not usually present in ideal elliptical cases, and which are characterized by a predominantly evanescent behavior (imaginary part of kz much larger than the real part). In the case B when ε//' < 0 < εz', we find that the dispersion diagram present hyperbolic branches for $|k_x| > k_x^*$, as well as elliptical curves at small k_x.

These diagrams are related to the strong optical anisotropy of the lamellar stack, obtained as a consequence of the resonant nature of the NC layers. The significant losses (Re(kz) ≈Im(kz)) associated with the hyperbolic propagation are another consequence of this resonant nature.

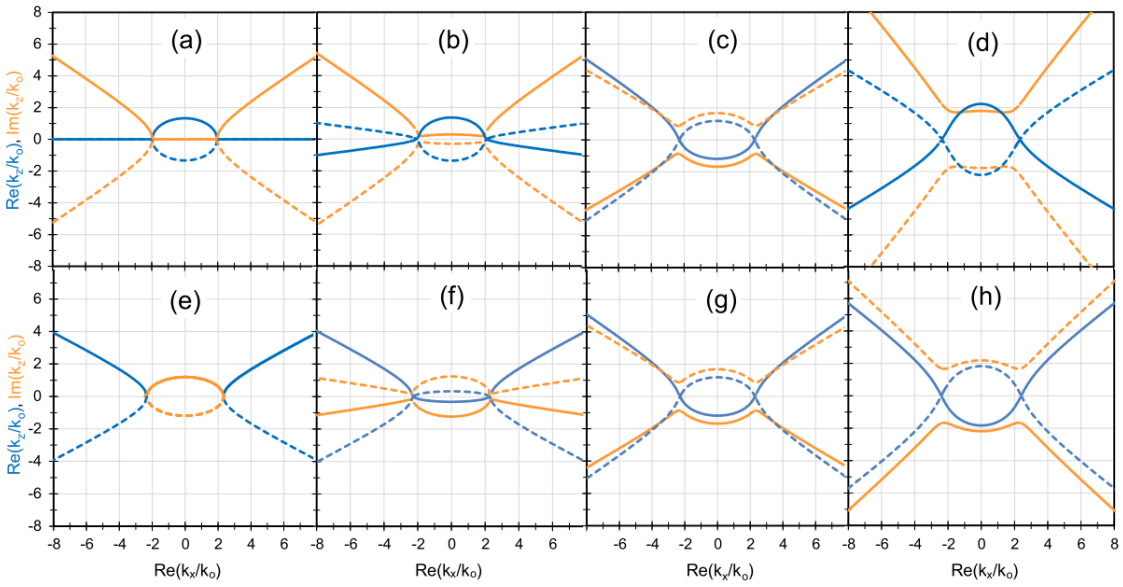

Figure VI. 35 Dispersion relations at k_y=0, showing the real (blue line) and imaginary (orange line) parts of the k_z component of the wave-vectors in the material as a function of the k_x component. Continuous and dashed lines correspond to opposite solutions of Equation 1-22. The plots (a)–(d) (resp. (e)-(h)) correspond to fictional elliptical (resp. hyperbolic) cases with ε//' and εz' set to the values for case C (resp. B), and ε//"=4 εz"=0 (a) and (e); ε//"=4 εz"=0.8 (b) and (f); ε//"=4 εz"=4 (c) and (g); and ε//"=4 εz"=8 (d) and (h).

To understand the significance of these dispersion curves, it is useful to recall the usual description of elliptical and hyperbolic media. The ideal cases are displayed in the Figure VI. 35 a and d, where two fictitious materials are considered with the real parts of the permittivity tensor set to the experimentally determined values in cases C ($\varepsilon_{//}$'=1.77, ε_z'=3.85) and B ($\varepsilon_{//}$'=-1.42, ε_z'=5.42); and with imaginary parts set to zero: $\varepsilon_{//}$"=ε_z"=0 (lossless materials). We represent the dispersion relation (Chapter I.2.2 Equation 1-22) in the k_y=0 plane. In the elliptical ideal case (Figure VI. 35 (a)), the propagative modes (Re(k_z) ≠0) are restricted to small wavenumbers ($|k_x| < k_x^*$), while all possible large-$|k_x|$modes are forbidden[17] and only purely evanescent (Re(k_z)=0). In the hyperbolic ideal case (Figure VI. 35(d)), we observe the opposite situation, with forbidden, purely evanescent modes (Re (k_z)=0) for small $|k_x|$ and purely propagative modes (Re (k_z) ≠ 0, Im(k_z)=0) for large $|k_x|$, the latter potentially providing the super-resolution property. The hyperbolic branches for $|k_x| < k_x^*$present the shape of a one-fold hyperboloid, with a forbidden gap in k_x, as expected for a "metallic" [18] or type II[19] hyperbolic medium, when the permittivity tensor ε has two negative and one positive components.

To depart from these idealized situations, let us now introduce a small amount of losses in the materials, see Figure VI. 35(b) and (e) (here we arbitrarily took $\varepsilon_{//}$"=4 ε_z"=0.8): the dispersion curves become hybrid rather than purely elliptical or hyperbolic and present finite Re(k_z) and Im(k_z) at all values of k_x, allowing previously forbidden modes to propagate weakly. Purely evanescent waves for the hyperbolic medium at small $|k_x|$ and the elliptical medium at large $|k_x|$ become weakly propagative with Re(k_z) ≠ 0 and Im(k_z) >> Re(kz). The large-$|k_x|$ branches of the hyperbolic medium (Figure VI. 35 f) present the same one-fold hyperboloid shape as that of the no-loss case (Figure VI. 35 e). Interestingly, when the imaginary parts $\varepsilon_{//}$" and ε_z" are further increased to simulate more losses (Figure VI. 35 (c-d) and (g-h)), the modification of the propagative and evanescent modes continues to occur, so much so that over most of the whole $|k_x|$ range, more or less strongly attenuated, propagative modes are observable. In particular, we note that the intermediate hyperbolic cases (as represented in Figure VI. 35 f and g) still present predominantly propagative modes at large $|k_x|$, which can support super-resolution properties: these are the cases corresponding to our experimental system in the B situation in Figure VI. 34.

In conclusion, the volume fraction of gold nanoparticles in the nanocomposite layers plays an important role for defining the position and amplitude of the resonance. The results also demonstrate the capacity of our bottom-up self-assembled multilamellar stack to respond as a hyperbolic effective medium in a given region of the visible spectrum (520 < λ < 560 nm). In the hyperbolic region, the dispersion relation allows propagative modes for large values of $|k_x|$, potentially providing super-resolution. These hyperbolic modes are however significantly attenuated due to the lossy nature of the media, in which the hyperbolic property is obtained from the resonant nature of the permittivity. These detrimental losses need now to be minimized by tuning the nature, size, size dispersity and organization of the nanoparticles. Furthermore, the same self-assembly methodology for lamellar stacks fabrication could be used with other nanoparticles with a resonance of better quality factor, or with a lamellar system including gain species (fluorophores or quantum dots) which could amplify the plasmons and compensate the losses. In any case, we have demonstrated for the first time the possibility of using a self-assembly methodology for the fabrication of bulk hyperbolic material, which opens new fabrication routes for metamaterials aiming at super-resolution lenses.

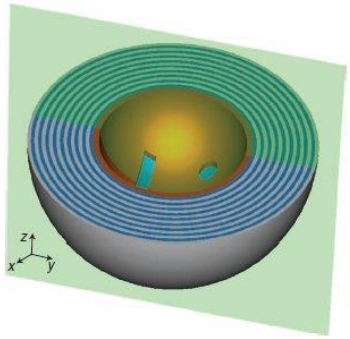

Figure VI. 36 Working principle of the spherical hyperlens: Schematic of a spherical hyperlens comprised of nine pairs of silver and titanium oxide layers[20].

Moreover, the self-assembly methodology we have developed could be beneficial for the fabrication of multilayer films of non-planar geometries, such as what is used in devices in which hyperbolic metamaterials are used as super-resolution enlarging lenses[20].

References

1. Centeno, E. & Moreau, A. Effective properties of superstructured hyperbolic metamaterials: How to beat the diffraction limit at large focal distance. Phys. Rev.

B 92, 45404 (2015).

2. Belov, P. A. & Hao, Y. Subwavelength imaging at optical frequencies using a transmission device formed by a periodic layered metal-dielectric structure operating in the canalization regime. Phys. Rev. B 73, 113110 (2006).

3. Kang, X.-B., Tan, W. & Wang, Z.-G. Validity of effective medium theory for metal-dielectric lamellar gratings. Opt. Commun. 284, 4237–4242 (2011).

4. Vieaud, J. et al. Effective medium description of plasmonic couplings in disordered polymer and gold nanoparticle composites. Thin Solid Films 603, 452–464 (2016).

5. Wold, S. Spline functions in data analysis. Technometrics 16, 1–11 (1974).

6. Unser, M., Aldroubi, A. & Eden, M. B-spline signal processing. I. Theory. IEEE Trans. signal Process. 41, 821–833 (1993).

7. Johnson, P. B. & Christy, R.-W. Optical constants of the noble metals. Phys. Rev. B 6, 4370 (1972).

8. Jellison Jr, G. E. & Modine, F. A. Parameterization of the optical functions of amorphous materials in the interband region. Appl. Phys. Lett. 69, 371–373 (1996).

9. Chen, H. & Shen, W. Z. Perspectives in the characteristics and applications of Tauc-Lorentz dielectric function model. Eur. Phys. J. B-Condensed Matter Complex Syst. 43, 503–507 (2005).

10. Zhou, M., Bron, M. & Schuhmann, W. Controlled synthesis of gold nanostructures by a thermal approach. J. Nanosci. Nanotechnol. 8, 3465–3472 (2008).

11. Zheng, L., Liu, J., Ding, Y. & Han, Y. Morphology evolution and structural transformation of solution-processed methanofullerene thin film under thermal annealing. J. Phys. Chem. B 115, 8071–8077 (2011).

12. Ehrhardt, K. Mesures, modélisations et simulations numériques des propriétés optiques effectives de métamatériaux auto-assemblés. (2014).

13. Vieaud, J. Propriétés optiques effectives de films composites de polymère et de nanoparticules d'or. (2011).

14. Ponsinet, V. in Polymer Surfaces in Motion 73–97 (Springer, 2015).

15. Lazzari, M. & De Rosa, C. Methods for the Alignment and the Large- Scale Ordering of Block Copolymer Morphologies. Block Copolym. Nanosci. 191–231 (2006).

16. Garnett, J. C. M. Colours in metal glasses and in metallic films. Philos. Trans. R. Soc. London Ser. A 203, 385–420 (1904).

17. Repän, T., Lavrinenko, A. V & Zhukovsky, S. V. Dark-field hyperlens: Super-resolution imaging of weakly scattering objects. Opt. Express 23, 25350–25364 (2015).

18. Ishii, S., Kildishev, A. V, Narimanov, E., Shalaev, V. M. & Drachev, V. P. Sub-wavelength interference pattern from volume plasmon polaritons in a hyperbolic medium. Laser Photon. Rev. 7, 265–271 (2013).

19. Ferrari, L., Wu, C., Lepage, D., Zhang, X. & Liu, Z. Hyperbolic metamaterials and their applications. Prog. Quantum Electron. 40, 1–40 (2015).

20. Rho, J. et al. Spherical hyperlens for two-dimensional sub-diffractional imaging at visible frequencies. Nat. Commun. 1, 143 (2010).

21. Bohren, C. F. & Huffman, D. R. Absorption and scattering of light by small particles. (2008).

22. O.Hunderi et al. Effective-medium description of superlqttices and effect on non-locqlity. Superlqtt. Micro. 3, 193-198 (1987.)

23. Toudert, J. et al. Plasmonic Optical Interferences for Phase-Monitored Nanoscale Sensing in Low-Loss Three-Dimensional Metamaterials. ACS photonics 2, 1443−1450 (2015).

24. Wang, X. et al. Hyperbolic-by-design self-assembled metamaterial based on block copolymers lamellar phases. Opt. Laser Technol. 88, 85–95 (2017).

General conclusion

Hyperbolic metamaterials have appeared about ten years ago. They consist in anisotropic metal-dielectric nanocomposites and they have innovative optical properties for light of wavelength greater than the characteristic size of the internal structure of the material. In order to have access to these new properties in visible light, resonant nano-objects must be organized on a scale of a few tens of nanometers.

Our strategy has been to fabricate such structures by assembling gold nanoparticles in ordered phases of nanostructured diblock copolymers, in order to obtain plasmonic and anisotropic nanocomposites. A state of the art on the different ways of incorporating nanoparticles into a single block of a self-assembled diblock copolymer of lamellar morphology allowed us to define a fabrication methodology taking into account the complexity of these nanocomposite systems and giving access to controlled structures.

Homogeneous thin films of poly(styrene)-block-poly(2vinylpyridine) (PS-block-P2VP) were obtained by spin-coating on silicon wafer. Their thickness is measured precisely by ellipsometry. With certain spin-coating conditions, the thickness of film can be controlled by the concentration of polymer solutions. We optimized the spin-coating conditions sing Taguchi optimization methodology, and determined that the most important factor influencing the thickness of films is the acceleration and deceleration time, with longer times producing thicker films. Typical film thicknesses used in our study lie in the range 300-700nm.

We used commercial PS-block-P2VP symmetrical diblock copolymers with various polymerization degrees. We showed by small-angle X-ray scattering that the PS-block-P2VP copolymers exhibit a lamellar morphology at thermodynamic equilibrium. The results are in good agreement with the generic phase diagram of block copolymers symmetrical compositions. when annealed PS_{102k}-*block*-$P2VP_{96k}$, PS_{25k}-*block*-$P2VP_{25k}$, and $PS_{8.2k}$-*block*-$P2VP_{8.3k}$ with the volume fractions of the P2VP blocks f_{PVP}≈0.5 form lamellar phases with characteristic size α 78 nm, 37 nm and 16 nm, respectively. The characteristic size at scales far below the wavelength of visible light ($\alpha < \lambda/10$). The film structures were studied by electron microscope. In order to

minimize the surface energy, the PVP block has a preferential interaction with the substrate while the PS block prefers the free interface with air. This leads to the asymmetric wetting configuration. Finally, this process combining spin-coating of a relatively dilute polymer solution on a selective surface and thermal annealing, produces a flat and homogeneous film with a parallel alignment of the 3-D organized structures, throughout the thickness of the film between 20 and 700 nm. This ordered structure spans an area as large as the spin-coating process can produce (10*10mm^2 wafers in our case, or larger).

From the aligned lamellar structures, we fabricate the target multilayer nanocomposites consisting in alternate layers of pure polymer and polymer/nanoparticles composite, using two different *in situ* synthesis of gold nanoparticles, namely a one-step method and an impregnation process. Both of the methods take advantage of the amine group in the P2VP domains. The amine group can bind with gold salt. The one-step method consists in blending a gold salt solution with the copolymer before casting the film and letting it reach microphase separation at thermodynamic equilibrium. This method is not efficient because the presence of the gold salt modifies the properties of the copolymer, which does not achieve a lamellar morphology. In the impregnation process, the pure copolymer film is first produced and aligned by a thermal annealing process. Then, the film-bearing wafer is dipped into an Au salt ($HAuCl_4$) solution for 5 mins and then into a reducing agent ($NaBH_4$) solution for 30 s. This process mostly preserves the lamellar structure of the diblock copolymers and realizes the target structure on large areas. Due to the strong insolubility of PS in polar solvents, on the one hand, and the strong affinity of P2VP to Au, on the other hand, Au nanoparticles form selectively within the P2VP layers, thus producing a structure of alternating pure PS and (NC) (Au nanoparticles:P2VP nanocomposite) layers. We developed an impregnation cycles procedure, in order to increase, in a controlled way, the volume fraction of nanoparticles in the (NC) layers, by repeating the double dipping process N times. Each cycle increases the purple color of the film, related to the localized surface plasmon resonance of the nucleated gold nanoparticles. Structural and optical studies of the film were performed at different steps along the fabrication process, so that the same film was investigated for different values of N, which we called “kinetic” measurements. Using scanning electron microscopy (SEM), we fully characterize the structure of the studied multilayer films.

In the case of the impregnation process, we studied the reactants loading process by varying the metal salt (from gold to silver) and the impregnation solvent. The salt solution is diffusing through the PS and PVP layers. The pathway of reactant diffusion is from the top of samples and pass though PS and PVP layers easily. After compare the same process performance in silver. The reactants are diffused though the pathway from the top. Ethanol play an important role in this diffusion, because it is a selective solvent for PVP. In the study of penetration of solvent in multilayers, where the solvent is selective for only one block, the other block will retard the diffusion of the solvent. In addition, even if the solvent also pass though the defects, there is no penetration after several layers. In order to get selectively loading and well penetration of precursor, the solvent of precursors is the key factor.

The gold nanoparticles synthesized in the PS_{25k}-*block*-$P2VP_{25k}$ films were studied by SAXS and TEM. The nanoparticles in the PVP layers present a controlled size around 10 nm. This size can be controlled by the PVP layer thickness (size ca. 17nm). The volume fraction of gold nanoparticles in PVP layers were studied by spectroscopic ellipsometry (SE) and quartz crystal microbalance (QCM) for different values of the number N of impregnation cycles. The SE data were analyzed with a simple multilayer model of alternate polymer and nanocomposite layer, the latter being modeled with a Gannett effective medium law. We find that the amount of gold in the composite layers can be varied up to typically 40 volume%. The data from QCM measurements were analyzed based on the Sauerbrey relation, valid for solid films. The results of both methods gave similar volume fraction of gold f_{Au}: f_{Au}~10% when N=5 and f_{Au}~23% when N=10.

Finally, we analyzed the optical indices for a sample of bilayer thickness 37nm with increasing values of N (from 0 to 25), using spectroscopic ellipsometry. Two models were set up to account for the spectroscopic ellipsometry measurements. The Model 1, is a perfect periodic superlattice with polymer and nanocomposite layer (NC layer), which is considered to determine the optical properties of the individual layers of the stack. The optical properties of the PS layer are fixed to those tabulated. The permittivity ε_{NC} of the NC layers is determined by fitting the Model 1 to the SE data using a BSPLINE function available in the Complete Ease software and using a Maxwell- Garnett Effective medium as an initial guess. From N=5 to N=30 the optical properties of the Au-loaded polymer NC layer are dominated by a resonance at λ~580 nm, close to that expected for the plasmon resonance of the gold NPs present in the

NC layers, with an amplitude increasing with the number of loading cycles N. In the second model (Model 2), we consider the thin film as an anisotropic uniaxial effective medium and each component $\varepsilon_{//}$ and $\varepsilon_{\perp}$ is fitted by a BISPLINE function. This gives similar results as Model 1.

Following the first step of Model 1, the dielectric constants of the uniaxial effective medium $\varepsilon_{//}(\lambda)$ and $\varepsilon_z(\lambda)$ are first determined using the optical properties of the fitted NC and the PS layer. The dielectric functions ε// and εz both present a resonance at the wavelength λ~580 nm (or alternatively a photon energy of 2.1 eV), close to the plasmon resonance of the gold nanoparticles. However, the resonance amplitudes of the two components significantly differ. In the case of ε_z, this amplitude is limited and varies only little with the value of N, in direct relation with the amount of gold nanoparticles in the nanostructure. By contrast, the resonance of $\varepsilon_{//}$ is stronger and its amplitude significantly increases with N, reaching a regime of negative values beyond N=20. As a result, strong artificial anisotropies with different characteristics are found across the spectrum. Then iso-frequency dispersion diagrams of the constitutive material can be produced using the experimental dielectric functions. Results demonstrate the capacity of our bottom- up self-assembled multilamellar stack to respond as a hyperbolic effective medium in a given region of the visible spectrum ($520 < \lambda < 560$ nm). In the hyperbolic region, the dispersion relation allows propagative modes for large values of $|k_x|$, potentially providing super-resolution. We have thus successfully achieved the first self-assembled hyperbolic metamaterials. Their hyperbolic-type propagative modes are, however, significantly lossy, due to the strong absorption associated with the plasmon resonance. An interesting perspective for future work would be to produce similar systems with less lossy resonances, for example based on elongated or silver nanoparticles.

The self-assembly methodology we have developed could be beneficial for the fabrication of multilayer films of non-planar geometries, such as what is used in devices in which hyperbolic metamaterials are used as super-resolution enlarging lenses.